Dynamics of
Open Quantum Systems

Dissertation
zur
Erlangung des Doktorgrades (Dr. rer. nat.)
der
Mathematisch-Naturwissenschaftlichen Fakultät
der
Rheinischen Friedrich-Wilhelms-Universität Bonn

vorgelegt von
Stefan Wolff
aus
Recklinghausen, Deutschland

Bonn, 2019

Angefertigt mit Genehmigung der Mathematisch-Naturwissenschaftlichen Fakultät
der Rheinischen Friedrich-Wilhelms-Universität Bonn

1. Gutachterin: Prof. Dr. Corinna Kollath
2. Gutachter: apl. Prof. Dr. Ralf Bulla

Tag der Promotion: 24.04.2019
Erscheinungsjahr: 2019

Abstract

Remarkable experimental progress and theoretical advancements in the study of strongly correlated systems have opened up new doors towards a better understanding of interesting states of matter. Such states could possibly be used to develop novel technological applications based on the principles of quantum mechanics. In recent years, the investigation of both complex solid state and ultracold atom systems has lead to a number of fascinating discoveries with regards to their non-equilibrium properties. One route to probe non-equilibrium physics is to consider the evolution of open systems defined by the coupling to an external environment introducing dissipation. Engineering the environment according to predefined requirements can then be used to dynamically prepare states which are difficult to access otherwise.

This thesis explores the dynamics of many-body open quantum systems aiming at understanding the effects resulting from the interplay of kinetic motion, interactions and dissipation in different physical settings. First, we build upon recent developments concerning the coupling of ultracold atoms to optical resonators which are subject to photon losses. We show how the dissipation can trigger an attractor dynamics towards a topologically non-trivial steady state that is robust against perturbations. The numerically obtained full open system evolution enables us to not only characterize in detail the steady state but also to analyze the features of the approaching dynamics. Second, we study the propagation of two-time correlation functions in interacting quantum spin-$\frac{1}{2}$ chains in contact with an environment causing dephasing. Provided with the numerically exact full time-evolution, we identify an algebraic scaling regime where time-translation invariance breaks down and uncover the emergence of aging dynamics. Finally, we study a system of interacting fermionic atoms in a one-dimensional lattice with particle loss at the central site. There we report on the dissipation-induced deceleration of the non-equilibrium dynamics known as the quantum Zeno effect. As in the majority of cases quantum many-body systems are not solvable analytically, another central aspect of this thesis deals with adapting numerical methods based on matrix product state algorithms to investigate open quantum systems dynamics.

Zusammenfassung

Bemerkenswerte experimentelle Fortschritte und theoretische Weiterentwicklungen in der Erforschung stark korrelierter Systeme haben neue Möglichkeiten zum besseren Verständnis interessanter Materiezustände eröffnet. Solche Zustände können möglicherweise genutzt werden, um neue technologische Anwendungen zu entwickeln, die auf den Prinzipien der Quantenmechanik beruhen. In den letzten Jahren hat die Untersuchung sowohl komplexer Festkörper als auch ultrakalter Atomsysteme zu einer Reihe faszinierender Entdeckungen in Bezug auf ihre Nichtgleichgewichtseigenschaften geführt. Ein Weg zur Untersuchung der Nichtgleichgewichtsphysik besteht darin, die Zeitentwicklung offener Systeme zu betrachten, die durch die Kopplung an eine externe Umgebung Dissipationseffekte einführen. Die speziell zugeschnittene Realisierung einer Umgebung nach vordefinierten Anforderungen kann weiter dazu verwendet werden, Zustände dynamisch zu erzeugen, die sonst schwer zugänglich sind.

Diese Arbeit untersucht die Dynamik von offenen Vielteilchen-Quantensystemen und zielt darauf ab, die Effekte zu verstehen, die sich aus dem Zusammenspiel von kinetischer Bewegung, Wechselwirkungen zwischen einzelnen Teilchen und Dissipation in verschiedenen physikalischen Situationen ergeben. Zuerst knüpfen wir an die jüngsten Entwicklungen im Kontext der Kopplung von ultrakalten Atomen an optische Resonatoren unter zusätzlicher Berücksichtigung von Photonenverlusten an. Wir zeigen, wie die Dissipation eine Attraktor-Dynamik hin zu einem topologisch nicht-trivialen stationären Zustandes auslösen kann, der robust gegen Störeinflüsse ist. Die numerisch gewonnene vollständige Zeitentwicklung des offenen Systems ermöglicht es uns, nicht nur den stationären Zustand im Detail zu charakterisieren, sondern auch die Eigenschaften der Annäherungsdynamik zu analysieren. Außerdem untersuchen wir die Ausbreitung von Zwei-Zeit-Korrelationsfunktionen bei wechselwirkenden Quantenspin-$1/2$-Ketten die in Kontakt mit einer Umgebung stehen, die eine Dephasierung verursacht. Mit Hilfe der numerisch exakten Zeitentwicklung identifizieren wir ein algebraisches Verhalten, bei dem die Zeittranslationsinvarianz zusammenbricht und die Entstehung von Alterungsdynamik aufgedeckt wird. Schließlich untersuchen wir ein System von wechselwirkenden fermionischen Atomen in einem eindimensionalen Gitter mit Teilchenverlust im Zentrum. Dort berichten wir über die dissipationsbedingte Verzögerung der Nicht-Gleichgewichtsdynamik, bekannt als Quanten-Zeno-Effekt. Da in den meisten Fällen Vielteilchen-Quantensysteme nicht analytisch lösbar sind, beschäftigt sich ein weiterer zentraler Aspekt dieser Arbeit mit der Anpassung numerischer Methoden auf der Grundlage von Matrix-Produkt-Zustandsalgorithmen zur Untersuchung der Dynamik offener Quantensysteme.

List of publications related to this thesis

- C. Kollath, A. Sheikhan, S. Wolff and F. Brennecke, *Ultracold Fermions in a Cavity-Induced Artificial Magnetic Field*, *Phys. Rev. Lett.* **116**, 060401 (2016)

- S. Wolff, A. Sheikhan and C. Kollath, *Dissipative time evolution of a chiral state after a quantum quench*, *Phys. Rev. A* **94**, 043609 (2016)

- S. Wolff, J.-S. Bernier, D. Poletti, A. Sheikhan and C. Kollath, *Evolution of two-time correlations in dissipative quantum spin systems: aging and hierarchical dynamics*, *arXiv:1809.10464*, submitted (2018)

- S. Wolff, A. Sheikhan and C. Kollath, *Benchmark of Monte-Carlo wave functions approaches for two- time correlation functions using matrix product states*, in preparation (2019)

- S. Wolff, A. Sheikhan and C. Kollath, *Zeno dynamics of interacting fermions with a dissipative defect*, in preparation (2019)

Acknowledgements

Contents

Contents

<div align="right">

Chapter 1

</div>

Introduction

In many branches of natural sciences understanding the dynamics of systems coupled to an environment is of paramount importance. For instance, to model local weather and climate patterns [1], hydrodynamic flow in bodies of water [2], pedestrian dynamics and traffic flow [3], heat engines [4] and electric charge currents all require to take into account exchanges with the surrounding. This is also the case in the context of quantum many-body systems, where investigating their dynamics while in contact with large environments has attracted a lot of attention in recent years [5–9]. In this setting, the environment introduces dissipation effects for quantum systems, in analogy to, for example, the friction of a moving body or the damping of electromagnetic waves in classical systems. More precisely, dissipation is defined by the effect of a larger environment on a quantum system, which is then commonly termed an open quantum system [6] to distinguish it from closed systems, which are completely isolated from external effects.

Understanding the dissipative dynamics of large many-body systems is particularly interesting and at the same time extremely challenging as different mechanisms of similar magnitude are competing. This is already the case in closed systems which exhibit comparable energetic contributions of the particle motion and the inter-particle interaction enabling the emergence of interesting collective phenomena such as superconductivity, quantum magnetism or Bose-Einstein condensation [10]. These difficulties are now compounded by the addition of dissipative channels. This field of research has benefited greatly from the experimental developments concerning ultracold atoms in optical lattices [11], which allows to simulate lattice models with system parameters that are highly tunable up to remarkable accuracy and where dissipation can be introduced in a controlled manner. This has been realized for example in form of a variable light intensity in an imaging procedure [12, 13] or by off-resonant excitation of Rydberg atoms [14, 15].

While the additional inclusion of a dissipative coupling to an environment appears on first sight as a further complication, it turns out, that non-equilibrium effects can also be utilized constructively. For example, complex quantum states can possibly be generated with an environment specially tailored to the situation [16, 17]. Reaching these states is based on the principle, that the associated time evolution is determined by an exponentially fast approach of one or more steady states. The latter are stable against perturbations and depend on both

the properties of the system and the environment. This even promises to pave the way for producing new quantum materials possessing sought-after characteristics. One example being the theoretical prediction of dissipatively prepared topological states of matter [18–20] which are known to be very robust against decoherence and therefore are candidates for emerging quantum technologies [21, 22].

A category of set-ups providing access to dynamical open system phenomena is given by cold atoms that are coupled to the light modes of an optical cavity [23] with one fascinating highlight being the experimental realization of the non-equilibrium dynamical Dicke phase transition [24, 25]. In fact, in the course of this work we will show, how the dissipative dynamics of a system that couples cold atoms, an optical cavity mode and the periodic driving field of a laser beam can evoke a self-organization process towards a topologically non-trivial steady state.

Despite the great efforts and considerable progress on both sides, theoretical and experimental, most results are focused on the description of steady states, while the time evolution of these complex systems is still largely unexplored. One way to approach the characterization of non-equilibrium dynamics is to describe the propagation of correlations in the system. Experimentally, this is directly linked to the spectroscopy of strongly correlated electron materials using very short laser pulses in pump-probe protocols [26–28] which, for example enabled the detection of signatures of light-induced superconductivity [29]. From a theoretical point of view, the description of closed interacting many-body quantum systems is already very challenging. Since a quantum mechanical state is described as a weighted superposition of all possible configurations, the dimension of the associated Hilbert space grows exponentially with the number of particles. Although analytical solutions exist for some special cases, often computational methods are necessary to obtain numerically exact solutions. The difficulty of the task is exacerbated for open quantum systems, as the evolving object is the density matrix, so that the corresponding Hilbert space dimension is the square of the dimension of the original space. To overcome this challenge, we adapt the time-dependent matrix product state algorithm [30] to open quantum systems. In particular, this novel approach enables us to determine the propagation of correlation functions and the evolution of local observables. We can then quantitatively characterize new evolution regimes and identify the processes governing the dynamics in large interacting open quantum systems.

Outline of the thesis

Chapter 2: We begin with a thorough definition of open quantum systems and the notion of time evolution in this context in Chap. 2. Throughout this work we consider systems, for which the system-environment coupling can be assumed to be Markovian. We show how this constraint leads to the representation of the effective open system dynamics by the Lindblad quantum master equation. The interplay of dissipative and Hamiltonian dynamics and the resulting concepts of steady states and attractor dynamics are demonstrated using three examples.

Chapter 3: To lay the foundation for our theoretical study, we introduce the set of numerical and analytical tools appropriate for investigating dynamics in strongly correlated systems in Chap. 3. As a central element we describe the matrix product state (MPS) formalism and how it is employed to efficiently represent many-body quantum states in an exponentially large

Hilbert space with polynomial complexity while keeping an accuracy close to machine precision. Building up on this, we further derive algorithms enabling the accurate computation of the time evolution and the low-energy states of the system. This method is complemented by the technique of adiabatic elimination, which provides an analytic access to the dissipative dynamics in the strong dissipation limit and opens the way for further numerically less costly effective numerics in this regime.

Chapter 4: In Chap. 4 we present two different methods to simulate open Markovian systems using matrix product states. To do so, a full evolution of the reshaped density matrix, a process known as purification, is compared to a Monte-Carlo wave function (MCWF) sampling of quantum trajectories. We work out advantages, disadvantages and beneficial application cases for both approaches. Finally, we outline two competing schemes for adapting the stochastic sampling of quantum trajectories to the calculation of two-time correlation functions, which are powerful tools to capture the open system's non-equilibrium dynamics. We motivate the use of the entanglement production as a benchmark measure and compare both strategies in a specific case study.

Chapter 5: Turning to the first physical results, we consider quasi-one-dimensional ultracold fermionic atoms places inside a single mode optical cavity with photon loss. The atoms are coupled to the cavity mode such that an artificial magnetic field is induced via this coupling. This triggers a feedback mechanism between atoms and cavity field which leads to the emergence of self-organized topologically non-trivial phases. These are the steady states of the dissipative attractor dynamics which makes them robust against perturbations. Furthermore, we shed more light on the dynamics by finding a non-monotonic dependence of the time-scale for the steady state approach on the dissipation strength, which we will attribute to the quantum Zeno effect. We study this open quantum system numerically using the exact diagonalization method and compare the results with analytical mean field considerations.

Chapter 6: Adapting matrix product state methods to the time evolution of Markovian open system dynamics enables us to numerically exactly probe two-time correlation functions in large many-body quantum systems. This allows us for the first time to investigate two-time correlations in strongly interacting systems exposed to Markovian dephasing noise. Examining the two-time correlations of spin-$\frac{1}{2}$ operators in a one-dimensional chain of interacting spins reveals that the evolution is affected significantly by the dissipation. In fact, we could distinguish three successive dynamic regimes. At early times, the system is mostly influenced by the Hamiltonian evolution of the initial state. In contrast to that, the dissipation evokes a very surprising behavior in the long-time evolution which can be classified as aging dynamics. For strong spin couplings along the z-direction we further observe an intermediate regime, where the time range of existence depends highly on the initial state. We will comment how this can be employed to extract information of the Hamiltonian spectrum of the closed system, which is hard to obtain otherwise. With the help of many-body adiabatic elimination techniques we present a path to gain more physical insights regarding the decisive processes, which enables us to identify the long-time dynamics as a diffusive evolution and provides the exponent of the scaling in the aging regime analytically.

Chapter 7: Finally, we present results on the dissipative dynamics of spinless fermions in a one-dimensional optical lattice potential with nearest neighbor interactions in Chap. 7. Starting from the ground state of the closed system, a sudden switch-on of a particle loss channel causes a drain of particles at the central site. The time evolution, monitored by the time dependence of the spatial resolved density, undergoes two distinct time regions before reaching the limits of finite system sizes. The evolution is computed numerically using the Monte-Carlo wave function algorithm interfaced with the time-dependent matrix product state algorithm. The early behavior is governed by the emptying of the central occupation of the initial state, given by the uniform density distribution in the equilibrium ground state. Interestingly, a quasi-stationary density distribution forms in the vicinity of the central lattice site in the subsequent second time region. We compare the time scale of the emerging particle loss in dependence of the dissipation for different interaction strengths, including attractive, repulsive and non-interacting settings. By doing so, we find an occurrence of Zeno behavior, which causes the particle loss to counter-intuitively slow down for stronger dissipative couplings. We verify this analytically by adiabatic elimination calculations in the strong dissipation limit.

<div align="right">

Chapter **2**

</div>

Open quantum systems

This chapter is dedicated to the description of open quantum systems with a special focus on their evolution in time. To this end, we start by introducing the Lindblad equation which describes the system's dynamics and outline the derivation including the conditions for its validity. Then we supplement the introduced formalism with examples.

2.1. Open system dynamics and Markovian quantum master equations

An open system S is a quantum system, which is in contact with another system E, called the environment. The paradigm of open systems is to reduce the consideration exclusively to the system part, including the effect of the environment on the latter, rather than investigating the full composite set-up. Typically, the environment is chosen to be much larger than the system, such as, for example, a reservoir with infinitely many degrees of freedom. As a result, the coverage of the full system is not feasible. Nevertheless, it is often possible to extract the essential system dynamics, provided that certain assumptions are fulfilled. The Hilbert space of the system is defined as $\mathcal{H}_S$ and the one of the environment as $\mathcal{H}_E$, such that the full space is given by $\mathcal{H}_S \otimes \mathcal{H}_E$. Consequently, the Hamiltonian, describing the dynamics of the full system is a combination of parts acting only on system or environment as well as a coupling terms between the two

$$H = H_S \otimes \mathbb{1} + \mathbb{1} \otimes H_E + H_{SE}. \tag{2.1}$$

A natural description for this situation is offered by the notion of density matrices, which are capable of representing statistical mixtures of pure quantum states $|\psi_i\rangle$ by

$$\rho = \sum_i p_i |\psi_i\rangle\langle\psi_i|, \tag{2.2}$$

where the individual states are weighted with the classical probabilities p_i. The distribution between system and environmental contributions in relation in terms of the Hamiltonian, the density matrix and the Hilbert spaces is shown in Fig. 2.1. In this framework, quantum mechanical expectation values of an operator A are calculated using the trace over the full system $\langle A \rangle = \text{tr}[A\rho]$. The density matrix of one subpart is further obtained by performing the partial trace according to the Hilbert space of the other part, i.e. $\rho_S = \text{tr}_E(\rho)$ for the system's

full system: $\{\mathcal{H}_S \otimes \mathcal{H}_E, H_S + H_E + H_{SE}, \rho\}$
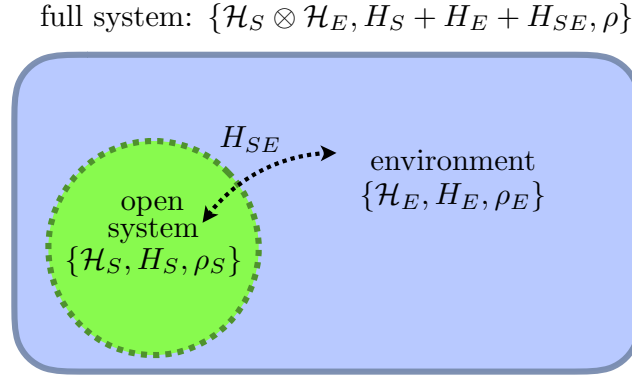
Figure 2.1.: Sketch of a system embedded in a larger environment with the different Hilbert spaces, Hamiltonians and density matrices.

density matrix and $\rho_E = \mathrm{tr}_S(\rho)$ for the environment. Translating the Schrödinger equation for the evolution of states $i\hbar\partial_t|\psi(t)\rangle = H|\psi(t)\rangle$ to the density matrix formalism results in the von-Neumann equation for the evolution of the density matrix of the full system

$$\frac{\mathrm{d}}{\mathrm{d}t}\rho(t) = -\frac{i}{\hbar}\left[H, \rho(t)\right].$$

(2.3)

The formal integration of Eq. 2.3 for time-independent Hamiltonians followed by tracing out the environment, provides the time evolution of the density matrix of the system

$$\rho_S(t) = \mathrm{tr}_E\left[U(t,0)\,\rho(0)\,U^\dagger(t,0)\right],$$

(2.4)

with the unitary time-evolution operator $U(t,t_0) = \exp[-iH(t - t_0)/\hbar]$ of the full system. However, by applying the trace over the environment, the effective dynamics in the reduced system is no longer unitary and can therefore be considered as a form of dissipation. Due to the usually large size of the environmental Hilbert space, an exact expression for the full evolution is inaccessible in most of the cases of interest. Instead, it is desirable to limit oneself to the temporal evolution of the system and to express the effects of the environment by system operators. To achieve this, it is first assumed that the system and environment are decoupled from each other at the beginning and that the environment remains constant in time

$$\rho(t = 0) = \rho_S(t) \otimes \rho_E.$$

(2.5)

This assumption is realistic if the environment is, for example, given by a large reservoir that is in good approximation unaffected by the dynamics of the system. This can then be used to specify a dynamic map that calculates the system's density matrix at a given point in time,

which is formally defined by

$$V(t) : \mathcal{H}_S \to \mathcal{H}_S$$
$$\rho_S(0) \mapsto V(t)\rho_S(0) \equiv \mathrm{tr}_E \left[U(t,0) \left(\rho_S(t) \otimes \rho_E \right) U^\dagger(t,0) \right]. \tag{2.6}$$

While this formulation is generally valid, a great simplification can be achieved by additionally assuming that the dynamical map satisfies the condition of Markovianity, expressed by the continuous version of the Chapman-Kolmogorov equation [6]

$$V(t_1 + t_2) = V(t_2)V(t_1), \quad \forall t_1, t_2 \geq 0. \tag{2.7}$$

The essence of the above equation is that the future time evolution of the open system depends solely on the current state and is insensitive to the past trajectory of the system in time. From a physical point of view this consideration is valid if the investigated system-environment coupling takes place on time scales, which are significantly larger than any time scale of correlations in the environment. That means, the relaxation of the environment is much faster, than the dissipative reaction in the system. This becomes particularly evident in an alternative derivation of the Lindblad equation from microscopic principles [6, 31]. Strictly speaking, the posed condition is already required by the assumption in Eq. 2.5. In addition, Markovianity enforces that there is no retroactive effect from earlier dissipative events on the current state of the system. The Markov condition always needs to be carefully verified. Nevertheless, in realizations form the field of quantum optics and cold atoms, it is typically well-fulfilled, as, for example, photon or particle losses happen fast compared to the system evolution and do not act back on the latter at later times. However, if this condition is met, the family of dynamical maps, parameterized by the time t, forms a dynamic semigroup $\{V(t) \,|\, t \geq 0\}$, with the semigroup property of Eq. 2.7. It was found by G. Lindblad in 1976 [32], that the most general form of the generator $\mathcal{L}$ of the semigroup, defined by

$$V(t) = \mathrm{e}^{\mathcal{L}t}, \tag{2.8}$$

is expressed for a finite dimensional Hilbert space by the following equation, known as the Markovian quantum master equation in Lindblad form, or simply Lindblad equation

$$\frac{\mathrm{d}}{\mathrm{d}t}\rho_S = \mathcal{L}\rho_S = -\frac{i}{\hbar} [H_S, \rho_S] + \mathcal{D}(\rho_S) \tag{2.9}$$
$$\text{with } \mathcal{D}(\rho_S) = \sum_{j=1}^{N^2-1} \gamma_j \left[L_j \rho_S L_j^\dagger - \frac{1}{2} \left(L_j^\dagger L_j \rho_S + \rho_S L_j^\dagger L_j \right) \right].$$

The operators L_j are called Lindblad operators or jump operators and represent the effects of the environment felt by the system. The superoperator $\mathcal{L}$ which generates the full Markovian time evolution is commonly known as *Lindbladian*. While the first term of Eq. 2.9 is the von Neumann equation for the unitary time development of an isolated system under the system Hamiltonian H_S, the operator $\mathcal{D}(\rho)$ introduces the Markovian dissipative nature of the open

system and is therefore called dissipator. The strength of the coupling to the environment is specified separately for each Lindblad operator by γ_j and defines the time scale of the respective system-environment interaction process. The number N is the dimension of $\mathcal{H}_S$. All possible operations on the system's density matrix can be expressed in terms of a N^2-dimensional basis of operators, where the requirement of trace-preservation for $V(t)$ reduces the total number of Lindblad operators by one. That the trace-preservation is satisfied by the Linblad equation is directly shown by using the cyclic properties of the trace, yielding $\mathrm{tr}[\mathcal{L}\rho_S(t)] = 0$, which is consistent with $\partial_t \mathrm{tr}[\rho(t)] = 0$. Furthermore, the Lindblad equation preserves the hermiticity and semi-positivity of density matrices [33]. As these conditions are required for a density matrix to present a physical state as defined in Eq. 2.2, we can conclude that the evolution under Eq. 2.9 of a physical density matrix again represents a statistical mixture of quantum states. As the only measurable quantities in quantum mechanics are expectation values of operators $\langle A \rangle = \mathrm{tr}[\rho A]$, the time evolution can be associated either with the operator A or the density matrix ρ, i.e. $\langle A \rangle(t) = \mathrm{tr}[A\rho(t)] = \mathrm{tr}[A(t)\rho]$. In the case of time-dependent operators the generator is denoted by $\mathcal{L}^\dagger$ and the time evolution is given by the so-called adjoint Lindblad equation

$$\frac{\mathrm{d}}{\mathrm{d}t} A(t) = \mathcal{L}^\dagger A(t) = \frac{i}{\hbar}[H_S, A(t)] + \sum_{j=1}^{N^2-1} \gamma_j \left[L_j^\dagger A(t) L_j - \frac{1}{2}\left(L_j^\dagger L_j A(t) + A(t) L_j^\dagger L_j \right) \right]. \quad (2.10)$$

Since this work deals only with the description of the open system, we will drop the index marking the system's density matrix and will use $\rho \equiv \rho_S$ from now on. Solving Eq. 2.9 provides the time evolution of the density matrix, given by

$$\rho(t) = \mathrm{e}^{\mathcal{L}t}\rho(t=0). \quad (2.11)$$

The Lindblad superoperator $\mathcal{L}$ is a linear operator acting on the space of system density matrices. Therefore, the exponential in Eq. 2.11 can be computed by transforming to the eigenbasis of $\mathcal{L}$. The time evolution is then calculated by evolving the eigenstates, weighted with their overlap with the initial state at time zero. As $\mathcal{L}$ is a non-hermitian operator, the corresponding eigenvalues are in general complex and can have a finite imaginary part. However, the property of the trace preservation of the Lindblad equation leads to restrictions on the eigenspectrum. More precisely, the real part of the eigenvalues needs to be less than or equal to zero to prevent an increase of the trace with time. At the same time, there needs to be at least one eigenstate with vanishing eigenvalue such that the density matrix does not decay totally over time. Thus, states satisfying the condition

$$\mathcal{L}\rho_{\mathrm{st}} = 0 \quad (2.12)$$

do not evolve in time $\rho_{\mathrm{st}}(t) = \rho_{\mathrm{st}}$ and are called *steady states*. Depending on the system, the steady state can be unique or not. Indeed we will encounter situations with several steady states later in this thesis. All other eigenstates ρ_j with the corresponding eigenvalues $\lambda_j = -\lambda_j^R + i\lambda_j^I$

are subject to an exponential damping with time

$$\rho_j(t) = e^{-\lambda_j^R t + i\lambda_j^I t}\rho_j(0) \xrightarrow{t \to \infty} 0, \quad \text{with } \lambda_j^R \in \mathbb{R}_0^+, \lambda_j^I \in \mathbb{R}. \tag{2.13}$$

As a direct consequence of the last two equations, every state converges to a mixture of steady states after sufficient long evolution times. The mixing weights are determined by the overlap of each steady state with the initial state. In the case of unique steady states the system always evolves towards a steady state – a behavior known as *attractor dynamics*.

2.2. Examples of open quantum systems

To build up an intuition for the Lindblad dynamics we continue by describing three different open quantum system realizations. The first two are analytically accessible models from the field of quantum optics and are related to the work presented later. The third example shows how cold atoms in optical lattices offer a possible way to implement interacting many-body open quantum systems.

2.2.1. Optical single-mode cavity with photon losses

Let us begin, by considering a single bosonic mode represented by the Hamiltonian $H = \hbar\omega_0\, a^\dagger a$. Here a and $a^\dagger$ are annihilation and creation operators, which satisfy the bosonic commutation relation $[a, a^\dagger] = 1$. The Hilbert space of this problem is spanned by the Fock states defined by the occupation number n as $|n\rangle$, with the operator actions $a|n\rangle = \sqrt{n}|n - 1\rangle$ and $a^\dagger|n\rangle = \sqrt{n + 1}|n + 1\rangle$. This setting appears, for example, when studying a single mode of a photon field in an optical cavity formed by two mirrors, facing each other. The open system nature is introduced by adding photon losses to the model caused by the imperfect mirrors. Consequently, the only Lindblad operator is here the photon loss operator a with the loss rate κ so that the associated Lindblad equation is given by

$$\frac{\mathrm{d}}{\mathrm{d}t}\rho(t) = -i\omega_0\left[a^\dagger a, \rho(t)\right] + \kappa\left(a\rho(t)a^\dagger - \frac{1}{2}a^\dagger a\rho(t) - \frac{1}{2}\rho(t)a^\dagger a\right). \tag{2.14}$$

The adjoint Lindblad equation from Eq. 2.10 for the photon number operator $N_a(t) = a^\dagger a(t)$ together with the bosonic commutation relation, yields the differential equation $\partial_t\langle N_a(t)\rangle = -\kappa\langle N_a(t)\rangle$ which is readily solved by

$$\langle N_a(t)\rangle = e^{-\kappa t}\langle N_a(t = 0)\rangle. \tag{2.15}$$

Here the unique steady state is the vacuum state $|0\rangle$ and the exponential decay of the occupation number in Eq. 2.15 displays the attractor dynamics towards this state in time.

2.2.2. Driven two-level system

Let us now turn to a more involved example which shows the interplay and competition between the unitary evolution defined by the system Hamiltonian of an open system with the dissipation caused by the interaction with the environment. To this end, we present the example of a single atom with two internal states $|g\rangle$ and $|e\rangle$, which can be identified as the ground state
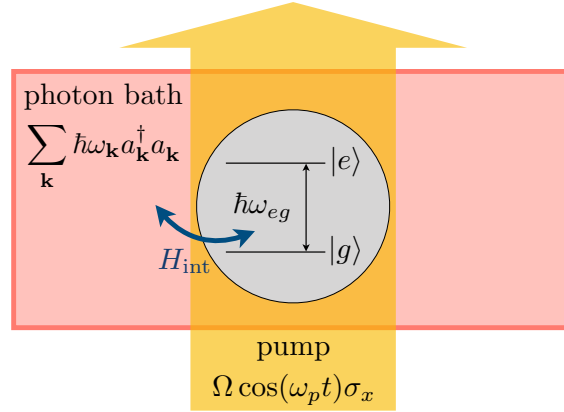
Figure 2.2.: Full model configuration of a two-level atom driven by a laser beam and coupled to the environment of a photon bath.

and the excited state separated by the energy $\hbar\omega_{eg}$ which is further coupled to a bath of photon modes [31, 34, 35]. After the so-called rotating wave approximation [35], the corresponding Hamiltonian reads

$$H = H_A + H_{\text{int}} + H_{\text{Bath}}, \tag{2.16}$$

with the contributions

$$H_A = \frac{\hbar\omega_{eg}}{2}\sigma^z,$$

$$H_{\text{int}} = \hbar\sum_{\mathbf{k}} g_{\mathbf{k}}\left(a_{\mathbf{k}}\sigma^+ + a_{\mathbf{k}}^\dagger\sigma^-\right),$$

$$H_{\text{Bath}} = \sum_{\mathbf{k}} \hbar\omega_{\mathbf{k}} a_{\mathbf{k}}^\dagger a_{\mathbf{k}}. \tag{2.17}$$

Here, σ^z represents the third Pauli matrix for the two atomic states defined by $\sigma^z = |e\rangle\langle e| - |g\rangle\langle g|$ and $\sigma^+ = |e\rangle\langle g|$ is the excitation and $\sigma^- = |g\rangle\langle e|$ the deexcitation operator. The photon modes labeled by the wave vector $\mathbf{k}$ are represented by the bosonic annihilation (creation) operators $a_{\mathbf{k}}(a_{\mathbf{k}}^\dagger)$. When reducing the consideration to a single photon mode, a scenario which is, for example, arising for a photon field in an optical cavity, the model becomes the well-known Jaynes-Cummings model [35]. In addition to the Hamiltonian from Eq. 2.16 the atom is further exposed to a pump beam which acts as a classical coherent light field driving

$$H_{\text{drive}} = \hbar\Omega\cos(\omega_p t)\sigma^x, \tag{2.18}$$

with $\sigma^x = \sigma^+ + \sigma^-$. The full set-up is sketched in Fig. 2.2. Instead of working with the total Hamiltonian model, the photon bath is now regarded as an environment connected to the two-level atom which plays the role of an open system. While also atomic transitions can be induced by a reservoir with a finite number of photons, the example here should be limited to the photon vacuum and only takes into account the process of spontaneous atomic deex-

citations accompanied by the emission of photons. For fast relaxation times of the bath after the photon emission and negligible back-action of the photon on the atom, the atomic open system dynamics can be assumed to be Markovian. Transforming the remaining atomic Hamiltonian, i.e. $H_A + H_{\text{drive}}$, to a frame rotating with the pump frequency ω_p by the transformation $U = \exp[i\omega_p t/2\sigma^z]$ and tracing out the environment, the evolution of the two-level system is described by the Lindblad master equation

$$\frac{\mathrm{d}}{\mathrm{d}t}\rho(t) = -i\frac{\Delta}{2}\left[\sigma^z, \rho\right] - i\frac{\Omega}{2}\left[\sigma^x, \rho\right] + \gamma\left(\sigma^-\rho\sigma^+ - \frac{1}{2}\sigma^+\sigma - \rho - \frac{1}{2}\rho\sigma^+\sigma-\right). \qquad (2.19)$$

Here, the detuning $\Delta = \omega_{eg} - \omega_p$ and the dissipation strength of the spontaneous decay γ have been introduced. With the general representation of the system's density matrix

$$\rho(t) = \rho_{ee}(t)|e\rangle\langle e| + \rho_{eg}(t)|e\rangle\langle g| + \rho_{ge}(t)|g\rangle\langle e| + \rho_{gg}(t)|g\rangle\langle g|, \qquad (2.20)$$

the Lindblad equation can be reformulated in matrix form as

$$\frac{\mathrm{d}}{\mathrm{d}t}\begin{pmatrix}\rho_{ee}(t)\\\rho_{eg}(t)\\\rho_{ge}(t)\\\rho_{gg}(t)\end{pmatrix} = \begin{pmatrix}-\gamma & \frac{i\Omega}{2} & -\frac{i\Omega}{2} & 0\\\frac{i\Omega}{2} & -i\Delta - \frac{\gamma}{2} & 0 & -\frac{i\Omega}{2}\\-\frac{i\Omega}{2} & 0 & i\Delta - \frac{\gamma}{2} & \frac{i\Omega}{2}\\\gamma & -\frac{i\Omega}{2} & \frac{i\Omega}{2} & 0\end{pmatrix}\begin{pmatrix}\rho_{ee}(t)\\\rho_{eg}(t)\\\rho_{ge}(t)\\\rho_{gg}(t)\end{pmatrix}. \qquad (2.21)$$

To access the full time evolution, the matrix of Eq. 2.21 needs to diagonalized and exponentiated. For the case of resonant driving ($\Delta = 0$) and an initial preparation of the atom in the ground state $|g\rangle$ the occupation probability of the excited state is

$$\rho_{ee}(t) = \frac{\Omega^2}{\gamma^2 + 2\Omega^2}\left[1 - e^{-\frac{3\gamma}{4}t}\left(\cos(\Omega' t) + \frac{3\gamma}{4\Omega'}\sin\left(\Omega' t\right)\right)\right], \qquad (2.22)$$

with the effective frequency $\Omega' = \sqrt{\Omega^2 - \gamma^2/16}$. We show the time-dependence of ρ_{ee} for different parameter combinations of driving and dissipation strength in Fig. 2.3. It becomes clear that the time evolution is determined on the one hand by oscillations that can be identified for the dissipation-free case ($\gamma = 0$) as the known Rabi oscillations in a driven two-level system [35]. Nevertheless, these oscillation are also affected by the dissipation, as the effective frequency also depends on γ. Furthermore, there is an exponential attenuation, with a damping strength that depends on the dissipative coupling. Namely, stronger dissipations here result in a faster decay of the oscillations towards a stationary value. This value is the occupation of the excited atomic state in the steady state, and is given by

$$\rho_{ee}(t) \xrightarrow{t\to\infty} \frac{\Omega^2}{\gamma^2 + 2\Omega^2}. \qquad (2.23)$$

It depends non-linearly on both, the driving Ω and the dissipation γ, which underlines the interwoven contribution of both aspects. In summary, the presented model is an example of
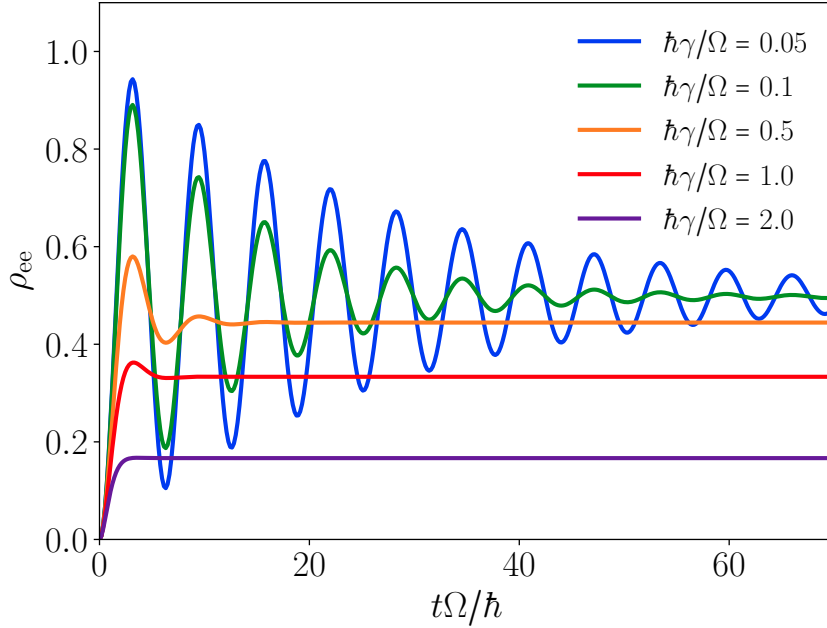
Figure 2.3.: Evolution of the excited state occupation of a driven two-level atom coupled to the environment of a photon bath causing atomic deexcitations due to spontaneous emission events. Rabi oscillations originating in the Hamiltonian motion are exponentially damped when approaching the steady state expectation value. The initial state is here chosen as $\rho(t=0) = |g\rangle\langle g|$.

how dissipation effects and unitary Hamiltonian dynamics both have a substantial influence on the attractor dynamics as well as on the steady state. Throughout this thesis we will present results aiming to understand the interplay of Hamiltonian and dissipative dynamics, similar to this simple example, in the context of large strongly-correlated many-body systems, where we will uncover and interpret the occurrence of interesting phenomena, regarding both, the steady state and the dissipative dynamics.

2.2.3. Cold atoms and optical lattices as a realization for interacting open many-body systems

A physical situation in which strong interactions in many-particle systems as well as dissipative effects occur, is given by the field of cold atoms subjected to optical lattice potentials. As the open systems investigated in this thesis are mostly formulated with this realizations in mind, we briefly present the basics of the concept here and comment on possible influences of Markovian noise.

The idea relies on using light-matter interaction to first cool neutral atoms to very low temperatures, where quantum fluctuations become relevant, and to build a periodic lattice potential subsequently. The former is achieved by a technique known as laser cooling [36], which employs absorption and spontaneous emission of a cloud of atoms, and can be followed by evaporative cooling which removes the hotter fraction of atoms from the sample [37]. This

makes it possible to cool down atoms to the scale of a few nano Kelvin and observe phenomena such as Bose-Einstein condensation [38] or a degenerate Fermi gas [39]. In contrast to that, the creation of a potential felt by the cooled neutral atoms is implemented using the conservative dipole interaction of a laser light-field with the electric dipole moment of the atoms induced by the AC stark shift. As the energy shift is proportional to the intensity of the classical beam, optical standing waves formed by counter-propagating laser beams create space-dependent periodic potentials for the atoms [40]. Deep optical lattices enforce the atoms to be well-localized in space and allow the expansion in Wannier functions, which enables the restriction to discrete lattice sites. This method is known as the tight-binding approximation [41]. This enables the establishment of an analogy to the type of potentials felt by valence electrons in a solid. However, cold atoms in optical lattice bear the advantage, that the system properties like depth, geometry and effective dimensionality of the potential as well as the inter-particle interaction strength [42–44] are highly tunable. Furthermore, the lattice is not perturbed by lattice vibrations or potential defects. A two-dimensional optical square lattice potential $V(x, y)$ with the corresponding discrete lattice is shown in Fig. 2.4.

It has been found that cold atoms in optical lattices are an ideal test environment for observing a variety of interesting many-body quantum effects for both bosonic and fermionic atoms [45]. Examples include the experimental observation of the superfluid to Mott insulator transition [46], the BEC-BCS crossover [47, 48] or the implementation of artificial magnetic fields to simulate topological quantum matter [49]. When extending the consideration by the coupling to a Markovian environment, the emergent attractor dynamics can be used as a robust way to stabilize complex many-body states as steady states of the corresponding Lindbladian [50]. To achieve this, the form of the bath is designed accordingly. Experimental setups

Figure 2.4.: Optical lattice potential $V(x, y)$ with localized sites of the tight-binding approximation.

of open quantum systems with cold atoms have already been realized for example by coupling the atoms to an external laser[12, 13] or by off-resonant excitations of Rydberg atoms [14, 15]. While the preparation of long-lasting steady states is interesting for its own sake, this thesis shows in a variety of instances, that also the approaching dynamics shows non-trivial behavior. On the one hand, this determines the speed of the convergence to the steady state, but also shows unexpected properties such as aging, known from the non-equilibrium relaxation dynamics of glasses.
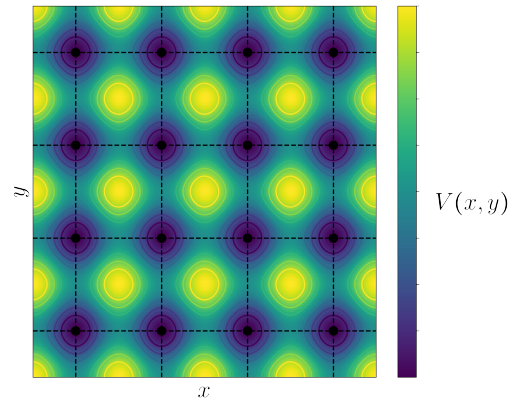
<div align="right">

Chapter 3

</div>

Methods

This chapter contains the approaches and prerequisites, we will use for accessing the dynamics of large interacting many-body system in contact with Markovian environments throughout the rest of the thesis. First of all, we introduce matrix product states in Sec. 3.1, which puts us in the position to analyze the full time evolution of large interacting complex systems quasi-exactly with an accuracy close to machine precision. Important algorithms are the variational ground state search in Sec. 3.1.3 and the time-evolution in Sec. 3.1.4. After that, we show, how an exact diagonalization of the Lindblad matrix of the corresponding differential equation can be employed for the simulation of small systems in Sec. 3.2. We also present opportunities for stretching the limits, posed by the exponential growing Hilbert space, as far as possible. Finally, we present an analytical tool in Sec. 3.3, going by the name of adiabatic elimination, which is based on the separation of different time scales for strong dissipations, allowing the introduction of a perturbative approximation.

3.1. Matrix product state techniques

This section gives an introduction and overview over different methods in the formulation of matrix product states (MPS), where we focus in this chapter on the description of pure multi-particle states and introduce an analogous formalism for density matrices in the next chapter. The concept of matrix product states relies on the reduction of the large set of degrees of freedom of the quantum many-body wave function, which is growing exponentially with system size, to the most important contributions. In fact, the state representation can be broken down to polynomial complexity regarding the system size by exploring only the most relevant subspace of the Hilbert space. As it will turn out, the corresponding approximation is valid, if the entanglement between two subsystems, created from a splitting of the original systems into two parts, is small. This is, for example, fulfilled by low-dimensional ground states of short-ranged gapped Hamiltonians, where the entanglement scales with the surface of the boundary instead of the volume of the system[51]. Consequently, matrix product states are a helpful tool to express ground states of gapped one-dimensional models, as for example spin-chains [52] or the (Bose) Hubbard model [53, 54], where the boundary between subsystems is zero-dimensional. A variational systematic ground state search, the density matrix renormalization group (DMRG), makes it possible to extract, among other things, ground state energies, excitation gaps and

correlation functions. Although the scheme is especially good for one-dimensional set-ups, there also exist successful approaches to extend the method to two-dimensional problems [55–57]. Another very impactful extension is the application of the MPS formalism to the real-time dynamics of quantum states, where the wave function is approximately constrained to a subspace, that is adapted continuously during the course of time evolution [58]. Given that the initial state is well represented by a MPS and that the entanglement growth for local Hamiltonians is limited by the Lieb-Robinson bound [59], a valid compression scheme for evolved states is guaranteed up to some threshold time marking the limit of convergence. In the last years a lot of effort has been devoted to the implementation of these methods in the form of open source packages, including ALPS [60], Open Source MPS [61] and ITensor [62]. Here we use the latter, due to its flexible interface, the efficient implementation and the native support of the inclusion of conserved quantities.

This subsection is structured such, that we begin with a general introduction of matrix product states and matrix product operators. Then we discuss in Sec. 3.1.2, how the representation can benefit from conserved quantities originating from symmetries of the model, given by the Hamiltonian for closed systems or the Lindbladian for their open counter parts. Thereafter, we present a variational method to find the ground state known by the name density matrix renormalization group algorithm (DMRG) in Sec. 3.1.3, as well as an approach to access the system dynamics in the language of MPS in Sec. 3.1.4. The description of the methods mentioned so far is loosely oriented at the review article by U. Schollwöck of Ref. [30]. The discussion on possibilities to extend the existing time evolution algorithms to Markovian non-equilibrium situations is moved to its own chapter (Chap. 4), where we show a variety of different approaches and comment on the computational efficiency in different scenarios.

3.1.1. Matrix product states and matrix product operators

The key problem addressed by the matrix product state formalism is to find an efficient way to encode the quantum many-body wave function, based on an approximation, which is well-understood on physical grounds due to a direct link to the entanglement between two subsystems. To emphasize this, let us begin by considering a bipartite system which can be decomposed into the two parts A and B, so that the common Hilbert space is given by $\mathcal{H} = \mathcal{H}_A \otimes \mathcal{H}_B$. Regarding the complex amplitudes of a wave function as a matrix, allows for the rewriting of a pure quantum state by performing a singular value decomposition (SVD)

$$|\psi\rangle = \sum_{ij} c_{ij}|i\rangle_A \otimes |j\rangle_B \stackrel{SVD}{=} \sum_{ij\alpha} U_{i\alpha} S_\alpha V^\dagger_{\alpha,j}|i\rangle_A \otimes |j\rangle_B. \tag{3.1}$$

Here, the rectangular amplitude matrix of dimension $N_a \times N_B$ with matrix elements c_{ij} is decomposed into a product of three matrices. The S matrix is a diagonal matrix

$$S = \mathrm{diag}(s_1, s_2, \ldots, s_{\min(N_A, N_B)}), \tag{3.2}$$

with the dimension being the minimum of the dimensions of the two participating subspaces, i.e. $\min(N_A, N_B)$. The diagonal elements, which are all real and non-negative, are called singu-

lar values and in the following we will assume a descending order $s_1 \leq s_2 \leq \ldots \leq s_{\min(N_A, N_B)}$.
The matrix U has the dimension $N_A \times \min(N_A, N_B)$ and the additional property $U^\dagger U = \mathbb{1}$.
In the case of $N_A \leq N_B$, U is also a square matrix and therefore unitary. On the other side,
there is the matrix $V^\dagger$ with dimension $\min(N_A, N_B) \times N_B$, which also satisfies the equation
$V^\dagger V = \mathbb{1}$, and similarly, if $N_B \leq N_A$, this matrix is unitary. Reformulating Eq. 3.1 leads to

$$|\psi\rangle = \sum_{\alpha=1}^{\min(N_A, N_B)} s_\alpha \left[\left(\sum_i U_{i\alpha} |i\rangle_A \right) \otimes \left(\sum_j V_{j\alpha}^* |j\rangle_B \right) \right] \equiv \sum_{\alpha=1}^{\min(N_A, N_B)} s_\alpha |\alpha\rangle_A \otimes |\alpha\rangle_B, \quad (3.3)$$

which is the well-known Schmidt decomposition with $\{|\alpha\rangle_A\}$ and $\{|\alpha\rangle_B\}$ forming an orthonor-
mal basis of the respective Hilbert subspaces A and B due to the properties of U and $V^\dagger$. One
of the remarkable features of the Schmidt decomposition is the direct connection to the von-
Neumann entanglement entropy S_{vN}, a measure of the entanglement between two subsystems.
More precisely, using the reduced density matrix for one of the subsystems, defined as

$$\rho_A = \operatorname{tr}_B \left[|\psi\rangle\langle\psi| \right] = \sum_{\alpha\beta\gamma} s_\alpha s_\beta \, {}_B\langle\gamma|\alpha\rangle_A |\alpha\rangle_B {}_A\langle\beta|_B \langle\beta|\gamma\rangle_B = \sum_\alpha s_\alpha^2 |\alpha\rangle_A {}_A\langle\alpha|, \quad (3.4)$$

the entanglement entropy can then be written as

$$S_{vN} = -\operatorname{tr} \left[\rho_A \log \rho_A \right] = -\sum_\alpha^r s_\alpha^2 \log \left(s_\alpha^2 \right).$$

The limit of the sum is denoted by r, which stands for the number of non-vanishing singu-
lar values, which is equal to the rank of the original matrix. This relation of singular values
to the entanglement entropy provides the possibility for a physical intuition concerning this
representation of the quantum state. In addition to this, the reformulation in terms of the sin-
gular value decomposition offers another big advantage, as it makes it possible to establish a
well-controlled approximation scheme. A common way to compress a rectangular matrix is to
perform a singular value decomposition and to truncate the matrix S at a maximal dimension
$D < r$. Indeed, this truncation scheme generates the rank-D matrix with the lowest deviation
from the original matrix according to the Frobenius norm [30]. If the singular values decay
fast enough, such that the sum of truncated values is small, the combined size of the three
matrices in the matrix product can be reduced significantly without loosing too much infor-
mation. This will prove to be very helpful in quantum many-body systems, where the Hilbert
space dimension grows exponentially. Apart from that, the same idea is used in a variety of dif-
ferent contexts, including image compression [63] and the principal component analysis from
statistics, aiming to find the best independent statistical variables [64].

In the following, we will make extensive use of singular value decompositions, resulting in
a large amount of tensors and tensor contractions. A tensor of rank r is defined as a r-fold
indexed object, so that a vector, for example, is a rank-1 or a matrix a rank-2 tensor. A set of
several tensors, which are connected via shared indices is known as a tensor network [65]. In

order to keep a clean overview, a graphical notation offers a clearer view on the topic. In this setting, a tensor is represented as a shape, for example a circle, and its indices are marked by lines. A contraction of two tensors according to one index can the be visualized by connecting the corresponding index lines. This gives rise to the representation of

$$
\text{a vector } \vec{v} = (\vec{v})_i \equiv \quad , \quad \text{a matrix } M = M_{ij} \equiv \quad , \quad \text{and a rank-3 tensor } T_{ijk} \equiv \quad . \tag{3.5}
$$

Applying this to the singular value decomposition from Eq. 3.1 yields

$$
c_{ij} = \quad \overset{SVD}{=} \quad = \sum_{\alpha} U_{i\alpha} S_{\alpha} V_{\alpha j}^{\dagger}. \tag{3.6}
$$

Here, the matrices U, S and $V^{\dagger}$ can be contracted by their shared index α.

With these prerequisites, we can now turn to the introduction of matrix product states. Let us consider a one dimensional finite system on a discrete lattice with L sites and d different states at each of these sites. The basis of the Hilbert space is given by $\mathbb{B} = \{|\sigma_1, \sigma_2, \ldots, \sigma_L\rangle\} \equiv \{|\vec{\sigma}\rangle\}$ with the local states $\sigma_l \in \{1, \ldots, d\}$ at site l. In the following, we present a calculation resulting in a decomposition of the many-body wave function of a quantum state into local rank-3 tensors with both, the usual tensor index notation and the diagrammatic approach. The starting point is the representation of a general pure state as a superposition of basis states. The amplitudes can then be identified with a rank-L tensor

$$
|\psi\rangle = \sum_{\sigma_1, \ldots, \sigma_L} c_{\sigma_1, \ldots, \sigma_L} |\vec{\sigma}\rangle = \sum_{\sigma_1, \ldots, \sigma_L} \quad |\vec{\sigma}\rangle, \tag{3.7}
$$

with the abbreviation $|\vec{\sigma}\rangle \equiv |\sigma_1, \ldots, \sigma_L\rangle$. This tensor has d^L elements, originating from the local Hilbert space dimension d. In this thesis we follow the convention of using vertical lines for the indices of the local basis, which we will also refer to as the physical or the site indices. Also, a tensor with physical indices sticking out from the top are depicting ket-states like $|\psi\rangle$, and tensors with site indices at the bottom are depicting their self-adjoint bra-states $\langle\psi|$. The first step is to reshape the amplitudes by isolating the index from the first site σ_1 and combining the remaining indices to one large index, such that the tensor becomes a matrix of the form

$$
|\psi\rangle = \sum_{\sigma_1, \ldots, \sigma_L} c_{(\sigma_1)(\sigma_2, \ldots, \sigma_L)} |\vec{\sigma}\rangle. \tag{3.8}
$$

3.1 Matrix product state techniques

It is then straight-forward to apply a SVD to the now rectangular matrix giving

$$|\psi\rangle \overset{SVD}{=} \sum_{\sigma_1,\dots,\sigma_L} \sum_{a_1} A_{1,a_1}^{\sigma_1} \left(SV^\dagger\right)_{a_1,\sigma_2,\dots,\sigma_L} |\vec{\sigma}\rangle = \sum_{\sigma_1,\dots,\sigma_L} \sum_{a_1} \overset{\sigma_1}{\underset{A}{\bigcirc}} \overset{a_1}{\boxed{}} |\vec{\sigma}\rangle.$$
(3.9)

We denoted the matrix originally introduced as U by A for a reason which will become clear soon. Also, A has been reshaped to a third order tensor by adding a dummy index of extend one for later consistency. We now have separated the contribution from site one to the wave function which is now covered by a single tensor, connected to the rest of the wave function via the index a_1 of the singular value matrix S. In contrast to the physical site indices, this index type is known as a bond index, where we use the convention to write bond indices as subscripts and site indices as superscripts. Repeating this procedure for the second site combining indices as $(a_1, \sigma_2), (\sigma_3, \dots, \sigma_L)$ results in

$$|\psi\rangle \overset{SVD}{=} \sum_{\vec{\sigma}} \sum_{a_1,a_2} A_{1,a_1}^{\sigma_1} A_{a_1,a_2}^{\sigma_2} \left(\tilde{S}\tilde{V}^\dagger\right)_{a_2,\sigma_3,\dots,\sigma_L} |\vec{\sigma}\rangle = \sum_{\vec{\sigma}} \sum_{a_1,a_2} \overset{\sigma_1}{\underset{A}{\bigcirc}} \overset{a_1}{\underset{A}{\bigcirc}} \overset{a_2}{\boxed{}} |\vec{\sigma}\rangle.$$
(3.10)

Iterating this operation for all sites, we arrive at the form

$$|\psi\rangle = \sum_{\vec{\sigma}} A^{\sigma_1} A^{\sigma_2} A^{\sigma_3} \dots A^{\sigma_L} |\vec{\sigma}\rangle = \sum_{\vec{\sigma}} \sum_{a_1,\dots,a_{L-1}} \overset{\sigma_1}{\underset{A}{\bigcirc}} \overset{a_1}{\underset{A}{\bigcirc}} \overset{a_2}{\underset{A}{\bigcirc}} \overset{a_3 \ \ a_{L-1}}{\underset{A}{\bigcirc}} |\vec{\sigma}\rangle. \quad (3.11)$$

In this equation we omitted the bond indices, so that the amplitude is ultimately given by a product of indexed matrices A^{σ_l}, which is why this representation is known as a matrix product state. The dimension of these matrices can be deduced from the dimension of the U matrix in the SVD, for an even number of sites one finds $(1 \times d), (d \times d^2), \dots, (d^{L/2-1} \times d^{L/2}), (d^{L/2} \times d^{L/2-1}, \dots, (d \times 1)$. While this is an exact representation for an arbitrary pure state, the maximal value for the dimension of bond indices close to the chain center grows exponentially with the system size. However, assuming a sufficiently fast decay of the singular values associated with each bond, it is possible to truncate the S matrix and to maximally keep D singular values at each SVD application. The quality of this cutoff approximation is controlled by the truncation error, sometimes also called truncation weight, defined at bond $(l, l+1)$ as the sum of discarded squared singular values

$$\epsilon_l(D) = \sum_{a_l > D} s_{a_l}^2.$$
(3.12)

The truncation error is typically aimed to be kept of the order 10^{-10} or lower. Via the Schmidt decomposition this approximation is directly linked to the entanglement. For example, if two subsystems separated at the bond $(l, l+1)$ are given by a product state and therefore do not show any entanglement, only one singular value needs to be kept. On the other hand, an equal

superposition of states, which is maximally entangled, can not be approximated well by this truncation scheme, as all singular value are equal and no hierachical order exists. As mentioned earlier, from a physical point of view, the criterion of fast decaying singular values is fulfilled, for example, by ground-states of one-dimensional short-ranged gapped Hamiltonians or the evolution of initial states with with low entanglement between subparts.

Investigating the A^{σ_l} matrices from Eq. 3.11 reveals another relation. As the matrices correspond to the matrix U from the SVD, we can conclude

$$\sum_{a_{l-1},\sigma_l} U^*_{a_{l'},(a_{l-1},\sigma_l)} U_{(a_{l-1},\sigma_l),a_l} = \delta_{a_l,a_{l'}} \Leftrightarrow \sum_{\sigma_l} A^{\sigma_l\dagger} A^{\sigma_l} = \mathbb{1}_{a_l,a_l'} \Leftrightarrow$$

(3.13)

Tensors, fulfilling this condition are called left-normalized and if every local site tensor is left-normalized, the state is a left-canonical MPS. In the construction above this relation is true for all site tensors A^{σ_l}, which we illustrate from now on by the shared green color. Nevertheless, the matrix product state representation is not unique. In fact, every two tensors connected by a bond are subject to a gauge degree of freedom as

$$\sum_{\sigma_1,\ldots,\sigma_L} A^{\sigma_1} \ldots A^{\sigma_L} |\sigma_1,\ldots,\sigma_L\rangle = \sum_{\sigma_1,\ldots,\sigma_L} A^{\sigma_1} X_1 X_1^{-1} A^{\sigma_2} X_2 X_2^{-1} \ldots X_{L-1} X_{L-1}^{-1} A^{\sigma_L} |\sigma_1,\ldots,\sigma_L\rangle.$$

(3.14)

For example, another way to build an MPS, is to first isolate the site L on the right lattice boundary, perform an SVD and assign the $V^\dagger$ matrix as the site tensor $B^{\sigma_L}_{a_L,1}$. Iterating this gives the following MPS form

In contrast to the left-normalized MPS, the B^{σ_L} matrices inherit the characteristics from the $V^\dagger$ matrix such that the following relation is satisfied
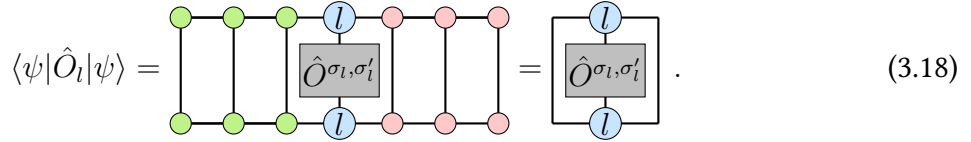
$$\sum_{\sigma_l} B^{\sigma_l} B^{\sigma_l\dagger} = \mathbb{1}_{a_{l-1},a'_{l-1}} \Leftrightarrow$$

(3.16)

This gauge choice is defined as right-normalized, corresponding matrices are colored red in the tensor network diagrams and states constructed from right-normalized matrices only, are dubbed right-canonical states. Another representation which will turn out to be quite useful is the so-called mixed-canonical form. In this case a orthogonality center is introduced at some site l, for which all sites left to this site are left-normalized and all sites right to it are right-normalized

$$|\psi\rangle = \sum_{\sigma_1,...,\sigma_L} A^{\sigma_1} \ldots A^{\sigma_{l-1}} M^{\sigma_l} B^{\sigma_{l+1}} \ldots B^{\sigma_L} |\sigma_1, \ldots, \sigma_L\rangle. \tag{3.17}$$

This form is particularly handy, when calculating expectation values of local variables such as $\hat{O}_l = \sum_{\sigma_l,\sigma_l'} O^{\sigma_l,\sigma_l'} |\sigma_l\rangle\langle\sigma_l'|$. The properties for left- and right-normalized tensors from Eq. 3.13 and 3.16 makes it possible to reduce the calculation to tensor contractions, which only involve the corresponding local tensor at site l

$$\langle\psi|\hat{O}_l|\psi\rangle = \quad \hat{O}^{\sigma_l,\sigma_l'} \quad = \quad \hat{O}^{\sigma_l,\sigma_l'} \quad . \tag{3.18}$$

Having established the picture of single site operators as tensors, now brings us to a more general approach to dealing with operators in the tensor network formalism. Indeed it is beneficial to develop a local tensor representation of operators which include contributions from different sites, as for example for interacting Hamiltonian and Lindbladian operators. In analogy to the formalism for states, we introduce matrix product operators (MPO), where an operator acting on all sites is decomposed into a product of local rank-4 site tensors in the following way

$$\hat{O} = \sum_{\substack{\sigma_1,...,\sigma_L \\ \sigma_1',...,\sigma_L'}} c^{(\sigma_1,...,\sigma_L),(\sigma_1',...,\sigma_L')} |\vec{\sigma}'\rangle\langle\vec{\sigma}| = \sum_{\substack{\sigma_1,...,\sigma_L \\ \sigma_1',...,\sigma_L'}} \quad |\vec{\sigma}'\rangle\langle\vec{\sigma}|$$

$$= \sum_{\substack{\sigma_1,...,\sigma_L \\ \sigma_1',...,\sigma_L'}} \sum_{b_1,...,b_{L-1}} W_{1,b_1}^{\sigma_1,\sigma_1'} W_{b_1,b_2}^{\sigma_2,\sigma_2'} \ldots W_{b_{L-1},1}^{\sigma_L,\sigma_L'} |\vec{\sigma}'\rangle\langle\vec{\sigma}| \tag{3.19}$$

$$= \sum_{\substack{\sigma_1,...,\sigma_L \\ \sigma_1',...,\sigma_L'}} \sum_{b_1,...,b_{L-1}} \quad |\vec{\sigma}'\rangle\langle\vec{\sigma}|$$

To distinguish the local MPO tensors from MPS tensors, we will use squares instead of circles in the tensor diagrams. It is now left to show, that this kind of representation is feasible in practical applications, which means, that the formulation is possible and efficient in terms of a not too large bond dimension. We demonstrate a way to achieve this for a Hamiltonian, which

couples only nearest neighbor sites by the operators $\hat{P}$ and $\hat{Q}$, given by

$$H = \sum_{j=1}^{L-1} P_j Q_{j+1}, \tag{3.20}$$

with $P_j Q_{j+1} = \mathbb{1} \otimes \ldots \otimes \mathbb{1} \otimes \hat{P} \otimes \hat{Q} \otimes \mathbb{1} \otimes \ldots \otimes \mathbb{1}$. Let us arbitrarily pick one of theses operator strings corresponding to the interaction according to one bond. Building up the tensor product of operators from the right lattice boundary at site L, there can be either a identity or a Q operator. In the latter case, the P operator needs to follow immediately when going to the next site. Otherwise, either another identity or the Q operator can follow. Therefore, there are three distinct states during the creation process: (1) only identity have been encountered so far, (2) the previous site was covered by a Q operator and (3) the PQ-coupling term has been passed already and there are just unities up to the left boundary. This construction process of building an operator string s with the three states is visualized by this computational graph
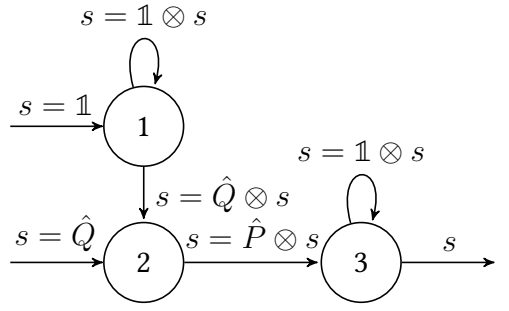
where we have the two possible inputs $\mathbb{1}$ and Q as operators for site L, followed by the procedure outlined above. Another way to represent this is to use transition matrices, giving the product $H = \prod_{j=1}^{L} W^j$ with

$$W^{[1]} = \begin{pmatrix} \hat{0} & \hat{P} & \mathbb{1} \end{pmatrix}, \text{ for } 1 < l < L : W^{[l]} = \begin{pmatrix} \mathbb{1} & \hat{0} & \hat{0} \\ \hat{Q} & \hat{0} & \hat{0} \\ \hat{0} & \hat{P} & \mathbb{1} \end{pmatrix}, W^{[L]} = \begin{pmatrix} \mathbb{1} \\ \hat{Q} \\ \hat{0} \end{pmatrix}. \tag{3.21}$$

This is exactly what we were looking for to achieve a representation as in Eq. 3.19. Due to the number of different internal states during the construction, the matrix dimension and with it the bond dimension of the MPO-formulation for this Hamiltonian is three, so that we can conclude that there exists a very efficient MPO representation for nearest neighbor Hamiltonians. This scheme can be straight-forwardly extended, for example, to external field or next-nearest neighbor terms, which come at the cost of a larger bond dimension. We will use this method later for example to implement the Hamiltonian for interacting spinless fermions in Chap. 7 or the Lindbladian of a XXZ spin-½ chain with dephasing in Chap. 6.

3.1.2. Quantum number conservation

While the MPS formalism is already a very powerful tool for the efficient representation of states, it can benefit even further by adding symmetry considerations to the approach [30]. If a Hamiltonian is invariant according to a symmetry transformation, the corresponding matrix can be block-diagonalized into several symmetry blocks. In the Hamiltonian setting, each symmetry can also be associated with a conserved quantity, so that single symmetry blocks can be labeled by the value of said observable defining a quantum number. Prominent examples are the conservation of the total magnetization in a Heisenberg spin chain or the particle number conservation in Hubbard-type models. We restrict ourselves here to Abelian symmetries, where symmetry transformations of the same symmetry group commute. Nevertheless, non-Abelian symmetries have also been studied within the framework of tensor networks [66] and promise further computational improvement. For the Lindbladian the situation is more involved, and will be discussed in more detail in Sec. 3.2, but also there special cases exist where symmetry blocks can be connected to quantum numbers.

In this thesis we use the quantum number conservation features provided by the ITensor libraries [62]. Here we also follow parts of the documentation concerning the encoding of quantum numbers in the implementation [67]. In the tensor network language it is useful to express this property via assigning additional information to the tensor indices. More precisely, a quantum number is assigned to each index and the indices are grouped according to this numbers, respectively. A helpful concept is to regard the quantum numbers as a flux which enters or leaves a tensor through the indices. This suggests to also extend the graphical notation by assigning arrows indicating the direction of the flux. The convention here is that the quantum number flux of indices entering a tensor, as labeled by the arrows, is subtracted from the flux leaving the tensor. Furthermore, it is important that this flux is well-defined for every allowed tensor, meaning, that it is possible to classify the tensor to a single symmetry block by summing over the impact of all indices. To demonstrate this implementation, let us consider two spin-$1/2$ sites coupled via the Hamiltonian $H = J_x(S_1^x S_2^x + S_1^y S_1^y) + J_z S_1^z S_2^z$, with $S^\alpha = \frac{\hbar}{2}\sigma^\alpha$, where σ^α are the Pauli matrices. Using the basis $\mathbb{B} = \{|\uparrow\uparrow\rangle, |\uparrow\downarrow\rangle, |\downarrow\uparrow\rangle, |\downarrow\downarrow\rangle\}$, the Hamiltonian matrix is block diagonal (here we choose $\hbar^2 J_x = 2$ and $\hbar^2 J_z = 4$)

$$
H = \begin{array}{c} \\ \\ \end{array} \;
\begin{array}{c}
\color{red}{1} \quad \color{red}{0} \;\; \color{red}{-1} \\
\begin{array}{r}
\color{red}{1} \\
\color{red}{0} \\
\\
\color{red}{-1}
\end{array}
\left(
\begin{array}{c|cc|c}
1 & & & \\ \hline
& 1 & 1 & \\
& 1 & 1 & \\ \hline
& & & 1
\end{array}
\right)
\end{array} .
\tag{3.22}
$$

This Hamiltonian conserves the total magnetization $M = \sum_j S_j^z$ which can be used to define conserved quantum numbers, so that the two original four-dimensional indices have been distributed on the three arising quantum number sectors, denoted by the red numbers. Only index combinations contribute to the tensor, which have the same incoming and outgoing quantum

number flux, whose direction is visualized by the arrows. Consequently H has a well-defined total flux of zero. To give an example for the use of the diagrams, the application of the Hamiltonian to the up-down state is expressed by

$$H|\uparrow\downarrow\rangle = \boxed{H} = |\downarrow\uparrow\rangle = \bigcirc . \tag{3.23}$$

Applying this quantum number flux to matrix product states for large systems, offers a neat way of restricting the MPS manifold to certain symmetry sectors without having to go through the exponentially large Hilbert space to select states exhibiting a certain quantum number. Therefore, starting with an MPS in one sector ensures that it never leaves this sector, as long as no operators with finite flux are applied. This is for example a typical scenario in the ground state search or the time evolution algorithms presented in the next two sections. On the other hand, switching between blocks with different quantum number is computationally just as easy, as only one operator with a well defined non-zero flux divergence needs to be applied.

3.1.3. Ground state search - Density matrix renormalization group (DMRG)

We will continue by presenting the very successful applications of tensor network based algorithms to the problem of finding the ground state of a large many-body Hamiltonian. The procedure can also be generalized to the optimization problem of finding the eigenstate for the lowest eigenvalue of an operator which can be efficiently represented in MPO form, although a general statement according the fast decay of singular values and therefore the quality of the approximation can not be made. Originally, the method goes by the name density matrix renormalization group (DMRG) and has been developed in the formalism of density matrices by S. White [68]. However, it turned out that matrix product states naturally arise in the course of the algorithm and a tensor network formulation is very rewarding, especially in terms of the interpretability due to the link to the entanglement entropy [30, 69].

The optimization problem for finding the ground state $|gs\rangle$ is defined as

$$|gs\rangle = \text{argmin}_{|\psi\rangle} \frac{\langle\psi|H|\psi\rangle}{\langle\psi|\psi\rangle}, \tag{3.24}$$

with the constraint for the wave function to have unit norm, i.e. $\langle\psi|\psi\rangle = 1$. The Hamiltonian is assumed to be well-representable as an MPO with a not too large dimension D_W of the bond indices b_l (cf. Eq. 3.19) and the wave function is represented in MPS form with bond dimension D and local physical dimension d. Using the Langrange formalism for constrained optimization

problems, the Langrange function is given by

$$\langle\psi|H|\psi\rangle - \lambda\left(\langle\psi|\psi\rangle - 1\right) = \sum_{\substack{\sigma_1,\ldots,\sigma_L \\ \sigma_1',\ldots,\sigma_L'}} \sum_{\substack{a_1,\ldots,a_{L-1} \\ a_1',\ldots,a_{L-1}'}} \sum_{b_1,\ldots,b_{L-1}} \left[A_{1,a_1'}^{\sigma_1'*} \ldots A_{a_{l-2}',a_{l-1}'}^{\sigma_{l-1}'*} M_{a_{l-1}',a_l'}^{\sigma_l'*} B_{a_l',a_{l+1}'}^{\sigma_{l+1}'*} \ldots B_{a_{L-1}',1}^{\sigma_L'*} \right.$$

$$\times A_{1,a_1}^{\sigma_1} \ldots A_{a_{l-2},a_{l-1}}^{\sigma_{l-1}} M_{a_{l-1},a_l}^{\sigma_l} B_{a_l,a_{l+1}}^{\sigma_{l+1}} \ldots B_{a_{L-1},1}^{\sigma_L}$$

$$\left. \times W_{1,b_1}^{\sigma_1,\sigma_1'} W_{b_1,b_2}^{\sigma_2,\sigma_2'} \ldots W_{b_{L-1},1}^{\sigma_L,\sigma_L'} \right],$$

$$- \lambda \left\{ \sum_{\sigma_1,\ldots,\sigma_L} \sum_{\substack{a_1,\ldots,a_{L-1} \\ a_1',\ldots,a_{L-1}'}} \left[A_{1,a_1'}^{\sigma_1*} \ldots A_{a_{l-2}',a_{l-1}'}^{\sigma_{l-1}*} M_{a_{l-1}',a_l'}^{\sigma_l*} B_{a_l',a_{l+1}'}^{\sigma_{l+1}*} \ldots B_{a_{L-1}',1}^{\sigma_L*} \right. \right.$$

$$\left. \left. \times A_{1,a_1}^{\sigma_1} \ldots A_{a_{l-2},a_{l-1}}^{\sigma_{l-1}} M_{a_{l-1},a_l}^{\sigma_l} B_{a_l,a_{l+1}}^{\sigma_{l+1}} \ldots B_{a_{L-1},1}^{\sigma_L} \right] - 1 \right\}$$

$$= \;\; \text{(diagram)} \;\; - \lambda \left\{ \;\; \text{(diagram)} \;\; - 1 \right\} , \quad (3.25)$$

with the Lagrange parameter λ. We used here the mixed canonical form of Eq. 3.17 for the MPS as also indicated by the colors (green = left- and red=right-normalized) in the diagram. The number of tensor elements to be optimized is of the order of $D^{L-1}d^L$, so that this problem has by far to many degrees of freedom to be tackled in its entirety. The key idea of the DMRG algorithm for approaching this task, is to variationally updating a single local tensors at a site l of the MPS to approximate the total minimum from Eq. 3.24, while keeping the rest of the MPS fixed, which corresponds to the following local update scheme

$$(3.26)$$

The full algorithm is then an iteration of successive single site minimizations. Exploiting the properties of the mixed canonical state, the expression of the norm can be simplified to the contribution at site l as

$$\langle\psi|\psi\rangle = \sum_{a_{l-1},\sigma_l,a_l} M_{a_{l-1},a_l}^{\sigma_l*} M_{a_{l-1},a_l}^{\sigma_l}. \quad (3.27)$$

The expectation value of the Hamiltonian has, apart from the variational site tensor at site l, three constant constituents:

- all the contracted tensors left from site l which we define as $L_{a_{l-1},b_{l-1},a_{l-1}'}$, as displayed in Eq. 3.26,
- all the contracted tensors right from site l, defined as $R_{a_l,b_l,a_l'}$, also marked in Eq. 3.26,
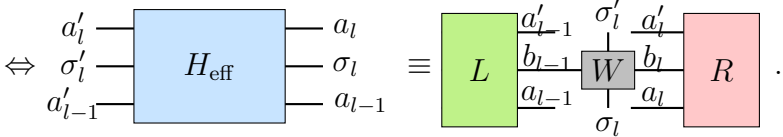
- and the local MPO tensor of the Hamiltonian at site l, which is $W^{\sigma_l,\sigma_l'}_{b_{l-1},b_l}$.

Using all the introduced objects, the Lagrange function from Eq. 3.25 can be rewritten as

$$\sum_{\sigma_l,\sigma_l'} \sum_{\substack{a_l,b_l,a_l' \\ a_{l-1},b_{l-1},a_{l-1}'}} L^{a_{l-1},a_{l-1}'}_{b_{l-1}} W^{\sigma_l,\sigma_l'}_{b_{l-1},b_l} R^{a_l,a_l'}_{b_l} M^{\sigma_l*}_{a_{l-1},a_l} M^{\sigma_l'}_{a_{l-1}',a_l'} - \lambda \left\{ \sum_{a_{l-1},\sigma_l,a_l} M^{\sigma_l*}_{a_{l-1},a_l} M^{\sigma_l}_{a_{l-1},a_l} - 1 \right\}.$$

(3.28)

We can then summarize the influence of the tensors L, R and $W^{[l]}$ by executing all tensor contractions of indices not connected to M^{σ_l} or $M^{\sigma_l'}$, giving rise to an effective tensor

$$(H_{\text{eff}})^{a_{l-1}',\sigma_l',a_l'}_{a_{l-1},\sigma_l,a_l} \equiv \sum_{b_{l-1},b_l} L^{a_{l-1},a_{l-1}'}_{b_{l-1}} W^{\sigma_l,\sigma_l'}_{b_{l-1},b_l} R^{a_l,a_l'}_{b_l}$$

(3.29)

In fact this tensor is an effective Hamiltonian, giving the total energy of the system when contracted with a local site tensor at site l. The minimal energy under the norm constraint is then found by solving the Lagrange equation of the first kind. The requirement for the derivative of the Lagrange function with respect to $M^{\sigma_l*}_{a_{l-1},a_l}$ to vanish, then translates to to the effective eigenequation

$$H_{\text{eff}} \cdot \vec{v} = \lambda \vec{v},$$

(3.30)

where H_{eff} is a matrix with the combined row [column] index $i = (a_{l-1}',\sigma_l',a_l') \ [j = (a_{l-1},\sigma_l,a_l))]$ and $\vec{v}$ is the local MPS tensor $M^{\sigma_l}_{a_{l-1},a_l}$. Due to the hermiticity of the full many-body Hamiltonian, also H_{eff} is hermitian, so that the matrix can be diagonalized and the optimal local tensor corresponds to the eigenvector for the lowest eigenvalue. At the same time, this eigenvalue is also the estimated ground state energy at this step of optimization. Although the computational complexity has been reduced remarkably, the dimension of the effective Hamiltonian $(dD^2) \times (dD^2)$ can be quite large. Fortunately, we are just interested in the lowest eigenvalue and its eigenvector for the ground state search, so that Lanczos type algorithms for finding only a certain part of the eigenspectrum can be employed in this part. We will comment on this method in further detail in Sec. 3.2.

After having solved the constrained optimization problem for one site, we can apply this consecutively on all sites. This is commonly referred to as sweeping through the lattice, where one sweep starts with an entirely right-normalized state, optimizes the first site, uses an SVD to left normalize it and then moves on to the second site. This is repeated until the right system boundary at site L is reached. Then the process is inverted, so that the MPS is optimized according to site L, which is then right normalized before the method moves on to site $L-1$. A sweep is finished once the left boundary is reached again. The initial state is usually a random MPS initialized with the chosen maximal bond dimension D, which never changes during the

updates. Then the sweeping takes place until the change of the found ground state energy is below a predefined threshold. One important practical detail is, that a construction of the L and R tensors is computationally very expensive due to the many contractions at each site. As their size $(D^2 D_W) \times (D^2 D_W)$ allows us to keep them in memory, it is favorable to store the $(L, R)_l$ pairs for each site l and update them with the new site tensors after the one-site optimization at the corresponding site. This also makes it possible to recycle the L matrices generated during a right sweep, as they reappear when sweeping left again. The same is true for the R matrices when switching directions after sweeping left.

One problem arising in this single-site optimization concept is the possibility to get stuck in a local minimum as the optimization is limited to the state manifold with fixed bond dimension D. A way to improve on this issue is to apply the local minimization on two sites simultaneously

$$\tag{3.31}$$

The ground state can be found analogously to the one-site algorithm, by rewriting the Lagrange equation as a eigen equation and using a sparse matrix eigensolver yielding an optimal two-site tensor. This tensor can be decomposed back to the two site tensors with the SVD

$$M^{\sigma_l, \sigma_{l+1}}_{a_{l-1}, a_{l+1}} = U^{\sigma_l}_{a_{l-1}, \alpha} S_\alpha V^\dagger_{\alpha, a_{l+1}}, \tag{3.32}$$

so that when sweeping from left to right, site l is updated with the U matrix and site $l + 1$ with $SV^\dagger$ and when sweeping from right to left site $l + 1$ is updated with $V^\dagger$ and site l with US. It is important to note here, that the new index α can have a dimension of up to dD so that S needs to be truncated to recover the original bond dimension D. Although this step is computationally more costly compared to the one-site optimization, the convergence is usually faster, as the optimization is done in a higher-dimensional space from which the most influential contribution is selected when truncating the singular values. For this reason, we will use this method later for calculating ground states.

3.1.4. Time evolution - Time-dependent matrix product state algorithm (tMPS)

Another large area of applications of matrix product states is the time-evolution of states in correlated one-dimensional quantum systems. We will present the unitary evolution of a pure quantum state here and extend this to Markovian open quantum systems in Chap. 4. For a time-independent Hamiltonian H, the time-evolved state at time t of a system which has initially been prepared as $|\psi(t = 0)\rangle$ is obtained from the formal solution of the Schrödinger equation

$$|\psi(t)\rangle = \mathrm{e}^{-iHt/\hbar}|\psi(t = 0)\rangle. \tag{3.33}$$

This problem can also be reformulated for finding the ground state by performing an evolution with an imaginary time $\beta = it$. Nevertheless, usually the DMRG algorithm from the previous

Order	Suzuki-Trotter decomposition
1st order	$e^{-iH\Delta t/\hbar} = e^{-iH_{\text{odd}}\Delta t/\hbar}e^{-iH_{\text{even}}\Delta t/\hbar} + \mathcal{O}(L\Delta t^2)$
2nd order	$e^{-iH\Delta t/\hbar} = e^{-iH_{\text{odd}}\Delta t/2\hbar}e^{-iH_{\text{even}}\Delta t/\hbar}e^{-iH_{\text{odd}}\Delta t/2\hbar} + \mathcal{O}(L\Delta t^3)$
4th order	$e^{-iH\Delta t/\hbar} = U(\tau_1)U(\tau_2)U(\tau_3)U(\tau_2)U(\tau_1) + \mathcal{O}(L\Delta t^5)$,
	with $U(\tau_i) = e^{-iH_{\text{odd}}\tau_i/2\hbar}e^{-iH_{\text{even}}\tau_i/\hbar}e^{-iH_{\text{odd}}\tau_i/2\hbar}$
	and $\tau_1 = \tau_2 = \frac{1}{4-4^{1/3}}\Delta t$, $\tau_3 = \Delta t - 2\tau_1 - 2\tau_2$

Table 3.1.: Suzuki-Trotter decompositions of the time-evolution operator for a short-ranged Hamiltonian, which only connects nearest neighbor sites [30].

section shows better performance, and is therefore preferred. Tensor networks are one possibility to encode the effect of the time evolution operator, which is infeasible to calculate exactly in larger interacting systems. The basic concept is to restrict the states to a subspace of the Hilbert space which is adapted during the course of time-evolution [58].

While it is possible to express a large range of Hamiltonians rigorously as MPOs with low bond dimension, the exponentiation in the corresponding time evolution operator produces again a large rank-L tensor

$$
e^{-iHt/\hbar} = \exp\left[-\frac{it}{\hbar}\sum_{\vec{\sigma},\vec{\sigma}'} \,\middle|\, \vec{\sigma}'\rangle\langle\vec{\sigma}\,\middle|\,\right]
$$

$$
= \sum_{\vec{\sigma},\vec{\sigma}'} \,\middle|\, \vec{\sigma}'\rangle\langle\vec{\sigma}\,\middle|\, . \tag{3.34}
$$

As a first step, the full operator is split up into many small time steps. With $t = N\Delta t$, the evolution operator equals $(\exp[-i\Delta tH/\hbar])^N$. There exist approximations for the exponential, which are exact up to first or second order in the time step without further restrictions for the model [70]. Another recent development has shown that it is possible to adapt the DMRG algorithm to the problem of time-evolution using the projector on the tangent space of the MPS manifold [71, 72], known as the time-dependent variational principle (TDVP). Nevertheless, the task is simplified substantially, when assuming short-ranged Hamiltonians which only couple adjacent sites $H = \sum_{j=1}^{L-1} h_{j,j+1}$, appearing in many places across quantum many-body physics in one dimension. In this case, each of the bond-Hamiltonians $h_{j,j+1}$ commutes with the Hamiltonian of all other bonds, except its direct neighbors. It is advantageous to divide the full model

3.1 Matrix product state techniques

Hamiltonian into the groups of odd and even bonds

$$H = \sum_{j=1}^{\frac{L-1}{2}} h_{2j-1,2j} + \sum_{j=1}^{\frac{L-1}{2}} h_{2j,2j+1} \equiv H_{\text{odd}} + H_{\text{even}}, \tag{3.35}$$

where $[H_{\text{odd}}, H_{\text{even}}] \neq 0$ but each bond summand of the even and odd sums commutes with all other summands, allowing the exact decompositions $e^{-iH_{\text{odd}}t/\hbar} = \prod_j e^{-ith_{2j-1,2j}/\hbar}$ and $e^{-iH_{\text{even}}t/\hbar} = \prod_j e^{-ith_{2j,2j+1}/\hbar}$. If the time step Δt is then chosen to be sufficiently small, the full evolution operator can be approximated by the Suzuki-Trotter decomposition [73, 74]. In fact, there exists a whole family of associated decompositions, distinguished by the order of the exponent. Table 3.1 lists the first, second and fourth order decomposition. The time-evolution steps for a single bond,

$$e^{-ih_{j,j+1}t/2\hbar} = \sum_{\substack{\sigma_j,\sigma_{j+1} \\ \sigma'_j,\sigma'_{j+1}}} \boxed{e^{-ih_{j,j+1}\Delta t/2\hbar}} \; |\sigma'_j\sigma'_{j+1}\rangle\langle\sigma_j\sigma_{j+1}| \tag{3.36}$$

are called gates and can be calculated either by diagonalizing and exponentiating the two-site Hamiltonian or by using a very large order expansion, which is possible to do for tensors of this size. The bond gate, as defined in Eq. 3.36, can be seen as a matrix with dimension $(d^2 \times d^2)$, resulting in a bond dimension of d^2 when rewriting in terms of local operators using an SVD. As a consequence, the contraction of this bond gate with two sites of an MPS, M^{σ_j} and $M^{\sigma_{j+1}}$, yields a two-site tensor, which, when divided into two sites again, has an increased bond dimension of $d^2 D$. Therefore, similar to the two-site DMRG optimization, the growing bond dimension eventually needs to be truncated to be computationally realizable. The process of a bond gate application can be seen as an exploration of a subspace of the Hilbert space larger than the one covered by the MPS with the fixed bond dimension D, followed by a projection on the latter. Working again with MPSs in mixed canonical form, a full time step for the second order formula from Table 3.1 starts with successively applying all odd gates starting from the left lattice boundary with time step $\Delta t/2$ while moving the orthogonality center to the left site before every gate. This is followed by applying all even gates with Δt with a pass of the chain from right to left and then again an application of all odd gates from left to right with the time

step $\Delta t/2$. In terms of the diagram representation the order of gate application is expressed by

$$|\psi(t + \Delta t)\rangle = \mathrm{e}^{-iH\Delta t/\hbar}|\psi(t)\rangle = \mathrm{e}^{-iH_{\mathrm{odd}}\Delta t/2\hbar}\mathrm{e}^{-iH_{\mathrm{even}}\Delta t/\hbar}\mathrm{e}^{-iH_{\mathrm{odd}}\Delta t/2\hbar}|\psi(t)\rangle + \mathcal{O}(L\Delta t^3)$$

$$= \sum_{\sigma_1,\ldots,\sigma_{10}} \quad |\vec{\sigma}\rangle + \mathcal{O}(L\Delta t^3), \tag{3.37}$$

where the purple gates represent odd an the orange gates even bonds and the dotted arrow illustrates the order of gate applications. An alternative for the second order decomposition, is a back and forth sweep of bond gate applications through the lattice

$$\mathrm{e}^{-iH\Delta t/\hbar} = \prod_{j=1}^{L-1} \mathrm{e}^{-ih_{j,j+1}\Delta t/2\hbar} \prod_{j=L-1}^{1} \mathrm{e}^{-ih_{j,j+1}\Delta t/2\hbar} + \mathcal{O}(\Delta t^2), \tag{3.38}$$

which has the same order of accuracy in the time step. Regarding the convergence of the method, we need to keep track of two error sources: On the one hand, there is the truncation error caused by the compression occurring after each gate application. The needed bond dimension scales exponentially with the von Neumann entropy $D \sim \exp[S_{\mathrm{vN}}(t)]$ [75], which is restricted by the Lieb-Robinson bound [59] to a maximally linear growth in time for local Hamiltonians [76]. Therefore, when starting with a low entangled state, as for example a product state, there typically exists a threshold time for each defined maximally bond dimension, after which the truncation error exceeds a predefined accuracy goal due to the increase of entanglement. This time, which marks the time region of convergence for the cutoff error and is sometimes referred to as run-away time, can be determined as the time where two identical time evolution calculations for different values of D begin to deviate. On the other hand, a systematic error is induced by the finite time step, which controls the quality of the Suzuki-Trotter representation. As a result there exists a trade-off among these two error sources: Increasing the order of the Suzuki-Trotter decomposition causes a lower time step error but at the same time needs more gate applications and therefore more truncation procedures so that the truncation error increases.

Let us present a case study to support this statement with data. For this purpose we consider the XX spin-½ model

$$H_{XX} = J \sum_{j=1}^{L-1} \left(S_j^x S_{j+1}^x + S_j^y S_{j+1}^y \right) \tag{3.39}$$

with $S^\alpha = \frac{\hbar}{2}\sigma^\alpha$ for a chain of spins with length L. We compute the time-evolution of the state with all spins in the first half of the system aligned upwards and all spins in the second half downwards $|\psi(t = 0)\rangle = |\uparrow \ldots \uparrow\downarrow \ldots \downarrow\rangle$. The local magnetization $\langle S_j^z \rangle$ can be accessed ana-
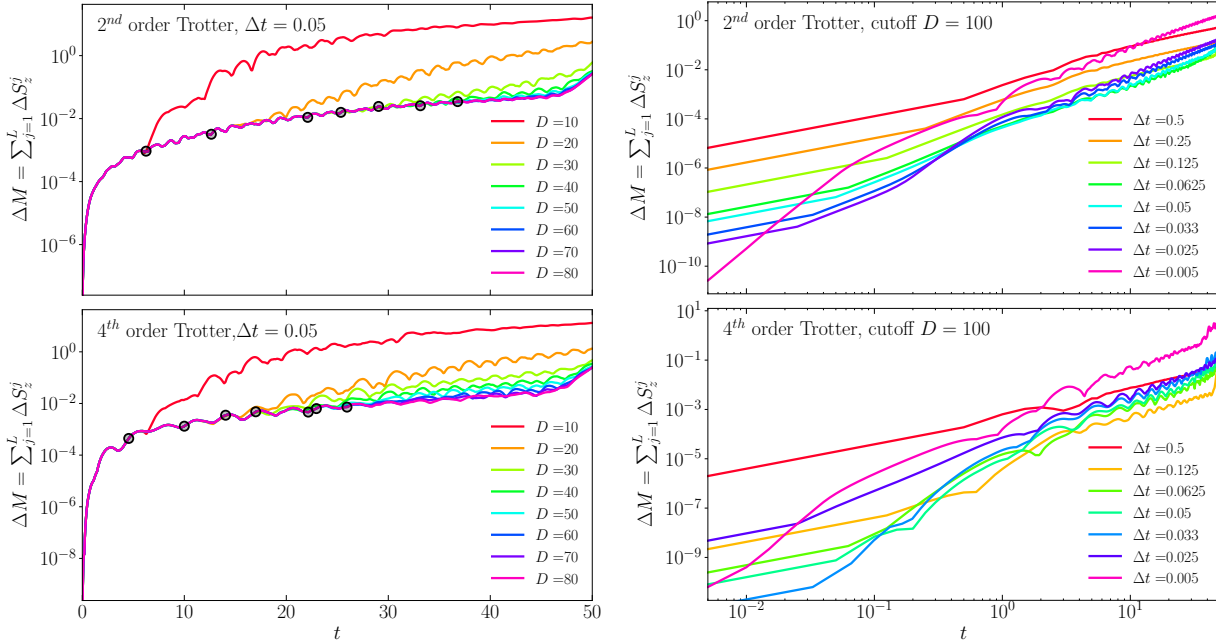
Figure 3.1.: Deviation of tMPS results from exact analytic calculations for a XX spin-½ chain of length $L = 100$, $J = 1$ and initial state $|\psi_0\rangle = |\uparrow \ldots \uparrow\downarrow \ldots \downarrow\rangle$. Left panels: For a fixed time step, different bond dimensions are compared and run-away times (black markers) are determined accordingly. Right panels: Deviation for fixed bond dimension and different time step sizes are plotted. Both second (top panel) and fourth (bottom panel) Suzuki-Trotter orders are shown.

lytically for the XX-model [77, 78]. We show the time dependence of the deviation of a tMPS calculation from the exact solution in Fig. 3.1. First of all, we observe that the run-away times as displayed by the black markers move to later times for larger bond dimension of the MPS. Moreover, for a fixed time step (left panel) we see, that a larger order of the decomposition of the time evolution operator results in earlier run-away times. On the other side, when keeping the bond dimension constant, a smaller time step does not necessarily show a better accuracy, but there rather exists a minimum of the deviation for intermediate time step sizes.

3.2. **Exact diagonalization of the Lindbladian**

For small systems it is possible to access the non-equilibrium properties of finite open systems by computing the full Lindbladian spectrum or parts of it by employing exact diagonalizaton (ED) techniques. This method, which is generally suitable for solving first order differential equation systems, is also well-established in computational many-body physics of closed quantum systems, where it has been successfully used to describe low-energy features in the proximity of the models' ground states, as well as for the time-evolution of the wave function [79, 80]. Among others, application include work on quantum magnetism [81–83] and fermionic models such as the t-J model [84, 85] or the Hubbard model [86, 87]. For these examples, the differential equation, generating the dynamics, is given by the Schrödinger equation $i\hbar\partial_t|\psi(t)\rangle = H|\psi(t)\rangle$,

so that the problem breaks down to the diagonalization of the Hamiltonian matrix H. The first step of this procedure is to find an efficient way to represent the basis of the corresponding Hilbert space $\mathcal{H}$. For example, the basis states of a spin-½ chain model, given by a lattice of spins with local basis $\mathbb{B}_i = \{|\uparrow\rangle, |\downarrow\rangle\}$ at site i, can be conveniently labeled using binary numbers

$$| \uparrow\uparrow\downarrow\uparrow\downarrow\downarrow \rangle = |110100_2\rangle = |52_{10}\rangle. \tag{3.40}$$

The next step is to compute the matrix elements of the Hamiltonian, where it is often beneficial to make use of the potential sparseness of the matrix in favor of memory and run time. Once the matrix is set-up, it is usually the most practical approach to use an eigensolver of an already implemented linear algebra backend like for example one of the various versions of LAPACK (Linear Algebra Package). In the work presented in this thesis, we use the optimized extension MKL (Math Kernel Library) provided by Intel. The usual approach of these packages to extract the eigensystem of a matrix first uses a sequence of similarity transformations like Jacobi or Hausholder transformations, followed by a QR decomposition. For details we refer to chapter 11 of Ref. [88]. Now there are two possible paths to follow. Either one aims at the full spectrum of the matrix, where suitable algorithms have a cubic space and time complexity $\mathcal{O}(D^3)$, with D being the dimension of the Hilbert space. In other cases, the consideration is focused on a certain region of the eigenspectrum exclusively. The latter allows to use Lanczos-type methods[89], where the original matrix is truncated to the so-called Krylov space, where it has the form of a tridiagonal matrix. The Krylov space is engineered such that the lowest (or largest) eigenvalue of the resulting matrix coincides with the one from the original matrix. In this case, the most expensive part of the algorithm is the application of the Hamiltonian matrix to a state vector. Repeating the steps of this procedure for the space orthogonal to the found state of lowest energy additionally provides access to the excitation spectrum and also enables an approximative determination of the system dynamics [90]. In Chap. 5, we determine the full spectrum but will also comment on the relevance of the contribution of different eigenstates. A challenge, shared by all applications, is the exponential growth of the Hilbert space dimension with the system size as for example the number of sites of a lattice L. For the spin model from Eq. 3.40 with local dimension being two, the linear matrix extension grows with 2^L, resulting in already 32,768 states for only 15 sites, which already makes the numerical solution impractical for this system size using standard algorithms without additional input. Recently, parallelizing subparts of the diagonalization routines in terms of using distributed memory, for example in the appearing matrix products, leads to notable advancements for the reachable system sizes [91]. We will introduce further, more physically oriented, strategies to expand these boundaries and soften the limitations.

Let us now shift to the time evolution of open system described by the Lindblad equation, introduced in Eq. 2.9. This increases the complexity further, as the object of interest is the density operator

$$\rho = \sum_{m,n} \rho_{mn} |m\rangle\langle n|, \tag{3.41}$$

a matrix with a linear extend of $\dim(\mathcal{H})$. To be able to use diagonalization techniques for the super operator $\mathcal{L}$, we reshape the density matrix to vector form, which is then an element of

the super space formed by the tensor product of the original Hilbert space with its dual space $\mathcal{H}_{\text{super}} = \mathcal{H} \otimes \mathcal{H}^*$. We denote elements of this space with double angular parentheses $|\cdot\rangle\!\rangle$. The space $\mathcal{H}_{\text{super}}$ is again a Hilbert space with the corresponding inner product $\langle\!\langle \rho_1 | \rho_2 \rangle\!\rangle = \text{tr}(\rho_1^\dagger \rho_2)$. In our case we sort the new basis such that the reshaped vector is given by stacking the matrix rows. For a two-dimensional space this works as follows

$$\rho = \sum_{m,n} \rho_{mn} |m\rangle\langle n| \longrightarrow |\rho\rangle\!\rangle = \sum_{m,n} \rho_{mn} |m,n\rangle\!\rangle, \text{ and } \begin{pmatrix} \rho_{11} & \rho_{12} \\ \rho_{21} & \rho_{22} \end{pmatrix} \longrightarrow \begin{pmatrix} \rho_{11} \\ \rho_{12} \\ \rho_{21} \\ \rho_{22} \end{pmatrix}. \tag{3.42}$$

Matrix multiplications in the original space are also represented differently in the super space: $A \cdot \rho \to (A \otimes \mathbb{1}) \cdot |\rho\rangle\!\rangle$ and $\rho \cdot B \to (\mathbb{1} \otimes B^T) \cdot |\rho\rangle\!\rangle$. This notation enables us now to write down the Lindblad equation in matrix form

$$\frac{\mathrm{d}}{\mathrm{d}t} |\rho(t)\rangle\!\rangle = \left[-\frac{i}{\hbar} H \otimes \mathbb{1} + \frac{i}{\hbar} \mathbb{1} \otimes H^T \right.$$
$$\left. + \sum_j \gamma_j \left(L_j \otimes (L_j^\dagger)^T - \frac{1}{2} L_j^\dagger L_j \otimes \mathbb{1} - \frac{1}{2} \mathbb{1} \otimes (L_j^\dagger L_j)^T \right) \right] |\rho(t)\rangle\!\rangle. \tag{3.43}$$

We summarize all terms of the matrix acting on the vectorized density matrix on the right hand side, by defining them as the Lindblad matrix $M_{\mathcal{L}}$. In contrast to the Hamiltonian, this matrix is in general not hermitian. In a scenario where we build up this matrix by iterating through the basis states, it is also convenient, to specify the element-wise form of this equation given by

$$\frac{\mathrm{d}}{\mathrm{d}t} \rho_{mn}(t) = -\frac{i}{\hbar} \sum_k \left(H_{mk} \rho_{kn}(t) - \rho_{mk}(t) H_{kn} \right) \tag{3.44}$$
$$+ \sum_j \gamma_j \sum_{k,l} \left[(L_j)_{mk} \rho_{kl}(t) (L_j)_{nl}^* - \frac{1}{2} (L_j)_{km}^* (L_j)_{kl} \rho_{ln}(t) - \frac{1}{2} \rho_{mk}(t) (L_j)_{lk}^* (L_j)_{ln} \right],$$

where each ρ_{mn} is the coefficient of one basis vector in a linear combination representation of $|\rho\rangle\!\rangle$. A crucial property of the Lindblad matrix is, that its linear extent is quadratic in the dimension of the system Hilbert space, i.e. $M_{\mathcal{L}} \in \mathbb{C}^{D^2 \times D^2}$. This amplifies the restrictions to small systems, originating in the exponential growth of the system space, even further. Formally, Eq. 3.43 can be solved by $|\rho(t)\rangle\!\rangle = \exp(M_{\mathcal{L}} t) |\rho(t=0)\rangle\!\rangle$. To be able to calculate the exponential, we use the numerical diagonalization of the Lindblad matrix yielding $U^{-1} M_{\mathcal{L}} U = \text{diag}[\lambda_1, \ldots, \lambda_{D^2}]$, so that the full time evolution can be determined as

$$|\rho(t)\rangle\!\rangle = U \, \text{diag}\left[e^{\lambda_1 t}, \ldots, e^{\lambda_{D^2} t} \right] U^{-1} |\rho(t=0)\rangle\!\rangle. \tag{3.45}$$

At this point, it makes sense to recapitulate the features of the Lindbladian eigenspectrum in-
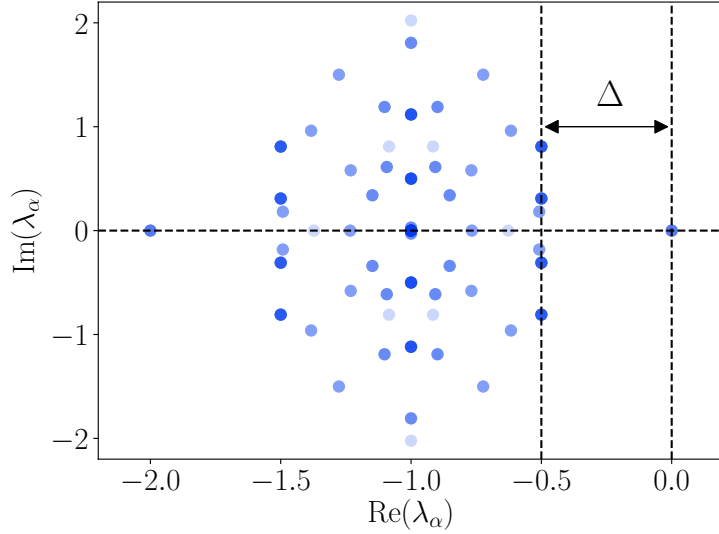
Figure 3.2.: Eigenspectrum of the Lindblad matrix $M_\mathcal{L}$ of an open XX spin chain of size $L = 4$ dissipatively connected to a Markovian environment via the Lindblad jump operators $L_j = S_j^z$, with a dissipative coupling strength $\hbar\gamma/J = 1$. The dissipative gap is denoted by Δ, and the points are plotted with an opacity of 20% so that degenerate eigenvalues appear darker.

troduced in Sec. 2.1. As the Lindblad equation conserves the norm the real part of the complex eigenvalues need to be non-positive, i.e.

$$\{\lambda_\alpha = -\lambda_\alpha^R + i\lambda_\alpha^I | \lambda_\alpha^R \in \mathbb{R}_0^+, \lambda_\alpha^I \in \mathbb{R}\}. \tag{3.46}$$

To present an example, we investigate the spectrum of the XX spin-½ chain defined by the Hamiltonian from Eq. 3.39 with a dissipator that introduces bulk dephasing noise represented by the Lindblad operators $\{S_j^z\}$

$$\mathcal{D}(\rho) = \gamma \sum_j [S_j^z \rho S_j^z - \rho/4]. \tag{3.47}$$

The corresponding spectrum is shown in Fig. 3.2. Another feature of the spectrum portrayed in Fig. 3.2 is the mirror symmetry of eigenvalues of the Lindblad matrix around the real axis. This originates in the conservation of hermiticity by the Lindblad evolution, $(\mathcal{L}\rho)^\dagger = \mathcal{L}\rho^\dagger$ which guarantees, that if there is a eigenvector of $M_\mathcal{L}$ with finite imaginary part, there also exists a eigenvector for the complex conjugated eigenvalue. As a consequence of these spectral properties, the contribution of an eigenstates of the Lindblad matrix $M_\mathcal{L}$ to the dynamics, is either restricted to a complex phase factor or is exponentially damped in time. Of special interest are the states with the largest non-vanishing real part eigenvalue, a quantity also known as the dissipative gap of the spectrum and denoted by Δ in the spectrum of Fig. 3.2. These states are the non-steady states which survive the longest and therefore have the largest impact on the

late dynamics in the approach of the steady state(s). At the same time, at least one vanishing eigenvalue needs to exist, so that the state does not decay entirely. This can either be a unique eigenstate or a manifold spanned by eigenstates of zero eigenvalues. The rigorous condition for the uniqueness of the steady state requires the Lindblad matrix to be (i) irreducible and (ii) aperiodic [92]. This, together with the Perron-Frobenius theorem [93] ensures a unique steady state. Intuitively, the conditions mean, that all states are connected by the Lindbladian, so that states from different regions in state space do not evolve decoupled from one another, and that there do not exist periodic structures in the dynamics leading to repeating circular movement involving a subset of all states only. Importantly, not all of the states of a manifold of eigenstates with vanishing eigenvalues translate to physical density matrices, defined by the properties

1. the density matrix is hermitian, $\rho = \rho^\dagger$,
2. it has unit trace, $\mathrm{tr}(\rho) = 1$,
3. it is positive semi-definite, $\langle \psi | \rho | \psi \rangle \geq 0 \ \forall \ | \psi \rangle \in \mathcal{H} / \{ \vec{0} \}$.

Although there is no straight-forward way to find linear independent eigenstates fulfilling these conditions, a few strategies can help to resolve the problem. One option to obtain one physical state is to start with a certain valid state and calculate the time evolution for very long times which then is essentially a physical stationary state, as the Lindblad dynamics conserves the posed conditions. A more pragmatic approach, is to conduct a grid search over eigenstate combinations, which is only a doable way if the degeneracy is small. One can improve on this by incorporating the hermiticity and unit trace condition in the search. More systematically, one could also use the given restrictions to build a linear equation system which needs to be solved accordingly.

Nevertheless, before doing so, it turns out to be very rewarding to look out for symmetries of the Lindbladian first. As we see later, this allows the block diagonalization of the corresponding matrix, and therefore clearly breaks the condition of irreducibility and aperiodicity for the uniqueness of steady states introduced above. Therefore, the goal is to split up the Lindbladian in irreducible, aperiodic blocks with maximally one steady state. In Hamiltonian systems, this has been proven to be a very impactful simplification of the problem, as it allows to block-diagonalize the Hamiltonian matrix and treat the single symmetry blocks independently. For a unitary time evolution, the following equivalence relations hold

$$\text{given } \phi \in \mathbb{R}, J = J^\dagger : H = \mathrm{e}^{i\phi J} H \mathrm{e}^{-i\phi J} \Leftrightarrow [J, H] = 0 \Leftrightarrow \frac{\mathrm{d}}{\mathrm{d}t} \langle \psi(t) | J | \psi(t) \rangle = 0 \qquad (3.48)$$

That means, models that are invariant under symmetry transformations generated by an observable J, conserve this observable in the course of quantum dynamics. For Lindbladian systems the situation is more complicated [94, 95]. A symmetry of the Lindbladian is present, if transforming the density matrix of the initial state with the corresponding symmetry transformation, time-evolving the transformed state before applying the inverse transformation is equivalent to the bare Lindblad dynamics, i.e.

$$\mathrm{e}^{-i\phi J} \left[\mathcal{L} \left(\mathrm{e}^{i\phi J} \rho(t=0) \mathrm{e}^{-i\phi J^\dagger} \right) \right] \mathrm{e}^{i\phi J^\dagger} \equiv \mathcal{U}^\dagger \mathcal{L} \mathcal{U} \rho(t=0) \Leftrightarrow \mathcal{L} = \mathcal{U}^\dagger \mathcal{L} \mathcal{U} \qquad (3.49)$$

Here we defined the symmetry transformation $\mathcal{U}$ as applied to density matrices. Using the introduced notation for operators acting on the super space $\mathcal{H}_{\mathrm{super}}$ of vectorized density matrices $|\rho\rangle\!\rangle$, this is given by $\mathcal{U} = \exp[i\phi(J \otimes \mathbb{1} - \mathbb{1} \otimes J^*)]$ [95]. Together with Eq. 3.49, one finds that the commutator $[\mathcal{L}, J \otimes \mathbb{1} - \mathbb{1} \otimes J^*]$ vanishes. As this commutator is not directly linked to the time evolution of the operator J, as it is in unitary systems via the Heisenberg equation of motion, it is not possible to draw conclusions about conservation laws. The latter is much rather characterized by eigenstates corresponding to vanishing eigenvalues of the Lindblad master equation for operators satisfying $\frac{\mathrm{d}}{\mathrm{d}t}\tilde{J} = \mathcal{L}^\dagger \tilde{J} = 0$, with $\tilde{J} = J \otimes \mathbb{1} - \mathbb{1} \otimes J^*$. Nevertheless, one special case, which we will also employ later in Chap. 5, is when an operator J commutes with both, the Hamiltonian and all Lindblad jump operators. This satisfies the commutator relation mentioned before and therefore guarantees a symmetry relation as in Eq. 3.49 but also poses a conserved quantity. Independent of the existence of conservation laws, symmetries always guarantee the possibility of decomposing the Lindblad matrix $M_{\mathcal{L}}$ into symmetry blocks and therefore reduce the numeric complexity of the problem remarkably. Coming back to the issue of degenerate zero-eigenvalue states, this decomposition can also help by engineering the symmetry blocks such, that ideally only one zero-eigenvalue state exists per block. This state is then necessarily a physical steady state, because it is attractively approached in time by a physical initial state prepared in the part of the space of density matrices.

3.3. Many-body adiabatic elimination

An analytic approach to the time evolution of the density matrix generated by the Lindblad master equation introduced in Eq. 2.9 can be obtained by focusing on the parameter regime, where the dissipation plays the dominant role. A method exploiting this property is given by the so-called many-body adiabatic elimination. This section gives a general introduction of this method along the lines of [96] and outlines ways to extract information analytically as well as shows how it can be employed to implement approximative numerical methods which are computational more feasible than the full solution.

The first step is to identify the kernel of the dissipator $\mathcal{D}$, also known as the dissipation-free subspace, denoted by Λ^0 and defined as

$$\Lambda^0 \equiv \{\rho \mid \mathcal{D}(\rho) = 0\}. \tag{3.50}$$

Next, the full Lindblad superoperator $\mathcal{L}$ is split up into $\mathcal{L} = \mathcal{L}_0 + \mathcal{L}_{\mathcal{V}}$, where $\mathcal{L}_0$ is defined such, that its application to every state in Λ^0 is again an element of the dissipation-free subspace,

$$\mathcal{L}_0 = -i\left[H_D, \cdot\right] + \mathcal{D}, \tag{3.51}$$
$$\mathcal{L}_{\mathcal{V}} = -i\left[H_{\mathcal{V}}, \cdot\right], \tag{3.52}$$
$$\text{where } H = H_D + H_{\mathcal{V}} \text{ and } \mathcal{L}_0\rho^0 \in \Lambda^0 \ , \ \mathcal{L}_{\mathcal{V}}\rho^0 \notin \Lambda^0 \quad \forall \rho^0 \in \Lambda^0.$$

Now, for strong dissipation strengths the dissipator becomes the dominant part of the model, which results in the formation of bands of the eigenvalues of $\mathcal{L}_0$ in the complex plane perpen-
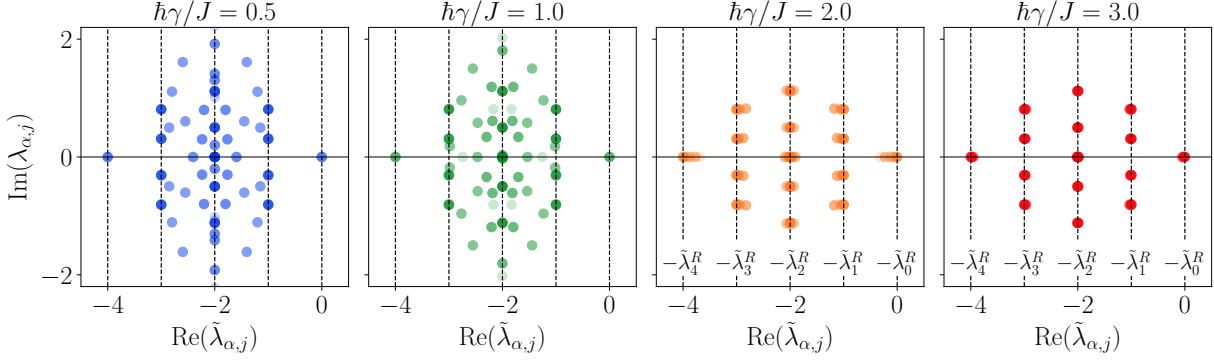
Figure 3.3.: Numerically computed eigenspectra of the Lindbladian of the open XX spin-½ chain of length $L = 4$, defined by Eq. 3.39 and Eq. 3.47. The real part has been rescaled as $\tilde{\lambda}_{\alpha,j} = \lambda_{\alpha,j} 2/\gamma^2$. For large dissipation strength the spectrum forms bands, parallel to the imaginary axis which can be labeled by their shared real part value, as displayed in the panels for $\hbar\gamma/J = 2, 3$.

dicular to the real axis. To emphasize this we plot the eigenspectrum of the open XX spin-½ chain, as defined in Eq. 3.39 and Eq. 3.47, for different dissipation strengths in Fig. 3.3. It becomes clear that here the real parts of the eigenvalues will move to certain well-separated fixed values as soon as the dissipation exceeds the Hamiltonian contributions, where the distance in between bands depends on the dissipation strength. In this regime, we denote the eigenvalues by $\lambda_{\alpha,j} = -\lambda_\alpha^R + i\lambda_{\alpha,j}^I$ with $\lambda_\alpha^R \geq 0$ and $\lambda_{\alpha,j}^I \in \mathbb{R}$, where the bands are labeled by α, accounting for the shared real part of the eigenvalues. The naming order is consistent with the order of the real parts, i.e. $0 = \lambda_0^R \geq \lambda_1^R \geq \lambda_2^R \geq \ldots \geq \lambda_N^R$. The bands can be associated with higher dissipative subspaces, which we denote by Λ^α accordingly. As a consequence, the operator $\mathcal{L}_0$ applied to states in a given subspace causes an evolution, which is limited to the respective subspace, while $\mathcal{L}_\mathcal{V}$ enables the switching between different spaces. This behavior is portrayed in Fig. 3.4.

Using the projector P^α for the αth dissipative subspace, all physical density matrices can be expressed as a superposition of its projection on the different subspaces $\rho = \sum_\alpha P^\alpha \rho$. With the definition $\mathcal{V}^{\alpha\beta} \equiv P^\alpha \mathcal{L}_\mathcal{V} P^\beta$, the full dynamics of the density matrix can be rewritten as

$$\frac{\mathrm{d}}{\mathrm{d}t}\rho = (\mathcal{L}_0 + \mathcal{L}_\mathcal{V})\,\rho = \sum_\alpha \mathcal{L}_0 P^\alpha \rho + \sum_{\beta \neq \alpha} \mathcal{V}^{\beta\alpha}\rho.$$

(3.53)

For times $t \gg 1/\gamma$, the time evolution is dominated by states from the dissipation free subspace, as all eigenvalues with non-vanishing real part, cause an exponential decay of the associated states

Figure 3.4.: Dissipative subspaces, spanned by the eigenvectors of $\mathcal{L}_0$ with equal real part of the eigenvalues, λ_α^R.

in time. As a result, the higher dissipative subspaces can be *adiabatically eliminated*. A consistent derivation of the effective evolution in Λ^0 is presented in the appendix in section A.1, yielding the final result in Eq. A.6

$$\frac{\mathrm{d}}{\mathrm{d}t}\rho_j^0(t) \approx \lambda_{0,j}\rho_j^0(t) - \sum_{k,l,\alpha \neq 0} \frac{1}{\lambda_{\alpha,k}} \mathcal{V}_{j,k}^{0\alpha} \mathcal{V}_{k,l}^{\alpha,0} \rho_l^0(t). \tag{3.54}$$

Intuitively, this approximation takes into account the motion in the dissipation-free space originated in $\mathcal{L}_0$, as well as a transition to one of the higher subspaces, f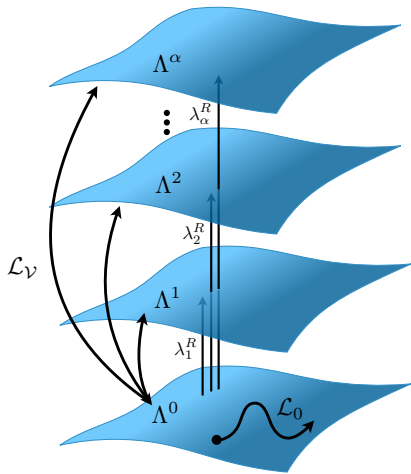ollowed immediately by a transition back to Λ^0. But it neglects for example the coupling between different higher subspaces, as these processes scales with the inverse product of two eigenvalues with non-vanishing real part.

While still describing the quantum motion of the system, Eq. 3.54 has the form of a classical Master equation [6]

$$\frac{\mathrm{d}}{\mathrm{d}t}\vec{P} = \mathbf{A}\vec{P}, \tag{3.55}$$

where $\vec{P}$ is a vector containing the weights associated with the coefficients of each element of the dissipation-free subspace, i.e. $\vec{P} = (\rho_1^0, \rho_2^0, \dots)^T$. The matrix $\mathbf{A}$ connects then elements of Λ^0 with the matrix elements $A_{jj} = \lambda_{0,j} - \sum_{k,\alpha \neq 0} \frac{1}{\lambda_{\alpha,k}} \mathcal{V}_{j,k}^{0\alpha} \mathcal{V}_{k,j}^{\alpha,0}$ and $A_{jl} = -\sum_{k,\alpha \neq 0} \frac{1}{\lambda_{\alpha,k}} \mathcal{V}_{j,k}^{0\alpha} \mathcal{V}_{k,l}^{\alpha,0}$ and fulfills the conditions for a stochastic matrix, given by $A_{ij} \geq 0$ for $i \neq j$ and $A_{ii} \leq 0$ as well as $\sum_i A_{i,j} = 0$. The latter property allows the rewriting of Eq. 3.55 as

$$\frac{\mathrm{d}}{\mathrm{d}t}P_j = \sum_{l \neq j} \left(A_{jl}P_l - A_{lj}P_j \right). \tag{3.56}$$

The time-discretizion of Eq. 3.55 fulfills the criteria for a Markov chain [6]

$$\mathrm{prob}\left(\rho_j^0(t_i) | \rho_{a_0}^0(t_0);\ \rho_{a_1}^0(t_1);\ \dots\ ;\ \rho_{a_{i-1}}^0(t_{i-1}) \right) = \mathrm{prob}\left(\rho_j^0(t_i) | \rho_{a_{i-1}}^0(t_{i-1}) \right). \tag{3.57}$$

In the course of this thesis, one application of this formalism uses Eq. 3.54 to derive a system of differential equations for correlators in spin-½ chains in a special case. The next section presents an alternative route, by developing a sampling method for solving Eq. 3.55 numerically.

3.3.1. Kinetic Monte-Carlo method

The findings in this section will enable a modeling of the master equation by the means of Monte Carlo averages over many different time-dependent trajectories in phase space. The probabilities of different states, summarized in the vector $\vec{P}$, are represented here by the weights of different elements of Λ_0. This sampling procedure is know as the kinetic Monte Carlo algorithm [97] and has repeatedly been applied to problems of non-equilibrium dynamics [98–100]. A first order approximation of Eq. 3.55 gives

$$P_j(t + \Delta t) = P_j(t) + \Delta t \sum_l (\mathbf{A})_{j,l} P_l. \tag{3.58}$$

Algorithm 1: Kinetic Monte Carlo (KMC)

Input : # samples, dissipation strength γ, Hamiltonian parameters, t_{final}, Δt
Output: MC average of observable measurements

1 *time steps* $\leftarrow$ range of times from $t = 0$ to t_{final} in steps of Δt ;
2 **for** $n \leftarrow 1$ **to** *number of MC samples* **do**
3   initialize initial state p;
4   **for** $t_i \in$ *time steps* **do**
5   measure observables and update MC average;
6           $\eta \leftarrow \text{rand}[0, 1)$;
7           $S = 0$;
8   **for** $q \in$ *states* $/\{p\}$ **do**
9               $S \leftarrow S + \text{rate}(p \to q)$;
10   **if** $S > \eta$ **then**
11                   $p \leftarrow q$;
12   **break**;

The matrix $\mathbf{A}$ covers both, the gain and loss of P_j from and to other states of the state space. The creation of a trajectory in time works then as follows. First, an initial state is defined, which could be either a hand-selected state or just a random choice, followed by the computation of the rates corresponding to the transfer from this state to any other state and to itself

$$\text{rate}(j \to j) = 1 - \Delta t \sum_{l \neq j} A_{l,j} \tag{3.59}$$

$$\text{rate}(j \to l) = \Delta t (\mathbf{A})_{l,j}. \tag{3.60}$$

Then a new state is stochastically selected according to the rates in Eq. 3.59 and 3.60. Computationally, it is the most efficient way to draw a random number $\eta \in [0, 1)$ and iteratively add up the rates $\text{rate}(j \to l \neq j)$. When the accumulated sum surpasses the value of η, the corresponding transition to the most recently added rate is realized, i.e. the state is updated for the next time step $t + \Delta t$. When η is not reached after all possible changes have been proposed, no update needs to be done. These steps are repeated until the desired time is reached. If a sufficiently large number of trajectories is sampled, the Monte Carlo average of measured time-dependent observables approaches the solution of Eq. 3.55. The algorithm is summarized in Alg. 1. We will apply this algorithm for the XXZ spin-½ chains considered in Chap. 6.

Chapter 4

Matrix product state techniques for Markovian open system dynamics

4.1. Introduction

In this chapter, we present how the concept of tensor networks, as introduced for Hamiltonian systems in Sec. 3.1.1, can be generalized to the description of the dynamics of open quantum systems in contact with a Markovian environment. The time evolution is given by the Lindblad master equation

$$\frac{\mathrm{d}}{\mathrm{d}t}\rho = \mathcal{L}\rho = -\frac{i}{\hbar}\left[H, \rho\right] + \sum_j \gamma_j \left(L_j \rho L_j^\dagger - \frac{1}{2} L_j^\dagger L_j \rho - \frac{1}{2}\rho L_j^\dagger L_j \right) \tag{4.1}$$

and therefore needs to be expressed in terms of the system's density matrix ρ. A variety of approaches for one-dimensional systems utilizes tensor network representation for an efficient, simulation of the dynamics [101]. Here we will outline two prominent strategies, both of which will be applied to research problems from non-equilibrium many-body dynamics in Chap. 6 and Chap. 7. The first idea, described in Sec. 4.2, consists of reshaping the density matrix to vector form by defining an auxiliary space and parsing it to a matrix product state structure [30, 102, 103]. The time-evolution for short-ranged Lindbladians can then be formulated analogously to the procedure portrayed in Sec. 3.1.4. This approach is closely related to the problem of finding quantum states at a finite temperature [30, 102], which typically are mixed states and therefore given by density matrices as well. Subsequent thereto, we present an alternative pathway in Sec. 4.3, consisting of a Monte-Carlo average of stochastically sampled time-evolved wave function trajectories, where the effect of the environment is included by a probabilistic application of jump operators L_j, which interrupts the otherwise deterministic evolution [6, 104, 105]. This method has been interfaced with different many-body time evolution techniques [106] including the successful integration of matrix product state methods [107–109]. In this context we will pay special attention to the computation of two-time correlation functions of the form $\langle \hat{A}(t_2)\hat{B}(t_1)\rangle$ and will present a comprehensive study, comparing the convergence of two different approaches in Sec. 4.4 as proposed by Breuer, Kappler and Petruccione [34] on

4.2. Purification of the density matrix

To be able to employ the techniques developed for quantum states from Sec. 3.1.4 for dissipative Lindblad dynamics, the density matrix needs to be encoded as an MPS. This can be achieved by adding an auxiliary space $\mathcal{H}_{\mathrm{aux}}$ to the consideration, which is a copy of the original physical space $\mathcal{H}_{\mathrm{phys}}$ [30]. Using Choi's isomorphism [111], we can rewrite a density matrix ρ of a mixed state in the physical space as a pure state $|\rho\rangle\!\rangle$ in the doubled Hilbert space $\mathcal{H}_{\mathrm{phys}} \otimes \mathcal{H}_{\mathrm{aux}}$

$$\rho = \sum_\alpha s_\alpha^2 |\alpha\rangle_{PP}\langle\alpha| \longrightarrow |\rho\rangle\!\rangle = \sum_\alpha s_\alpha^2 |\alpha\rangle_P \otimes |\alpha\rangle_Q, \tag{4.2}$$

where $|\alpha\rangle_P \in \mathcal{H}_{\mathrm{phys}}$ and $|\alpha\rangle_Q \in \mathcal{H}_{\mathrm{aux}}$. This procedure is known as purification, where the original density matrix is recovered by tracing out the auxiliary space, i.e.

$$\rho = \mathrm{tr}_Q\left(|\rho\rangle\!\rangle\langle\!\langle\rho|\right) = \sum_\alpha s_\alpha^2 |\alpha\rangle_{PP}\langle\alpha|. \tag{4.3}$$

The cyclic property of the trace leaves a freedom of choice for the auxiliary space such that the transformation as presented in Eq. 4.2, is not unique. More precisely, the trace condition is satisfied for a general rewriting of the density matrix as $|\rho\rangle\!\rangle = \sum_\alpha s_\alpha^2 |\alpha\rangle_P \otimes U|\alpha\rangle_Q$ with U being an arbitrary unitary transformation.

4.2.1. Purification of a matrix product state

The first step in using the tMPS machinery, is to encode the initial purified state as a matrix product state. Given a basis $\{|\sigma_1, \ldots, \sigma_L\rangle\}$ of a one dimensional lattice system with L sites, it is straightforward to define a basis state in the MPS formalism. As the state is a product state of all sites, the bond dimension is zero and the corresponding purified MPS reads

$$|\sigma_1, \sigma_2, \ldots \sigma_L\rangle_{PP}\langle\sigma_1, \sigma_2, \ldots \sigma_L| \longrightarrow |\sigma_1\sigma_1\sigma_2\sigma_2 \ldots \sigma_L\sigma_L\rangle\!\rangle. \tag{4.4}$$

Here, the auxiliary sites are included in between the physical sites. The construction for a state vector $|\psi\rangle_P$ with finite bond dimension D is more involved [102]. It begins with making a copy $|\psi'\rangle$ of the original state and assign it to the auxiliary state, so that the purified state is given by

$$|\psi\rangle_P \otimes |\psi'\rangle_Q = \sum_{\substack{\sigma_1 \ldots \sigma_L \\ \sigma_1' \ldots \sigma_L'}} M^{\sigma_1} \ldots M^{\sigma_L} M^{\sigma_1'} \ldots M^{\sigma_L'} |\sigma_1, \sigma_1', \ldots, \sigma_L \sigma_L'\rangle\!\rangle$$

$$= \sum_{\substack{\sigma_1 \ldots \sigma_L \\ \sigma_1' \ldots \sigma_L'}} \left[\begin{array}{c} \sigma_1 \;\; \sigma_2 \;\; \sigma_3 \cdots \;\;\;\; \sigma_L \;\;\; \sigma_1' \;\; \sigma_2' \;\; \sigma_3' \cdots \;\;\;\; \sigma_L' \\ \text{(tensor network diagram)} \end{array} |\sigma_1, \sigma_1', \ldots, \sigma_L \sigma_L'\rangle\!\rangle \right]. \tag{4.5}$$

Next, the tensors of physical and auxiliary sites are combined for all lattice sites by element-wise multiplication

$$
M^{\sigma_l}_{a_{l-1},a_l} M^{\sigma'_l}_{a'_{l-1},a'_l} \to (MM)^{\sigma_1,\sigma'_1}_{a_{l-1},a'_{l-1},a_l,a'_l} \equiv \quad\text{(4.6)}
$$

The sticking out bond indices are combined to a joint bond index by $(a_{l-1}, a'_{l-1}) \to \tilde{\lambda}'_{l-1}$. Starting then from the left side, the physical and the auxiliary site are separated using a SVD on the matrix obtained by regrouping the indices by $(\sigma_l, \tilde{\lambda}'_{l-1}) \times (\sigma'_l, \tilde{\lambda}'_l)$. The index of the singular value spectrum, which we name λ_l is truncated at the maximal allowed bond dimension D. Truncating also the merged external indices $\tilde{\lambda}'_l$ via SVD, yielding a new bond index λ'_l. Iterating this for all sites brings the purified state to the form

$$
|\rho\rangle\!\rangle = \sum_{\substack{\sigma_1\ldots\sigma_L \\ \sigma'_1\ldots\sigma'_L}} A^{\sigma_1} A^{\sigma'_1} \ldots A^{\sigma_L} A^{\sigma'_L} |\sigma_1, \sigma'_1, \ldots, \sigma_L \sigma'_L\rangle\!\rangle
$$

$$
= \sum_{\substack{\sigma_1\ldots\sigma_L \\ \sigma'_1\ldots\sigma'_L}} \quad |\sigma_1, \sigma'_1, \ldots, \sigma_L \sigma'_L\rangle\!\rangle \ .
$$

To summarize this, having started from a pure state in MPS form with bond dimension D, the purified state of the corresponding density matrix has been created with the same bond dimension. It is important to notice here, that the truncations, used in the SVD steps, are quite drastic approximations. Considering the bond SVD between sites σ_l and σ'_l, the dimension is broken down from dD^2 to D. For the merged indices between sites σ'_l and σ_{l+1} the reduction is done from D^2 to D. That means, if we for example want to calculate the dissipative evolution of the ground state of the Hamiltonian system found by DMRG, we are confronted with the following fact. The accuracy of performing the ground state search with maximal bond dimension D followed by a purification including SVD truncations cutting the bond index back to D, is equivalent to doing the ground state search with a bond dimension $\sqrt{D}$ and purifying without truncation. In other words, if we want to keep the accuracy of the ground state search, and do not truncate in the course of the purification, the bond dimension of the purified MPS increases quadratically. Therefore, the dissipative time evolution of higher entangled initial states poses a scenario, where already the construction of the initial state is very costly so that the Monte-Carlo wave function method, presented in the next section, can be advantageous.

4.2.2. Time evolution of the purified density matrix

The Lindbladian's action on the doubled Hilbert space is equivalent to the definition in Eq. 3.43 of Sec. 3.2 and is explained in detail there. Analogous to the Sec. 3.1.4, we now assume only nearest-neighbor coupling of the Hamiltonian and add the constraint of allowing only jump operators localized to a single site. Consequently, sites σ_l and σ_{l+1} as well as σ'_l and σ'_{l+1}
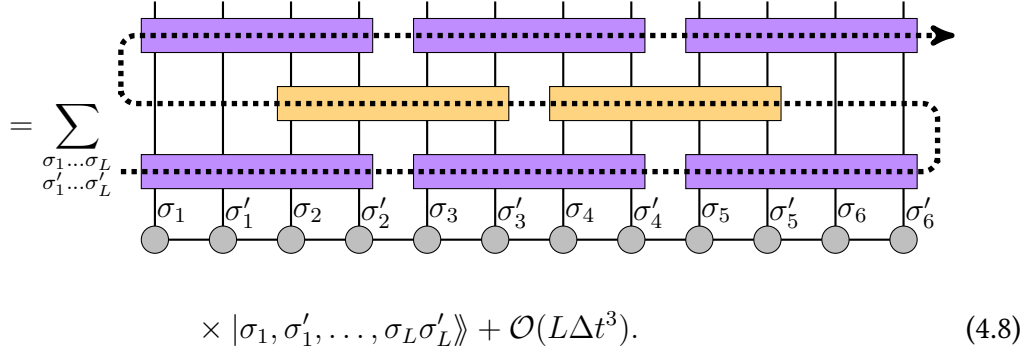
are coupled via the Hamiltonian and sites σ_l and σ_l' are coupled by the first term of the dissipator, i.e. $L_i \rho L_i^\dagger$. The Lindbladian can then be split up into the parts

$$\mathcal{L} = \sum_{l=1}^{L-1} \mathcal{L}_{2l-1,2l,2l+1,2l+2} = \sum_{l=1}^{L-1} \mathcal{L}_{4l-3,4l-2,4l-1,4l} + \sum_{l=1}^{L-1} \mathcal{L}_{4l-1,4l,4l+1,4l+2} \equiv \mathcal{L}_{\text{odd}} + \mathcal{L}_{\text{even}}, \quad (4.7)$$

with $[\mathcal{L}_{\text{odd}}, \mathcal{L}_{\text{even}}] \neq 0$, but all summands of the odd and even Lindbladian commute. The associated time evolution operators $\exp[\mathcal{L}_{\text{odd}}\Delta t]$ and $\exp[\mathcal{L}_{\text{even}}\Delta t]$ can therefore be decomposed into sets of four-site gates, acting on the physical and auxiliary part of two neighboring sites, represented by the four indices in Eq. 4.7 . Just as in the unitary time evolution case, we can now use a Suzuki-Trotter decomposition, for example with a second order accuracy, and approximate the evolution of the purified density matrix by one time step as a sequence of gates

$$|\rho(t+\Delta t)\rangle\!\rangle = \mathrm{e}^{\mathcal{L}\Delta t}|\rho(t)\rangle\!\rangle = \mathrm{e}^{\mathcal{L}_{\text{odd}}\Delta t/2}\mathrm{e}^{\mathcal{L}_{\text{even}}\Delta t}\mathrm{e}^{\mathcal{L}_{\text{odd}}\Delta t/2}|\rho(t)\rangle\!\rangle + \mathrm{O}(L\Delta t^3)$$

$$\times\, |\sigma_1, \sigma_1', \dots, \sigma_L \sigma_L'\rangle\!\rangle + \mathcal{O}(L\Delta t^3). \qquad (4.8)$$

Again, the odd gates are colored purple and the even gates orange and the dotted arrow specifies the gate application order. The single time step evolution is repeated iteratively until the desired final time is reached. When applying one four-site gate to an MPS, the bond dimension increases on the three affected bonds as can be read off from the following tensor diagram, where the dimensions are annotated next to the indices in blue color.
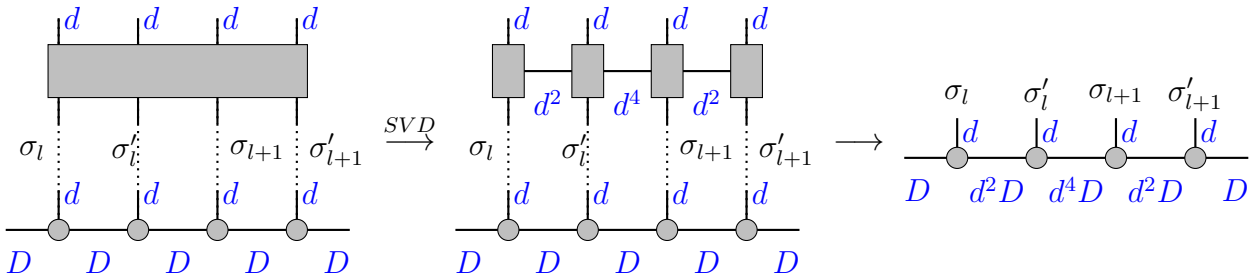
Therefore, assuming a previous bond dimension of D results in a dimension $d^2 D$ at the outer two bonds and a dimension of $d^4 D$ at the central bond. Hence, another compression back to D using the established SVD method, is necessary. Intuitively, the evolution of one time step includes the exploration of a larger subspace of the full Hilbert space $\mathcal{H}_{\text{phys}} \otimes \mathcal{H}_{\text{aux}}$ before

being projected onto the most important states of the D-dimensional MPS manifold. The gate contractions can be optimized further by utilizing so-called swap gates [112], which we will not discuss here.

A decisive restriction is encountered, when extending the purification method in terms of MPS using quantum number conservation in the fashion of Sec. 3.1.2. More precisely, the Lindbladian can only be represented by quantum number conserving MPO tensors, when each jump operator also respects the same conversation law. Otherwise, it is not possible to assign a well-defined quantum number flux to the dissipator, and with it also not to the Lindbladian. To demonstrate this fact, we consider the example of a two-level systems with the basis $\mathbb{B} = \{|0\rangle, |1\rangle\}$, where the unitary evolution is described by a diagonal Hamiltonian H, which conserves a quantum number indicated by the basis labels. The effect of the environment is mimicked by the deexcitation operator $\sigma^- = |0\rangle\langle 1|$ as a jump operator, which does not conserve the quantum number. For this set-up, we find the following total quantum number flux for the different parts of the dissipator

$$
\begin{aligned}
\sigma^- |n\rangle\langle n|\sigma^+ &= \delta_{n,1}|0\rangle\langle 0| \longrightarrow \Delta\mathrm{QN} = -2, \\
\sigma^+\sigma^- |n\rangle\langle n| &= \delta_{n,1}|1\rangle\langle 1| \longrightarrow \Delta\mathrm{QN} = 0, \\
|n\rangle\langle n|\sigma^+\sigma^- &= \delta_{n,1}|1\rangle\langle 1| \longrightarrow \Delta\mathrm{QN} = 0,
\end{aligned}
\tag{4.9}
$$

where σ^+ is the hermitian conjugate of σ^-. Consequently, the dissipator has finite contributions from different flux sectors and the time evolution of the MPS of a purified density matrix can not be restricted to a single symmetry block. That means that important application instances, as for example those containing dissipation in the form of particle loss or deexcitation mechanisms, lack the improvement opportunities offered by simulation with quantum number conserving codes.

4.2.3. Calculation of expectation values

Provided with the time evolved purified density matrix, we are left with the task to calculate expectation values of observables to extract information about the system. The trace relation for the expectation value of an operator A translates to a scalar product

$$
\langle A \rangle = \mathrm{tr}(\rho A) = \langle\langle \mathbb{1}|A|\rho\rangle\rangle, \quad \text{with} \quad |\mathbb{1}\rangle\rangle = \bigotimes_{l=1}^{L} \sum_{\sigma_l} \left[|\sigma_l\rangle_P \otimes |\sigma_l\rangle_Q \right].
\tag{4.10}
$$

At the same time, the state $|\mathbb{1}\rangle\rangle$ is the purification of the unnormalized infinite temperature state [113]. Unfortunately, the possibility to be able to encode this state as a product state as shown in Eq. 4.10 gets lost, when using good quantum numbers, where the vector of the purified density matrix can not be separated into contributions of the single sites anymore. Another obstacle becoming apparent when exploiting good quantum numbers in the algorithm, is that $|\mathbb{1}\rangle\rangle$ spans over all symmetry blocks, so that a restriction to a certain quantum number sector makes a manual selection of basis states fulfilling this condition very cumbersome. Here we show, how we make use of the gauge degree of freedom for the auxiliary space of the constituents of $|\mathbb{1}\rangle\rangle$,

4.2 Purification of the density matrix

defined by

$$|\sigma_l\rangle_P \otimes |\sigma_l\rangle_Q \longrightarrow |\sigma_l\rangle_P \otimes U|\sigma_l\rangle_Q \equiv |\sigma_l\rangle_P \otimes |\tilde{\sigma}_l\rangle_Q, \tag{4.11}$$

to overcome this hurdle. To this end, the transformation U is chosen such, that the quantum number of the full initial state is equally distributed to the local pairs of physical and auxiliary states by

$$QN\left(|\sigma_l\rangle_P \otimes |\tilde{\sigma}_l\rangle_Q\right) = \frac{1}{dL}QN\left(|\rho(t=0)\rangle\!\rangle\right), \ \forall l \in \{1, \dots, L\}. \tag{4.12}$$

This practice automatically guarantees the restriction of the trace generating state $|\mathbb{1}\rangle\!\rangle$ to the symmetry sector selected by the initial state. Supposing that the observable can be brought to an efficient MPO representation, we can then proceed to calculate the expectation value. In the exemplary and important case of a local observable the measurement is carried by the following tensor contractions
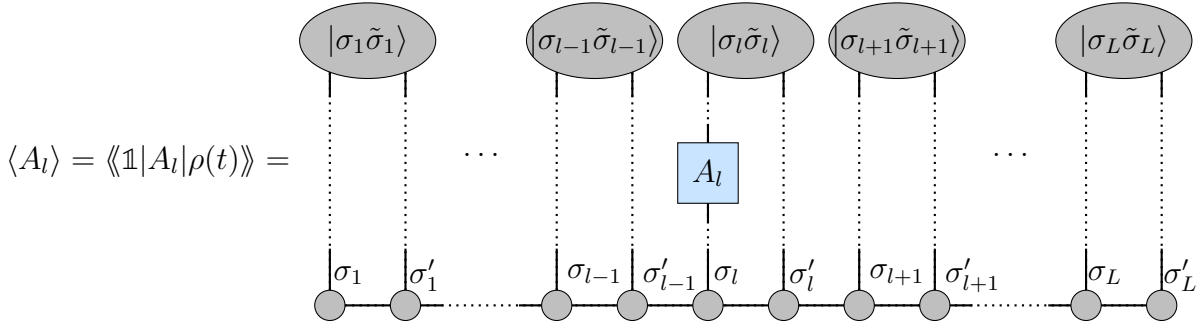
With this decomposition into local tensors, the problems of selecting basis states respecting the quantum number conservation as well as the large bond dimension of an MPS representation of $|\mathbb{1}\rangle\!\rangle$ are both solved. Finally, also the initial state and the Lindbladian gates need to be adapted to be consistent with this auxiliary gauge choice. With $\mathcal{U} = \bigotimes_{l=1}^{L}(\mathbb{1} \otimes U)$, the transformation relations are

$$\begin{aligned}
\mathcal{L} &\longrightarrow \mathcal{U}^\dagger \mathcal{L} \mathcal{U} \\
|\rho(t=0)\rangle\!\rangle &\longrightarrow \mathcal{U}|\rho(t=0)\rangle\!\rangle.
\end{aligned} \tag{4.13}$$

A very useful property of the full density matrix evolution and the scheme for measuring observables is the straight-forward access to two time correlation functions of the form

$$\langle A(t_2)B(t_1)\rangle = \mathrm{tr}\left(A\mathrm{e}^{\mathcal{L}(t_2-t_1)}B\mathrm{e}^{\mathcal{L}t_1}\rho(t=0)\right). \tag{4.14}$$

After purifying the initial state, the purified density matrix is evolved until time t_1, where the operator B is applied, followed by an evolution to t_2, where an ordinary measurement of A is carried out.

4.2.4. Purification approach for the open XXZ chain

As this formalism will be used later to calculate time-dependent correlation functions for a dissipative XXZ spin-1/2 chains with local dephasing noise in Chap. 6, we will present the

procedure for this example here. The corresponding Lindblad equation is given by

$$\frac{\partial}{\partial t}\rho(t) = \mathcal{L}_{XXZ} \cdot \rho(t) = -\frac{i}{\hbar}[H_{XXZ}, \rho(t)] + \gamma \mathcal{D}[\rho(t)], \qquad (4.15)$$

$$\text{with } H_{XXZ} = \sum_{j=1}^{L-1} \left[J_x \left(S_i^x S_{i+1}^x + S_i^y S_{i+1}^y \right) + J_z S_i^z S_{i+1}^z \right],$$

$$\mathcal{D}[\rho(t)] = \sum_{j=1}^{L} \left(S_j^z \rho(t) S_j^z - \frac{1}{4}\rho(t) \right),$$

and the basis is given by tensor product of the local S^z eigenbasis $\{|\sigma_1, \dots, \sigma_L\rangle\}$ with $\sigma_l \in \{\uparrow, \downarrow\}$. This model conserves the total magnetization and the covered initial states are all placed in the symmetry sector of vanishing magnetization. In fact, all initial states used in Chap. 6 are pure states of the form $|\sigma_1, \dots, \sigma_L\rangle_P$. According to the conservation of the magnetization, a transformation of the auxiliary sites, satisfying the condition posed in Eq. 4.12 is given by the Pauli matrix in x-direction $U = \sigma^x$. With this we can rewrite the state $|\mathbb{1}\rangle\!\rangle$ for the trace calculation as

$$|\mathbb{1}\rangle\!\rangle = \bigotimes_{l=1}^{L} \sum_{\sigma_l} |\sigma_l\rangle_P |\sigma_l\rangle_Q$$

$$\longrightarrow \left[\bigotimes_{l=1}^{L} (\mathbb{1} \otimes \sigma^x) \right] \bigotimes_{l=1}^{L} \sum_{\sigma_l} |\sigma_l\rangle_P |\sigma_l\rangle_Q = \bigotimes_{l=1}^{L} \left[|\uparrow\rangle_P |\downarrow\rangle_Q + |\downarrow\rangle_P |\uparrow\rangle_Q \right] \qquad (4.16)$$

With the relation for the spin operators,

$$(\sigma^x)^\dagger S^x \sigma^x = S^x, \quad (\sigma^x)^\dagger S^y \sigma^x = -S^y, \quad \text{and} \quad (\sigma^x)^\dagger S^z \sigma^x = -S^z, \qquad (4.17)$$

the only effect of the associated transformation from Eq. 4.13 on the Lindbladian, is the addition of a negative sign for the $S_j^z \rho S_j^z$ parts in the dissipator. Moreover, the purification of the studied initial states with this gauge choice, includes a flipping of the physical spins for the auxiliary sites, so that $|\sigma_1 \dots \sigma_L\rangle\langle\sigma_1 \dots \sigma_L| \rightarrow |\sigma_1 \bar{\sigma}_1 \dots \sigma_L \bar{\sigma}_L\rangle\!\rangle$, with $\bar{\sigma}$ pointing in the opposite spin direction of σ.

In conclusion, the purification of the density matrix, followed by a time evolution approximated by a sequence of gates originating from a Suzuki-Trotter decomposition can be a powerful tool for the prediction of Markovian quantum many-body dynamics. The compression of the density matrix by the means of singular value decomposition and the step size of the time discretization offer good ways to control the convergence of the simulation. Difficulties can arise due to the effective doubling of the system size so that the bond dimension for a exact representation at the central bond can be as large as d^L, compared to $d^{L/2}$ for a pure state MPS, with L being the size of the physical system. Furthermore, in contrast to pure states, the bond dimension of the purified states can not be linked to a physical quantity as the von-Neumann entropy, so that the applicability and quality of the truncation procedure is subject to tests for
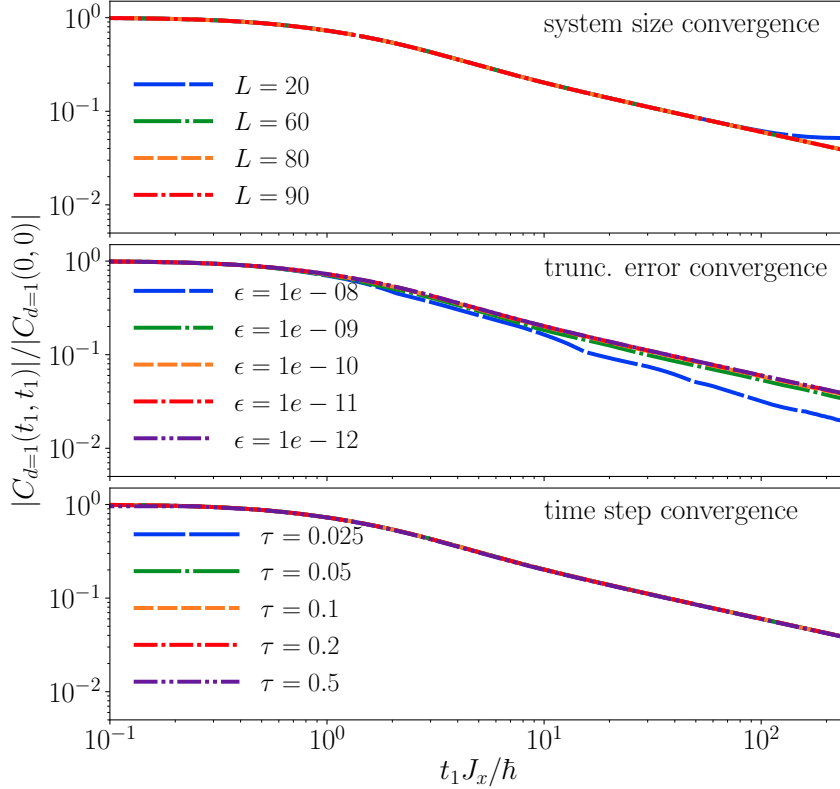
Figure 4.1.: Convergence of tMPS method according to system size L (upper panel), discarded truncation weight ϵ (middle panel) and time step τ (lower panel). Model parameters here are $\hbar\gamma/J_x = 4.0$ and $J_z/J_x = 2$. The initial state is the Neel state. If not specified differently, the convergence parameters are chosen as $L = 80$, $\epsilon = 10^{-12}$ and $\tau = 0.05$.

every situation. As mentioned before, the purification of highly entangled pure states can be very challenging memory-wise, with resource requirements of several hundred gigabytes of RAM. Nevertheless, starting with an initial density matrix, that can be encoded as a purified state with a low bond dimension, as for example a basis state of the corresponding many-body basis, the rise of the bond dimension during the dissipative evolution typically allows computations up to long evolution times. In these cases, large systems can be simulated efficiently with an state approximation accuracy for the SVD truncation error of the order of 10^{-10}, which we regard as quasi-exact.

Nevertheless, there are several aspects, crucial for the validity of the results, which need to be kept track of to guarantee the numerical convergence. More precisely, the following three different parameters, influencing the physical accuracy of the tMPS simulations:

- The system size L: As we strive for connecting our findings to macroscopic quantum materials, the influence of finite size effects should be eliminated as well as possible. To do so, it is necessary to ensure, that the local region of observable measurements,

is governed by the actual dynamics of the bulk instead of boundary influences. This criterion can be confirmed for simulation measurements by comparing different chain lengths L, and identifying the time when the deviation becomes non-negligible.

- The truncation weight ϵ: Here, as well as in Chap. 6, the initial states used, are exclusively product states, corresponding to matrix product states with unit bond dimension. In the subsequent time evolution the necessary bond dimension to represent the density matrix as an MPS grows. To cover this correctly, the truncation weight ϵ needs to be monitored. In analogy to the system size analysis above, the time region where the results are converged, is determined by comparing different truncation weight thresholds for the same model realization.

- The Suzuki-Trotter time step τ: Inherent to the second order Suzuki-Trotter decomposition of the exponential, the finite time step results in a systematic error. Again, contrasting different time steps allows to judge the influence of this point on the overall convergence.

The outlined procedure is exemplified in Fig. 4.1 for the equal-time correlations of operators measuring the spin along the z-orientation

$$\hbar C_d(t_1, t_1) = \langle S^z_{L/2}(t_1) S^z_{L/2+d}(t_1) \rangle, \tag{4.18}$$

where the system has been initial prepared in the Neel state $\rho(t = 0) = |\psi_{\text{Neel}}\rangle\langle\psi_{\text{Neel}}|$, with

$$|\psi_{\text{Neel}}\rangle = |\uparrow\downarrow\uparrow\downarrow \ldots \uparrow\downarrow\rangle. \tag{4.19}$$

From the plot we can read off, that we need a system with at least $L = 60$ sites and a truncation weight of maximally $\epsilon = 10^{-10}$ to describe the shown time region well. Furthermore, the size of the time step, does not show a very large influence on this variable, which might change drastically by switching to other observables. This convergence analysis has been done for all data shown in Chap. 6, including also the computations of two-time functions.

4.3. Monte-Carlo wave functions - stochastic sampling of quantum trajectories

After having discussed the procedure and the advantages and disadvantages of the expression and time evolution of the full density matrix in terms of tensor networks, let us now introduce a technique going by the name of Monte-Carlo wave function method as introduced by [104, 105] and summarized in [6]. This idea for modeling the dynamics of Markovian open quantum system is based on the replacement of the system's density matrix evolution, generated by the Lindblad equation (Eq. 2.9), by stochastic processes in the Hilbert space. Therefore, the description is broken down to the evolution of states in Hilbert space, rather than density matrices. The action of the environment is included as a probabilistic element. The density matrix can be retrieved by computing the expectation value, denoted by $\mathbb{E}$, via the integration

4.3 Monte-Carlo wave functions - stochastic sampling of quantum trajectories
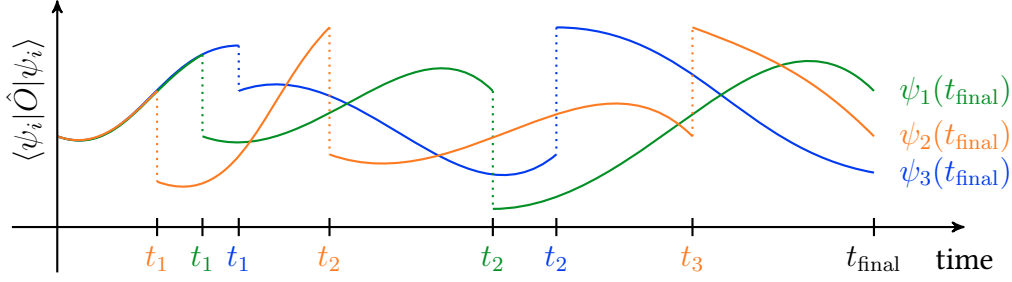
Figure 4.2.: Sketch of the Monte-Carlo wave function sampling. The evolution is here exemplary displayed by the expectation value of an observable $\hat{O}$ for three distinct trajectories, where the stochastic jump operator applications cause discontinuities in time.

over the full Hilbert space

$$\rho(t) = \mathbb{E}\left(|\psi\rangle\langle\psi|\right) = \int \mathcal{D}\psi\mathcal{D}\psi^* |\psi\rangle\langle\psi| \, T\left[\psi, t|\psi_0, t_0\right], \tag{4.20}$$

where the conditional transition probability for the system to be in state $|\psi\rangle$ at time t, given that it was initially prepared in $|\psi_0\rangle$, is denoted by $T\left[\psi, t|\psi_0, t\right]$ [6]. In this concept, the state vector $|\psi\rangle$ is a random variable in Hilbert space and the transition probability needs to be constructed such, that the expectation value of Eq. 4.20 satisfies the Lindblad equation for the density matrix. This procedure is known as the unravelling of the master equation. In this work we chose the formulation in terms of piece-wise-deterministic processes as used in [104], since this approach is straight-forward to integrate with the established tMPS algorithm. Alternatively, implementations using diffusion processes also exist [114, 115]. The statistical nature of the unravelling allows direct access to the dynamics by Monte-Carlo simulations [116], providing time-resolved expectation values of observables via a sampling and subsequent averaging of statistically independent trajectories in Hilbert space and time, see [106] and references therein. This section is structured such, that we first introduce the algorithm for the trajectory sampling according to the piece-wise deterministic processes, followed by proving its equivalence to the Lindblad master equation.

4.3.1. Stochastic sampling algorithm for quantum trajectories

In line with the derivation in [106], we first introduce a non-hermitian effective Hamiltonian and rewrite the Lindblad equation (Eq. 2.9) as

$$\frac{\mathrm{d}}{\mathrm{d}t}\rho = -i\left[H_{\text{eff}}, \rho\right] + \sum_j \gamma_j L_j \rho L_j^\dagger, \quad \text{with } H_{\text{eff}} = H - \frac{i}{2}\sum_j \gamma_j L_j^\dagger L_j. \tag{4.21}$$

The full time evolution is then split up into small time steps Δt starting from a normalized initial state $|\psi_0\rangle = |\psi(t=0)\rangle$. If the initial state is not pure, but a mixed state

$$\rho_0 = \sum_s p_s |\psi_0^s\rangle\langle\psi_0^s|, \tag{4.22}$$

the initial state vector is sampled according to the classical probabilities p_s. The computation of a single time step Δt starts with evolving the state under the effective Hamiltonian

$$|\psi(t+\Delta t)\rangle = U(\Delta t)|\psi(t)\rangle = \mathrm{e}^{-iH_{\mathrm{eff}}\Delta t}|\psi(t)\rangle \tag{4.23}$$

As H_{eff} is not hermitian, the time evolution operator $U(\Delta t)$ is also non-unitary, which leads to a strictly monotonic decay of the norm. Assuming a normalized state at time t the squared norm equals

$$\langle\psi(t+\Delta t)||\psi(t+\Delta t)\rangle = 1 - p, \text{ with } p \in (0,1]. \tag{4.24}$$

Moreover, a first order expansion of the evolution operator $U(\Delta t) = 1 + i\Delta t H + \mathcal{O}(\Delta t^2)$ determines the loss in norm as

$$p = \sum_j \underbrace{\Delta t\, \gamma_j \langle\psi(t)|L_j^\dagger L_j|\psi(t)\rangle}_{\equiv p_j} + \mathcal{O}(\Delta t^2) = \sum_j p_j + \mathcal{O}(\Delta t^2). \tag{4.25}$$

Next, the stochastic component is added to the algorithm: A random number $\eta \in [0,1)$ is chosen from a continuous uniform distribution. Depending on the random number, one of the following actions is performed:

1. if $\eta > p$: update the state vector at the new time with the normalized state, that has been already obtained from the deterministic evolution with the effective Hamiltonian

$$|\psi(t+\Delta t)\rangle \longleftarrow \frac{\mathrm{e}^{-iH_{\mathrm{eff}}\Delta t}|\psi(t)\rangle}{\sqrt{1-p}}, \tag{4.26}$$

2. if $\eta < p$: select one of the jump operators with regard to the probability distribution $\Pi_j = p_j/p$ and apply it to the original state at time t with subsequent normalization

$$|\psi(t+\Delta t)\rangle \longleftarrow \frac{L_j|\psi(t)\rangle}{\sqrt{\langle\psi(t)|L_j^\dagger L_j|\psi(t)\rangle}}. \tag{4.27}$$

Iterating this for all time steps up to the final time provides a single evolved trajectory. As sketched in Fig. 4.2, different trajectories are characterized by longer periods of deterministic time evolution, which are interrupted by sudden changes caused by the occasional application of jump operators. The frequency of jump applications is defined by the steepness of the norm decay and therefore related to the strength of the dissipative coupling of the jump operators given by $\{\gamma_j\}$. To simulate the open system dynamics properly a sufficiently large number of these samples R is needed to reflect the derived properties for the expectation value. More pre-

cisely, the expectation values of an observable $\hat{O}$ is approximated by the Monte-Carlo average over all trajectory realizations [6]

$$\langle \hat{O}(t) \rangle = \int \mathcal{D}\psi \mathcal{D}\psi^* \langle \psi | \hat{O} | \psi \rangle T[\psi, t | \psi_0, t_0] \approx \langle\!\langle \hat{O} \rangle\!\rangle \equiv \frac{1}{R} \sum_{r=1}^{R} \langle \psi_r(t) | \hat{O} | \psi_r(t) \rangle. \qquad (4.28)$$

We will use the notation of $\langle\!\langle \ldots \rangle\!\rangle$ for the Monte-Carlo averages over many trajectories $|\psi_r(t)\rangle$, to distinguish them from usual quantum expectation values, which should not be confused with the notation for a purified state. The accuracy of this estimation depends on the sample size, and can be quantified by the standard deviation of the mean for a measured expectation value

$$\sigma_{\mathrm{mean},t}(\hat{O}) = \frac{\sigma_t(\hat{O})}{\sqrt{R}} = \sqrt{\frac{1}{R(R-1)} \sum_{r=1}^{R} \left(\langle \psi_r(t) | \hat{O} | \psi_r(t) \rangle - \langle\!\langle \hat{O} \rangle\!\rangle \right)^2}. \qquad (4.29)$$

As the sampling process of different trajectories is independent from each other, the standard deviation of the mean decreases with an increasing number of samples as $\sigma_{\mathrm{mean},t}(\hat{O}) \sim 1/\sqrt{R}$.

From an implementation perspective, the statistical independence of the different trajectories allows a straight-forward parallelization of the method. With the Monte-Carlo average being the only interaction point of the different samples, the scaling to many processes is near to optimal. For this thesis we use the OpenMPI C++ library package [117] to distribute the trajectory sampling over a large number of cores of a computer cluster consisting of several nodes.

4.3.2. Equivalence to the Lindblad master equation

It is still left to show, that this algorithm simulates the Lindblad dynamics correctly. In order to show this, let us start with the Monte-Carlo approximation of the expectation value defined in Eq. 4.20, i.e. $\rho(t) = \mathbb{E}[|\psi(t)\rangle\langle\psi(t)|]$ which we will name $\bar{\sigma}$ here. According to the algorithm, the time evolution stochastically chooses between deterministic evolution and jump application by

$$\bar{\sigma}(t + \Delta t) = (1 - p) \left[\frac{e^{-iH_{\mathrm{eff}}\Delta t}}{\sqrt{1-p}} \bar{\sigma}(t) \frac{e^{iH_{\mathrm{eff}}^\dagger \Delta t}}{\sqrt{1-p}} \right] + p \left[\sum_j \left(\gamma_j \Pi_j \frac{\Delta t}{p_j} L_j \bar{\sigma}(t) L_j^\dagger \right) \right]. \qquad (4.30)$$

Here we used the expression for p_j from Eq. 4.25. Expanding the non-unitary evolution operator up to the first order, brings the equation to the form

$$\bar{\sigma}(t + \Delta t) = (1 - iH_{\mathrm{eff}}\Delta t) \bar{\sigma}(t) \left(1 + iH_{\mathrm{eff}}^\dagger \Delta t \right) + \Delta t \sum_j \left(\gamma_j L_j \bar{\sigma}(t) L_j^\dagger \right) + \mathcal{O}(\Delta t^2), \qquad (4.31)$$

which can be further rewritten as

$$\bar{\sigma}(t + \Delta t) = \bar{\sigma}(t) + \Delta t \Big\{ -i\left[H, \bar{\sigma}(t)\right]$$

$$+ \sum_j \gamma_j \left(L_j \bar{\sigma}(t) L_j^\dagger - \frac{1}{2} \bar{\sigma}(t) L_j^\dagger L_j - \frac{1}{2} L_j^\dagger L_j \bar{\sigma}(t) \right) \Big\} + \mathcal{O}(\Delta t^2).$$

$$(4.32)$$

Building the difference quotient, the resulting equation reflects the Lindblad equation for the density matrix, which is reconstructed from averaged wave functions. As a result, the introduced piece-wise deterministic process poses a valid way for unravelling the Lindblad master equation, given that the time step is sufficiently small.

Observing the derivation in Eq. 4.32, the repeated appearance of first order expansions raises the question, if there is room for improving the time step accuracy. Indeed, it is possible to identify the last line of the former equation as a first order Taylor expansion. It is possible to extend this to, for example, a second order accuracy by expanding the density matrix as

$$\rho(t + \Delta t) = \rho(t) + \Delta t \frac{\mathrm{d}}{\mathrm{d}t} \rho(t) + \frac{1}{2} (\Delta t)^2 \frac{\mathrm{d}^2}{\mathrm{d}t^2} \rho(t) + \mathcal{O}(\Delta t^3). \qquad (4.33)$$

Inserting this into the Lindblad equation for the respective derivatives makes it possible to derive a more complex combination of different types of jump operator sampling schemes. Nevertheless, this construction is numerically more costly than the first order approximation with a smaller chosen time step, as it involves significantly more evaluations of expectation values at each time step.

So far, we have left open the question on how to compute the time step of the deterministic evolution as presented in Eq. 4.26. As mentioned before, in particular for many-body quantum systems, the exponentiating of the Hamiltonian is potentially very complicated for its own sake. In fact, the MCWF approaches has been interfaced with many different integration techniques from the field of condensed matter numerics [106]. A very efficient variant is to apply the tMPS algorithm, developed in Sec. 3.1.4. To this end, the states in the stochastic evolution are formulated as MPSs and the dynamics can be found by successively applying bond gates to them, given that the Hamiltonian consists of only short-ranged terms. The fact, that we are only dealing with wave functions brings many benefits in comparison to the purification approach. More precisely, we circumvent the challenge of purification arising from highly entangled initial states. As we bypass the reformulation of the full density matrix, there is no increase in bond dimension because of this. Furthermore, we can keep the interpretability of the bond dimension by its connection to the von-Neumann entanglement entropy. In addition to that, the effective Hamiltonian can be assigned to a well-defined quantum number flux in most cases, as the term $L_j^\dagger L_j$ is typically quantum number conserving, even if the sole jump operators L_j are not. This is for example true for particle loss (gain) and (de-)excitation operators. Also these jump operators have a unambiguous flux, which can be non-zero, such that their applications are realizable in the framework of quantum number conservation. This increases the efficiency in

the trajectory sampling drastically.

Nevertheless, it is important to note, that these advantages are situation dependent. One systematic comparison study has been implemented in [118] for the Bose-Hubbard model. Indeed, evolving a low-entangled initial state, where the purified density matrix does not increase too fast, might be favored over the sampling of a large number of state trajectories, where the sample size is typically of the order of 10^4. With the MPS point of view in mind, a closer look on the jump probabilities in Eq. 4.25 reveals that the determination of the single probabilities can be rather expensive, due to the necessary calculation of expectation values for all jump operators, which is especially tedious in settings with large sets of Lindblad operators $\{L_i\}$. An improvement regarding this issue can be formally achieved by sampling a so-called waiting time τ, which defines the length of the deterministic evolution until the next jump occurs. The corresponding cumulative distribution is specified by the decay of the norm

$$P(t, \tau) = 1 - \|\exp\left(-iH_{\text{eff}}\tau\right)|\psi(t)\rangle\|. \tag{4.34}$$

Practically, this can be implemented by drawing a random number $\eta \in [0, 1)$ and performing the non-unitary deterministic time evolution until the norm passes the threshold posed by the random number. This approach reduces the frequency of jump probability calculations to the number of time steps where actual jumps are happening and therefore reduces the computational load substantially.

4.3.3. Monte-Carlo wave functions for the open XXZ-chain

Similar to the purification section, we continue by testing the algorithm for the spin-$1/2$ chain under the influence of bulk dephasing as modeled by the Lindblad equation Eq. 4.15. To illustrate the process of the trajectory sampling, Fig. 4.3 shows the Monte-Carlo average of the local S^z-correlations at the central bond, as established in Eq. 4.18, over a large number of wave function measurements in comparison to the expectation values of single trajectories. It is clearly visible, that the single trajectories are decomposed into intervals of smooth time evolution, which are separated by kinks, marking the times of stochastic jump applications. The statistical errors as provided by the standard deviation of the mean are smaller than the linewidth in the plot and are here of the order of 10^{-4}. A further important measure of convergence is the von-Neumann entropy. More specifically, as the MPS is brought to mixed canonical form before the gate contractions, an SVD on the bond of the gate application, brings the state in the form of the Schmidt decomposition. For this reason, the strength of the entanglement determines what bond dimension needs to be kept, to fulfill a certain accuracy goal for the truncation error. More than that, it provides a way to draw an unbiased conclusions on the numeric complexity, independent of precise hardware specifications. To underline the relation of entanglement and bond dimension, we show in the left panel of Fig. 4.4 the time-dependent entanglement entropy for a single trajectory and several different maximally allowed bond dimensions. The displayed entropy shows the entanglement of the two sub-parts connected by the bond with the largest bond dimension in the chain, which is typically the chain center. As expected, larger values of the entanglement entropy require a large bond dimension. The kinks can be identified with the stochastic jumps, where usually a jump results in a change of en-
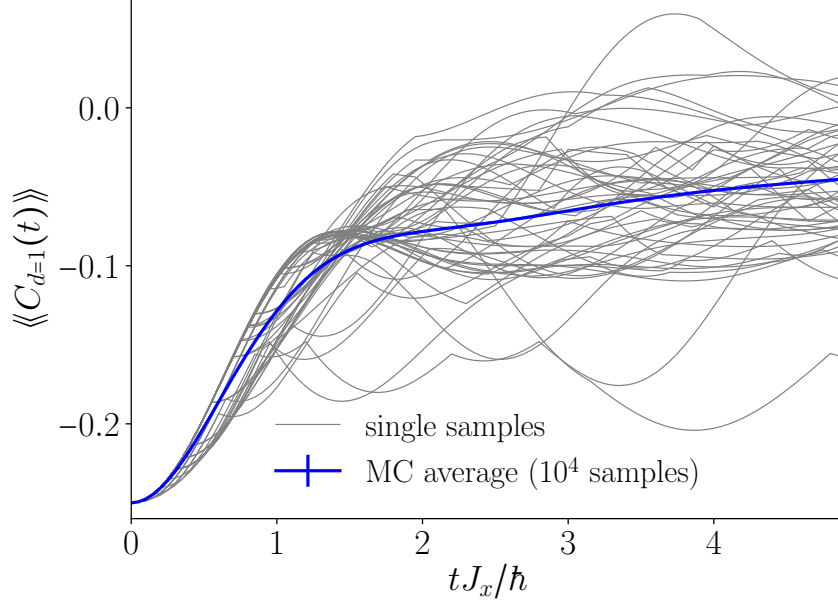
Figure 4.3.: MCWF average for the time evolution of local z-directional spin correlations defined in Eq. 4.18 for an open XXZ-chain of length $L = 32$, with model parameters $J_z/J_x = \hbar\gamma/J_x = 1$ and initial state $|\psi_0\rangle = |\psi_{\text{Neel}}\rangle = |\uparrow\downarrow\uparrow\downarrow\ldots\rangle$. The average is compared to the result of 50 single trajectories, the statistic errorbars are smaller than the line width. Time step and bond dimension are choose as $\Delta t J_x/\hbar = 0.05$ and $D = 100$

tropy. However, as we are dealing with a stochastic process in time, the von-Neumann entropy is subject to statistical fluctuations. The right panel of Fig. 4.4 shows the average entropy as well as the entropy of 50 single trajectories. While the statistical average of the entropy is a good general indicator, it becomes apparent, that the simulation needs to be capable of much stronger entangled states as well. This fact needs to be taken into account in the next section, where we benchmark different ways of evaluating two-time correlation functions.

4.4. Comparison of different sampling approaches for two-time correlation functions

The Monte-Carlo method, as introduced in the previous section, can also be extended to the calculation of two-time correlation functions, defined by the expectation value of the product of two operators, measured at different times, formally given by

$$\langle B(t_2)A(t_1)\rangle = \text{tr}\left[BV(t_2 - t_1)AV(t_1)\rho(t = 0)\right], \tag{4.35}$$

where we used the definition for the propagator of the Lindblad superoperator $V(t) \equiv \exp[\mathcal{L}t]$ from Eq. 2.6. Two time correlations are relevant in many physical situations, they enter, for example in the determination of the g_2 function which gives a measure for coherence of atomic
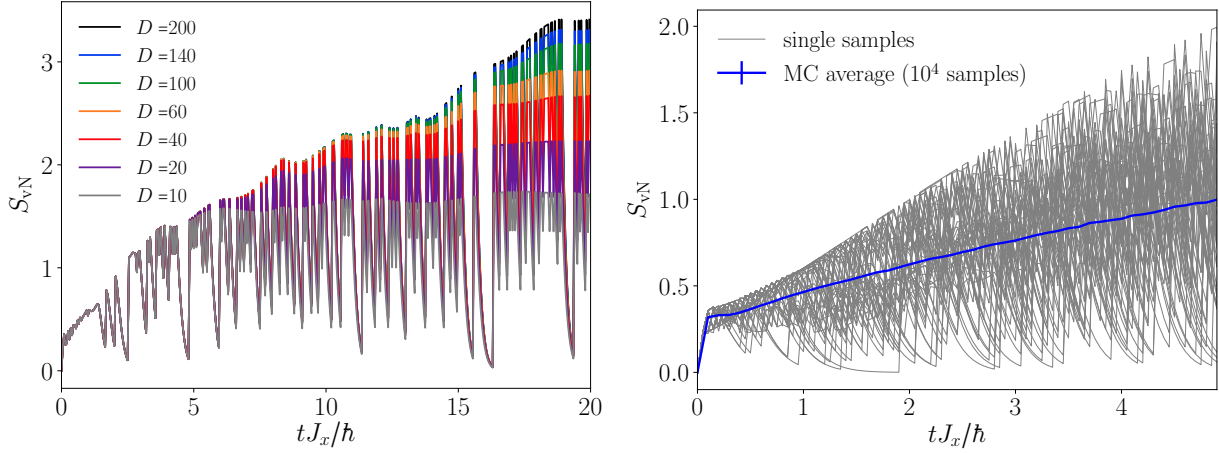
Figure 4.4.: Von-Neumann entanglement entropy at the bond with the maximal value for stochastically sampled quantum trajectories for a dissipative XXZ chain with $L = 32$ and $J_z/J_x = \hbar\gamma/J_x = 1$ starting from $|\psi_0\rangle = |\psi_{\mathrm{Neel}}\rangle$. Left panel: time dependence of a single wave function with different maximal bond dimension but same random number seed. Right panel: Monte-Carlo average compared to 50 single trajectories in time, with a maximal bond dimension of $D = 100$. The tMPS time step is $\Delta t J_x/\hbar = 0.05$ and statistical errors smaller than the line width.

clouds [119], the computation of spectral functions [120] and also the detection of aging dynamics as presented in Chap. 6. As the operators are applied at different times, computing two-time correlation functions is more involved than equal-time observables. More precisely, when defining $|\phi(t_1)\rangle \equiv A|\psi(t_1)\rangle$, where $|\psi(t_1)\rangle$ is obtained from the evolution of the initial state $|\psi(t_0)\rangle$ by the piece-wise deterministic processes, the measurement from Eq. 4.35 breaks down to the calculation of matrix elements of time-dependent Heisenberg operators [121]

$$\langle B(t_2)A(t_1)\rangle = \langle\psi(t_1)|B(t_2)|\phi(t_1)\rangle = \mathrm{tr}\left[B\,V(t_2 - t_1)|\phi(t_1)\rangle\langle\psi(t_1)|\right]. \tag{4.36}$$

While this expression is well-defined in the superspace of reshaped matrices, the unravelling by the means of trajectory sampling is not straightforward. The problems arise due to the arbitrariness of the object $|\phi(t_1)\rangle\langle\psi(t_1)|$, which is not restricted to matrices, fulfilling the requirements for physical density matrices. If the matrix, for instance, is not semi-positive definite, the ability of rewriting it as a mixed state, defined by a superposition of states weighted with classical probabilities as in Eq. 4.22 is not guaranteed. Therefore, a stochastic modeling of this matrix by wave functions, where the initial state is chosen according to these probabilities, is generally not possible.

In the following, this section continues with outlining two solutions: the approach of Breuer and Petruccione [34] on the one side and Mølmer, Castin and Dalibard [110] on the other side. The entanglement between two subparts of the whole system is the significant property, influencing the quality of the MPS compression. Therefore we will use it to quantify the computational effort for computing two time correlations in both cases. This sets the foundation for a

convergence comparison, presented subsequently.

4.4.1. Joint evolution of two states– approach of Breuer et al. [34]

The idea of Breuer et al. [34], is based on the doubling of the Hilbert space at the first application time t_1, by defining a normalized vector in the superspace and the corresponding density matrix

$$|\Theta(t_1)\rangle = \frac{1}{\sqrt{2}} \begin{pmatrix} |\psi(t_1)\rangle \\ |\phi(t_1)\rangle \end{pmatrix}, \text{ and } \tilde{\rho}(t_1) = |\Theta(t_1)\rangle\langle\Theta(t_1)| = \begin{pmatrix} |\psi(t_1)\rangle\langle\psi(t_1)| & |\psi(t_1)\rangle\langle\phi(t_1)| \\ |\phi(t_1)\rangle\langle\psi(t_1)| & |\phi(t_1)\rangle\langle\phi(t_1)| \end{pmatrix}.$$

It is important to notice, that $\tilde{\rho}(t_1)$ fulfills all properties of a physical density matrix so that it can be reformulated in terms of averages over wave functions in Hilbert space. The following strategy relies on finding an operator acting on the superspace, which generates a time evolution for the off-diagonal elements, which recovers the right-hand side of Eq. 4.36. For this purpose, the following operators are defined

$$\tilde{H} = \begin{pmatrix} H & 0 \\ 0 & H \end{pmatrix}, \quad \tilde{L}_j = \begin{pmatrix} L_j & 0 \\ 0 & L_j \end{pmatrix}. \tag{4.37}$$

It turns out, that formulating a Lindblad type equation in superspace with $\tilde{H}$ as Hamiltonian and $\tilde{L}_j$ as jump operators

$$\frac{\mathrm{d}}{\mathrm{d}t}\tilde{\rho} = -\frac{i}{\hbar}\left[\tilde{H}, \tilde{\rho}\right] + \tilde{\mathcal{D}}(\tilde{\rho}), \text{ with } \tilde{\mathcal{D}}(\tilde{\rho}) = \sum_j \gamma_j \tilde{L}_j \tilde{\rho}\tilde{L}_j^\dagger - \frac{1}{2}\tilde{L}_j^\dagger \tilde{L}_j \tilde{\rho} - \frac{1}{2}\tilde{\rho}\tilde{L}_j^\dagger \tilde{L}_j, \tag{4.38}$$

results in Lindblad equations for all matrix blocks of the defined density matrix and therefore matches exactly the condition requested for the unravelling. Building upon this, we can continue by unravelling the Lindblad master equation in the doubled Hilbert space analogous to Sec. 4.3. An important feature here is, that neither $\tilde{H}$ nor $\tilde{L}_j$ couple the states $|\psi(t_1)\rangle\langle\psi(t_1)|$ and $|\phi(t_1)\rangle\langle\phi(t_1)|$. Hence, the time evolution of the two states can be calculated independently, but the probability for the application of jump operators needs to be evaluated according to the joint loss in norm. The full procedure can be summarized as follows:

1. Initialize the wave function in the original Hilbert space of states to $|\psi(t=0)\rangle = |\psi_0\rangle$. Compute the time evolution of this state up to t_1 following the rules for the piece-wise deterministic process from Sec. 4.3, giving $|\psi(t_1)\rangle$.

2. Make a copy of the state and apply the operator A to it, $|\phi(t_1)\rangle \equiv A|\psi(t_1)\rangle$ and define the state in the doubled Hilbert space as $|\Theta(t_1)\rangle = \frac{1}{\sqrt{n}}(|\psi(t_1)\rangle, |\phi(t_1)\rangle)^T$, where the normalization factor $n = \langle\Theta(t_1)|\Theta(t_1)\rangle/\langle\psi(t_1)|\psi(t_1)\rangle$ ensures the transfer of the accumulated jump probability at time t_1 to the doubled space representation.

3. Draw a random number $\eta \in [0,1)$ and time evolve both states independently with the effective Hamiltonian H_eff defined in Eq. 4.21, i.e. $|\psi(t+\Delta t)\rangle = \mathrm{e}^{-iH_\text{eff}\Delta t}|\psi(t)\rangle$ and $|\phi(t+\Delta t)\rangle = \mathrm{e}^{-iH_\text{eff}\Delta t}|\phi(t)\rangle$ and calculate the joint squared norm for the jump probability

4.4 Comparison of different sampling approaches for two-time correlation functions

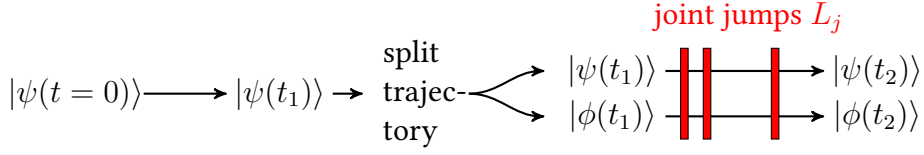**Figure 4.5.:** Sketch of the creation of one sample for the computation of two-time correlators following [34]. After the usual evolution up to t_1 the trajectory is copied, followed by a time span characterized by an independent deterministic non-unitary evolution interrupted by joint jump operator applications.

$$\mathcal{N} = \langle \Theta(t + \Delta t) | \Theta(t + \Delta t) \rangle = \langle \psi(t + \Delta t) | \psi(t + \Delta t) \rangle + \langle \phi(t + \Delta t) | \phi(t + \Delta t) \rangle.$$

4. a) If $\eta < 1 - \mathcal{N}$: Select a jump operator according to the distribution $\Pi_j = p_j / \sum_j p_j$, where $p_j = \langle \psi(t) | L_j^\dagger L_j | \psi(t) \rangle + \langle \phi(t) | L_j^\dagger L_j | \phi(t) \rangle$ and apply it to both states at time t.

   b) Else: Keep the evolved stats $|\psi(t + \Delta t)\rangle$ and $|\phi(t + \Delta t)\rangle$

5. Repeat step 3 and 4 until time t_2 is reached.

6. Compute the two-time correlation function as the Monte-Carlo average over many trajectories and compensate for the normalization factor from step 2 by $\langle\!\langle n \langle \psi(t_2) | B | \phi(t_2) \rangle \rangle\!\rangle$.

The whole sampling process for one trajectory, which exhibits a splitting at time t_1 followed by a distinct evolution of the pair of states, which is only connected by the jump applications until t_2, is sketched in Fig. 4.5. This method can also be extended to the simulation of non-equilibrium multi-time correlation functions

$$\langle A_N(t_N) \dots A_2(t_2) A_1(t_1) \rangle \quad \text{with} \quad t_1 < t_2 < \dots < t_N, \tag{4.39}$$

where the trajectory is splitted at t_1 and the operators are applied to one of the arising branches at their respective time, so that the complexity is still limited to the evolution of two wave functions. Finally, in the Monte-Carlo average, the normalization factors from each time $\{t_1, \dots, t_N\}$ need to be taken into account. Before presenting results from numerical experiments, we present the other approach of how to obtain two-time correlators using Monte-Carlo wave functions.

4.4.2. Separate evolution of four trajectories – approach of Mølmer et al. [110]

An alternative to the procedure from Sec. 4.4.1 has been established in Ref. [110] and reviewed in detail in Ref. [106]. It is based on the quantum regression theorem [6], connecting equal-time to two-time correlations. First of all, it is important to note, that a closed set of equations for the expectation value of an arbitrary operator formulated in the orthonormal basis $\mathbb{B} = \{|i\rangle\}$ as $\hat{O} = \sum_{ij} O_{ij} |i\rangle\langle j|$ is provided by the Lindblad equation for operators

$$\frac{\mathrm{d}}{\mathrm{d}t} \hat{O} = \mathcal{L}^\dagger \hat{O} \Leftrightarrow \frac{\mathrm{d}}{\mathrm{d}t} \langle O_{ij}(t) \rangle = \sum_{kl} \mathcal{L}_{ijkl} \langle O_{kl}(t) \rangle. \tag{4.40}$$

4.4.2 Separate evolution of four trajectories – approach of Mølmer et al. [110]

In general, if a relation for an equal-time measurement is known, the quantum regression theorem states, that if we are provided with the closed differential equation system

$$\frac{\mathrm{d}}{\mathrm{d}t_1}\langle B_i(t_1)\rangle = \sum_j G_{ij}\langle B_j(t_1)\rangle \tag{4.41}$$

with the kernel G_{ij}, the time dependence of two-time correlations $\langle B(t_2)A(t_1)\rangle$ is generated by the same kernel [6]

$$\frac{\mathrm{d}}{\mathrm{d}(t_2 - t_1)}\langle B_i(t_2)A(t_1)\rangle = \sum_j G_{ij}\langle B_j(t_2)A(t_1)\rangle. \tag{4.42}$$

Using this relation, the concept of Monte-Carlo wave function integration is to express the two-time correlator at time t_1 in terms of equal-time expectation values of newly created states. Because of the shared evolution kernel, matching the initial conditions guarantees also the equivalence at each later point in time. One option to do this is to introduce the following four states at t_1

$$|\chi_R^\pm(t_1)\rangle = \frac{1}{\sqrt{\mu_R^\mp}}\,(\mathbb{1} \pm A)\,|\psi(t_1)\rangle$$

$$|\chi_I^\pm(t_1)\rangle = \frac{1}{\sqrt{\mu_I^\mp}}\,(\mathbb{1} \pm iA)\,|\psi(t_1)\rangle \tag{4.43}$$

with the normalization defined by the factors

$$\mu_R^\pm = \langle\psi(t_1)|\,(\mathbb{1} \pm A)^\dagger\,(\mathbb{1} \pm A)\,|\psi(t_1)\rangle \ \text{ and }\ \mu_I^\pm = \langle\psi(t_1)|\,(\mathbb{1} \pm iA)^\dagger\,(\mathbb{1} \pm iA)\,|\psi(t_1)\rangle. \tag{4.44}$$

The states $|\psi(t_1)\rangle$ should be thought of as states obtained from a MCWF unraveling up to time t_1. A direct calculation shows, that a proper grouping of expectation values of A at t_1 indeed restores the corresponding two-time value. The exact form is given by

$$\begin{aligned}C(t_2 = t_1, t_1) &\equiv \frac{1}{4}\big[\mu_R^+\langle\chi_R^+(t_1)|B|\chi_R^+(t_1)\rangle - \mu_r^-\langle\chi_R^-(t_1)|B|\chi_R^-(t_1)\rangle\\ &\quad - i\mu_I^+\langle\chi_I^+(t_1)|B|\chi_I^+(t_1)\rangle + i\mu_I^-\langle\chi_I^-(t_1)|B|\chi_I^-(t_1)\rangle\big] \tag{4.45}\\ &= \frac{1}{4}\langle\psi(t_1)|2BA + 2A^\dagger B - i\left(i2BA - 2iA^\dagger B\right)|\psi(t_1)\rangle \tag{4.46}\\ &= \langle\psi(t_1)|B(t_2 = t_1)A(t_1)|\psi(t_1)\rangle.\end{aligned}$$

In conclusion, evolving two time correlations $\langle B(t_2)A(t_1)\rangle$ with Eq. 4.42 is equivalent to evolving each of the four equal-time expectation values on the right-hand side of Eq. 4.45 according

independent evolution

$|\psi(t=0)\rangle \longrightarrow |\psi(t_1)\rangle \rightarrow$ split trajectories

$|\chi_R^+(t_1)\rangle \longrightarrow |\chi_R^+(t_2)\rangle$
$|\chi_R^-(t_1)\rangle \longrightarrow |\chi_R^-(t_2)\rangle$
$|\chi_I^+(t_1)\rangle \longrightarrow |\chi_I^+(t_2)\rangle$
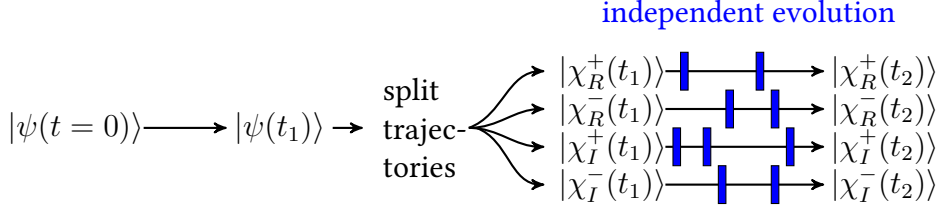$|\chi_I^-(t_1)\rangle \longrightarrow |\chi_I^-(t_2)\rangle$

Figure 4.6.: Sketch of the creation of one sample for the computation of two-time correlators following Ref. [110]. The initial dynamics up to time t_1 is followed by the splitting of the wave function into four trajectories from which the two-time expectation value at t_1 can be reconstructed. Then the each sub-trajectory is evolved separately.

to Eq. 4.41 and combine them afterwards, such that

$$C(t_2, t_1) \equiv \frac{1}{4}\big[\mu_R^+\langle\chi_R^+(t_2)|B|\chi_R^+(t_2)\rangle - \mu_r^-\langle\chi_R^-(t_2)|B|\chi_R^-(t_2)\rangle$$
$$- i\mu_I^+\langle\chi_I^+(t_2)|B|\chi_I^+(t_2)\rangle + i\mu_I^-\langle\chi_I^-(t_2)|B|\chi_I^-(t_2)\rangle\big] \tag{4.47}$$

Let us also outline the trajectory sampling for this case:

1. Define the initial state $|\psi(t=0)\rangle = |\psi_0\rangle$ and employ the introduced stochastic evolution up to time t_1 to compute $|\psi(t_1)\rangle$.

2. Create four copies of $|\psi(t_1)\rangle$ and modify them by the operator applications leading to the states $|\chi_R^\pm(t_1)\rangle$ and $|\chi_I^\pm(t_1)\rangle$ as defined in Eq. 4.43. Evaluate the norm factors $\mu_R^\pm$ and $\mu_I^\pm$ accordingly and store them for later use in the weighted average.

3. Evolve each of the four states independently up to t_2, with the standard procedure of non-unitary deterministic evolution and jump applications. The single trajectory measurement of the two-time function can then be calculated with Eq. 4.47.

4. Produce a large number of quantum trajectories and find the Monte-Carlo average.

The scheme for obtaining one sample is sketched in Fig. 4.6. In contrast to the proposal by Breuer et al., there is no obvious way to generalize this method to multi-time correlations. On first sight, the fact that this approach needs twice as many trajectories for the creation of one sample might suggest that it is computationally less favorable. However, the situation is not that clear, as the decisive factor is the built up entanglement which correlates to the MPS bond dimension. As the entanglement behavior of many-body quantum systems is not trivial and very sensitive to the physics of the considered case, one can not make a general statement.

There are two special cases, distinguished by special properties of the operators A and B, to which we want to pay more attention. Firstly, Eq. 4.46 shows that if the operator at the first time is hermitian, i.e. $A = A^\dagger$, and it further commutes with B, it is sufficient to only keep $|\chi_R^\pm\rangle$, reducing the number of trajectories after t_1 to two. The second case is more subtle; suppose we are dealing with an open system that exhibits a symmetry, which enables the
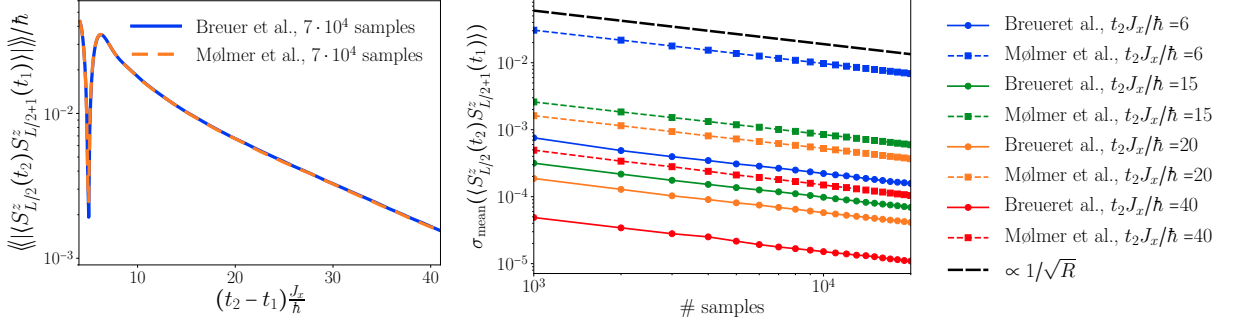
Figure 4.7.: Two-time correlation with different MCWF methods. We compare data from methods introduced by Breuer et al. [34] and Mølmer et al. [110]. Left panel: Two-time correlations of z-directional spin operators applied at the same site on different times. Right panel: Standard deviation of the mean for the same quantity at different times as a function of the number of samples. The black dashed line is a guide to the eye for the inverse square root scaling with the number of samples R. Model parameters for both plots are $L = 14$, $J_z/J_x = \hbar\gamma/J_x = 1$ and $t_1 J_x/\hbar = 1$. The initial state is the Neel state and the Suzuki-Trotter time step is $\Delta t J_x/\hbar = 0.05$ and the bond dimension is exact.

block-diagonalization of the Lindbladian. If operator A does not conserve this symmetry, but rather maps the wave function to a different sector, the states $|\chi_{R,I}^{\pm}\rangle$ can not be assigned to a well-defined quantum number. A workaround for this can be implemented by noting that the contributions $|\psi(t_1)\rangle$ and $A|\psi(t_1)\rangle$ are totally decoupled at any time, other than in the selection process for jumps. Elaborating on this reveals, that it is possible to evolve the latter two states separately and then construct the $|\chi_{R,I}^{\pm}(t)\rangle$ states at every given time $t > t_1$ from them. On closer inspection, it turns out, that the evolution scheme in this case is exactly equivalent to the approach from the last section (Sec. 4.4.1).

4.4.3. Comparison of the introduced MCWF two-time schemes for the XXZ model

As a case study, whose physical interpretation will be discussed in Chap. 6 in detail, we extract two-time correlation functions from the open XXZ spin-1/2 chain where the spins are subjected to dephasing noise using both presented approaches. The Lindblad equation has been introduced in Eq. 4.15. To gain a first intuition, we evaluate the correlator

$$\langle S_{L/2}^z(t_2) S_{L/2+1}^z(t_1)\rangle, \tag{4.48}$$

which will turn out to exhibit interesting physics later. Here, the operators at the two different times are hermitian and commute with each other, so that the method of Sec. 4.4.2 only needs to make use of the evolution of two trajectories. The comparison in the left panel of Fig. 4.7 shows, that both method arrive at the same results as expected. We continue by analyzing the convergence of the two methods. As one source of inaccuracy is the statistical error, inherent to the stochastic sampling, we investigate the standard deviation of the mean (cf. Eq. 4.29) as plotted in the right panel of Fig. 4.7 at different times. Both methods show the expected inverse
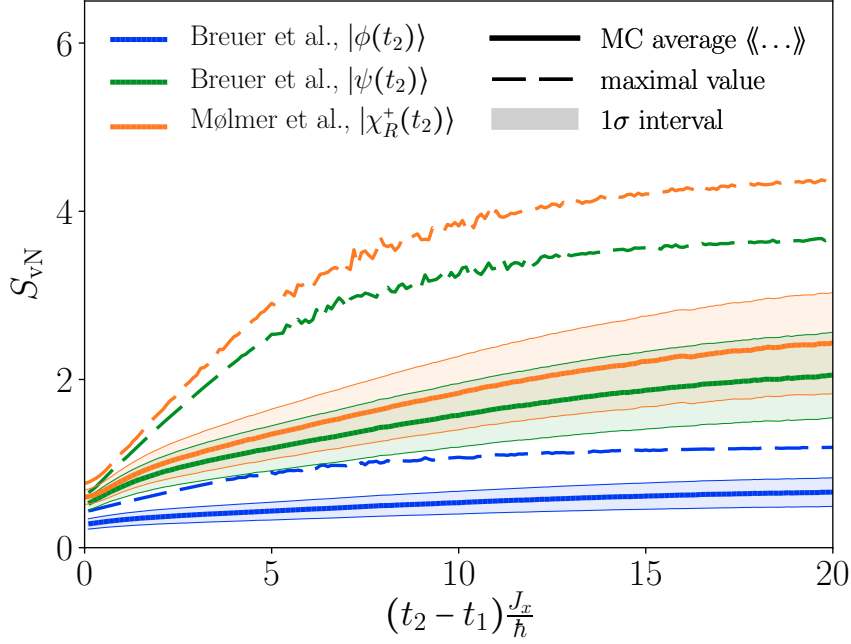
Figure 4.8.: Entropy evolution for branches of different MCWF two-time schemes. Monte-Carlo average, maximal value among all trajectories and interval of width σ are shown for the different branches (represented by different colors) after the split at t_1 of both methods for a chain of $L = 15$ spins, with $J_z/J_x = \hbar\gamma/J_x = 1$, $t_1 J_x/\hbar = 1$, $|\psi_0\rangle = |\psi_{\text{Neel}}\rangle$ and Suzuki-Trotter time step $\Delta t J_x/\hbar = 0.05$.

square root dependence on the number of samples R, as a comparison with the black dashed line shows. This originates from the statistical independence of the sampling. However, the standard deviation of the mean for the computation with the scheme of Breuer et al. is roughly a whole order of magnitude smaller compared to the one of Mølmer et al. for all times, so that also the number of trajectories needed to reach a certain accuracy for this two-time correlation function is significantly smaller using the first approach. Remarkably, the convergence of the Monte-Carlo average is faster for later times, which hints to the convergence of this expectation value towards the steady state value. The steady state is known to be unique and the infinite temperature state.

To judge the efficiency, it remains to benchmark the cost of creating a single trajectory. To this end, we show in Fig. 4.8 the properties of the entanglement entropy, essential for the approximation quality of the bond dimension truncation. The bond dimension has the larges influence on the needed computational resources, as it is typically larger than the local physical dimension. It appears quadratically in the matrix dimension of singular value decompositions, which have a cubic complexity in runtime and memory requirements. We consider the entropy of single branches of the evolution at times $t_2 > t_1$, including the two branches $|\psi(t_2)\rangle$ and $|\phi(t_2)\rangle$ of the joint evolution from Sec. 4.4.1, where $|\phi(t_1)\rangle \equiv S_{L/2}^z |\psi(t_1)\rangle$, as well as the two trajectories from the method in Sec. 4.4.2, i.e the states $|\chi_R^{\pm}(t_2)\rangle$. The results for the latter, give

the exact same behavior for both states, which is why we only added the data for $|\chi_R^+(t_2)\rangle$ to Fig. 4.8. As in Sec. 4.3.3, we select for each time and trajectory sample the bond with maximal entanglement in the chain to compute the von-Neumann entropy. The measurement is exact as the small system of size $L = 15$ allows a full MPS representation, which has a maximal bond dimension of 128. The plot contains information about three different features of the entropy in the simulation. First, we are interested in the average work load of the trajectory creation, which can be accessed by the Monte-Carlo average of the von-Neumann entropy. In addition to that, the maximal entropy among all trajectories for each point in time is an important measure, as it reflects the worst case scenario for the bond dimension of an MPS at the given time. Since we can not guarantee the occurrence of every possible trajectory realization in the stochastic sampling, this is a quantity, which can in principle only be assessed approximately using Monte-Carlo wave functions, and the occurrence of larger values can not be excluded. The third quantity addresses the strength of fluctuations by displaying the interval $[\langle\!\langle S_{\mathrm{vN}}\rangle\!\rangle - \sigma_t(S_{\mathrm{vN}})/2, \langle\!\langle S_{\mathrm{vN}}\rangle\!\rangle + \sigma_t(S_{\mathrm{vN}}))/2]$ around the Monte-Carlo average, using the standard deviation $\sigma_t(S_{\mathrm{vN}})$ as defined in Eq. 4.29. While we see a monotonic increase of the entanglement in each of the branches, both of the evolutions originating from splitting in the procedure of Breuer et al. show lower entropy values for all times and the given parameter set. This is true for the average as well as the maximal entropy, which is of the order of twice the measured mean. The standard deviation increases, pointing out the broadening of entanglement distribution according to the participating quantum trajectories, which is causing a larger spectrum of numerical effort for different samples. We conclude, that in this case study considering this specific model and parameter set, the approach of Breuer et al. prevails against the one by Mølmer et al. in terms of both, memory and run time.

4.5. Conclusion and summary of the results of Chap. 4

In this chapter we introduced different matrix product state approaches to the simulation of Lindblad dynamics of open quantum systems. The first option is given by a reformulation of the density matrix as a pure state, with the help of an auxiliary space. We showed how the initial state can be translated to this framework and subsequently time evolved by a sequence of gate applications for short-ranged Lindbladian models. A peculiarity is given by the extension of the established method by implementing a efficient measurement scheme for expectation values, while exploiting the benefits of conserved quantum numbers of the model. The method bears the advantage that it finds the quasi-exact dynamics without any other approximation than the well-controlled truncation and the size of the Suzuki-Trotter time step. A limitation occurs, when the initial state is already strongly entangled, which requires a large bond dimension for the MPS representation, as it is for example the case for ground states obtained from preceding DMRG calculations. In these situations the quadratic increase in bond dimension associated with the purification process, becomes quickly numerically infeasible. Last but not least, the effective doubling of the system size, increases the requirements of computational resources.

Therefore, we outlined an alternative approach, which promises to overcome some of these obstacles, at the cost of other approximations. The unravelling of the Lindblad master equation by a stochastic sampling of quantum trajectories by piece-wise deterministic processes has been

shown to be equivalent to the evolution in terms of density matrices. Consequently, a Monte-Carlo scheme mimicking this sampling can be implemented, by a piece-wise evolution of wave-functions in the original Hilbert space. While this circumvents the problems of the purification mentioned above, the sample size to reach an acceptable statistical error is typically of the order of 10^4 and therefore quite large. The statistical accuracy, given by the standard deviation from the Monte-Carlo average, depends on the observable and the time and has been shown to be up to 10^{-2} for the z-directional correlator. Consequently, if a very high precision is required, the MCWF becomes challenging.

Finally, we compared the performance of two different ways to measure two-time correlation functions given by Breuer et al. and Mølmer et al. for the XXZ-model with local dephasing at each site. The statistical error for the local equal-time correlations, which shows the expected inverse square root scaling with the number of samples, reveals about one order of magnitude of difference between the two proposals, favoring the one of Breuer et al. Observing the entanglement entropy as a measure for the numerical cost related to the bond dimension in all branches which contribute to the time evolution after the first application time, we have found that also here, the approach by Breuer et al. needs a lower bond dimension for both trajectory parts, since the entropy is smaller for all times, in the studied example case. Due to the current restriction on this special model choice, future work is needed to test this statement for other models, parameter regimes, initial states and observables.

Dissipative attractor dynamics towards a chiral state in fermionic ladders coupled to an optical cavity

5.1. Introduction

In this chapter we propose how to create and investigate a chiral state of spin-polarized fermionic atoms subjected to a ladder geometry. The atoms are further coupled to a single mode of a standing-wave light field created by a cavity formed by two oppositely aligned mirrors. The realized state is a self-organized steady state of the underlying dissipative dynamics induced by cavity losses. It is approached exponentially fast in time and is characterized by the appearance of chiral currents cycling around the ladder boundaries. The chiral state is similar to the observed chiral currents of edge states present in topological non-trivial materials. These are known to be very robust to external perturbations imposed on the state. We will pay attention to the properties of the emerging steady state as well as to the dynamics leading thereto. The introduction to this chapter is structured such, that we start by briefly introducing the applications of topology in condensed matter physics, in the way it is appearing in the considered model, then present the concept of self-organization and its implementation in various aspects, and finally describe how we proceed in the presentation of the obtained results in a short outline.

5.1.1. Topological states in condensed matter physics

A prominent example of topological phases is given by the integer quantum Hall effect [122], where an electric current created by the motion of an ultracold two-dimensional electron gas, is penetrated by a magnetic field perpendicular to the two-dimensional area, which gives rise to a voltage measured orthogonal to the movement of the electrons. Surprisingly, the corresponding Hall conductivity is constant over large regions of different magnetic field strengths, and only changes rapidly at very distinct values, resulting in a step-wise structure of the conductance. This behavior can be related to the topology of the eigenstates $\{|u_\mu(\mathbf{k})\rangle\}$, belonging to the eigenenergies $\{E_\mu\}$ of the system, which form the electronic band structure [123]. The topology

of phases of matter is expressed by topological invariants, which in the case of the quantum hall effect are determined by the Chern number ν_μ assigned to each electronic band. Assuming translation invariance justifies the use of periodic boundary conditions. The Chern number of one band is then given by the following integral over the first Brillouin zone, which is for the two-dimensional case a torus

$$\nu_\mu = \frac{i}{2\pi} \int_{1.\text{BZ}} \Omega_\mu(\mathbf{k}) \mathrm{d}\mathbf{k}, \tag{5.1}$$

where we used the Berry curvature defined in [124] and given by

$$\Omega_\mu(\mathbf{k}) = i \left(\left\langle \frac{\partial u(\mathbf{k})}{\partial k_x} \bigg| \frac{\partial u(\mathbf{k})}{\partial k_y} \right\rangle - \left\langle \frac{\partial u(\mathbf{k})}{\partial k_y} \bigg| \frac{\partial u(\mathbf{k})}{\partial k_x} \right\rangle \right). \tag{5.2}$$

The latter can be viewed as the geometric phase, also known as Berry phase, which is picked up by the eigenstate when moving along an infinitesimal small closed path in k-space. As the Chern number takes integer values and the Hall conductance is found to be directly related to it for low enough temperatures,

$$\sigma_H = \frac{e^2}{h} \sum_{E_\mu < E_F} \nu_\mu, \tag{5.3}$$

the step structure of the Hall conductance can be related to the topology of the bulk. The integer value of the Chern number is insensitive to adiabatic deformations of the model, as small changes in the Berry curvature are compensated on a global scale. This leads to the great robustness of the Hall plateaus. Interestingly, in the plateau regions of the Hall conductance, in the thermodynamic limit the Fermi energy lies in an energy gap of the energy spectrum, prohibiting any hopping in the bulk of the material. The fact that a finite conductance is measured is a result of the nature of the finite sample size, where contributions from the boundary become important. Indeed, the current is induced by states located at the edges of the system in real space, with an energy placed in the bulk gap. In general, the so-called bulk-edge correspondence states that the number of emerging edge states equals the total Chern number of occupied bulk states in the infinite system [125]. Consequently, edge states are also topologically protected and robust against external noise, which makes them potentially useful for promising applications such as quantum computing [21, 22] which rely on long-lasting coherent quantum states.

Recently, topological effects have been discovered in many different areas of condensed matter physics, one example being the experimental detection of signatures of topological insulators, as for example the existence of edge states, in two and three dimensions [126]. Furthermore, a list of models has been implemented in the field of ultra-cold atoms, which are trapped in optical lattices [127], in particular using strong artificial magnetic fields [128], for example to realize the two-dimensional fermionic Hofstadter model [49, 129] or to create chiral current bearing states in bosonic ladder geometries [130]. In the mentioned examples, the artificial magnetic phase is generated by an external phase imprint. In this chapter we present, how a chiral state can be prepared with the help of an optical cavity in a dynamical self-organized fashion. Theoretically, the field of cold atoms in ladder geometries has been studied extensively

for both bosonic and fermionic atoms [19, 131–134].

5.1.2. Self-organization of states in open systems

Instead of carefully constructing specific quantum states in an equilibrium setting, it can be advantageous to design the environment of an open quantum systems in a way, that the steady state is the targeted state acting as an attractor in time [135]. In this approach, certain perturbations to the steady state are corrected exponentially fast in time. Provided that the steady state is unique, the dynamics leading to the state can be seen as a self-organization process, vastly independent of the initial state of the system. One example for this is given by the coupling of a photon-leaking cavity to a gas of cold atoms, where the photon field mode effectively mediates a global long-range coupling between the atoms causing an accelerated formation of the steady state. Moreover, a feedback loop between atoms and photons can be established, which is able to affect the light field considerably. One remarkable experiment is the observation of the Dicke quantum phase transition in the form of a non-equilibrium dynamical phase transition [24, 25]. To this end, a Bose-Einstein condensate of atoms is placed in a cavity, coupled to a transverse standing wave pump laser oriented perpendicular to the cavity axis. Increasing the pump strength with time above a certain threshold gives rise to a reordering of the atoms into a checkerboard density pattern via two-photon scattering processes involving both, pump and cavity photons, as predicted in earlier theoretical studies [23, 136–139]. Moreover, externally controlled optical lattices have been created inside optical resonators, enabling, for example, the experimental realization of a non-equilibrium superfluid to Mott-insulator transition [140, 141], which raises the hope for future experimental feasibility of the proposed fermionic model.

5.1.3. Outline of the chapter

We continue this chapter by introducing the system and its most important characteristics in Sec. 5.2 and present a detailed derivation of the model afterwards in Sec. 5.3. Subsequently, we describe how analytic findings, suitable for steady-state predictions, are obtained using the adiabatic elimination of the mean field of the cavity field in Sec. 5.4, as well as the implementation of exact numerical computations, providing the full open system evolution by diagonalizing the Lindblad superoperator $\mathcal{L}$ exactly in Sec. 5.5. Results concerning features of the steady state are discussed in Sec. 5.6 and properties of the dissipative dynamics are determined in Sec. 5.7.

5.2. General description of the model and scope of the work

Before we present a detailed derivation of the Hamiltonian part under consideration in the next section, let us begin with a description of the model at hand [142–144] and with an overview of the different components. Here we turn our attention to a gas of ultra-cold non-interacting spinless fermionic atoms suddenly coupled to the single mode of a lossy Fabry-Perot cavity. The action of the cavity can be interpreted as the mediation of an effective long-range interaction between the fermions. In addition to that, the atoms are confined to the localized sites of a two dimensional optical lattice potential created by orthogonal standing wave lasers. The lattice geometry is displayed in Fig. 5.1 and consist of a usual lattice in x-direction and a superlattice structure in y-direction, which is chosen to be parallel to the cavity axis. The superlattice establishes an energy off-set $\hbar\Delta$ on every second site. Due to the low temperature,
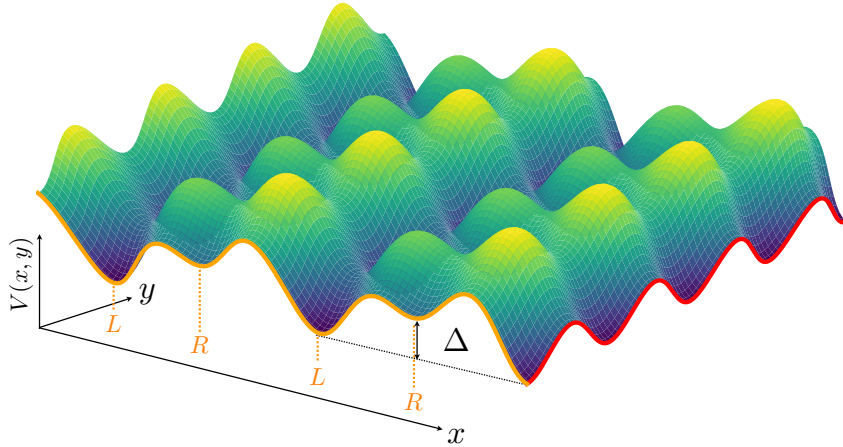
Figure 5.1.: Sketch of optical lattice potential, placed inside the cavity created by perpendicular standing wave laser beams, showing the superlattice with the energy offset Δ in x-direction and a lattice with simple periodicity ini y-direction.

quantum fluctuations are not negligible but rather play an important role regarding the spatial movement. This enables quantum tunneling, in the context of a discrete lattice also known as hopping in between sites. While the hopping of particles in y-direction is unconstrained, the superlattice structure in x-direction results in a high suppression of the corresponding tunneling process.
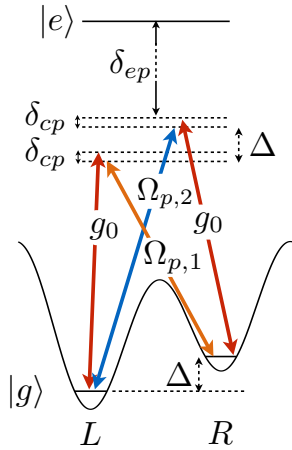
Figure 5.2.: Level-scheme of balanced Raman transitions.

Another contribution to the set-up is given by two running-wave pump lasers with frequencies $\omega_{p,1} = \omega_c - \Delta/\hbar$ and $\omega_{p,2} = \omega_c + \Delta/\hbar$, which are suddenly switched on and cross the cavity in opposite directions parallel to the y-axis. As sketched in Fig. 5.2, the pump beams can scatter inelastically with the atoms, represented by the states $|g\rangle$ and $|e\rangle$, and the cavity via two-photon Raman transitions. The parameters, are the Rabi frequencies associated with the cavity g_0 and the pump lasers $\Omega_{p,1}$ and $\Omega_{p,2}$ as well as the shifted cavity frequency δ_{cp} and different sites of the super lattice are labeled as L and R, as also denoted in Fig. 5.1. We will present in this chapter that above a critical pump intensity absorbing and emitting photons from the cavity mode with the help of one of the two pump beams can restore the hopping along the y-direction at every second bond, such that an array of decoupled ladders is formed. This introduces a feedback loop between the cavity and the atoms: The inelastic scattering of photons from the pump beams with the atoms reenables the hopping on the ladder rungs and populates the initially empty cavity mode. The cavity field in return, can scatter with the atoms causing photo-induced tunneling accompanied by the emission of a photon into the pump modes. An important consequence

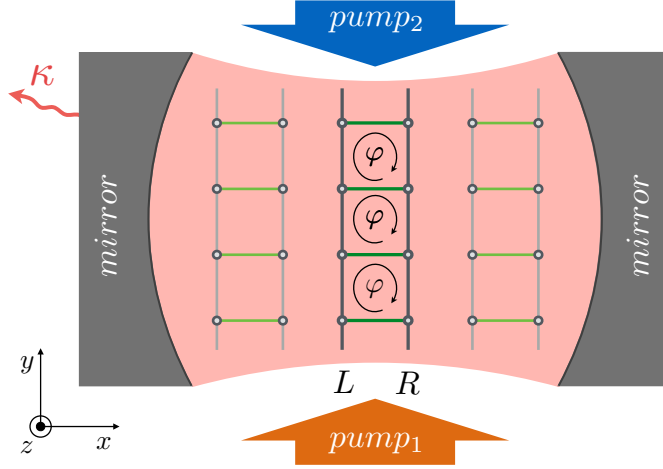**Figure 5.3.:** Sketch of the model: Ultracold fermionic atoms are trapped in a lattice of ladder geometry with legs L and R and coupled to a single-mode photon cavity, which is subject to losses controlled by the strength κ. The scattering of two transverse running wave pump beams with the fermions results in a phase imprint φ onto the atoms analogous to a magnetic field felt by charged particles.

of this feedback loop is that the running-wave character of the pump beams causes a space dependent phase transfer onto the fermions during the tunneling, giving rise to a flux imprint, which plays the role of an artificial magnetic field. The following derivation considering all the mentioned effects gives the effective Hamiltonian H for this setup in Eq. 5.17. As a last ingredient, we also add the loss of photons to our investigation. Since the dissipated photons in good approximation do not act back on the system inside the cavity the environment can be regarded as Markovian. The overall dynamics is then well-described by the Lindblad master equation

$$\frac{\mathrm{d}}{\mathrm{d}t}\rho = \mathcal{L}\rho = -\frac{i}{\hbar}\left[H, \rho\right] + \kappa\left(2a\rho a^{\dagger} - a^{\dagger}a\rho - \rho a^{\dagger}a\right), \tag{5.4}$$

with the dissipation strength κ and the annihilation operator of cavity photons a as the only Lindblad jump operator. A sketch, summarizing all different contributions to the model is presented in Fig. 5.3. As we will show, the feedback mechanism leads to the dynamical self-organization of a topologically non-trivial phase characterized by the presence of a chiral current flowing along the ladder edges. This state turns out to be an attractor state in the dissipative dynamics which is approached exponentially fast in time. Topological phases are known to be stable against external perturbations and therefore objects of interest. This case bears the advantage, that the dependence on the filling fraction of the lattice sites as well as on the strength of the pump beams open the possibility to shift between states of different topology. Also the fact, that the state is an attractor state, i.e. a steady state which does not evolve with time, guarantees a robust dynamic control.

5.3. Derivation of the model Hamiltonian

The first step in the study of the non-equilibrium properties is to derive the Hamiltonian of the equilibrium model for the coupled atom-cavity system without considering the photon losses, leading to the finial result in Eq. 5.17. To do so, we will first consider a set of non-interacting fermionic two-level atoms coupled to a cavity field and a transverse pump beam. Assuming that the pump frequency is far detuned from the two-level resonance frequency will allow us to adiabatically eliminate the higher energy state and describe the atom dynamics by an effective motion of the low energy state only. Furthermore, this effective evolution can be described by an effective model which yields the same equations of motion for both, the photons and the atoms. Using the tight-binding approach and constraints given by the underlying optical lattice geometry, we will finally arrive at the equilibrium Hamiltonian.

First of all, let us consider a single particle Hamiltonian of one two-level atom coupled to a single-mode cavity and a coherent running-wave pump beam, which crosses the cavity. After applying the rotating wave approximation, the atom-cavity coupling is described by the well-known Jaynes-Cummings model [23] and the full Hamiltonian reads

$$H^{\mathrm{sp}} = H^{\mathrm{sp}}_{\mathrm{atom}} + H^{\mathrm{sp}}_{\mathrm{cavity}} + H^{\mathrm{sp}}_{\mathrm{atom, cavity}} + H^{\mathrm{sp}}_{\mathrm{atom, pump}}, \tag{5.5}$$

with the contributions

$$
\begin{aligned}
H^{\mathrm{sp}}_{\mathrm{atom}} &= \frac{p^2}{2m} + V_e(\vec{r})|e\rangle\langle e| + V_g(\vec{r})|g\rangle\langle g| + \hbar\omega_{eg}|e\rangle\langle e| \\
H^{\mathrm{sp}}_{\mathrm{cavity}} &= \hbar\omega_c a^\dagger a \\
H^{\mathrm{sp}}_{\mathrm{atom, cavity}} &= \hbar g_0 \cos(\vec{k}_c\vec{r}) \left(|e\rangle\langle g|a + |g\rangle\langle e|a^\dagger\right) \\
H^{\mathrm{sp}}_{\mathrm{atom, pump}} &= \hbar\Omega_p \mathrm{e}^{i(\vec{k}_p\vec{r}-\omega_p t)}|e\rangle\langle g| + \hbar\Omega_p^* \mathrm{e}^{-i(\vec{k}_p\vec{r}-\omega_p t)}|g\rangle\langle e|.
\end{aligned}
$$

Here $|e\rangle$ and $|g\rangle$ denote excited and ground state of the atom, which are separated in energy by $\hbar\omega_{eg}$ and subjected to a state-dependent potential $V_{\alpha=g,e}$ in addition to the free Hamiltonian. The cavity with the frequency of the dominant mode ω_c is represented by the bosonic operators a and $a^\dagger$, with $[a, a^\dagger] = 1$. All other cavity modes are far detuned. The strengths of the coupling between the atoms and the pump laser or the cavity are given by the Rabi frequencies g_0 for the cavity and Ω_p for the pump beam. The pump laser is represented classically as an electro-magnetic plane wave propagating with momentum $\vec{k}_p$ and frequency ω_p. In contrast to that, the fixed boundary conditions of the resonator mirrors enforce a standing wave mode with momentum $\vec{k}_c$ and the mentioned operator algebra. After shifting to the reference frame rotating with the frequency of the pump laser, i.e. transforming H with $U = \mathrm{e}^{i\omega_p t(|e\rangle\langle e|+a^\dagger a)}$, we change to the many-body formalism using the concept of second quantization for the description of N fermionic atoms. By introducing field operators, depending on the location $\vec{r}$, which obey the

canonical anti-commutation relations

$$\left\{ \Psi_f(\vec{r}), \Psi_{f'}^\dagger(\vec{r}') \right\} = \delta^3(\vec{r} - \vec{r}')\delta_{f,f'},$$

$$\text{and } \left\{ \Psi_f(\vec{r}), \Psi_{f'}(\vec{r}') \right\} = \left\{ \Psi_f^\dagger(\vec{r}), \Psi_{f'}^\dagger(\vec{r}') \right\} = 0 \quad \text{with } f, f' \in \{e, g\},$$

the full Hamiltonian for a gas of non-interacting spinless fermionic atoms coupled to a cavity and a pump beam is given by

$$\tilde{H} = \tilde{H}_{\text{atom}} + \tilde{H}_{\text{cavity}} + \tilde{H}_{\text{atom, cavity}} + \tilde{H}_{\text{atom, pump}}. \tag{5.6}$$

The first term covers the free evolution of the atoms. In analogy to the Jaynes-Cummings model, we only consider two internal states of atoms with mass m, a ground and an excited state. The corresponding Hamiltonian reads

$$\tilde{H}_{\text{atom}} = \int \mathrm{d}^3 r \left[\Psi_g^\dagger(\vec{r}) \left(-\frac{\hbar^2 \nabla^2}{2m} \right) \Psi_g(\vec{r}) + \Psi_e^\dagger(\vec{r}) \left(-\frac{\hbar^2 \nabla^2}{2m} + \hbar\omega_{egp} \right) \Psi_e(\vec{r}) \right], \tag{5.7}$$

where we define the shifted resonance frequency $\omega_{egp} = \omega_{eg} - \omega_p$ in the rotating frame. Note here, that we have not taken into account an overall external potential here. Nevertheless, we will employ the impact of an optical lattice potential later. Again, the change to the interaction picture causes also a shift for the cavity frequency, so that the contribution of the bosonic standing wave mode of the cavity is given by

$$\tilde{H}_{\text{cavity}} = \hbar\omega_{cp} a^\dagger a, \quad \text{with } \omega_{cp} = \omega_c - \omega_p. \tag{5.8}$$

In analogy to equation 5.5, the couplings of the atoms to the cavity and to the pump beam have the forms

$$\tilde{H}_{\text{atom, cavity}} = \hbar g_0 \cos(\vec{k}_c \vec{r}) \int \mathrm{d}^3 r \left(\Psi_e^\dagger(\vec{r}) \, a \, \Psi_g(\vec{r}) + \Psi_g^\dagger(\vec{r}) \, a^\dagger \, \Psi_e(\vec{r}) \right),$$

$$\tilde{H}_{\text{atom, pump}} = \int \mathrm{d}^3 r \left[\hbar\Omega_p \Psi_e^\dagger(\vec{r}) \, \mathrm{e}^{i\vec{k}_p \vec{r}} \, \Psi_g(\vec{r}) + \hbar\Omega_p^* \Psi_g^\dagger(\vec{r}) \, \mathrm{e}^{-i\vec{k}_p \vec{r}} \, \Psi_e(\vec{r}) \right].$$

5.3.1. Adiabatic elimination of the excited state

In the following subsection, we will use the difference in the time scales in the dynamics generated by different scales of the model parameters of $\tilde{H}$, to adiabatically eliminate the impact of the excited state. This approach is based on the assumption, that the pump frequency is far detuned from the atomic resonance, such that $\omega_{eqp} \gg g_0, \Omega_p$. As we will see in the following, each of the operators $\Psi_e^{(\dagger)}(\vec{r}, t)$ and $\Psi_g^{(\dagger)}(\vec{r}, t)$ scales with g_0/ω_{egp} or Ω_p/ω_{egp}, so that we can, although dealing with fermions, assume $[\Psi_f(\vec{r}), \Psi_f^\dagger(\vec{r}')] \approx \delta^3(\vec{r} - \vec{r}')\delta_{f,f'}$. Another fact supporting this statement is the low occupation of the excited state, allowing to neglect operator

5.3 Derivation of the model Hamiltonian

combinations of the form $\Psi_e^\dagger \Psi_e$. This results in the following equations of motion

$$\frac{\mathrm{d}}{\mathrm{d}t}\Psi_e(\vec{r}) = -\frac{i}{\hbar}\left(H_0 + \hbar\omega_{egp}\right)\Psi_e(\vec{r}) - \frac{i}{\hbar}V_{\mathrm{eff}}\Psi_g(\vec{r}), \tag{5.9}$$

$$\frac{\mathrm{d}}{\mathrm{d}t}\Psi_g(\vec{r}) = -\frac{i}{\hbar}H_0\Psi_e(\vec{r}) - \frac{i}{\hbar}V_{\mathrm{eff}}^\dagger\Psi_g(\vec{r}), \tag{5.10}$$

where we define the effective potential $V_{\mathrm{eff}} \equiv [\hbar g_0 \cos(\vec{k}_c\vec{r})a + \hbar\Omega_p e^{i\vec{k}_p\vec{r}}]$ and the free Hamiltonian $H_0 = -\hbar^2\nabla^2/2m$. Working in the interaction picture again, by transforming the problem to the rotating frame of ω_{eqp} and formally integrating the differential equations it is possible to write the time dependencies of both field operators

$$\Psi_e(\vec{r}, t) = -\frac{i}{\hbar}\int_{t_0}^t e^{\frac{i}{\hbar}(H_0 + \hbar\omega_{egp})(\tau - t)}V_{\mathrm{eff}}(\tau)\Psi_g(\vec{r}, \tau)\mathrm{d}\tau,$$

$$\Psi_g(\vec{r}, t) = e^{\frac{i}{\hbar}H_0(t_0 - t)}\Psi_g(\vec{r}, t_0) - \frac{i}{\hbar}\int_{t_0}^t e^{\frac{i}{\hbar}H_0\tau}V_{\mathrm{eff}}^\dagger(\tau)\Psi_e(\vec{r}, \tau)\mathrm{d}\tau.$$

Although this system of differential equations is not closed, the framework of our assumption allows us to give an approximate solution for the excited state. To this end, we plug in the expression for the ground state in the formula of the excited state and apply an integration by parts on the first time integral. Doing this and keeping only terms which are linear in $V_{\mathrm{eff}}^{(\dagger)}/\omega_{egp}$ yields

$$\Psi_e(\vec{r}, t) \approx -\frac{1}{\hbar\omega_{egp}}\left(V_{\mathrm{eff}}(t)e^{-\frac{i}{\hbar}H_0(t - t_0)}\Psi_g(t_0) - e^{\frac{i}{\hbar}(H_0 + \hbar\omega_{egp})(t - t_0)}V_{\mathrm{eff}}(t_0)\Psi_g(t_0)\right). \tag{5.11}$$

Using the fact that the cavity is initially empty and the pump laser is switched off, i.e. $V_{\mathrm{eff}}(t_0) = 0$, we finally arrive at

$$\Psi_e(\vec{r}, t) \approx -\frac{1}{\omega_{egp}}\left(g_0 \cos(\vec{k}_c\vec{r})a + \Omega_p e^{i\vec{k}_p\vec{r}}\right)\Psi_g(\vec{r}, t). \tag{5.12}$$

As a side note, it is interesting to state, that the same result can be obtained by plausibility arguments: Taking into account Eq. 5.9 reveals, that if the pump is sufficiently far detuned, such that $\hbar\omega_{egp}$ dominates the free Hamiltonian, and the excited state dynamics is considered to reach a steady state fast, i.e. $\mathrm{d}\Psi_e(\vec{r}, t)/\mathrm{d}t \approx 0$, Eq. 5.12 arises naturally.

5.3.2. Effective Hamiltonian and expansion in Wannier basis

After having successfully eliminated the excited state, the dynamics of the operators of the ground state and the cavity field is given by

$$
\frac{\mathrm{d}}{\mathrm{d}t}a = -\frac{i}{\hbar}\left\{\left(\hbar\omega_{cp} - \frac{\hbar g_0^2}{\omega_{eqp}}\int \mathrm{d}^3 r \cos^2(\vec{k}_c\vec{r})\Psi_g^\dagger(\vec{r},t)\Psi_g(\vec{r},t)\right)a \right.
$$
$$
\left. -\frac{\hbar g_0\Omega_p}{\omega_{egp}}\int \mathrm{d}^3 r \cos(\vec{k}_c\vec{r})e^{i\vec{k}_p\vec{r}}\Psi_g^\dagger(\vec{r},t)\Psi_g(\vec{r},t)\right\}, \tag{5.13}
$$

$$
\frac{\mathrm{d}}{\mathrm{d}t}\Psi_g(\vec{r},t) = -\frac{i}{\hbar}\left\{H_0 - \frac{1}{\omega_{egp}}\left[\hbar g_0^2 \cos^2(\vec{k}_c\vec{r})a^\dagger a \right.\right.
$$
$$
\left.\left. +\hbar g_0 \cos(\vec{k}_c\vec{r})\left(\Omega_p e^{i\vec{k}_p\vec{r}}a^\dagger + \text{h.c.}\right) + \hbar|\Omega_p|^2\right]\Psi_g(\vec{r},t)\right\}. \tag{5.14}
$$

One can observe that the same dynamics of Eq. 5.13 and Eq. 5.14 is generated by the following effective Hamiltonian

$$
H^{\text{eff}} = H^{(\text{cavity})} + H^{(\text{gs})} + H^{(0)} + H^{(1)} + H^{(2)}. \tag{5.15}
$$

Here $H^{(\text{cavity})}$ has the same contribution from the cavity as in Eq. 5.8 and $H^{(\text{gs})}$ from the part of Eq. 5.7 concerning the atomic state $|g\rangle$ with lower energy, respectively. The other parts, involving atom photon interactions are given by

$$
H^{(0)} = -\frac{\hbar}{\omega_{egp}}\int \mathrm{d}^3 r |\Omega_p|^2 \Psi_g^\dagger(\vec{r},t)\Psi_g(\vec{r},t),
$$

$$
H^{(1)} = -\frac{\hbar}{\omega_{egp}}\int \mathrm{d}^3 r \left(g_0\Omega_p e^{i\vec{k}_p\vec{r}}a^\dagger + \text{h.c.}\right)\cos(\vec{k}_c\vec{r})\Psi_g^\dagger(\vec{r},t)\Psi_g(\vec{r},t),
$$

$$
H^{(2)} = -\frac{\hbar}{\omega_{egp}}\int \mathrm{d}^3 r g_0^2 \cos^2(\vec{k}_c\vec{r})a^\dagger a\Psi_g^\dagger(\vec{r},t)\Psi_g(\vec{r},t).
$$

At this point, we introduce a deep optical lattice potential felt by the atoms. A very strong optical lattice in z-direction confines the atoms to pancake-like arrangements, which restricts the geometry the x-y-plane as depicted in Fig. 5.3. Two perpendicularly oriented lattice lasers with half the wave lengths of the cavity mode $\lambda_x = \lambda_y = \lambda_c/2$ further create a square lattice structure in the two left space dimensions, where the dependence on the cavity wave length ensures the same intensity of the cavity field at all sites. Imposing an additional laser in x-direction with the doubled wave length, gives rise to a superlattice potential causing an effective additional energy offset Δ on every second lattice site along this direction. As the lattice potential is very deep, the spatial extension of the fermionic wave function is finite only in close vicinity of the lattice sites. Therefore, it makes sense to expand the field operators in the basis of well-localized Wannier functions

$$
\Psi_g^\dagger(\vec{r},t) = \sum_{m,n} \mathcal{W}^*(\vec{r} - \vec{R}_{m,n})c_{m,n}^\dagger, \tag{5.16}
$$

with the lattice vector $\vec{R}_{m,n} = ma_x\vec{e}_x + na_y\vec{e}_y$ and the lattice spacings $a_x = \lambda_x/2$ and $a_y = \lambda_y/2$. The operators $c_{m,n}^{(\dagger)}$ obey the fermionic anti commutation relations $\{c_{m,n}c_{m',n'}^\dagger\} = \delta_{m,m'}\delta_{n,n'}$ and $\{c_{m,n}c_{m',n'}\} = \{c_{m,n}^\dagger c_{m',n'}^\dagger\} = 0$.

Combining all this and transforming to a frame rotating with the energy offset Δ results in the final Hamiltonian which we will use in the subsequent work

$$H = H_{\text{cavity}} + H_\parallel + H_{\text{atom, cavity}}. \tag{5.17}$$

Again, the cavity part is given by $H_{\text{cavity}} = \hbar\delta_{cp}a^\dagger a$, with the shifted frequency $\delta_{cp} = \omega_{cp} - \Delta$. Restricting the free motion of the atoms in vertical direction to nearest neighbor hopping and neglecting hopping in horizontal direction to due to the superlattice structure, the free atomic part is given by

$$H_\parallel = -J_\parallel \sum_{m,n} \left(c_{m,n}^\dagger c_{m,n+1} + \text{h.c}\right), \tag{5.18}$$

with the hopping amplitude $J_\parallel = \int \mathrm{d}^3 r \, \mathcal{W}^*(\vec{r} - \vec{R}_{m,n})(-\hbar^2\nabla^2/2m)\mathcal{W}(\vec{r} - \vec{R}_{m,n})$. The cavity-atom interaction, including the effect of the pump beam is represented by

$$H_{\text{atom, cavity}} = -\hbar\tilde{\Omega} \sum_{m,n} \left(\mathrm{e}^{in\varphi}a^\dagger c_{2m,n}^\dagger c_{2m+1,n} + \text{h.c.}\right). \tag{5.19}$$

This means, the horizontal hopping, originally suppressed by the potential off-set of the superlattice, is restored on every second bond in x-direction by creating or annihilating cavity photons resulting in a potential shape of decoupled ladders (see Fig. 5.3). This form of the atom light interaction describes the inelastic Raman scattering of both, pump and cavity photons, with the fermionic atoms. An energy level scheme, discussing the various Raman processes involved, has been presented in Fig. 5.2. An important feature is the complex phase $\varphi = |\vec{k}_p|a_y$ imprinted on the fermions during the hopping process on the ladder rungs, which originates in the running wave nature of the pump beam. This results in an overall picked up complex phase of $\mathrm{e}^{i\varphi}$ by fermions, which moves around one square plaquet. Due to the similarity of this to the complex phase picked up by an electrically charged particle which moves along a closed trajectory in a region penetrated by a magnetic field, this phenomena are known as artificial magnetic fields. Note here, that φ can be tuned by tilting the pump lasers out of the x-y-plane. In this work we choose the flux transfer to be $\varphi = \pi/2$. It is clear, that the phase transfer of a pump photon depends on the spatial location as it propagates in a direction perpendicular to the tunneling process at hand. In contrast to that, the scattered cavity photons resemble a standing wave parallel to the hopping along the ladder rungs and therefore do not show a net phase transfer on the atoms. Compared to a static creation of artificial magnetic fields [19, 49, 145–149] involving usually a fine-tuning of the laser parameters, the artificial field here emerges dynamically in a self-organized way via the feedback mechanism. The strength controlling this

process combines properties of pump, cavity, atoms and lattice and is given by

$$\tilde{\Omega} = \frac{g_0 \Omega_p \phi_{y,0}(\vec{k}_p) \phi_x(\vec{k}_c)}{\omega_{egp}} \tag{5.20}$$

with the Wannier function integrals

$$\phi_{y,0}(\vec{k}_p) = \int \mathrm{d}y \mathcal{W}^*(y) \mathcal{W}(y) \mathrm{e}^{i|k_p|y}, \tag{5.21}$$

$$\phi_x(\vec{k}_c) = \int \mathrm{d}y \mathcal{W}^*(x) \mathcal{W}(x-1) \cos(|k_c|x). \tag{5.22}$$

As we also will take into account losses of cavity photons due to imperfections of the cavity mirrors later, the creation of of photons is less likely than the annihilation. Furthermore, an imbalance of the distribution of fermions on the ladder legs in the initial state can impede the occupation of the cavity mode. This can lead to a situation, where all atoms are pumped to the right leg of the ladder. In order to prevent the privileged direction of tunneling, we add another pump beam, running in the opposite direction of the first one, to our model. The frequency for this beam is chosen as $\omega_{p,2} = \omega_{p,1} + 2\Delta/\hbar$, giving rise to a Raman transition connected to the rung hopping process in the inverse direction. Focusing on one independent ladder, determines the atom-cavity part of the Hamiltonian to be

$$H_{\text{atom, cavity}} = -\hbar \tilde{\Omega} \left(a + a^\dagger \right) \sum_n \left(\mathrm{e}^{in\varphi} c_{0,n}^\dagger c_{1,n} + \text{h.c} \right). \tag{5.23}$$

To guarantee the two Raman processes are balanced [137] we choose the Rabi frequency for the second pump beam as $\Omega_{p,2} = \Omega_{p,1} \frac{\omega_e - \omega_{p,2}}{\omega_e - \omega_{p,1}}$.

5.4. Adiabatic elimination of the cavity field and effective fermionic Hamiltonian

Turning back to the full dissipative model, we continue by characterizing the properties of the steady state to which the non-equilibrium system converges for $t \to \infty$ by a mean field approach for the cavity field. This method has been discussed before [20, 23, 142–144, 150] and was also found to agree with experimental observations [24]. The idea is based on the assumption that the cavity dynamics happens on much faster time scales as compared to the atomic motion. Therefore it is possible to assume, that the photon field reaches its steady state instantaneously, such that it does not evolve, i.e. $\mathrm{d}a/\mathrm{d}t \approx 0$. From this we can derive the steady state expectation value of the cavity field operator

$$0 \approx \frac{\mathrm{d}}{\mathrm{d}t} \langle a \rangle = (\delta_{cp} - i\kappa) \langle a \rangle - \tilde{\Omega} \langle K_\perp + K_\perp^\dagger \rangle,$$

$$\Rightarrow \alpha \equiv \langle a \rangle = \frac{\tilde{\Omega}}{\delta_{cp} - i\kappa} \langle K_\perp + K_\perp^\dagger \rangle. \tag{5.24}$$

5.4 Adiabatic elimination of the cavity field and effective fermionic Hamiltonian

Here, we define the directed atomic coupling along all rungs by $K_\perp = \sum_{n=0}^{L-1} e^{in\varphi} c_{0,n}^\dagger c_{1,n}$ for ladders with L rungs. Moreover, we performed a mean field decoupling

$$\langle (a + a^\dagger)(K_\perp + K_\perp^\dagger) \rangle \approx \langle a + a^\dagger \rangle \langle K_\perp + K_\perp^\dagger \rangle \tag{5.25}$$

in this calculation. We will present a comparison with exact computations, which investigates the validity of this statement for the considered range of parameters later (cf. discussion concerning Fig. 5.15). As the fermionic operators commute with the Lindblad jump operator, i.e. the photon annihilation operator a, replacing the cavity field with its mean field α gives rise to an Hamiltonian effectively describing the motion of the fermions

$$H_F = H_\parallel - \left(J_\perp K_\perp + J_\perp K_\perp^\dagger \right), \tag{5.26}$$

$$\text{with } J_\perp = \hbar \tilde{\Omega}(\alpha + \alpha^*) = \frac{A}{2} \langle K_\perp + K_\perp^\dagger \rangle \in \mathbb{R}, \text{ and } A = \frac{4\hbar \tilde{\Omega}^2 \delta_{cp}}{\kappa^2 + \delta_{cp}^2}.$$

We assume, that the steady state can be identified with the ground state of H_F. From a plausibility point of view, this is reasonable due to the influence of the dissipation. The loss of photons can cause a decrease in energy, pushing the system towards the ground state. More quantitatively, the agreement of this method with exact results presented later in this chapter and in Refs. [142, 144] justifies this claim. It is an important point to note, that $J_\perp$ itself depends on the expectation value of fermionic operators. That means, ground state expectation values of the model in Eq. 5.26 are only meaningful, if the following self-consistency condition is met

$$\frac{J_\perp}{A} = \langle gs_{H(J_\perp)} | K_\perp | gs_{H(J_\perp)} \rangle. \tag{5.27}$$

The decoupling of photonic and fermionic operators further incorporates a Z_2 symmetry in the remaining model, i.e. $\text{sign}(\langle K_\perp + K_\perp^\dagger \rangle) = \text{sign}(\alpha + \alpha^*) = \pm 1$. This symmetry will be spontaneously broken in the experiment [24], here we chose, without loss of generality, the positive sign. This enforces the cavity detuning δ_{cp} to be positive which gives also a positive rung hopping amplitude $J_\perp$.

5.4.1. Bogoliubov transformation and spectrum of the effective Hamiltonian

As the Hamiltonian H_F is quadratic in the fermionic operators, we can diagonalize it and express the many-body ground state as the Fermi sea of quasi-particles. As usual for free systems, it is convenient to change into momentum space for the vertical direction by applying a Fourier transform to the operators $c_{m,n} = 1/L \sum_{ka_y} e^{-ika_y n} c_{m,ka_y}$ with the lattice spacing $a_y = \lambda_y/2$ yielding

$$\mathcal{F}(H_F) = -2J_\parallel \sum_{ka_y} \cos(ka_y) c_{m,ka_y}^\dagger c_{m,ka_y} - J_\perp \sum_{ka_y} \left(c_{0,ka_y+\varphi/2}^\dagger c_{1,ka_y-\varphi/2} + \text{h.c.} \right). \tag{5.28}$$

5.4.1 Bogoliubov transformation and spectrum of the effective Hamiltonian

Shifting the diagonal part corresponding to the y-directional movement accordingly, makes it possible to write down the matrix form in k-space

$$\sum_{ka_y} \begin{pmatrix} c^\dagger_{0,ka_y+\varphi/2} & c^\dagger_{1,ka_y-\varphi/2} \end{pmatrix} \begin{pmatrix} -2J_\| \cos(ka_y + \frac{\varphi}{2}) & -J_\perp \\ -J_\perp & -2J_\| \cos(ka_y - \frac{\varphi}{2}) \end{pmatrix} \begin{pmatrix} c_{0,ka_y+\varphi/2} \\ c_{1,ka_y-\varphi/2} \end{pmatrix}. \tag{5.29}$$

This is a symmetric matrix and therefore diagonalizable. More precisely, we use a Bogoliubov transformation to compute the eigenspectrum while preserving the fermionic anti-commutation relation. Doing this, provides the eigenenergies

$$E_\pm(k) = -2J_\| \cos(\varphi/2)\cos(ka_y) \pm \sqrt{J_\perp^2 + 4J_\|^2 \sin^2(\varphi/2)\sin^2(ka_y)}, \tag{5.30}$$

as well as the field operators of the two quasi-particles in momentum space

$$\gamma_{+,k} = v_k c_{0,k+\varphi/2a_y} - u_k c_{1,k-1\varphi/2a_y}, \tag{5.31}$$

$$\gamma_{-,k} = u_k c_{0,k+\varphi/2a_y} + v_k c_{1,k-1\varphi/2a_y}, \tag{5.32}$$

with the coefficients

$$u_k = \sqrt{\frac{1}{2}\left(1 - \frac{\sin(\varphi/2)\sin(ka_y)}{\sqrt{\left(\frac{J_\perp}{J_\|}\right)^2 + \sin^2(\varphi/2)\sin^2(ka_y)}}\right)},$$

$$v_k = \sqrt{\frac{1}{2}\left(1 + \frac{\sin(\varphi/2)\sin(ka_y)}{\sqrt{\left(\frac{J_\perp}{J_\|}\right)^2 + \sin^2(\varphi/2)\sin^2(ka_y)}}\right)}.$$

The dispersion of the eigenenergies is plotted in Fig. 5.4 for different rung hopping amplitudes $J_\perp/J_\|$. While we see two independent dispersion relations for decoupled ladder legs ($J_\perp = 0$), a finite but small coupling lifts the degeneracies at $k = 0$ and $k = \pm\pi$ and creates two separate bands, where the lower one exhibits two distinct minima. Increasing the coupling further to values $J_\perp/J_\| > \sqrt{2}$, results in the opening of a band gap and eventually the two minima merge to a single one at $k = 0$. The knowledge of the eigenbasis allows us to specify the ground state for N particles by successively filling up the N momentum states corresponding to the lowest energy states taking into account both, $E_+(k)$ and $E_-(k)$. The lattice filling, defined by the ratio of occupied to empty sites of the ladder geometry, i.e. $n = N/2L$, is then decisive for the ground state properties. As plotted in Fig. 5.5, there are certain crucial parameter regimes for different filling ratios. For $n = 1/2$ the gap opening at $J_\perp = \sqrt{2}J_\|$ marks a liquid to insulator transition, whereas for $n \le 1/4$ only states of the lower band contribute to the ground state. An interesting feature appears for even smaller fillings as for example $n = 1/8$, where the number of Fermi points changes from four to two by increasing the horizontal hopping amplitude. All
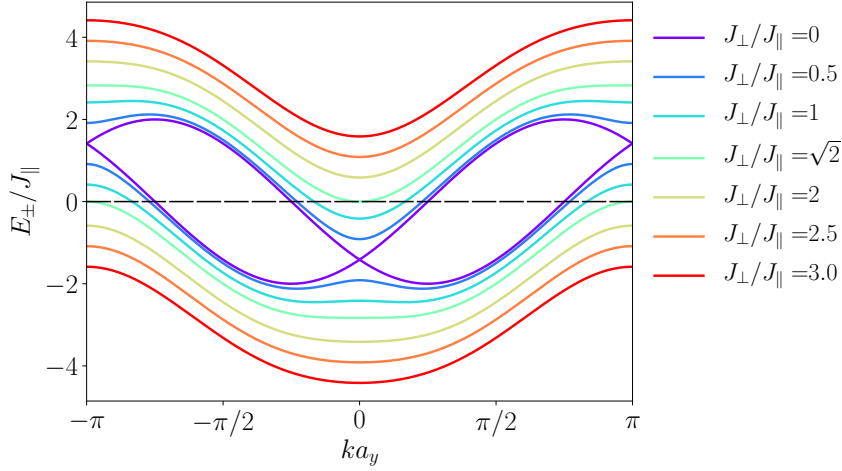
Figure 5.4.: Dispersion of quasiparticle energies of the effective Hamiltonian H_F for different perpendicular coupling strengths $J_\perp/J_\parallel$ and $\varphi = \pi/2$.
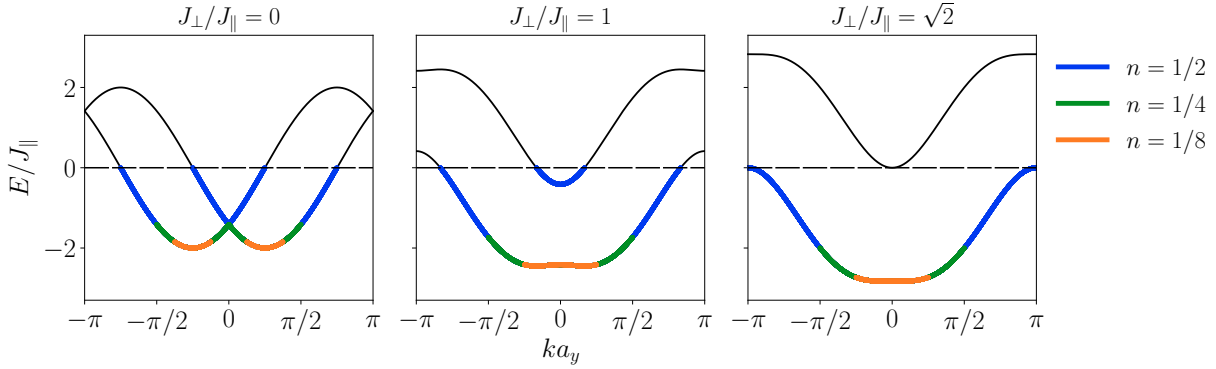

Figure 5.5.: Contribution of quasi-particle states to the many-body ground state of HF for different fillings n and couplings $J_\perp/J_\parallel$.

these features will reoccure in the discussion of the corresponding ground state expectation values later.

5.4.2. Solutions of the self-consistency equation

Now, that we outlined the determination of the ground state, we return to the condition posed by the by Eq. 5.27. This limits the set of valid steady states in this approximation to the ground state of models, containing rung hopping amplitudes which are self-consistent with the expectation value of the directed tunneling. The latter can be obtained, by transforming the corresponding operator to the basis of quasi-particles using Eq. 5.31 and 5.32 which results in

$$K_\perp = \sum_k u_k v_k \left(\gamma^\dagger_{-,k} \gamma_{-,k} - \gamma^\dagger_{+,k} \gamma_{+,k} \right). \tag{5.33}$$
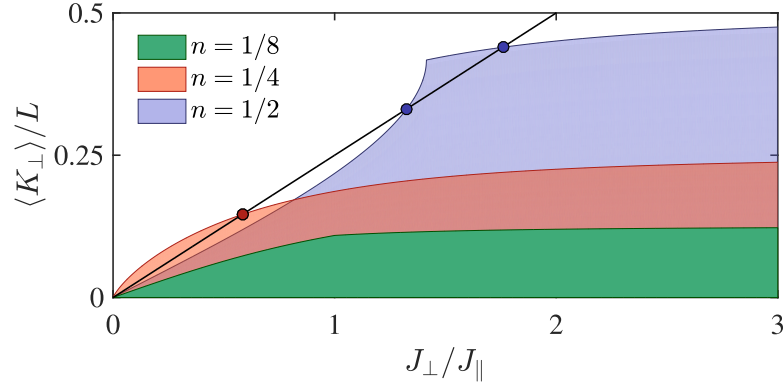
Figure 5.6.: Solutions of self-consistency condition of the directed tunneling for different fillings. The straight line is the parameter dependence linear in the horizontal tunneling with slope $1/A$. Intersections of this linear function with the computed ground state expectation value for $L \longrightarrow \infty$ correspond to self-consistent solutions (©2016 American Physical Society, published in Ref.[144]).

The ground state expectation value of the directed tunneling $\langle K_\perp \rangle / L$ is displayed in Fig. 5.6 as a function of $J_\perp / J_\parallel$ for different fillings. For situations, where the rung tunneling is much larger than the leg tunneling and in particular for $J_\perp / J_\parallel \gg \sqrt{2}$ an expansion of the expectation value of the directed rung yields $\langle K_\perp \rangle / L \approx a_y k_F / 2\pi$, with the momentum k_F at the Fermi point which depends linear on the filling n. At half-filling and low $J_\perp / J_\parallel$, $\langle K_\perp \rangle$ shows a concave curvature until the point when the band gap opens, causing a kink at $J_\perp / J_\parallel = \sqrt{2}$, followed by a linear increase. For lower fillings $n \leq 1/4$, this linear increase, complemented by a small logarithmic correction, can already be seen for low rung coupling strength, as only the lower band is occupied for these parameters. For even lower fillings additionally a cusp appears at the point where the number of Fermi points changes from four to two as explained above. For $n = 1/8$ this happens at $J_\perp / J_\parallel = 1$. The self-consistent solutions can then be extracted, by finding intersection points of this curves with the linear dependence originating from the mean field replacement of the photon field with the slope $1/A$. Notably, for half-filling, there is a critical slope $1/A_{cr}$ for finding solutions, with $A_{cr} = 4\pi J_\parallel / \sqrt{2}\mathcal{K}(-1) + \mathcal{K}(1/2) \approx 3.39 J_\parallel$ as derived in Ref. [143] for a general flux φ, where $\mathcal{K}$ is the elliptic integral of first kind. Translating this back to the model parameters leads to the conclusion that non-trivial steady states at half-filling can only be observed above a certain pump strength. Below the corresponding critical slope, i.e. above the critical pump strength, there is an intermediate region of two coexisting solutions, where one of them only survives over a certain range of slopes. We will discuss the implications of this on the physical properties of the steady state later in section 5.6. For $n = 1/4$ the analysis gives always one solution, independent of the pump strength, whereas for $n = 1/8$ again a critical value $\hbar\tilde{\Omega}_{cr}$ needs to be passed, after which a single solution exists.

5.5. Numerical implementation of the exact diagonalization of the Lindbladian

Having established the various different approximations leading to an analytical understanding of the steady state in Sec. 5.4, it becomes clear, that this treatment can benefit greatly from a comparison to numerically exact calculations. In summary, the mean field decoupling of fermionic and photonic fields, the assumption that the steady state is represented by the ground state of the effective fermionic model H_F (Eq. 5.26) and the requirement of a faster relaxation time scale of the cavity degrees of freedom compared to the atomic ones are potential sources of inaccuracy. To this end, we conduct an exact diagonalization study as introduced in Sec. 3.2 considering small system and the full Lindblad equation for the system's density matrix

$$\frac{\mathrm{d}}{\mathrm{d}t}\rho = \mathcal{L}\rho = -\frac{i}{\hbar}\left[H, \rho\right] + \kappa\left(2a\rho a^\dagger - a^\dagger a\rho - \rho a^\dagger a\right), \tag{5.34}$$

with the Hamiltonian from Eq. 5.17, i.e. $H = H_{\text{cavity}} + H_\parallel + H_{\text{atom, cavity}}$. Equally important, this also poses an unbiased approach to access the full time evolution of the system. This opens the opportunity to draw conclusions on the dynamics, which is inaccessible by the adiabatic elimination procedure.

As a first step, we need to find a basis for the Hilbert space. As this is a composition of cavity photons, which are bosons, and fermionic atoms on a ladder geometry the Hilbert space is given by the tensor product

$$\mathcal{H} = \mathcal{H}_{\text{cavity}} \otimes \mathcal{H}_{\text{atoms}}. \tag{5.35}$$

Here the cavity photon Hilbert space is given by the direct sum of Fock states for different particle numbers with the basis $\mathbb{B}_{\text{cavity}}\left\{|n^B\rangle : n^B \in \mathbb{N}_0\right\}$. The spinless fermions are expressed in the formalism of second quantization in the occupation basis, restricting the site occupation to zero or one. This space is spanned by $\mathbb{B}_{\text{atoms}} = \{|n^F_{0,0}, \ldots, n^F_{0,L-1}, n^F_{1,0}, \ldots, n^F_{1,L-1}\rangle\}$ with $n^F_{m,n} \in \{0, 1\}$. Furthermore, the fermionic nature of the atoms gives rise to a negative sign when exchanging particles. For this reason, the order of the different sites needs to be well-defined, here we choose the basis to be leg-wise ordered. This set-up then enables us to specify the Lindblad matrix $M_\mathcal{L}$ acting on the superspace $\mathcal{H} \otimes \mathcal{H}^*$ of vectorized density matrices $|\rho\rangle\!\rangle$ as explained in Sec. 3.2 and defined in Eq. 3.43.

5.5.1. Symmetries of the Lindbladian

Finding the full eigensystem of $M_\mathcal{L}$ also provides the eigenstates $|\tilde{\rho}_0\rangle\!\rangle$ corresponding to vanishing eigenvalues $M_\mathcal{L}|\tilde{\rho}_0\rangle\!\rangle = 0$. In the model under investigation these states are not unique, but span a manifold as discussed in 3.2. As also mentioned before, it is a good idea to identify symmetries [94, 95] in order to block-diagonalize $M_\mathcal{L}$ aiming for single zero-eigenvalues in seperate blocks. In the following, we prove that this route is here successful, such that we can construct physical density matrices for all steady states. In Table 5.1 we list the different number of found steady states for lattice fillings and system sizes.

A first symmetry to exploit is given by the fact, that the Lindblad equation conserves the number of fermionic atoms, since the dissipation acts on the cavity photons exclusively, so that
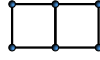
L	lattice	filling $n = N/2L$	#steady states
1		1/2	2
2		1/2	6
		1/4	2
3		1/2	6
		1/6	2

Table 5.1.: Number of steady states for different number of rungs of the ladder L, and different fillings n.
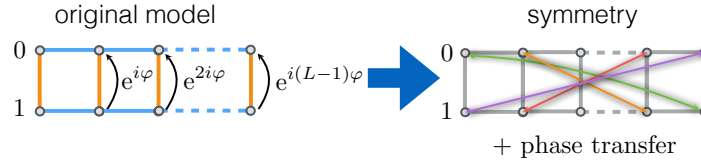

Figure 5.7.: S_1 symmetry transformation of fermions.

we can reduce the basis to the states containing the same number of atoms as the initial state. In addition, observing the Hamiltonian Eq. 5.17, reveals another symmetry for the atoms. As depicted in 5.7, the fermionic Hamiltonian exhibits a mirror symmetry including a correction for the transferred phase, leading to the transformation

$$S_1 : \begin{cases} c_{0,n} \to e^{i(L-1)\varphi/2} c_{1,L-1-n} \\ c_{1,n} \to e^{-i(L-1)\varphi/2} c_{0,L-1-n}. \end{cases} \tag{5.36}$$

Two consecutive applications result in the identity, which classifies the transformation as a $\mathbb{Z}_2$ symmetry and determines the eigenvalues to $\lambda_1 = \pm 1$. Since also both, $H_\parallel$ and $[K_\perp + K_\perp^\dagger]$ are invariant under S_1, switching to the eigenbasis which is sorted according to the eigenvalues, results in a block-diagonal form in the fermionic sector. The transformed operators read

$$\gamma_{\tilde{n}}^\dagger = \frac{1}{\sqrt{2}} \begin{cases} -e^{i(L-1)\varphi/2} c_{0,\tilde{n}}^\dagger + c_{1,\tilde{n}}^\dagger & : \tilde{n} \in \{0, \dots, L-1\}, \\ e^{i(L-1)\varphi/2} c_{0,\tilde{n}-L}^\dagger + c_{1,2L-\tilde{n}-1}^\dagger & : \tilde{n} \in \{L, \dots, 2L-1\}. \end{cases} \tag{5.37}$$

For the single-particle case, the degeneracies of the positive and negative eigenvalue are equal, such that the fermionic states $\gamma_{\tilde{n}}|0\rangle$ only couple to states of the same subspace, both of dimension L. More precisely, the values $\tilde{n} \in \{0, \dots, L-1\}$ correspond to the negative, and $\tilde{n} \in \{L, \dots, 2L-1\}$ to the positive eigenvalue of S_1. Due to the lack of fermionic operators in the dissipator the latter is invariant under this transformation and also the Lindblad matrix is block-diagonal. It is decomposed out of four blocks, as both components of the super space can be in either one of the two subspaces. For a many-body scenario, we can construct the basis ac-
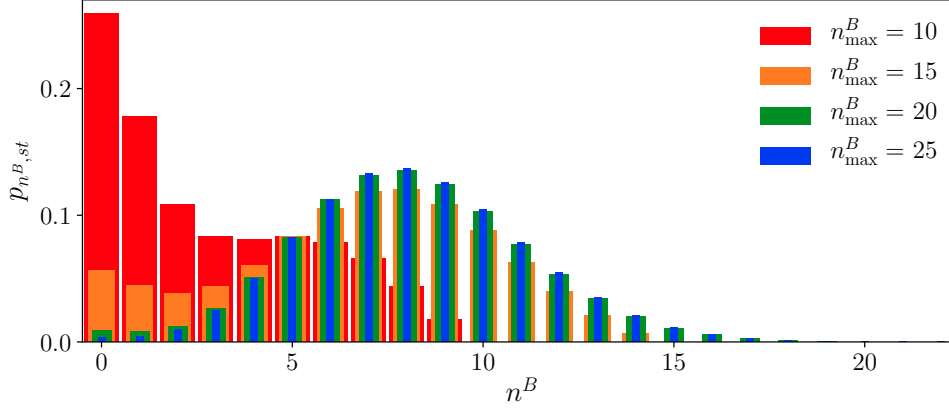
Figure 5.8.: Steady state photon number distribution for different truncation cut-offs n_{max}^B of the bosonic Hilbert space dimension of the cavity photons for a system of size $L = 3$ and $N = 3$ fermions. Model parameters here are $\hbar\kappa/J_\| = 0.25, \hbar\tilde{\Omega}/J_\| = \hbar\delta_{cp}/J_\| = 1$.

cordingly for N particles as $\gamma^\dagger_{\tilde{n}_N} \gamma^\dagger_{\tilde{n}_{N-1}} \ldots \gamma^\dagger_{\tilde{n}_1} |0\rangle$ producing again a block-diagonal Hamiltonian. In every case further unitary transformations can be found in the space of the quasiparticles of S_1, to balance the number of Hamiltonian blocks with the number of vanishing eigenvalues of the Lindbladian.

An interesting property is revealed by the already established $\mathbb{Z}_2$ symmetry regarding the coupling of the cavity field operators to the directed rung tunneling in $H_{\text{atom, cavity}}$ consisting in a joint sign flip of the two while leaving the parallel hopping unchanged

$$S_2 = \begin{cases} K_\perp + K_\perp & \to -(K_\perp + K_\perp), \\ a + a^\dagger & \to -(a + a^\dagger), \\ H_\| & \to H_\|, \end{cases} \Leftrightarrow \begin{cases} a & \to -a, \\ c_{0,n} & \to -c_{0,n}, \\ c_{1,n} & \to c_{1,n}. \end{cases} \tag{5.38}$$

As this symmetry does not commute with the jump operator it is considered to be a weak symmetry [94]. Consecutive application of S_1 and S_2 reveals that the two symmetry transformations anti-commute. From this we can draw the conclusion, that S_2 maps eigenstates of S_1 to the space of the opposite eigenvalues, as can be seen from

$$S_1 S_2 |\lambda_1 = \pm 1\rangle = -S_2 S_1 |\lambda_1 = \pm 1\rangle = \mp S_2 |\lambda_1 = \pm 1\rangle. \tag{5.39}$$

In addition, S_2 also commutes with the directed rung tunneling, so that we can deduce analogously, that S_2 maps eigenvalues of $[K_\perp + K_\perp^\dagger]$ to the space of the corresponding negative eigenvalue. These two insights together with the fact , that the cavity field expectation value α is proportional to the rung tunneling (cf. Eq. 5.24), allow the statement that the symmetry blocks of S_1 with different sign, also belong to cavity fields with opposite sign. We prove this behavior later in our study of the steady state.
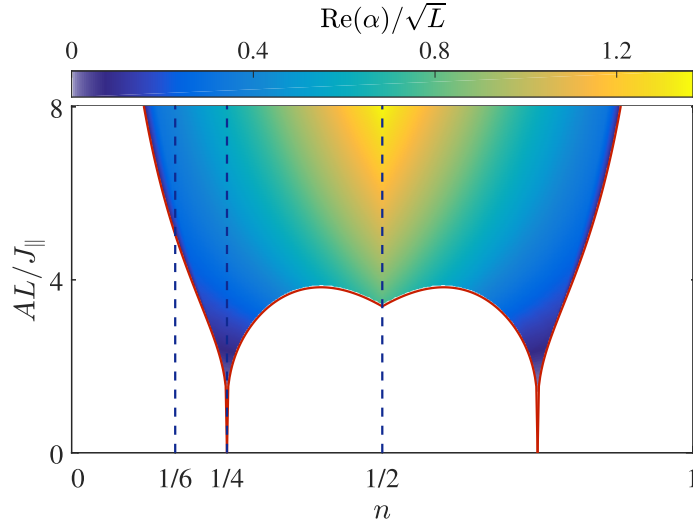
Figure 5.9.: Steady state diagram of the mean field of the photon field α as a function of the rescaled pump strength $AL/J_\parallel$ and the atomic filling of the lattice $n = N/2L$. Zero field regions are white and the critical pump strength is plotted as a red line. (©2016 American Physical Society, published in Ref. [144]).

5.5.2. Photon number restriction

While the fermionic space is finite, due to the finite system size, the conservation of the particle number by the Lindbladian and Pauli's exclusion principle, the bosonic space is in principle unbounded. In practice, we solve this problem by truncating the dimension of the bosonic Hilbert space at a maximal photon number $n_{\max}^B \equiv \dim(\mathcal{H}_{\text{cavity}})$, such that we end up with a model of finite size. On phenomenological grounds, this makes sense because we do not expect too large occupations of the cavity mode for the small systems and not to strong pump strength, which governs the photon creation via the cavity-assisted rung tunneling. Nevertheless, this statement needs always to be validated for the steady state and each time step. In Fig. 5.8 we show the occupation of the different photonic Fock states for the steady state in the symmetry block of a ladder with $L = 3$ rungs and $N = 3$ atoms which shows the maximal detected photon field. While increasing the cutoff from 10 to 15 Boson states, the distribution changes quite drastically, whereas this change is reduced for larger photon space dimensions. Notably, for $n_{\max}^B = 25$, the states of higher photon number are almost empty and the distribution equilibrates to the shown shape. If the threshold is chosen too small, this is also visible in other observables, indicated by the change of measured expectation values when increasing the cutoff. If not stated otherwise, we use $n_{\max}^B = 25$.

5.6. Properties of the steady state

After the presentation of the various available techniques for the description of the steady states which are reached after long times, we now continue with the characterization of the properties of these states. In the next section we will analyze the attractive dynamics towards
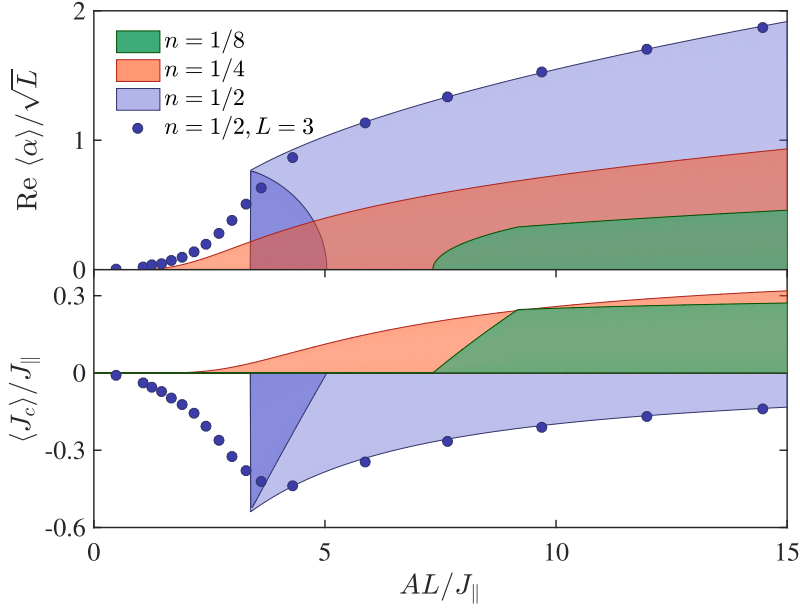
Figure 5.10.: Cavity field and Chiral current for infinitely long ladders. Adiabatic elimination results (lines) are compared to exact diagonalization steady state data (circles) for a small system of $L = 3$ rungs and $N = 3$ atoms with $\hbar\kappa = 0.05J_\parallel$ and $\hbar\delta_{cp} = J_\parallel$. (©2016 American Physical Society, published in Ref. [142]).

the steady states.

We begin with investigating the steady state expectation value of the cavity field α, which is a crucial component in our model, as it establishes a feedback mechanism between the photon field and the rung hopping, causing the creation of an artificial magnetic field. In the framework of adiabatic elimination from Sec. 5.4, the photon field in the steady state is linked to the ground state expectation value of the directed rung tunneling according to the effective fermionic model, with model parameters satisfying the introduced self-consistency condition. The result is shown in Fig. 5.9 as a steady state diagram for an infinitely long ladder ($L \to \infty$), where we show the real part of the photon field as a function of the atomic filling of the ladder lattice and the rescaled pump strength A as defined in Eq. 5.26. Due to the particle-hole symmetry of the fermions, this diagram is symmetric with regard to the $n = 1/2$ axis. In cases where combinations of pump strength and filling allow two self-consistent solution, as for example at half-filling and intermediate strong pump, the plot shows the maximal value. The red line represents the critical value A_{cr} as calculated in Ref. [143], here for the considered flux of $\varphi = \pi/2$. Interestingly, for almost all fillings, a critical minimal pump strength is needs to be crossed to have a finite occupation of the cavity mode. An exception of this is the situation of $n = 1/4$ and its hole equivalent $n = 3/4$, where the quasiparticle bands of the eigenstates of the effective Hamilton H_F (cf. Fig. 5.5) are filled exactly up to the crossing point of the bands in the case of decoupled legs ($J_\perp = 0$). This results in a logarithmic rise of the directed tunneling, enabling a self-consistent solution already for infinitesimal small values of the pump strength.

This is also demonstrated in the cuts at a few chosen fillings in the upper panel of Fig. 5.10. The shown lines represent data obtained from the adiabatic elimination for infinitely long ladders for three selected fillings. Independent of the filling, an expansion for strong pump strengths yields a linear dependence of the photon field on the pump intensity, i.e. $\alpha \approx [2\tilde{\Omega}L/(\delta_{cp} - i\kappa)][a_y k_F/(2\pi)]$. The slope here depends on the respective Fermi momenta, and therefore is stronger for larger fillings as long as $n \leq 1/2$.

Another remarkable feature of the steady state is, that a chiral current of atoms, circulating around the ladder edges, can be detected for a finite cavity field. The corresponding observable takes into account the opposite motion of the atoms on the two legs and is given by

$$J_c = \frac{1}{L-1} \sum_{n=0}^{L-2} (j_{0,n} - j_{1,n}) \, , \text{ with } j_{m,n} = -iJ_\parallel \left(c_{m,j}^\dagger c_{m,j+1} - \text{h.c.} \right) . \qquad (5.40)$$

The coincidence with the occupation photon field is rooted in the recovered cavity-assisted tunneling, which is also responsible for the artificial magnetic field felt by the fermions. Indeed, Fig. 5.10 verifies, that as soon as the cavity mode is occupied a non-vanishing directed current appears. The occurrence of edge currents is is a key signature of topologically non-trivial phases. As a consequence, the considered model promises to be an option for the stable creation of topological phases, as the steady states are stationary in time and exponentially fast approached. Even more, the control over the cavity mode occupation via the pump strength, holds out the prospect for fast dynamical switching between different topological phases, characterized here by a vanishing or finite chiral current. Note that chiral states located at the system boundary, have also been found in the two-dimensional equivalent of this model on a square lattice geometry using the same adiabatic elimination scheme in Ref. [20], which manifests the existence non-trivial bulk topology via the bulk-edge correspondence. This underlines the topological nature of the found chiral states in the ladder set-up.

Let us discuss the chosen fillings separately in more detail. At half-filling we see very clearly the sharp onset of a cavity occupation at the location of the critical pump strength. The two different curves for $n = 1/2$ represent the two possible self-consistent solutions (cf. Fig. 5.6), where the first one corresponds to a chiral liquid with $J_\perp < \sqrt{2}J_\parallel$ with occupations in both quasi-particle bands $E_\pm(k)$ and the second one is a chiral insulator, consisting of states from the E_--band exclusively. The second solution transitions to the asymptotic linear behavior for large pump strengths, mentioned above. The chiral current exhibits a more complex relation. At the critical strength, a jump occurs to a finite negative value, which reduces while increasing $AL/J_\parallel$. For this filling, Fig. 5.10 also includes findings from an exact diagonalization (ED) for a small system of three rungs. In this case, there are six steady states, of which we have chosen the one maximizing the cavity field, which is, at the same time, the state showing the best agreement with the second solution of the adiabatic elimination approach. The other solution, present for intermediate pump strength, could not be recovered by the exact study. We will discuss the nature of the steady states of the other blocks later. Notably, we see a good agreement for the chiral current and the photon field of both methods, strengthening the validity of the assumption made in the adiabatic elimination. The smearing out of the peak can
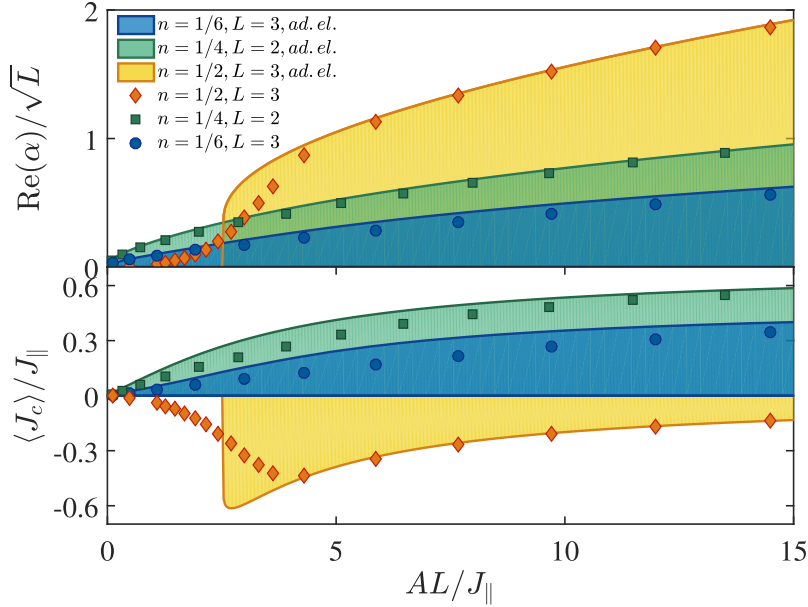
Figure 5.11.: Steady state expectation values of the cavity field (upper panel) and the chiral current (lower panel) for a finite system with $L = 3$ rungs and $N = 3$ atoms for different fillings. (©2016 American Physical Society, published in Ref. [144]).

be caused on the ED side by the smallness of the system, leaving space for a prominent role of quantum fluctuations of atoms and photons. On the other hand, from the adiabatic elimination perspective, these fluctuations might have been underestimated when we assumed the mean field decoupling of photons and atoms. For quarter-filling realizations, the existence of self-consistent solutions for the whole parameter space also results in a finite, smoothly increasing chiral current as soon as the pump is switched on. The system is then always in the state of a chiral insulator. The situation changes at $n = 1/8$, where a critical threshold exists. Furthermore a kink in both observables marks the point where the number of Fermi points changes from two, at low pump strength, to four.

A more direct comparison of both approaches is presented in Fig. 5.11, where the adiabatic elimination calculation is based on the same system size ($L = 3$), which is reachable numerically. We generally can infer that the findings delivered by both methods are consistent with each other. Especially the quarter and eighths filling curves show a good correspondence, whereas the half-filling inaccuracy at the sudden onset might suffer from the respective problems in the treatment of fluctuations. Nevertheless, the quality of the agreement strongly depends on the model parameters and in particular the strength of the dissipation, i.e. the loss rate of the cavity.

In the maximally reachable system for exact diagonalization, containing six sites distributed on two ladder lags, with a atom number of three, we can use the introduced symmetries to split the corresponding Hamiltonian matrix into 6 blocks of sizes $\{(1 \times 1), (3 \times 3), (6 \times 6), (3 \times 3), (6 \times 6), (1 \times 1)\}$, which we will refer to as block 1 to 6. We show the cavity field and the chiral
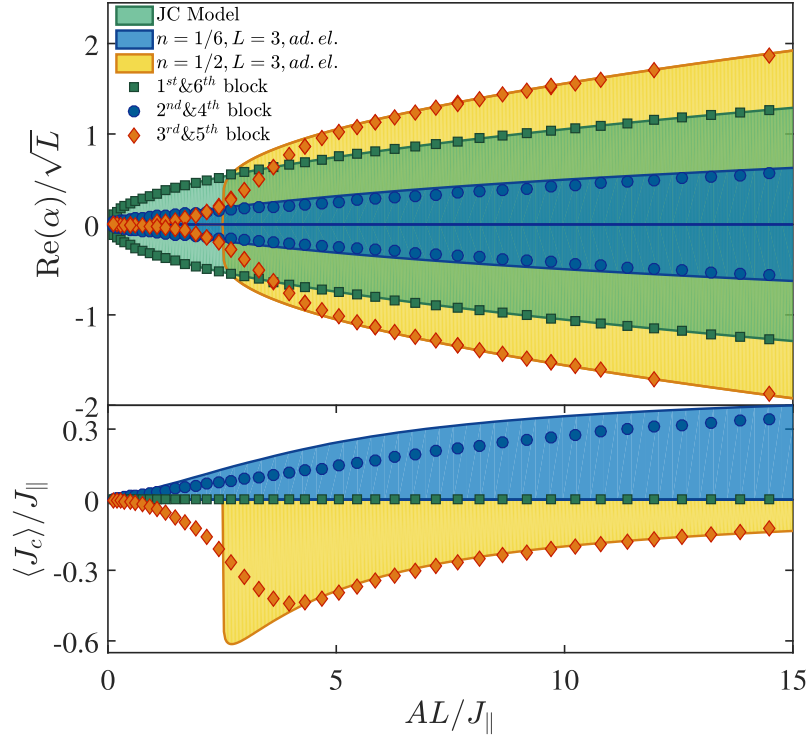
Figure 5.12.: Cavity field and chiral current for the six different blocks in the fermionic section of a system with $L = 3$ and $N = 3$. Adiabatic elimination is compared to exact diagonalization for $\hbar\kappa = 0.05 J_\parallel$ and $\hbar\delta_{cp} = J_\parallel$ (©2016 American Physical Society, published in Ref. [144]).

current for the unique steady states, of blocks where both, $|\ldots\rangle$ and $\langle\ldots|$ of the density matrix to vectorize are placed in the same symmetry sector in Fig. 5.12. The $\mathbb{Z}_2$ symmetry of the photon field expectation value of same-sized blocks, can be addressed to the S_2 symmetry (see Sec. 5.5.1 and Eq. 5.38). This does not affect the motion of the atoms along the legs. The states, which show the best agreement with the adiabatic elimination for the same finite system, subject to the discussed limitations, are located in the two blocks with the extend of six, i.e block 3 and 5. Moreover, block 1 and 6 belong to the fermion configurations where all three particles are found in the same symmetry sector of S_1, which prohibits any further fermion dynamics, resulting in a vanishing chiral current. A closer look reveals, that the model can be directly mapped to the well-known Jaynes Cummings model, describing a single two-level system in a cavity coupled to a cavity mode. In this case, the cavity field dependence on the pump strength exhibits a square root behavior. The two remaining blocks, i.e. block 2 and 4, interestingly match exactly with our simulation results for a single particle on a three rung ladder. This is also confirmed by the comparison with the corresponding adiabatic elimination calculation. The observations made for the cavity field so far, indicate a strong dependence on the coupling between atoms and photons, mediated by the pump strength. Figure 5.13 reveals that starting with an empty cavity at low values of $\hbar\tilde{\Omega}$, the low number states of the cavity mode start to be occupied as the
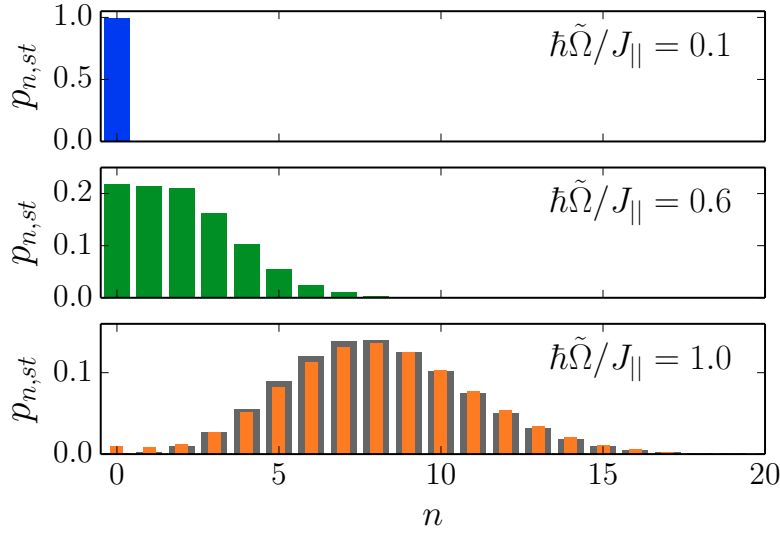
Figure 5.13.: Dependence of the photon number distribution of the steady state on the pump strength. Results are shown for $L = 3$ and half-filling for the block state which agrees with the adiabatic elimination, with parameters $\hbar\kappa = 0.25 J_{\|}$, $\hbar\delta_{cp} = J_{\|}$. The gray bars in the lower panel show a fit to a Possonian distribution. (©2016 American Physical Society, published in Ref. [144]).

coupling is increased. Further increasing $\hbar\tilde{\Omega}$ shifts the mean to larger values and also broadens the width of the arising distribution. As the photon number is limited by the system size, it is hard to extract the exact form of the distribution. For the current instance, neither a Gaussian nor a Poissonian could be rejected in a statistical test [151] with confidence interval of 99%. A practical consequence of this is, that our exact diagonalization method is limited by a certain maximal pump strength, as otherwise the number of necessary photon states would cause too large matrix dimensions.

So far, we restricted our consideration to fairly low values of the photon loss rate. In Fig. 5.14 we present the behavior for differently strong dissipative coupling strengths. As the dissipation strength is included in the definition of the rescaled pump strength A, also the sudden onset of the cavity mode occupation, as well as of the chiral current are shifted to larger values of $\hbar\tilde{\Omega}$ for less perfect cavity mirrors. While the smearing of the peak in the exact diagonalization is small in a low dissipation situation, it is amplified for larger dissipative couplings. Similarly, the peak magnitude of the current is suppressed for strong photon losses in the exact calculation. To support the argument that this is caused by the less accurate approximation made in the mean field decoupling of the photons, we directly measure the decoupled fields $\langle a \rangle_{\mathrm{st}}$ and $\langle a^{\dagger} \rangle_{\mathrm{st}}$ in our ED approach and compare them to the photon number in Fig. 5.15. It becomes clear, that the neglection of fluctuations is only valid for lower values of $\hbar\kappa$ and causes strong deviations otherwise. This discrepancy might be overcome in large systems, which are expected to produce a larger number of photons in the steady state and therefore are less dependent on fluctuations. Nevertheless, the strong dissipation regime for this system size, poses a good example of when
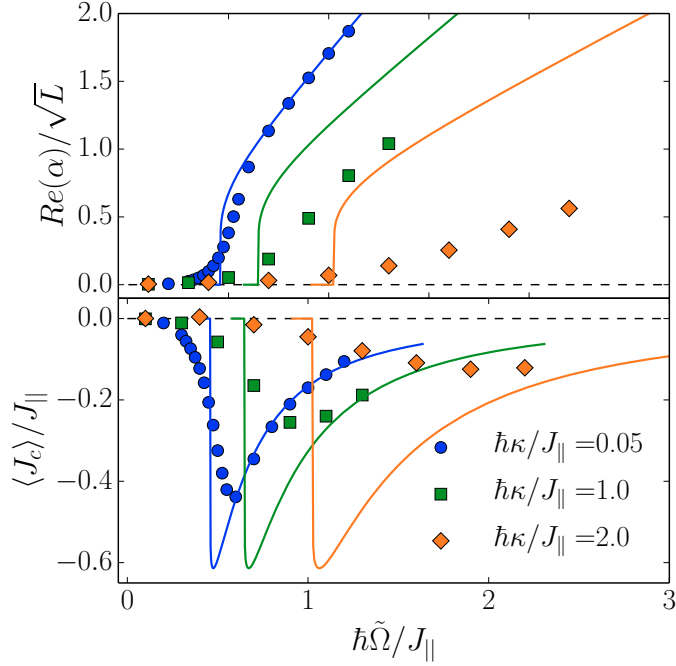
Figure 5.14.: Dissipation dependence of the steady state expectation value for different dissipation strengths. We compare the finite size adiabatic elimination (lines) with the exact diagonalization (markers), for $L = 3$, $N = 3$, and $\hbar\delta_{cp} = J_{\parallel}$ and a bosonic cutoff of $n_{\max}^B = 20$ (©2016 American Physical Society, published in Ref. [144]).

the exact diagonalization method is more suitable to describe steady state properties.

5.6.1. Non-destrucitve measurement scheme for chiral current in the steady state

From an experimental point of view, it is also noteworthy that it is possible to implement a measurement protocol which makes it possible to measure the expectation value of the chiral current in the steady state, without causing a collapse of the system onto the corresponding eigenstates as presented in Ref. [143]. In order to achieve this, a magnetic field gradient is applied in y-direction, yielding an additional linear term to the optical lattice potential, felt by the spin-polarized atoms. Adjacent sites are now separated by an energy off-set of Δ', prohibiting transport along the ladder lags. To restore the hopping, a second cavity mode with doubled frequency ω_c' is introduced. As displayed in the sketch, with the use of a probe laser beam, an inelastic Ra-
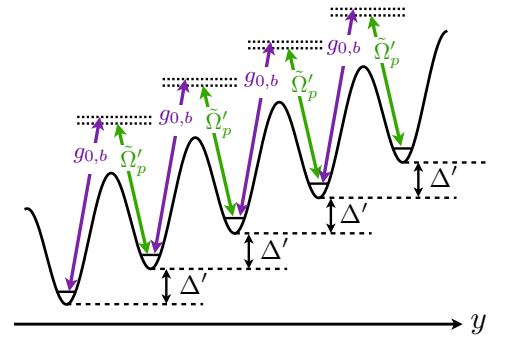
Inelastic Raman scattering of cavity photons and probe beam with Rabi frequencies $g_{0,b}$ and $\tilde{\Omega}_p'$ reenables fermionic hopping.
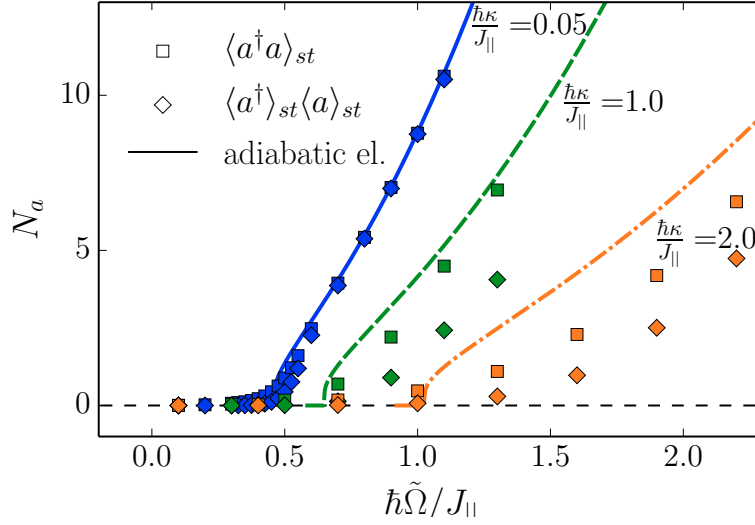
Figure 5.15.: Comparison of finite system adiabatic elimination data with ED results for the total photon number N_a in the cavity and explicitly decoupled photon fields $\langle a^\dagger \rangle \langle a \rangle = |\alpha|^2$ for a system of size $L = 3$, $N = 3$ atoms and $\hbar \delta_{cp}/J_\parallel = 1$ (©2016 American Physical Society, published in Ref. [144]).

man scattering process using probe and cavity photons reenables motion in this direction. The probe beam is passing through the cavity in z-direction, so that there is no net phase transfer and its frequency ω_p' is matching the cavity mode and the potential off-set. The corresponding Hamiltonian reads

$$H_{\text{probe}} = \hbar \delta_{cp}' b^\dagger b + \hbar \tilde{\Omega}' \sum_{j,m=0,1} (-1)^m \left(b^\dagger c_{m,j}^\dagger c_{m,j+1} + \text{h.c.} \right), \qquad (5.41)$$

with the annihilation operator of the new cavity mode b, the shifted cavity frequency $\delta_{cp}' = \omega_c' - \omega_p' + \Delta'/\hbar$ and the Rabi frequency of the probe beam $\tilde{\Omega}'$. The alternating sign takes into account the doubling of frequency of the original cavity mode. Using the definition $K_m = \frac{1}{L-1} \sum_j c_{m,j}^\dagger c_{m,j+1}$ it is possible to express the Hamiltonian in terms of the chiral current operator J_c as

$$\frac{H_{\text{probe}}}{L-1} = \frac{\hbar \tilde{\Omega}'}{2} \left[(b + b^\dagger) \sum_m (-1)^m \left(K_m + K_m^\dagger \right) + i(b - b^\dagger) J_c/J_\parallel \right] + \frac{\hbar \delta_{cp}'}{L-1} b^\dagger b \qquad (5.42)$$

Computing the equations of motion for the cavity mode are following from the Lindblad equation and are given by

$$-i\frac{\mathrm{d}}{\mathrm{d}t}\langle b\rangle = -\frac{(L-1)\tilde{\Omega}'}{2}\left[\sum_m(-1)^m\langle K_m + K_m^\dagger\rangle - i\langle J_c\rangle/J_\parallel\right] - \left(\delta'_{cp} - i\kappa\right)\langle b\rangle \tag{5.43}$$

$$-i\frac{\mathrm{d}}{\mathrm{d}t}\langle b^\dagger\rangle = +\frac{(L-1)\tilde{\Omega}'}{2}\left[\sum_m(-1)^m\langle K_m + K_m^\dagger\rangle + i\langle J_c\rangle/J_\parallel\right] + \left(\delta'_{cp} + i\kappa\right)\langle b^\dagger\rangle \tag{5.44}$$

Both of the left-hand terms vanish for the steady state, such that subtracting the right-hand side and rearranging the terms provides a relation of the chiral current steady state expectation value, which only depends on the quadratures of the new cavity mode

$$\langle J_c\rangle_{\mathrm{st}} = \frac{J_\parallel}{(L-1)\tilde{\Omega}'}\left(i\delta'_{cp}\langle b - b^\dagger\rangle_{\mathrm{st}} + \frac{\kappa'}{2}\langle b + b^\dagger\rangle_{\mathrm{st}}\right). \tag{5.45}$$

In summary, the original y-directional hopping is replaced by cavity assisted tunneling processes introduced with the help of an additional cavity mode and a probe beam. The motion in the steady state in that direction is the result of a self-organization process evoked by the feedback mechanism of cavity mode and leg hopping. It is therefore possible to associate this setting with the original model from Eq. 5.17, where the hopping strength $J_\parallel$ depends on the strength of the cavity assisted tunneling. The chiral current can then be directly measured by observing the leaked cavity photons of the new mode.

5.7. Dissipative attractor dynamics

After the presentation of different steady state characteristics, uncovering interesting properties such as an opportunity to control different topologically non-trivial phases, we will focus in this section on the dynamics originating in the self-organization process caused by the feedback mechanism between the atoms and the cavity field. To do so, we consider the process as a quantum quench initiated by a sudden switch-on of the running-wave pump laser beams. The cavity mode is initially unoccupied and the fermions are prepared as a pure state in one of the symmetry sectors of the Lindbladian containing a unique steady state. For the simulation data obtained from exact diagonalization presented here, we considered a fermionic ladder with $L = 3$ rungs and $N = 3$ particles. Using the eigenstates (Eq. 5.37) of the S_1 symmetry, the initial fermion configuration is chosen to be

$$|\psi(t = 0)\rangle_{\mathrm{fermion}} = \gamma_{\tilde{n}=0}^\dagger\gamma_{\tilde{n}=2}^\dagger\gamma_{\tilde{n}=4}^\dagger|0\rangle. \tag{5.46}$$

This state is placed in one of the (6×6)-blocks introduced in the previous section, where the steady state corresponds to the solution with the best agreement to the adiabatic elimination of a system of same size. As a consequence, it is sufficient to calculate the spectrum of the corresponding block to access the full open system dynamics. As an example we present the evolution of the chiral current in Fig. 5.16, outlining the approach of the stationary regime,
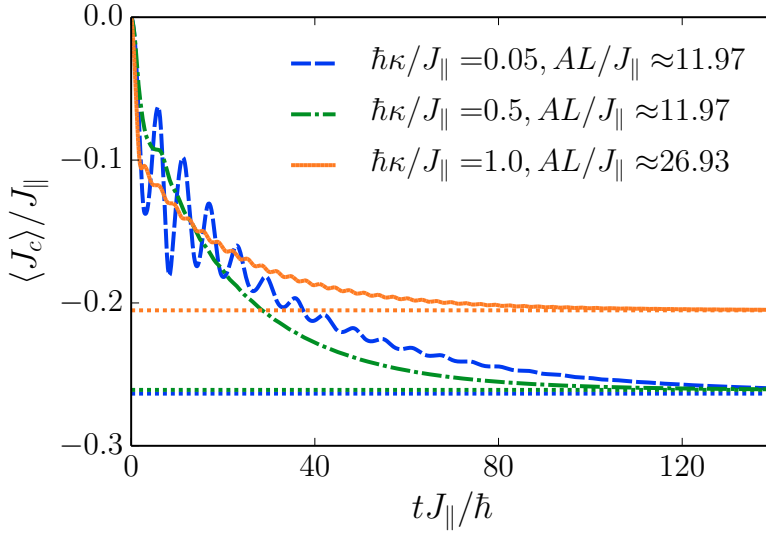
Figure 5.16.: Full time evolution of the chiral current for different parameter combinations obtain by exact diagonalization of a ladder with $L = 3$ rungs and three fermions. Initial state is a pure state placed in one of the symmetry blocks and the steady state approach strongly depends on the dissipative coupling (©2016 American Physical Society, published in Ref. [144]).

which can be regarded as an attractor, as all states in this block eventually converge to the steady state. As found by the adiabatic elimination, the steady state expectation values only depend on the scaled pump strength $AL/J_\parallel$. This is also confirmed here, whereas a small deviation is caused due to the dissipation dependence of the steady state diagram as shown for example in Fig. 5.14. Nevertheless, even if the same steady state configuration is reached, the attractor dynamics is very distinct. While the evolution with $\hbar\kappa/J_\parallel = 0.05$ is quite long dominated by oscillations, which are caused by the unitary Hamiltonian dynamics, this oscillating behavior is damped out quite fast for a stronger coupling, i.e. $\hbar\kappa/J_\parallel = 0.5$.

To investigate the dependence on the loss rate further we show the absolute value of the difference of the time-dependent current and the steady state value in Fig. 5.17 in a logarithmic plot. After a short initial period, an exponentially fast dynamics towards the stationary regime stands out clearly. Fitting exponential functions to the corresponding region, enables us to extract the time scales τ controlling the strength of the exponential scaling which appear as the inverse of the slope of the exponent as the overall behavior is proportional to $e^{-t/\tau}$. Interestingly we see a non-monotonic dependence of the time scales on the dissipation strength. Intuitively, one could expect, that the steady state is reached faster for stronger dissipations, because other contributions, as for example from the unitary motion are damped out faster. This can be read-off by comparing $\hbar\kappa/J_\parallel = 0.25$ and $\hbar\kappa/J_\parallel = 3$ in the plot, which show a faster decay for the larger photon loss-rate. However, increasing the dissipation even further slows down the dynamics again. The dependence over a larger dissipation range is plotted in Fig. 5.18. Here we show both the time scale of the exponential approach of the chiral cur-
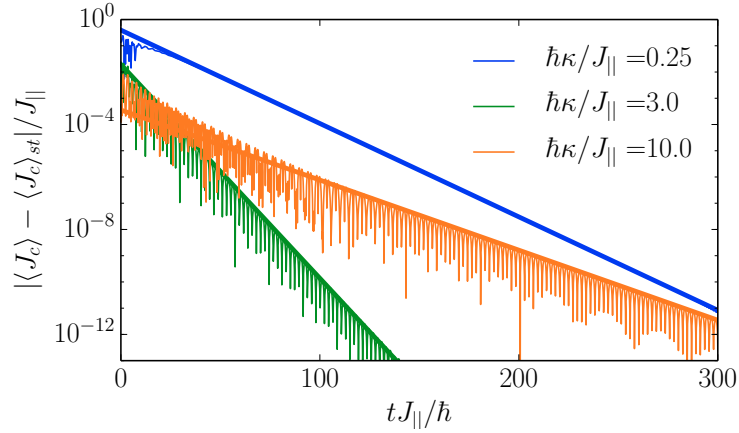
Figure 5.17.: Exponential approach of the steady state of the chiral current for different loss rates and $\hbar\Omega/J_\parallel = 0.8$, $\hbar\delta_{cp}/J_\parallel = 1$, $L = 3$ and $N = 3$. Straight lines are exponential fits providing access to the time scale. (©2016 American Physical Society, published in Ref. [144]).
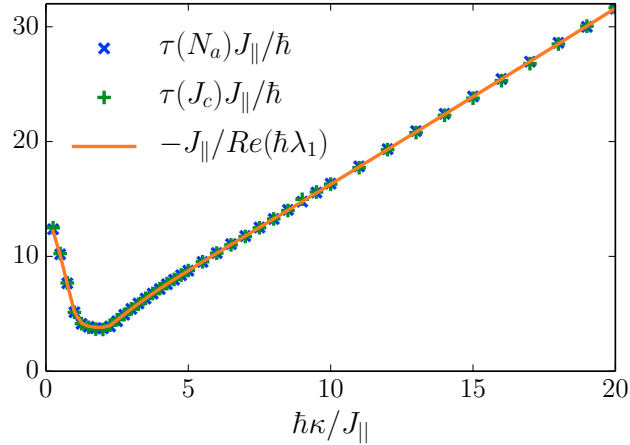
Figure 5.18.: Dissipation dependence on the exponential time scale in the attractor dynamics for the chiral current J_c and the cavity mode occupation N_a compared to the inverse of the $M_\mathcal{L}$ eigenvalue with the lowest absolute real part. The remaining parameters are $\hbar\Omega/J_\parallel = 0.8$, $\hbar\delta_{cp}/J_\parallel = 1$, $L = 3$ and $N = 3$. (©2016 American Physical Society, published in Ref. [144]).

rent (green crosses), representing the motion of the atoms, and the time scales obtained from the convergence to steady state value of the total number of photons in the cavity, $N_a = \langle a^\dagger a \rangle$ (blue crosses). Notably, we see a very good agreement for the time scales of atoms and photons. That puts in question the assumption used in the adiabatic elimination, where we assumed the dynamics of the cavity happening on much shorter time scales as the atom part of the system, which underlines the importance of the numerical verification. Another important finding, pre-

Figure 5.19.: (a) Time evolution of the chiral current for the considering all eigenstates (blue line), only the six eigenstates of the lowest absolute value real part eigenvalues (including the steady state) and the steady state expectation value. 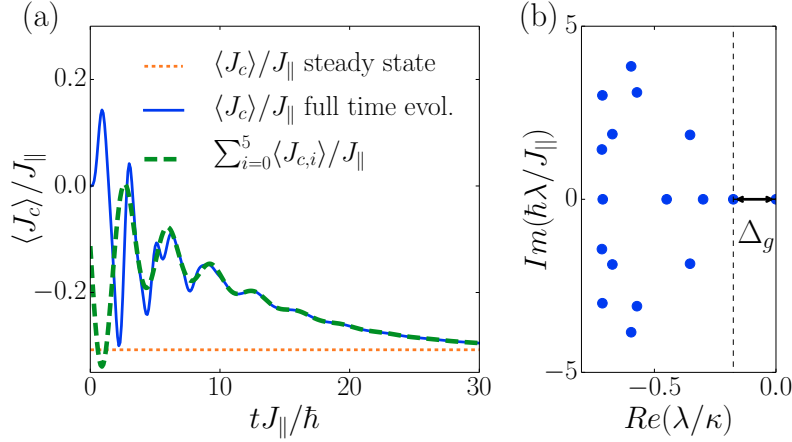(b) Part of the Lindbladian spectrum close to the steady state. Δ_g denotes the dissipative spectral gap. Model parameters were chosen as $L = 3$, $N = 3$, $\hbar\delta_{cp}/J_\parallel = 1$, $\hbar\kappa/J_\parallel = 5$ and $\hbar\tilde{\Omega}/J_\parallel = 0.8$. (©2016 American Physical Society, published in Ref. [144]).

sented in Fig. 5.18, is the matching of the time scales with the inverse of the dissipative gap, given by the real part of the eigenvalue λ_1 of the block of the Lindblad matrix, which has the lowest non-vanishing absolute real part. During the time-evolution, the states of these eigenvalues experience the lowest exponential suppression, and therefore are the non-steady states which survive the longest resulting in a dominant contribution in the long-term dynamics. This quantity is often referred to as the dissipative spectral gap $\Delta_g \equiv -J_\parallel/Re(\hbar\lambda_1)$, and is also annotated in the spectrum presented in Fig. 5.19 (b). To underline this connection, we illustrate in Fig. 5.19(a), that in the long-time limit only very few eigenstates contribute significantly to the evolution. Namely, we compare the dynamics using the full set of eigenstates to a limited consideration by restricting the evolution of the initial state to the space of vectorized density matrices spanned by the eigenstates corresponding to eigenvalues with the lowest absolute values of the real part. It turns out, that by only taking into account the first six states according to this order, the time dependence of the current can be represented by these states almost exactly, such that the discrepancy to the full evolution vanishes for late times, here $t \gtrsim 10\hbar/J_\parallel$. Taking a look at the excerpt of the Lindbladian spectrum for this set-up in Fig. 5.19 (b) shows, that the first six eigenvalues are separated by a small gap along the real axis from the rest of the spectrum, making this selection particularly appropriate.

Turning back to the discussion of Fig. 5.18, an interesting fact can be deduced: Instead of a decrease of the time scale while successively increasing the dissipation strength, a minimum exists at intermediate dissipation strength, after which the time scale counter-intuitively increases again. This can be explained by the quantum Zeno effect [152], where strong dissipation causes a frequent application of jump operators which resembles a continuous measurement process,
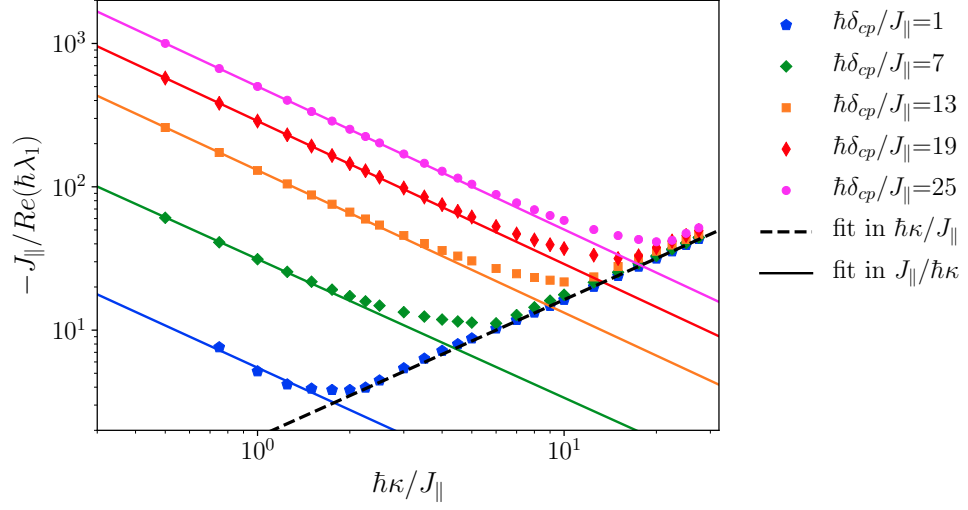
Figure 5.20.: We show ED results for the lowest absolute real part eigenvalue of the Lindbladian spectrum, corresponding to the time scale at long times for different rotating cavity frequencies δ_{cp} and find a $1/\kappa$ behavior for weak and a linear scaling in κ for strong dissipation. Further parameters are $L = 3$, $N = 3$ and $\hbar\Omega = 0.8J_\parallel$.

preventing the open system from evolving [6]. Quantitatively, the behavior in the two regimes, i.e. small and strong dissipation, is displayed in Fig. 5.20. For small dissipative couplings, the spectral gap decreases as $1/\kappa$. If increasing the loss rate, depending on the rotated cavity frequency δ_{cp}, a minimum is reached after which the Zeno limit is reached and the gap increases linearly in κ.

It is possible to isolate these two limiting regimes even for the reduced system of just a single rung, which is then effectively described by the Jaynes-Cummings model including photon loss

$$H_{\mathrm{JC}} = \hbar\delta_{cp}a^\dagger a - \hbar\tilde{\Omega}\left(a + a^\dagger\right)\left(c_0^\dagger c_1 + c_1^\dagger c_0\right),$$

$$\frac{\mathrm{d}}{\mathrm{d}t}\rho = -\frac{i}{\hbar}\left[H_{\mathrm{JC}}, \rho\right] + \kappa\left(2a\rho a^\dagger - a^\dagger a\rho - \rho a^\dagger a\right). \tag{5.47}$$

The fermionic part can be diagonalized with the two unique eigenvalues ± 1 and the corresponding eigenstates $|\pm\rangle$. As different fermionic eigenstates do not mix, the Lindblad matrix $M_\mathcal{L}$ can be block-diagonalized in four blocks. Restricting the photon number to $n^B \in \{0, 1\}$, allows the rigorous analytic calculation for the steady state and the spectral gap. The steady state is degenerate and is decomposed of the vacuum state of the cavity and a concentration of the fermions in one of the two eigensectors, i.e. $\rho_{st} = [|0\rangle_{\text{cavity}} \otimes |\pm\rangle][\langle 0|_{\text{cavity}}\langle\pm|]$. We can also access the spectral gap, which is for $\delta_{cp} = 0$ given by

$$\Delta_g = \frac{\kappa}{2}\left[-1 + \sqrt{1 - \left(\frac{4\Omega}{\kappa}\right)^2}\right]. \tag{5.48}$$

In the limit of low dissipation this scales with $1/\kappa$ and is for strong dissipation linear in κ. This coincides well with the results from Fig. 5.20. For finite shifted cavity frequency δ_{cp}, the expression for the gap is more complicated but still yields the same limiting behavior. It is left to mention, that the value of the dissipation strength corresponding to the minimal time scale, depends on the cavity frequency. That is, the region, where an inverse scaling in κ is observed, increases for larger cavity frequencies δ_{cp}. After passing the minimum, the time scales collapse to one linear curve representing the Zeno regime. As a result, a tuning of the cavity frequency, allows to influence the length of the time needed to reach the self-organized steady state.

5.8. Summary of the results of Chap. 5

We reported results on the Markovian open system dynamics of fermionic atoms subjected to a ladder potential, where the quantum tunneling along the rungs is coupled by two-photon Raman scattering to the single-mode of a lossy optical resonator as well as to two running-wave pump lasers. The steady states of the dissipative dynamics, have been found to display signatures of topologically non-trivial phases once a critical strength of the pump laser is passed. More precisely, for a strong enough pump strength, the initially empty cavity mode is populated and a finite atomic chiral current cycling around the ladder edge is detected for the stationary regime. We compared results obtained by the adiabatic elimination of the mean field of the cavity-field, including the approximation of a decoupling from the fermionic degrees of freedom with numerical exact results for small systems. The latter is possible due to the exploitation of Hamiltonian symmetries, which can be used to block-diagonalize the corresponding Lindbladian. Provided with numerical exact states, this enabled us to determine the region of validity of the approximative analytics. A study on the parameter dependence of the current and the photon field shows that the accuracy of the mean field decoupling is tied to small dissipation strengths. Furthermore, we describe the outline of a non-destructive procedure to measure the steady state expectation value of the chiral current.

Moreover, we investigated the non-equilibrium dynamics towards the steady state, where we have found that similar steady state expectation values can have very different attractor dynamics, mainly influenced by the strength of the dissipative coupling. The extraction of the time scales of the exponential approach for photonic and atomic quantities, revealed a non-linear behavior in the dissipation strength. Namely, starting from the small dissipation limit, increasing the photon loss rate accelerates the dynamics and the time scale shows an inverse behavior with the dissipation strength. Increasing the loss rate further shows, the time scale dependence on the dissipation strength saturates and then displays a linear relation, which can be addressed to the Zeno effect, where the action of the environment can be seen as a continuous measurement, preventing the quantum evolution by projections on the eigenstates of the Lindblad operators. The two limits can be motivated by analytic exact calculations for a system with only one rung of the fermionic ladder lattice, which reduces to the open Jaynes-Cummings model.

<div align="right">

Chapter 6

</div>

Dynamics of spin correlations and aging in open XXZ-chains

6.1. Introduction

In this chapter we study the non-equilibrium propagation of correlations in interacting many-body quantum systems. The chapter builds upon the work published in [153]. In this context, two-time correlation functions $\langle B(t_2)A(t_1)\rangle$ constitute a powerful tool to understand the open system evolution. In equilibrium this correlation is closely related to a number of experimental methods for extracting spectral properties, utilizing the time-translational invariance in Hamiltonian systems, stating that the exact times t_1 and t_2 are irrelevant but only the time difference $t_2 - t_1$ is important which can be associated with a single frequency accordingly. Examples include Angular Resolved Photon Emission Spectroscopy (ARPES) setups [154], which enable the momentum-resolved measurement of the electronic structure of condensed matter materials, neutron scattering experiments [155] where the magnetic interaction of the charge-free neutrons with material samples gives access to the spin structure, or spectroscopy using Raman or Bragg scattering [156]. When adding dissipation to the consideration, time-translation invariance is not longer guaranteed. In this situation, probing the system at different times allows to draw conclusions about the dynamical evolution, which is a generally hard task for open quantum systems so that there are many open research questions. Theoretical work has been done considering measurements of operator applications at equal time, as for example the spreading of density correlations in a dissipative Bose-Hubbard model [157] or the relaxation dynamics in Ising chains [158]. In contrast, two-time correlators have mainly been evaluated using approximative techniques [96, 159]. In this chapter we will help to fill the gap by presenting quasi-exact tMPS simulation results for two-time correlation functions for a system combining large spatial extend, interactions and dissipation. This enables us to identify an emergent aging regime, a phenomenon known for example from relaxation dynamics in glasses [160]. Moreover, we will show, that the long-time dependence can be understood in terms of an effective diffusive evolution.

We investigate an open spin chain, where each spin is coupled to an environment via dephasing noise. The latter is occurring in various different situations across different communities in

physics. In condensed matter setups, dephasing can emerge from fluctuation noise of external magnetic fields, observed for instance in superconducting flux qubits [161]. In a cold atom context, interacting atoms in optical lattices, can scatter inelastically with the lattice laser, leading to an effective dephasing with local density operators as jump operators [162]. In addition, a possible implementation of spin chains with ultracold atoms in optical lattices providing tunable dissipation and interaction strengths have been proposed [163]. Furthermore, recent theoretical studies, focusing on the interplay of interaction and dephasing dissipation, have uncovered interesting features like a suppression of decoherence in the presence of strong interactions [99] or dephasing-enhanced transport [164]. Related studies for the spin-chain with dephasing noise focus on equal-time correlations [165] or the two-time correlations with this special case of $t_1 = 0$ [100].

We choose for this chapter to use the tMPS time evolution of the purified density matrix exploiting the conservation of the total magnetization, covered in detailed for the specific model in Sec. 4.2.4. The low local physical dimension d being two, containing only the two distinct spin orientations per site, results in a comparably low numerical effort during the application of four-site bond gates, where the bond dimension increase scales with up to d^4. Also, the limitation by system size is quite low, enabling us to observe interesting dynamics for up to $L = 80$ spins. Resources for simulations of this kind require a typical runtime of the order of ten hours on machines with 2.6 GHz CPUs and less then 10 GB of RAM, so that the computations are within reach using HPC clusters. Building on the convergence analysis presented in Sec. 4.2.4, if not stated otherwise, we use systems of size $L = 80$, a Suzuki-Trotter time step of $\Delta t J_x/\hbar = 0.025$ and a truncation goal of $\epsilon_{\text{trunc}} = 10^{-12}$, while allowing a maximal bond dimension of $D = 500$.

The chapter begins with a description of the features of the closed system with an emphasis on the three distinct phases of the XXZ model and the corresponding properties in Sec. 6.2. Subsequent to the introduction of the dissipative model in Sec. 6.3, we report on the spreading of equal-time spin correlations and the diffusive nature of the underlying processes in Sec. 6.4. Building on this, we turn to the investigation of two-time correlations in Sec. 6.5 and distinguish three dynamic regimes, most notably a time regime displaying aging for long times.

6.2. Equilibrium properties of spin chains

In the later study of non-equilibrium dynamics of the XXZ model, the Hamiltonian properties are found to play a crucial role for the evolution in different time regimes. For this reason, we continue here by giving a short overview of the equilibrium properties of interacting spin-½ chains and the corresponding model for a closed quantum system. For this purpose we follow in parts the review of [166].

The Hamiltonian for the XXZ-model under consideration describes a one-dimensional equally spaced arrangement of interacting spins with $S = \text{½}$, which reads as

$$H_{XXZ} = \sum_{j=1}^{L-1} \left[J_x \left(S_j^x S_{j+1}^x + S_j^y S_{j+1}^y \right) + J_z S_j^z S_{j+1}^z \right], \tag{6.1}$$

including equal interaction strengths J_x for the exchange couplings of neighboring spins along

the x- and y-spin-direction and a different strength J_z for the z-direction correspondingly. Here $S^\alpha = \hbar/2\sigma^\alpha$ are the spin-½ operators along the directions $\alpha \in \{x, y, z\}$ and σ^α the Pauli matrices.

The XXZ-model is solvable by Bethe-Ansatz hence its ground state properties are analytically accessible. In the following we summarize several key aspects. Depending on the anisotropy J_z/J_x, marking the deviation from the totally rotation invariant Heisenberg model, the model exhibits three distinct phases, depicted in the following diagram.
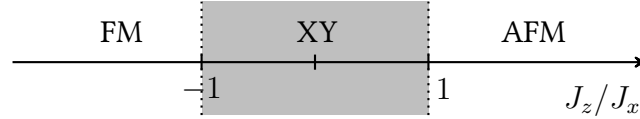
Namely, there is a ferromagnetic phase for $J_z/J_x < -1$, an antiferromagnetic phase for $J_z/J_x > 1$ and an intermediate phase exhibiting a gapless Luttinger liquid, also known as XY-phase, for $-1 \leq J_z/J_x \leq 1$. In the ferromagnetic phase, where the parallel alignment of neighboring spins is energetically favored by the J_z term, the ground state is represented by either all spins pointing up or down, resulting in a ground state magnetization in the z-direction of $\langle S^z \rangle_{gs} = \pm N/2$. The collective low-energy excitations, known as magnons, show a dispersion relation of $\epsilon(k) = J_x[1 - \cos(k) - (J_z/J_x + 1)]$ [166], yielding an approximately quadratic dispersion for small momenta on top of an excitation gap of $|J_z/J_x| - 1$ at zero momentum. When approaching $J_z/J_x = -1$, the rotation symmetry is restored and the originally gapped excitations become gapless for this anisotropy, as also required by the Goldstone theorem [167]. It is worth mentioning, that the same excitation gap of $|J_z/J_x| - 1$ applies to a state where the system is split into half, forming two ferromagnetic regions with opposite magnetization[168]. This state is also used in the course of the work presented in this chapter. In contrast to this, the low energy properties of the antiferromagnetic phase rely on the fact that antiparallel spin orientation is energetically preferred. For a finite-size system, the ground state is dominated by the mixing of the two possible configurations of alternating spin orientation. However, as the sublattice magnetization, which only takes into account the subset of either even or odd sites, is not conserved by the Hamiltonian evolution, there are contributions caused by quantum fluctuations to the ground state. For sufficiently strong but finite anisotropy $J_z/J_x \gg 1$, the excitations can be perturbatively understood by creating domain walls, which separate regions of alternating spins by bonds with equally aligned spins. By flipping a spin of the ground state, two domain walls arise, which can propagate in the course of the Hamiltonian time evolution through the system resulting in a continuum in the energy spectrum. The dispersion relation for excitations in the antiferromagnetic case is linear $\epsilon(k) \sim k$ on top of a gap opening at $J_z/J_x > 1$. The remaining phase to discuss is the XY-phase, where the absolute value of the anisotropy is smaller than one. While rigorous results can be obtained using Bethe Ansatz theory, the representation as free spinless fermions, known as Jordan-Wigner transformation and a perturbative inclusion of weak nearest neighbor interactions can give some additional intuition [169]. In this picture, the ground state of the free model ($J_z = 0$) is a Fermi sea, where, for large enough systems, excitation energies of particle-hole type excitations are arbitrarily

small, so that the spectrum is gapless. This property also survives when including finite but small S^z-coupling $|J_z/J_x| \ll 1$.

6.3. Spin-½ systems with local Markovian dephasing noise

Figure 6.1.: Dissipative coupling of a spin chain to an environment.

The scope of the work presented in this chapter, is to gain new insights into the dynamics of many-body quantum systems in the presence of both, interactions and dissipation. To this end, we consider XXZ-chains in contact with a Markovian environment causing local dephasing, i.e. the loss of phase coherence (see Fig. 6.1). The full quantum dynamics is described by the Lindblad equation introduced already in Eq. 4.15, which we repeat here for better readability

$$\frac{\partial}{\partial t}\rho(t) = \mathcal{L}_{XXZ} \cdot \rho(t) = -\frac{i}{\hbar}\left[H_{XXZ}, \rho(t)\right] + \gamma \mathcal{D}\left[\rho(t)\right], \tag{6.2}$$

$$\text{with } \mathcal{D}\left[\rho(t)\right] = \sum_{j=1}^{L}\left(S_j^z \rho(t) S_j^z - \frac{1}{4}\rho(t)\right).$$

Here the unitary part of the dynamics is generated by the Hamiltonian from Eq. 6.1, while the dissipation is represented by the set of all local S^z operators included as jump operators in the dissipator $\mathcal{D}[\rho]$. This process can be understood as a dephasing noise felt by the spins. The action of the dephasing is assumed to be independent of the position, so that all jump operators share the same dissipation strength γ. The steady state of this model, approached regardless of the initial state for infinite times, is unique and given by

$$\rho_{\text{steady}} = \frac{1}{2^L}\sum_{\sigma_1...\sigma_L}|\sigma_1 \ldots \sigma_L\rangle\langle\sigma_1 \ldots \sigma_L|, \tag{6.3}$$

also know as the state at infinite temperature $T \to \infty$, of the thermal density operator $\rho(T) = \exp(-\hat{H}/T)/Z(1/T)$.

Our main method of choice is are numerically exact tMPS simulations of the purified density matrix. However, to complement our numeric study, we work out solutions valid at long times using many-body adiabatic elimination, introduced in section 3.3. To this end, we first identify the dissipation-free subspace of the dissipator of Eq. 6.2 as the density matrices corresponding to the many-body basis states formed from the possible S^z-eigenstates of the single spins, i.e.

$$\Lambda^0 = \{\rho|\mathcal{D}(\rho) = 0\} = \text{span}\left\{|\vec{\sigma}\rangle\langle\vec{\sigma}|\right\}, \tag{6.4}$$
$$\text{where } \vec{\sigma} = (\sigma_1, \sigma_2, \ldots, \sigma_L) \text{ and } \sigma_i \in \{\uparrow, \downarrow\}.$$

We will only consider initial states which are located in the symmetry sector of $\langle S_{\text{tot}}^z\rangle = 0$. As the Lindbladian $\mathcal{L}_{XXZ}$ from Eq. 6.2 conserves the total magnetization, there is the additional

constraint requiring the considered basis states to have an equal number of sites with spins pointing up and down for being represented in Λ^0. As a consequence of the definition of Λ_0, we can decompose the Lindbladian as explained in section 3.3 into $\mathcal{L}_{XXZ} = \mathcal{L}_0 + \mathcal{L}_{\mathcal{V}}$, which is in this case

$$\mathcal{L}_0 = -\frac{i}{\hbar} J_z \sum_{i=1}^{L-1} \left[S_i^z S_{i+1}^z, \cdot \right] + \mathcal{D}(\cdot) \tag{6.5}$$

$$\mathcal{L}_{\mathcal{V}} = -\frac{i}{\hbar} J_x \sum_{i=1}^{L-1} \left[\left(S_i^+ S_{i+1}^- + S_i^- S_{i+1}^+ \right), \cdot \right]. \tag{6.6}$$

For times which are much larger than the time scale given by the inverse dissipation strength, the dynamics is dominated by density matrices from the region in the vicinity of Λ^0. Using the adiabatic elimination approximation (Eq. 3.54) and the fact that $\mathcal{L}_0 |\vec{\sigma}\rangle\langle\vec{\sigma}| = 0$, the effective dynamics for the amplitudes of a general state in Λ^0, i.e. $\rho = \sum_{\vec{\sigma}} \rho^0(\vec{\sigma}, t)|\vec{\sigma}\rangle\langle\vec{\sigma}|$, is given by

$$\frac{\mathrm{d}}{\mathrm{d}t}\rho^0(\vec{\sigma}, t) \approx - \sum_{\vec{\sigma}', \vec{\sigma}'', \alpha \neq 0} \frac{1}{\lambda_{\alpha, \vec{\sigma}'}} \mathcal{V}_{\vec{\sigma}, \vec{\sigma}'}^{0\alpha} \mathcal{V}_{\vec{\sigma}', \vec{\sigma}''}^{\alpha, 0} \rho^0(\vec{\sigma}'', t), \tag{6.7}$$

were the appearing elements were introduced in Sec. 3.3. We refer to the appendix A.2 for a detailed calculation, leading to

$$\frac{\mathrm{d}}{\mathrm{d}t}\rho^0(\vec{\sigma}, t) = \sum_{j=1}^{L-1} \frac{J_x^2 \gamma}{2\left[(J_z \alpha_j)^2 + (\hbar\gamma)^2 \right]} \delta_{\sigma_j, \bar{\sigma}_{j+1}} \left(\rho^0(\vec{\sigma}_j, t) - \rho^0(\vec{\sigma}, t) \right) \tag{6.8}$$

with $\vec{\sigma} = (\sigma_1, \ldots, \sigma_j, \sigma_{j+1}, \ldots, \sigma_L)$ and $\vec{\sigma}_j = (\sigma_1, \ldots, \sigma_{j+1}, \sigma_j, \ldots, \sigma_L)$,

where we define $\bar{\sigma} = -\sigma$ and $\alpha_j \equiv -2(\sigma_{j-1}\sigma_j + \sigma_{j+1}\sigma_{j+2})$. Intuitively, this equations represents a transition out of the dissipation free subspace by flipping a pair of antiparallel aligned neighboring spins in either $|\vec{\sigma}\rangle$ or $\langle\vec{\sigma}|$ followed by a transition back to Λ_0 by flipping the same pair in either the same or the other part of $|\vec{\sigma}\rangle\langle\vec{\sigma}|$. One example of this is sketched in Fig. 6.2. The form of Eq. 6.8 resembles a classical master equation. From this point on, there are two possible routes to follow:

- Applying kinetic Monte Carlo algorithms for Eq. 6.8.
- Striving for more analytical insights by introducing additional approximations.

We consider both approaches later.

Interestingly, the evolution of the system's density matrix under Eq. 6.2 is equivalent to an average of wave function trajectories obtained by a stochastic
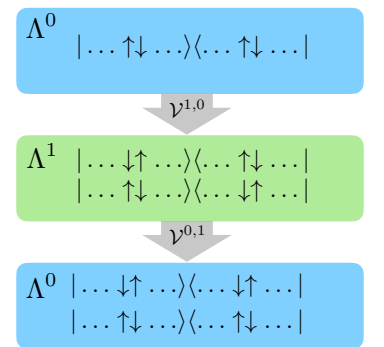

Figure 6.2.: Effective evolution in Λ^0.

Hamiltonian, which adds a random time-dependent magnetic field to H_{XXZ}

$$H_{\text{stoch.}} = H_{XXZ} + \sum_{j=1}^{L} \xi_j(t) S_j^z. \tag{6.9}$$

For this to hold, the random field needs to fulfill the properties of white noise, which is scaled with the dissipation strength, i.e. $\langle\!\langle \xi_i(t)\xi_j(t') \rangle\!\rangle = \gamma \delta_{i,j} \delta(t - t')$ and $\langle\!\langle \xi_i(t) \rangle\!\rangle = 0$. Nevertheless, from a simulation point of view it is in the application case discussed in the following more advantageous to work with the purified density matrix, as it is still computationally possible to reach sufficient large systems and does not require a sampling over many different realizations which are subject to site-dependent random fields.

6.4. Equal-time correlations of open spin chains

To begin with the presentation of our results on the open spin-½ XXZ-chain dynamics, we focus first on equal-time correlation functions consisting of local operators, which are applied at the same time. This type of observable will prove to show interesting dynamics, as will be presented in this chapter. The measurement time is referred to by t_1, to comply with the notation of the two-time correlation functions introduced in section 6.5. Moreover, understanding the temporal behavior of the equal-time correlation functions is essential for the multi-time correlators, as they represent the initial condition for the effective dynamics. The structure of the section is arranged such, that we first concentrate on tMPS simulation results for the open system evolution of an equal-time correlator which can be associated with the coherence, reflecting the effect of the interplay of interactions and dissipation on the system. Thereafter, the focus is put on the local correlation functions consisting of operators, which do note couple different dissipative subspace Λ^i, where the dynamics leads to a diffusive spreading of the correlations in space. We complement quasi-exact tMPS results, with the evolution obtained from adiabatic elimination and kinetic Monte-Carlo methods.

A way to quantify the time-dependence of the coherence for the dissipative model from Eq. 6.2, is to evaluate the $|\langle S_{L/2}^+ S_{L/2+1}^- \rangle|$ correlations, as was also found in a related study in Ref. [165]. For the initial state we choose the Neel state $\rho(t = 0) = |\psi_{\text{Neel}}\rangle\langle\psi_{\text{Neel}}|$, describing a chain of spins prepared with alternating spin orientation (cf. Eq. 4.19). We will discuss different choices for the initial state and their effect on the dynamics more thoroughly later. Figure 6.3 shows the time evolution of the correlation function, as computed by the tMPS algorithm for the purified density matrix. This displays the interesting result that the long-time behavior of the decoherence follows an algebraic decay, as also has been stated in [165]. This can be considered slow, compared to the commonly observed exponential decoherence decay in gapped equilibrium interacting many-body systems as well as in many dissipatively damped models. As a consequence, the inclusion of dissipative effects and nearest-neighbor spin interactions here leads to a longer conservation of coherence. Another notable property is the universal long-time scaling for different parameter choices, which only influence the time evolution at short times. This early regime is sustained longer for stronger anti-ferromagnetic couplings which is due to the more costly process of breaking up the energetically favored anti-parallel
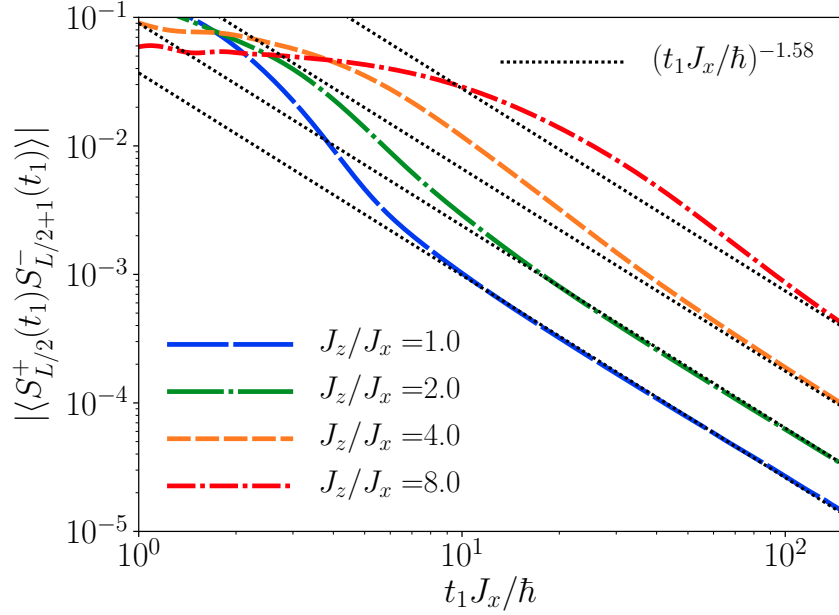
Figure 6.3.: Equal-time correlation function of S^+ and S^- at the system center for different z-directional couplings and $\hbar\gamma/J_x = 2.0$. The long-time scaling agrees with the exponent of approximately 1.58, as found in [165]. Convergence parameters were here $D = 500$ for the bond dimension and a Suzuki-Trotter time step of $\Delta t J_x/\hbar = 0.025$ for a system of size $L = 80$.

spin orientation of the Néel state.

As a next step, we focus on the equal-time correlation function of the spin operators along the z-direction, already introduced in Eq. 4.18 as $C_d(t_1, t_1)$, for several distances. This differs fundamentally from the $\langle S^+_{L/2} S^-_{L/2+1}\rangle$ correlations in the sense that the states of the dissipation-free subspace are eigenstates of the site-dependent S^z_j operators. We show the full dissipative time evolution, obtained by tMPS for the purified density matrix in Fig. 6.4 with $\rho(0) = |\psi_{\text{Neel}}\rangle\langle\psi_{\text{Neel}}|$ as initial state. As indicated by the fit (dotted line) the long-term behavior is governed by an algebraic decay with an exponent of -½ reached eventually by all correlation functions irregardless of the distance. This already hints towards a diffusive nature of the dynamics. This is also supported by the propagation of the S^z correlation as plotted in Fig. 6.5. The spreading of the correlation in time depends on the square of the spatial distance d — a behavior expected for diffusive dynamics.

To add some analytical insight, we apply the adiabatic elimination technique to the correlator. To do so, Eq. 6.8 can be used to derive a dynamical differential equation for the equal-time correlator

$$\frac{\mathrm{d}}{\mathrm{d}t} C_d(t,t) = \frac{\mathrm{d}}{\mathrm{d}t}\langle S^z_n S^z_{n+d}\rangle(t) = \sum_{\vec{\sigma},\vec{\sigma}} \langle\vec{\sigma}'| \left(S^z_n S^z_{n+d} \frac{\mathrm{d}\rho^0(\vec{\sigma},t)}{\mathrm{d}t} |\vec{\sigma}\rangle\langle\vec{\sigma}| \right) |\vec{\sigma}'\rangle. \tag{6.10}$$
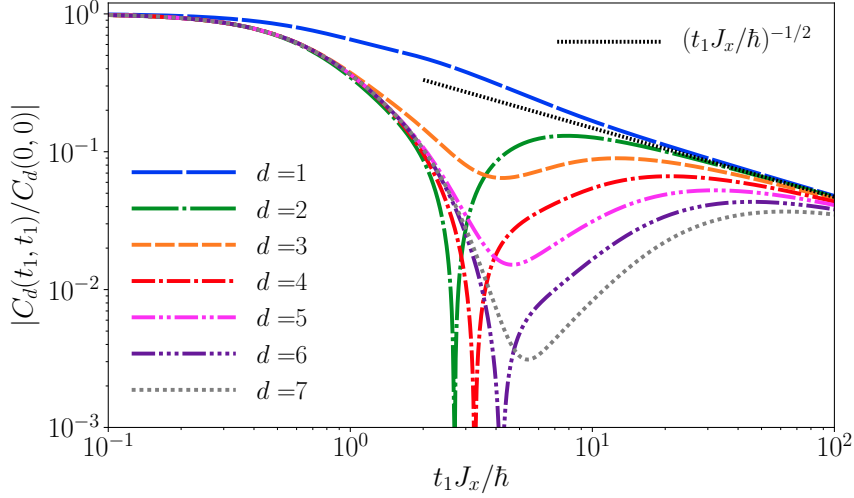
Figure 6.4.: Normalized equal-time correlations $C_d(t_1, t_1)$ for spins which are located at a distance of d sites from each other with $\hbar\gamma/J_x = 2.0$ and $J_z/J_x = 2.0$. For all distances, the long-time dynamics eventually approaches a power law with the exponent -1/2 (see the dotted line), suggesting a diffusive character of the underlying dynamics. Convergence parameters are again $D = 500$, $\Delta t J_x/\hbar = 0.025$ for a system of size $L = 80$.

If the coupling along the z-direction of the spins is negligible, meaning that $\hbar\gamma \gg J_z$, the fraction in the sum of Eq. 6.8 becomes independent of the specific bond corresponding to a spin pair to flip. In this limit it is possible to derive a closed set of differential equations for $\hbar^2 C_{j,j+d}(t) = \langle S_j^z(t) S_{j+d}^z(t)\rangle$, yielding

$$\frac{\partial}{\partial t_1} C_{j,j\pm1}(t) = \frac{D}{2} \left(C_{j\mp1,j\pm1} + C_{j,j\pm2} - 2C_{j,j\pm1} \right),$$

$$\frac{\partial}{\partial t_1} C_{j,j+d}(t) = \frac{D}{2} \left(C_{j+1,j+d} + C_{j-1,j+d} + C_{j,j+d+1} \right.$$
$$\left. + C_{j,j+d-1} - 4C_{j,j+d} \right), \quad \text{for } |d| > 1,$$

$$(6.11)$$

where $D = \frac{J_x^2}{\hbar^2\gamma}$. This constant indicates, that there is a slower evolution for stronger dissipation. The time scale, which is proportional to the inverse of D, scales linearly with γ – a fact that can be attributed to the Zeno effect, which has appeared already in Sec. 5.7 and can be interpreted as a continuous measurement of the system by the environment via the jump operators. If the initial state is translation invariant, which is the case for the Néel state with periodic boundary conditions, $C_{j,j+d}(t_1, t_1)$ just depends on the distance, i.e. $C_d(t_1, t_1)$, so that it is possible to
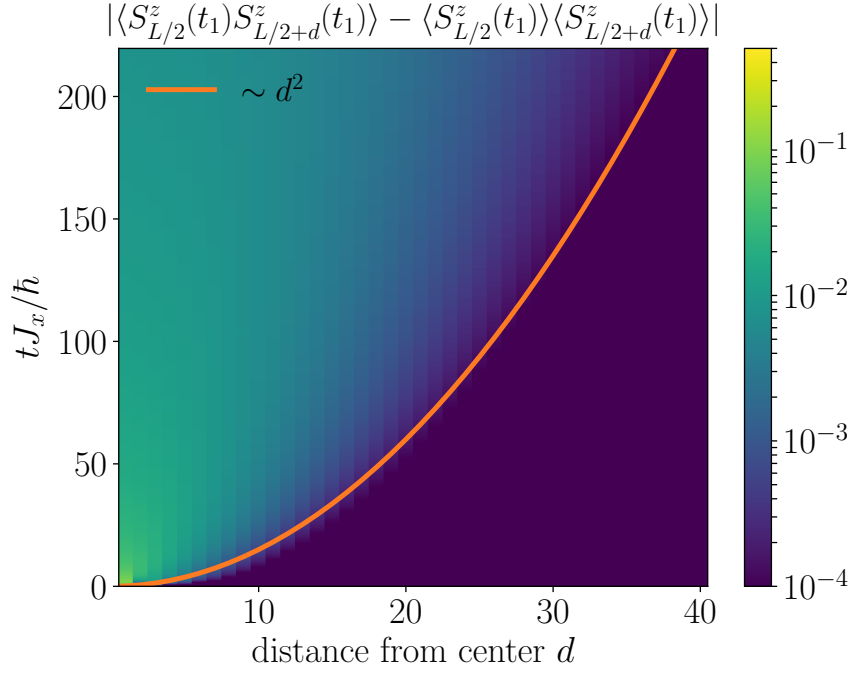
Figure 6.5.: Propagation of equal-time S^z-correlations showing qualitatively a quadratic time dependence of the spreading in time over distance, the orange line is a guide to the eye. The shown data is obtained for a spin chain of length $L = 80$, with $\hbar\gamma/J_x = 2$, $J_z/J_x = 2$, Suzuki-Trotter time step $\Delta t J_x/\hbar = 0.025$ and maximal bond dimension $D = 500$.

rewrite the equation system as

$$\frac{\partial}{\partial t_1} C_{\pm 1}(t_1, t_1) = D\left(C_{\pm 2} - C_{\pm 1}\right),$$

$$\frac{\partial}{\partial t_1} C_d(t_1, t_1) = D\left(C_{d+1} + C_{d-1} - 2C_d\right), \quad \text{for } |d| > 1. \tag{6.12}$$

To arrive at a single differential equation, describing the correlations for all distances, we re-define the correlation function by $\tilde{C}_d(t) = C_d$ for $d \geq 1$ and $\tilde{C}_{d+1}(t) = C_d(t)$ for $d \leq -1$. This is particularly useful, as it gives a common description for all correlation distances, excluding $d = 0$, which is constant as $S_j^z S_j^z = \mathbb{1}/4$. Finally, the set of differential equations is then represented by the following diffusion equation

$$\frac{\partial}{\partial t_1} \tilde{C}_d(t_1, t_1) = D\left(\tilde{C}_{d+1} + \tilde{C}_{d-1} - 2\tilde{C}_d\right), \tag{6.13}$$

which is valid for $-\frac{L}{2} + 2 \leq d \leq \frac{L}{2}$. In this interpretation, D is a diffusion constant. This differential equation system can be solved for $Dt \gg 1$. In short, the calculation is split up into the following steps: First, a discrete Fourier transformation is applied to $\tilde{C}(d, t_1, t_1)$, then the

differential equation is solved for the specific initial state, i.e. $\rho(t = 0) = |\psi_{\text{Neel}}\rangle\langle\psi_{\text{Neel}}|$. After going to the continuum limit in k-space, the result is further simplified by the means of Bessel functions of the first kind, with the identity $I_{|n|}(z) = \int_0^{2\pi} \frac{dk}{2\pi} e^{-ikn} e^{z\cos(k)}$. A detailed calculation, as presented in appendix A.3, gives

$$\tilde{C}_d(t_1, t_1) = \frac{1}{4} e^{-2Dt_1} \sum_{d'=-L/2+2}^{L/2} \left[(-1)^{d'} (1 - 2\delta_{d' \leq 0}) I_{|d'-d|}(2Dt_1) \right]. \tag{6.14}$$

Furthermore, we can use that for large values of z the Bessel functions can be approximated by $I_{|n|}(z) \approx e^z / \sqrt{2\pi z}$. Assuming also a large system size $L \gg 1$, the correlation functions are approaching the square root behavior, found in Fig. 6.4

$$C_d(t_1, t_1) \sim -\frac{1}{\sqrt{64\pi Dt_1}}. \tag{6.15}$$

While we were able to confirm the long-time exponent of the algebraic decay of the equal-time $S^z S^z$-correlations, a lot of additional assumptions were made on top of the many-body adiabatic elimination, including the neglect of the z-directional coupling, a continuum limit and further long-time limit identities for the appearing Bessel functions. Therefore, it is worthwhile to work out a numeric solution, working directly with Eq. 6.8. To do so, we implement the Kinetic Monte Carlo (KMC) algorithm introduced in section 3.3.1. Translating the elements of the current case to the KMC language, we can identify Λ^0 as the state space and extract from Eq. 6.8 the matrix elements responsible for state changes in the classical master Eq. 3.55

$$A(\vec{\sigma} \to \vec{\sigma}'_j) = \frac{J_x \hbar \gamma}{2 \left[(J_z \alpha_j)^2 + (\hbar\gamma)^2 \right]} \delta_{\sigma_j, \bar{\sigma}_{j+1}}, \quad \text{and} \quad A(\vec{\sigma} \to \vec{\sigma}) = -\sum_j A(\vec{\sigma} \to \vec{\sigma}'_j). \tag{6.16}$$

As a consequence the rates for state changes during the evolution of a Monte Carlo trajectory are $\text{rate}(\vec{\sigma} \to \vec{\sigma}'_j) = \Delta t A(\vec{\sigma} \to \vec{\sigma}'_j)$. Now all necessary information is available to implement the kinetic Monte-Carlo algorithm introduced in Sec. 3.3.1 with $|\psi_{\text{Neel}}\rangle$ as initial state.

As emphasized several times, the time interval where the above statements are valid depends on the dissipation strength. In Fig. 6.6 a comparison is drawn for the different methods. To this end, we contrast results from integrating Eq. 6.13, which relies on the assumption of a negligible z-directional coupling strength, with data obtained by applying the Kinetic Monte Carlo method as described in the previous paragraph and the quasi-exact tMPS solution for the full quantum evolution of the purified density matrix. The plot shows that for large dissipation strength ($\hbar\gamma/J_x = 10$, lower panel of Fig. 6.6), all methods are matching well. This makes sense as the condition $\hbar\gamma \gg J_z$ is well fulfilled and the time region, where many-body adiabatic elimination is valid, begins very early. For lower dissipative couplings, as shown in the middle and upper panel of Fig. 6.6, the analytic solution begins to deviate substantially. Especially the early dynamics is not well-described by this method in this parameter regime, whereas the long-term behavior still resembles the overall scaling. The Kinetic Monte-Carlo results perform better, and only show weak inconsistencies even for $\hbar\gamma/J_x = 2$. Nevertheless, the
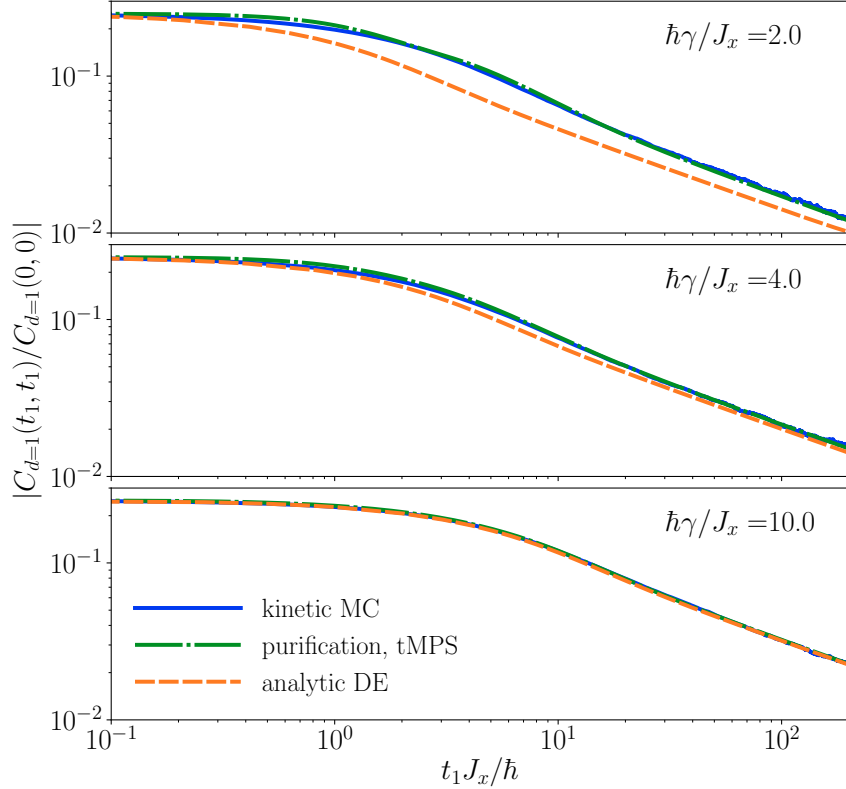
Figure 6.6.: Dissipation-dependent comparison of different methods, including tMPS evolution of the purified density matrix, Kinetic Monte-Carlo (KMC) techniques and an integration of Eq. 6.13 which we extracted from analytic approximation. This is data for a system of size $L = 80$, the S^z coupling strength $J_z/J_x = 2$ and the dissipation strength is given in the plot labels. For the KMC simulations we used $5 \cdot 10^6$ trajectory samples and a time step of $\Delta t J_x/\hbar = 0.025$. For the tMPS we allowed a truncation error of $\epsilon = 10^{-12}$ and used $\Delta t J_x/\hbar = 0.025$ for the time step.

initial dynamics, which is still highly influenced by the Hamiltonian dynamics can also not be modelled correctly. This results enables us to establish a quantitative judgment concerning the validity of the approximative mapping to a classical master equation for different choices of the model parameters. As a consequence, we can confirm that effective dynamics in the dissipation-free subspaces is also the dominant contribution to the full quantum evolution in the long-time range, yielding the derived inverse square root scaling of the equal-time correlations, which reflects the diffusive nature at long times.

6.5. Two-time correlations of spin operators

After the discussion of certain aspects of the equal-time correlation functions in the open spin chain, we turn our focus now towards the evolution of two-time correlation functions $\langle B(t_2)A(t_1) \rangle$ with $t_2 \geq t_1$, where we will consider spin operators along all direction as A and B. The different application times makes the description much more demanding, both

analytically and numerically, as it needs to cover two different periods in time, i.e. before and after the application time of the first operator at t_1.

6.5.1. Exponential decay of two-time correlations which excite outside of the dissipation-free subspace

We first discuss two-time correlation functions, where the application of the operator at t_1 leaves the dissipation-free subspace towards higher dissipative spaces. By recalling, that Λ^0 is the manifold of density matrices diagonal with respect to the eigenstates of the S_j^z operators, i.e $\Lambda^0 = \{|\sigma_1, \sigma_2, \ldots\rangle\langle\sigma_1, \sigma_2, \ldots|\}$, we can see that an application of S^- causes a transition out of Λ^0. For this reason we investigate the properties of the two-time correlation function $\langle S^+(t_2)S^-(t_1)\rangle$. As for a sufficient long time t_1, when the density matrix consists mainly of states of Λ^0, the projection of the ket-part of $\rho(t_1)$ on $|\downarrow\rangle$ by S^- results in a excitation to a higher dissipative space. This is followed by consecutive dynamics therein, before being projected back to the dissipation-free space by S^+ at time t_2. As a consequence of that, the non-vanishing impact of the dissipator imposes an exponential damping on the dynamics. Exactly this behavior is displayed by the tMPS results shown in Fig. 6.7. The plot reveals, that there is only a weak dependence of the considered correlator on the choice of the first application time. This is due to the fact that all chosen times are already in the algebraic regime of the equal-time correlations of $d = 1$ as a comparison with Fig. 6.4 shows. This points to the predominant contribution of the dissipation free-space to short distant correlations at t_1. In contrast, the dissipation strength notably effects the dynamics as the time scale of the exponential decay as a function of γ which agrees well with the findings of previous studies [96] for small systems. Because of the prevailing influence of the dissipation on the time evolution in this case, we turn our attention to the more subtle class of two-time correlations where the two application operators do not couple different subspaces and therefore allow the participation of a variety of different mechanisms.

6.5.2. Hierarchical non-equilibrium dynamics and aging

We consider now two-time correlators, which do not connect different subspaces, i.e. operators which commute with the action of $\mathcal{D}(\rho)$ when applied to a density matrix, a property which is met by the set of S_j^z spin operators. Indeed, the two-time correlation function

$$\hbar C_d(t_2, t_1) = \langle S_{L/2}^z(t_2)S_{L/2+d}^z(t_1)\rangle \tag{6.17}$$

will prove to display rich previously unobserved non-equilibrium quantum dynamics. Namely, we will identify three distinct time regimes. First we describe an initial period, where oscillations of expectation values in time mark the residual impact of the unitary part of the Lindblad equation, including the influence of the Hamiltonian parameters as well as the initial state. In the case of large anisotropies of the interaction strength along different spin directions, a hierarchical separation of time scales gives rise to an intermediate regime where the time dependence of the two-time correlation function follows a stretched exponential. Subsequently, a break-down of time-translation invariance and a scaling collapse give clear signatures of aging at long times. The properties of each of these time regions are discussed in detail in the
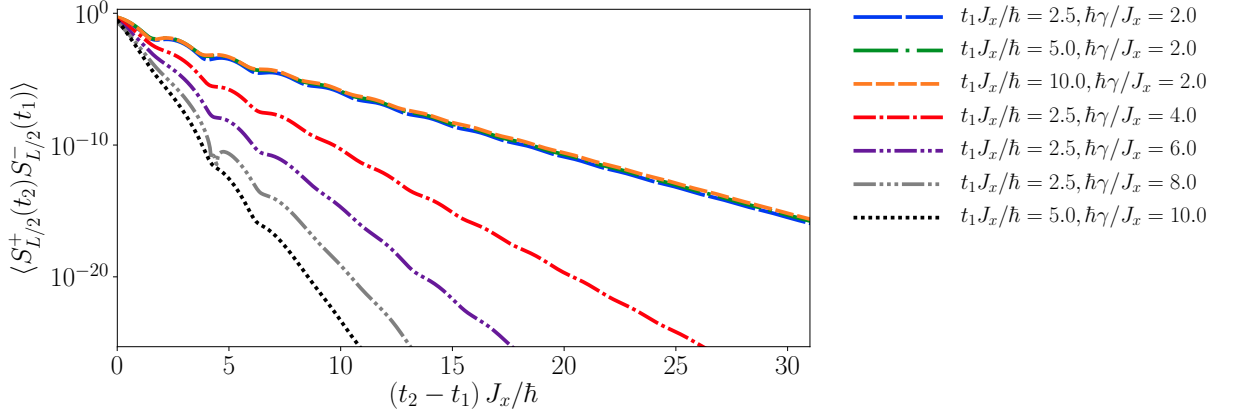
Figure 6.7.: tMPS simulation results of the two-time correlation function $\langle S^+(t_2)S^-(t_1)\rangle$ for spin chains of length $L = 80$, with anisotropy $J_z/J_x = 2$ and different dissipative couplings γ and application times t_1. The time scale of the observed exponential decay decreases for increasing dissipation strength. The convergence parameters are $D = 500, \Delta t J_x/\hbar = 0.025$ and $L = 80$.

following.

The first regime is visible in Fig. 6.8, which displays the quantum evolution of a system initially prepared in the Néel state, obtained by tMPS, as a function of $t_2 - t_1$ for different model parameter choices and different values of t_1. The comparison of the time dependence of the isolated system ($\gamma = 0$, grey dotted line in both panels of Fig. 6.8) with the same Hamiltonian system coupled to an environment, enables us to address the early oscillation close to t_1 to the coherent part of the dynamics. Strong interactions and the impact of a finite system size are reasons for the opening of a gap in the energy spectrum commonly causing oscillations of observable expectation values of the quantum systems in time. For longer times these oscillations are damped out by the fluctuations induced by the dephasing.

Before we discuss other aspects of the figure, we first want to focus on the long-time behavior of the two-time correlation $C_d(t_2, t_1)$, i.e. for times satisfying $t_2 J_x/\hbar \gg t_1 J_x/\hbar \gg 1$. Interestingly, examining in this regime the two-time functions, normalized to the equal-time correlations at t_1, we observe a breaking of time-translation invariance. As indicated in the top panel of Fig. 6.9, we can identify a time interval where the correlation function decays algebraically with regard to the ratio of t_2/t_1 with an exponent of -3/2 and therefore does not solely depend on time differences as for example $t_2 - t_1$. In fact, the two-time correlations are highly influenced by the value of t_1, i.e. the amount of time the open system has spent evolving before the first operator application. This is a well-known phenomenon in the context of non-equilibrium materials, like for example glasses, where a parameter, often the temperature, is suddenly changed from a high to a low value, crossing a characteristic value. The corresponding change of the thermodynamic potential often results in very slow relaxation dynamics due to competing energy minima. Two-time correlations then depend on the time passed since the temperature change, referred to as the age of the system, which is why we use this definition to
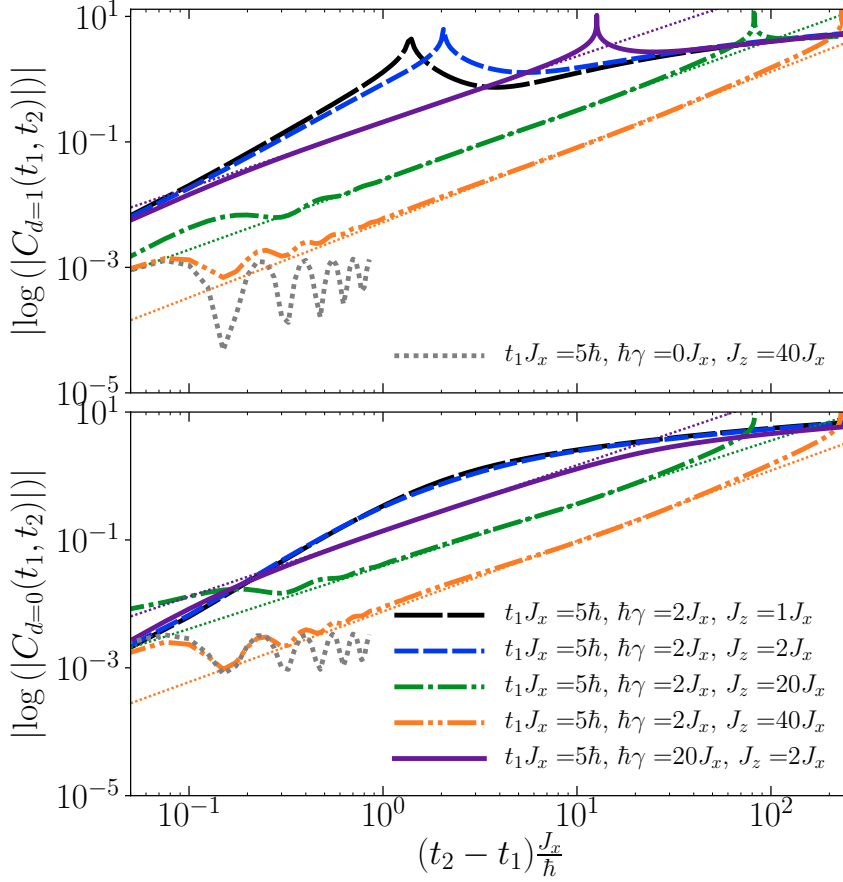
Figure 6.8.: Two-time correlation of z-directional spin operators acting on the same site in the center ($d = 0$) or two central sites separated by one lattice spacing ($d = 1$), for a system of length $L = 48$ and different model and dynamic parameter as specified in the plot legend. Convergence parameters for the algorithm are $D = 500$ for the bond dimension and a Suzuki-Trotter time step of $\Delta t J_x/\hbar = 0.025$.

characterize the process by the name aging[160, 170]. More formally, aging is defined in [170] by the three properties (1) a slow non-exponential relaxation of correlations, (2) the breaking of time-translational invariance and (3) the presence of a dynamical scaling collapse onto one a function of t_2/t_1. Remarkably, all of these conditions are satisfied in the long-time limit: Considering the upper panel of Fig. 6.9 the algebraic, time-translation breaking dynamics mentioned above can be identified as the emergence of a scaling regime reached for a range of different interaction anisotropies J_z/J_x, dissipation strengths γ and application times t_1. Therefore, we can conclude, that to our knowledge, for the first time, we have detected aging in the evolution of full interacting non-equilibrium quantum systems of large spatial extend. To further expand our understanding, we use many-body adiabatic elimination building up on the calculations of the equal-time correlation functions. While the details of the calculation are documented in the next section, one of the main findings is that the two-time correlations for for large times t_1
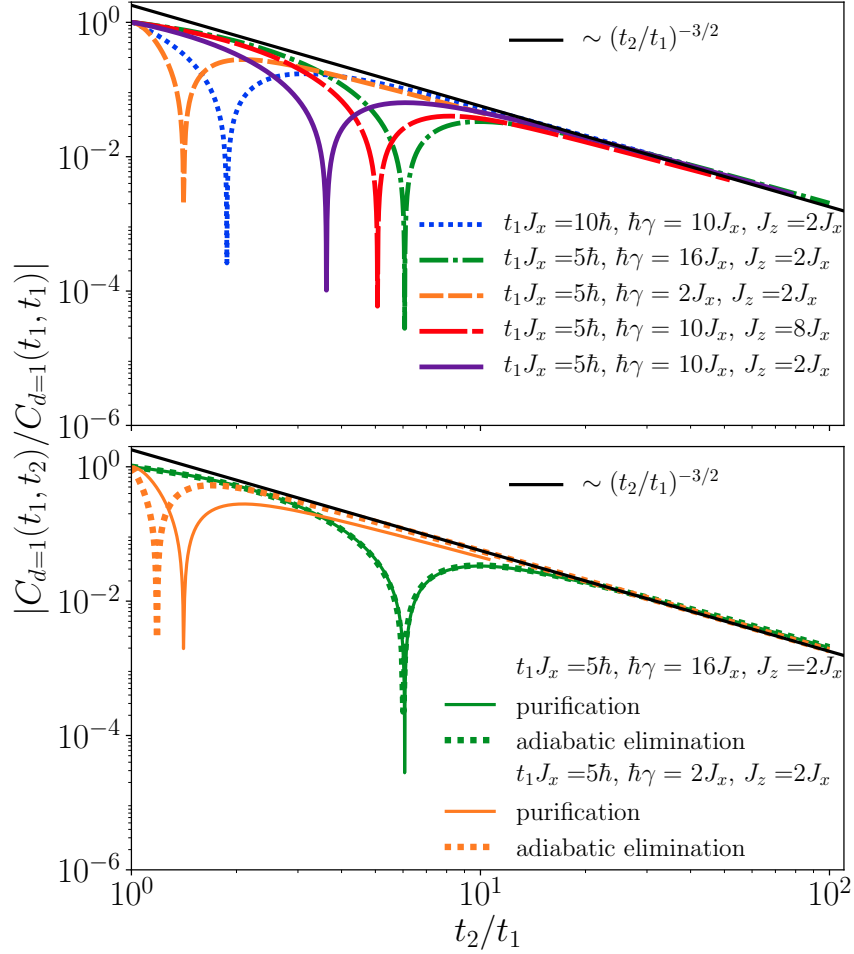
Figure 6.9.: Upper panel: Aging collapse of the normalized z-directional two-time correlation function for a range of different model parameters and first application times for spin chains of length $L = 80$ initially prepared in the Néel state. Lower panel: Comparison of solving the differential equation system obtained by many-body adiabatic elimination to the quasi-exact tMPS result for different dissipation strengths. Convergence parameters are chosen as $D = 500$ for the bond dimension and a Suzuki-Trotter time step of $\Delta t J_x / \hbar = 0.025$ for a system of size $L = 80$.

and t_2 can be described by an closed approximate differential equation system, which is strictly only valid for vanishing J_z coupling strength. As can be seen in the lower panel of Fig. 6.9, the Integration of this differential equation provides very well matching estimates for long times irregardless of the model parameters. Nevertheless, if the dissipation dominates the evolution, i.e. $\hbar\gamma/J_z \gg 1$, the adiabatic elimination computations reproduce the correct time dependence over the full time range. Furthermore, the careful scaling analysis in the next section, confirms the value of the scaling exponent being $-3/2$ for correlations of sites with a distance of at least one lattice spacing. It is worth noting, that the analytic treatment relies on large values of t_1,
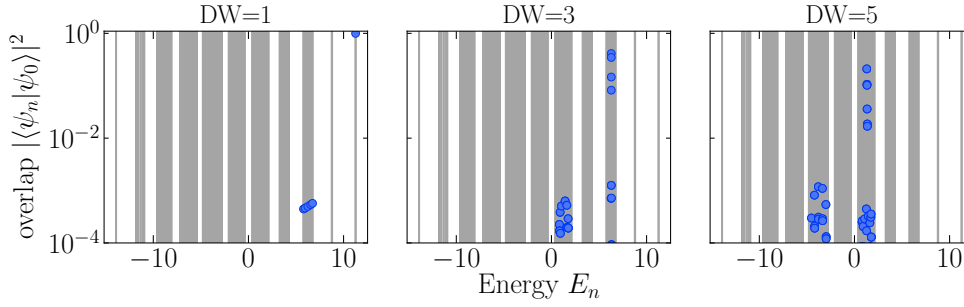
Figure 6.10.: Occupation of energy eigenstates of H_{XXZ} obtained from exactly diagonalizing the Hamiltonian for different initial states $|\psi_0\rangle$ distinguished by the number of existing domain walls for a chain of length $L = 12$ and interaction $J_z/J_x = 10$.

such that aging appears in regions where the waiting time before the first application is long enough for the equal-time correlations to be in the diffusive regime. Also, the occurrence of aging is not dependent on the initial state, as we tested several different initial system preparations, including for example the single-domain wall state.

Let us now return to the description of Fig. 6.8 by considering the behavior of the two-time correlations for finite dissipative couplings. It becomes apparent, that an intermediate time region emerges for increasingly strong interaction anisotropies. There the evolution of the logarithm of the two-time correlations follows a power-law, so that the total behavior has the form of a stretched exponential

$$C_d(t_2, t_1) \sim \mathrm{e}^{-\beta(\gamma)(t_2 - t_1)}. \tag{6.18}$$

A similar behavior has been predicted before, using the approximative approach of kinetic Monte-Carlo methods for a similar set-up, $t_1 = 0$ and the Néel state as initial state [100]. The key contribution to the dynamics can be explained by the dependence of the energy spectrum of the Hamiltonian. As depicted in Fig. 6.11, the spectrum splits up into bands for growing S^z-coupling strength J_z causing a separation of time scales, distinguishing between intra- and inter-band rates. Although the Néel state, i.e. the chosen initial state, is not the true ground state of the antiferromagnetic phase of the XXZ chain, it mainly occupies states
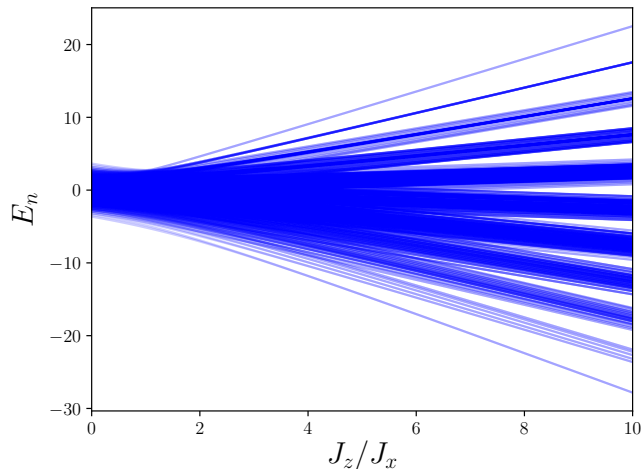

Figure 6.11.: Spectrum of H_{XXZ} vs. J_z/J_x, $L = 12$, in the $M_{\mathrm{tot}} = 0$ sector

at the low-energy end of the spectrum for $J_z/J_x > 1$. Due to the small number of available states and the large energetical separation of them, excitations in the form of reductions of the number of domain walls, separating areas of parallel aligned spins, happen on a much larger time scale then the motion of created effects inside the bands. Nevertheless, we want to emphasize, that this intermediate regime only exists for a limited duration and will eventually be transferred to the aging regime. This can be seen, by comparing the two purple lines corresponding to the same parameters in Fig. 6.8 and Fig. 6.9. The transition between the two time ranges is here marked by kinks in the $d = 1$ correlations caused by zero crossings of $C_{d=1}(t_2, t_1)$. This illustrates, that at long times, the stretched exponential gives way to the observed aging dynamics.

Obviously, the choice of the initial state plays an important role for the impact of the time scale separation on the overall two-time dynamics. To quantify this, we select initial states spanning different parts of the spectrum and observe their influence of this on the lifetime of the intermediate stretched exponential regime. More precisely, we use basis states with an increasing number of domain walls (DW), starting with one, i.e the state where we have two oppositely aligned domains $| \uparrow\uparrow \ldots \uparrow\downarrow\downarrow \ldots \downarrow\rangle$. The occupation of energy levels of the corresponding state, as represented in Fig. 6.10, exemplifies that the main contribution to the DW $= 1$ state resides in the well-separated high energy part of the spectrum, whereas more domain walls result in finite occupations in the center of the spectrum where the creation of defects is energetically less costly. Indeed, the two-time evolution in Fig. 6.12 for initial states with different domain walls numbers, shows shorter regions of stretched exponential behavior. This opens another application opportunity for the evolution of two-time correlations in this setting. As the duration of the existence of a stretched exponential is tied to the Hamiltonian energy levels, it is possible to probe the spectrum of spin chains using the system's non-equilibrium dynamics as a tool.

6.5.3. Derivation of long-term scaling

This section is dedicated to the development of an analytic understanding of the algebraic scaling of the two-time correlation functions $C_d(t_2, t_1)$ with regard to the ratio t_2/t_1 as it poses an important signature for the observed aging dynamics. Here we build up on our results for the equal-time correlation functions obtained by applying many-body adiabatic elimination techniques as presented in section 6.4. As starting point for our calculation we notice that the evolution of two-time correlation functions is connected to the dynamics of expectation values of equal-time observables via the quantum regression theorem [6]. The theorem states, that if an equation system for a set of equal-time observables $\{B_j\}$ exists, the two-time correlations are described by the same equations, i.e

$$\frac{\mathrm{d}}{\mathrm{d}t}\langle B_j(t)\rangle = \sum_l G_{jl}\langle B_l(t)\rangle$$

$$\Leftrightarrow \quad \frac{\mathrm{d}}{\mathrm{d}t}\langle B_j(t+\tau)A(t)\rangle = \sum_l G_{jl}\langle B_l(t+\tau)A(t)\rangle. \tag{6.19}$$
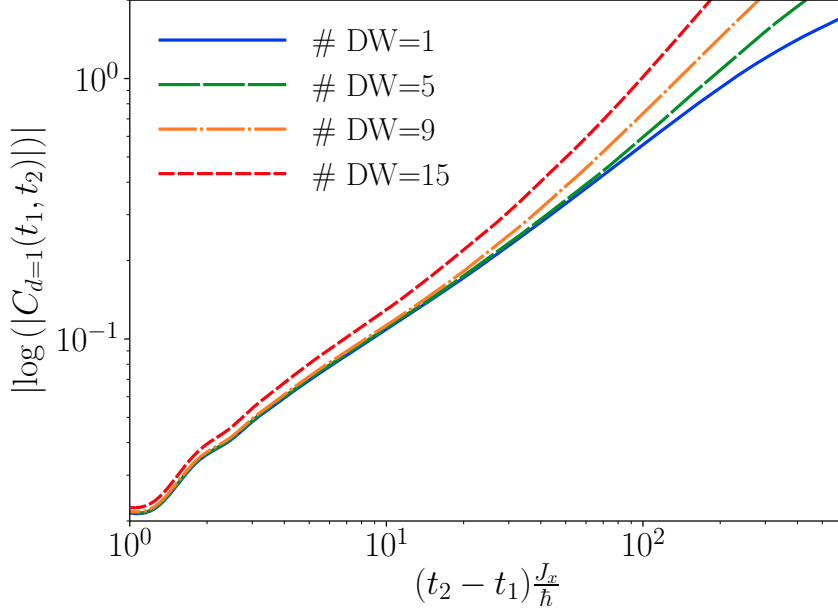
Figure 6.12.: Dependence of the length of the stretched exponential regime on number of domain walls in the initial state. The shown data is for $L = 64$, $\hbar\gamma/J_x = 2$ and $J_z/J_x = 10$. Convergence parameters where $D = 500$ and $\Delta t J_x/\hbar = 0.025$.

Consequently, in our case we need to find a system of equations describing the expectation values $\langle S_j^z(t_1) \rangle$. To do so, we follow the same route we used earlier for the derivation of the effective diffusion equation for the equal-time S^z-correlations. Using adiabatic elimination, the dynamics of the density matrix for time scales larger than $1/\gamma$ and strong dissipation strengths $\hbar\gamma \gg J_z$ can be approximated by Eq. 6.8. This procedure yields

$$\frac{\mathrm{d}}{\mathrm{d}t_1}\langle S_j^z(t_1) \rangle = \frac{D}{2}\sum_{l=1}^{L}(\delta_{j+1,l} + \delta_{j-1,l} - 2\delta_{j,l})\langle S_l^z(t_1) \rangle$$
$$= \sum_l G_{jl}\langle S_l^z(t_1) \rangle, \tag{6.20}$$

where we assumed periodic boundary conditions and used the already introduced diffusion constant $D = J_x^2/\hbar^2\gamma$. As a result we can now also specify the dynamics of the translation invariant two-time correlations $\hbar^2 C_d(t_2 = t_1 + \tau, t_1) = \langle S_j^z(t_1 + \tau)S_{j+d}^z(t_1) \rangle$ in the limits of the assumptions of weak z-directional spin coupling and long times $Dt_2 \gg Dt_1 \gg 1$

$$\frac{\partial}{\partial\tau}C_d(t_2, t_1) = \frac{D}{2}\left(C_{d-1}(t_2, t_1) + C_{d+1}(t_2, t_1) - 2C_d(t_2, t_1)\right). \tag{6.21}$$

Due to the similarity of this equation with Eq. 6.12, the solution can be found in close analogy. The situation is structurally different as we do not need to take special care of the case

$d = 0$, the previous equation is valid for all distances. As before, the differential equation is solved in Fourier space before we use the continuum limit in momentum space for the back transformation. Finally, exploiting the identity $I_{|n|}(z) = \int_0^{2\pi} \frac{dk}{2\pi} e^{-ikn} e^{z\cos(k)}$ for the modified Bessel functions $I_{|n|}(z)$, the general solution can be written as

$$C_d(t_2, t_1) = e^{-D(t_2-t_1)} \sum_{d'=-\frac{L}{2}+1}^{L/2} C_{d'}(t_1, t_1) I_{|d'-d|}(D(t_2 - t_1)). \tag{6.22}$$

To maintain the readability of the text, some calculations are moved to appendix A.4. The core idea of the next step is to split up the sum over distances in a helpful way and to insert the solutions of the equal-time correlations $C_d(t_1, t_1)$ as found in Eq. 6.14 for $d \geq 1$, using $C_{-d}(t_1, t_1) = C_d(t_1, t_1)$ and $C_0(t_1, t_1) = 1/4$ (cf. A.4.1). This yields the intermediate result for large system sizes $L \gg 1$

$$\begin{aligned}
C_d(t_2, t_1) =& \frac{1}{4} e^{-D(t_2-t_1)} I_{|d|}(D(t_2 - t_1)) \\
&+ \frac{1}{4} e^{-D(t_2+t_1)} \bigg[- I_{|d|}(t_2 + t_1)\delta_{d,0} \\
&(1 - \delta_{d,0})(-1)^d \sum_{j=1-d}^{d-1} (-1)^j I_{|j|}(D(t_2 + t_1)) \bigg] \\
&+ G_d(t_2, t_1),
\end{aligned} \tag{6.23}$$

where we defined

$$G_d(t_2, t_1) \equiv e^{-D(t_2-t_1)} \sum_{d'=1}^{\infty} C_{d'}(t_1, t_1) \left[I_{|d+d'|}(D(t_2 - t_1)) - I_{|d+d'-1|}(D(t_2 - t_1)) \right]. \tag{6.24}$$

We strive for the long-time scaling, so we are looking for a solution in a time limit where $Dt_2 \gg Dt_1 \gg 1$. To this end, we use an asymptotic expansion of the modified Bessel function for large arguments documented in formula 9.7.1 of [171]. Again we refer to the appendix for a careful evaluation of the scaling which is split up into the scaling of $G_d(t_2, t_1)$ in section A.4.2 and the full scaling including all terms in A.4.3. While the first two terms in Eq. 6.23 can be straightforwardly addressed by the mentioned expansion, we also need to take into account higher orders for the computation of $G_d(t_2, t_1)$ leading to the following scaling expression for the equal-time correlations

$$C_d(t_1, t_1) \sim -\frac{1}{4} \frac{1}{\sqrt{2\pi(t_2 - t_1)}} e^{-\frac{1}{2}\frac{d^2}{2Dt_1}}. \tag{6.25}$$

Using this and taking a continuum limit to resolve the sum over all distances we can determine the scaling. Due to the difference in the initial condition, i.e. the value of the equal-time correlations at t_1, we consider the distances $d = 0$ and $|d| \geq 1$ separately. For $|d| \geq 1$ the dominant

scaling of the normalized two-time correlation functions for long times is given by

$$\frac{C_d(t_2, t_1)}{C_d(t_1, t_1)} \sim -\sqrt{2} \left(\frac{t_2}{t_1}\right)^{-3/2} \left[1 + \frac{1}{\sqrt{\pi}}(Dt_1)^{-1/2} - \frac{1}{4}(Dt_1)^{-1}\right]. \tag{6.26}$$

For very large Dt_1, the leading contribution is prevalent. Therefore, we can conclude that this scaling agrees with the findings from our tMPS simulations shown in the previous section, and the long-time behavior for $|d| \geq 1$ scales as

$$\frac{C_d(t_2, t_1)}{C_d(t_1, t_1)} \sim \left(\frac{t_2}{t_1}\right)^{-3/2}. \tag{6.27}$$

As a result of the algebraic scaling with regard to the ratio of t_2/t_1, we can confidently state that the open spin chain exhibits aging caused by diffusive processes arising due to a coupling to a dephasing environment. One still needs to discuss the scaling of the two-time correlation at the same site, i.e. $d = 0$. For this, the equal-time correlation is always constant as $(S^z)^2 \sim \mathbb{1}$. Taking this into account leads to the following scaling of the normalized two-time correlations

$$\frac{C_0(t_2, t_1)}{C_0(t_1, t_1)} \sim \frac{1}{\sqrt{2\pi}}(Dt_1)^{-1/2} \left(\frac{t_2}{t_1}\right)^{-\frac{3}{2}} \left[1 + \frac{1}{\sqrt{\pi}}(Dt_1)^{-1/2} - \frac{1}{4}(Dt_1)^{-1}\right]. \tag{6.28}$$

It is important to note here, that, while time-translation invariance is still broken and a dominant algebraic scaling exists, the latter does not solely depend on t_2/t_1 and therefore the underlying dynamics can not be regarded as aging.

6.6. Summary of the results of Chap. 6

In summary, the novel contribution described in this chapter is based on the numerical quasi-exact determination of two-time correlations along different spin directions in an interacting many-body systems in contact with a environment. To do so, we have implementing an extension to the tMPS algorithm for systems exhibiting Markovian dissipation, which provides the full quantum evolution. We could separate the time dependence into three dynamic regimes. The first regime is dominated by the unitary evolution reflected by oscillations of the two-time correlation functions. For long times, we were able to detect the breaking of time-reversal invariance and the scaling collapse of two-time correlation functions to a algebraic decay following a behavior of $(t_2/t_1)^{-3/2}$, which is independent of model parameters. Therefore all criteria for the introduced definition for aging are fulfilled. For strong z-directional spin coupling between adjacent sites, the system undergoes an intermediate regime, originating from a hierarchical contribution of several time scales, determined by spectral properties of the Hamiltonian and the initial state. This relation, allows to draw conclusions concerning the spectrum of the system Hamiltonian by considering the evolution of a state. For local equal-time spin correlations, we were further able to show, that the dominant mechanisms can be understood as an effective diffusive process at long times.

The numeric analysis is compared to results from adiabatic elimination valid for long times.

The time evolution can then be described by an effective motion in the dissipation free subspace, which gives an analytic access to the problem. Using this approach, we verify the numerically found exponents for both, equal-time and two-time correlations, and find effective diffusion equations describing the evolution for both correlation functions.

Zeno dynamics of interacting fermions with a dissipative defect

7.1. Introduction

One of the key paradigms of quantum mechanics is the collapse of the wave function in the course of a measurement process. The obtained value of measuring an observable, which is represented as an hermitian operator, is one of its eigenvalues and the wave function directly after the measurement is given by the corresponding eigenstate. As the probability for obtaining a specific eigenvalue as a result is related to the overlap of the wave function with the eigenstate, repeatedly measuring the same observable in short time intervals has a high likelihood to result in the same measurement outcome. Consequently the system evolution is slowed down by the projection to one eigenstate. This phenomenon is known as the Zeno effect [152] and has, for example, been observed in ultracold atomic gases [12, 172]. Interestingly, the effect also appears in open systems as the effect of the environment can be seen as a sequence of measurements of the Lindblad jump operators. One example has been experimentally observed in a realization of the inelastic scattering of cold molecules trapped in optical lattice potentials [173]. In this framework, double-occupied sites are subjected to two-particle losses, where a fast on-site loss rate regarding double occupancies suppresses the hopping and freezes the system, which can be viewed as the creation of effective strong on-site repulsive interactions, penalizing occupations larger than one. Moreover, the dissipative Zeno effect has been detected in the context of highly localized Markovian defects in an atomic Bose-Einstein condensate caused by the exposure to an electronic beam with very sharp spatial extension [174]. Here, the Zeno effect is characterized by a non-monotonic dependence of the particle loss of condensed atoms on the effective dissipation strength. As the manipulation of single atoms, for example through the mentioned electron beam setup or by atomic excitations by laser beams [175–177] is possible, the extension of local dissipation implementations to strongly-correlated models on discrete lattice sites are reachable.

In this chapter we report the detection of Zeno dynamics in the setting of cold spinless fermionic atoms localized to the sites of an optical lattice with nearest-neighbor interactions. The fermions are further subjected to losses on the central site. The strong interactions require

a full solution of the master equation beyond mean field [178]. A related study concerning the numerically exact investigation of a similar bosonic system in Ref. [109], identified the Zeno effect for the density evolution in the strong dissipation limit. The limit of the equilibrium model for strong repulsive interactions is the Tonks-Girardeau gas, where the occupation of one site by two or more bosons is forbidden, which resembles Pauli's exclusion principle for fermions and is therefore very similar to the model considered in this chapter. The Tonks-Girardeau gas has been realized with cold atoms [179, 180]. Furthermore, analytical insights have been obtained using the Keldysh formalism for the same model under consideration in Ref. [181], where either the particle interaction or the dissipation has been treated perturbatively. In the present work, we employ the Monte-Carlo wave function (MCWF) technique (cf. Sec. 4.3) enabling an accurate description of the full quantum evolution for the fermionic case.

We begin with an introduction of the model at hand, followed by the presentation of three distinct dynamical regimes which are highly influenced by the dissipation strength and the nearest neighbor coupling. Finally we present the occurrence of Zeno behavior and justify our findings by adiabatic elimination calculations, valid for strong dissipative couplings.

7.2. Dissipative density evolution of interacting ultracold fermionic atoms

Here we consider a gas of cold spinless fermionic atoms confined to a one-dimensional optical lattice of equally spaced sites. In the tight-binding limit the fermions are localized to the discrete lattice sites, where each site can be maximally occupied by one atom because of Pauli's exclusion principle. Moreover, each atom interacts with the particles of the adjacent sites, so that the situation for a chain of length L is described by the following Hamiltonian

$$H = -J \sum_{l=-(L-1)/2}^{(L-1)/2-1} \left(c_l^\dagger c_{l+1} + \text{h.c.} \right) + V \sum_{l=-(L-1)/2}^{(L-1)/2-1} n_l n_{l+1} + V \left(n_{-(L-1)/2} + n_{(L-1)/2} \right) \frac{N}{L}, \quad (7.1)$$

with the fermionic annihilation (creation) operators c_l ($c_l^\dagger$), satisfying the anti-commutation relation $\{c_l, c_{l'}^\dagger\} = \delta_{l,l'}$, and the definition of the local density at site l as $n_l \equiv c_l^\dagger c_l$. The first term is the kinetic energy, represented by the hopping of atoms between neighboring sites controlled by the amplitude J. The second term contains the interaction via a coupling of the density of adjacent sites, which can be tuned by changing the coupling strength V to be either attractive for a negative or repulsive for a positive value of V. To lower the boundary effects, we have additionally included a term, which couples the density at the chain ends to the value of the average density, given by N/L, where N is the number of particles. In the equilibrium scenario, this model can be identified with the XXZ spin-1/2 model using the Jordan-Wigner transformation [169],

$$H = -2J \sum_{l=1}^{L-1} \left(S_l^x S_{l+1}^x + S_l^y S_{l+1}^y \right) + V \sum_{l=1}^{L-1} S_l^z S_{l+1}^z + \text{const.} \quad (7.2)$$

where the two different spin direction are related to the presence of particles or holes on the sites of the lattice. Consequently, it also exhibits the same phases and properties as outlined
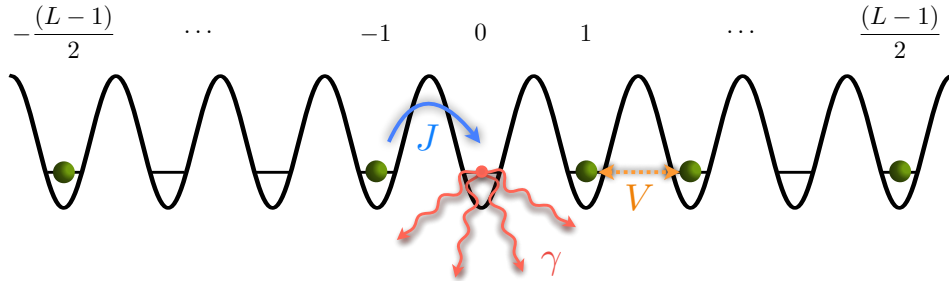
Figure 7.1.: Sketch of the set-up of interacting spinless fermions, displaying the interaction, the hopping and the Markovian losses at the central site.

in Sec. 6.2. Initially, the system is prepared in the ground state of the Hamiltonian. Then a contact to an environment at time $t = 0$ is established by a dissipative quench causing a loss of fermionic particles. The particle loss acts exclusively at the central lattice site. This process is assumed to happen very fast compared to the motion of the system, so that the back action of the lost particles on the system can be neglected and the process can confidently be described by the Markovian Lindblad master equation

$$\frac{\mathrm{d}}{\mathrm{d}t}\rho(t) = -\frac{i}{\hbar}\left[H, \rho(t)\right] + \mathcal{D}(\rho), \quad \text{with } \mathcal{D}(\rho) = \gamma\left(c_0 \rho c_0^\dagger - \frac{1}{2}c_0^\dagger c_0 \rho - \frac{1}{2}\rho c_0^\dagger c_0\right), \qquad (7.3)$$

where the index zero marks the central site and the dissipation strength is given by the loss rate γ. To keep the mirror symmetry, we will consider odd-sized chains, a restriction, which becomes irrelevant in the thermodynamic limit. The full model, including all mechanisms, is depicted in Fig. 7.1.

The work presented in this chapter is directed to uncover the dynamical properties after the dissipative quench. To this end, we access the time evolution by applying the Monte-Carlo wave function technique (MCWF) described in Sec. 4.3 interfaced with the tMPS algorithm (cf. Sec. 3.1.4) to the evolution of the ground state of the Hamiltonian. The latter is obtained using the DMRG algorithm from Sec. 3.1.3, which provides the ground state already in MPS form. One reason, why the MCWF method is preferred here to the purification approach, is that the ground state typically needs a bond dimension of the order of $D = 100$ to reach an adequate truncation accuracy, which results either in a very rough approximation or very high memory demands in the purification step. Moreover, the jump operator does not conserve the total particle number while the product with its hermitian conjugate $c_m^\dagger c_m$ does, so that we can only exploit conserved quantum number in the MCWF code and not in the purification method. The fact that only a single jump operator is present in the model, limits the space of possible time-evolved trajectories, so that the statistical sampling becomes feasible. Typically 10^4 trajectories provide a sufficient accuracy in terms of the standard deviation of the mean compared to magnitude of the expectation vales of the considered observables.

We will describe the long-time limit for models exhibiting strong dissipations with adiabatic elimination. For this purpose it is useful to define the dissipation-free subspace, which is not
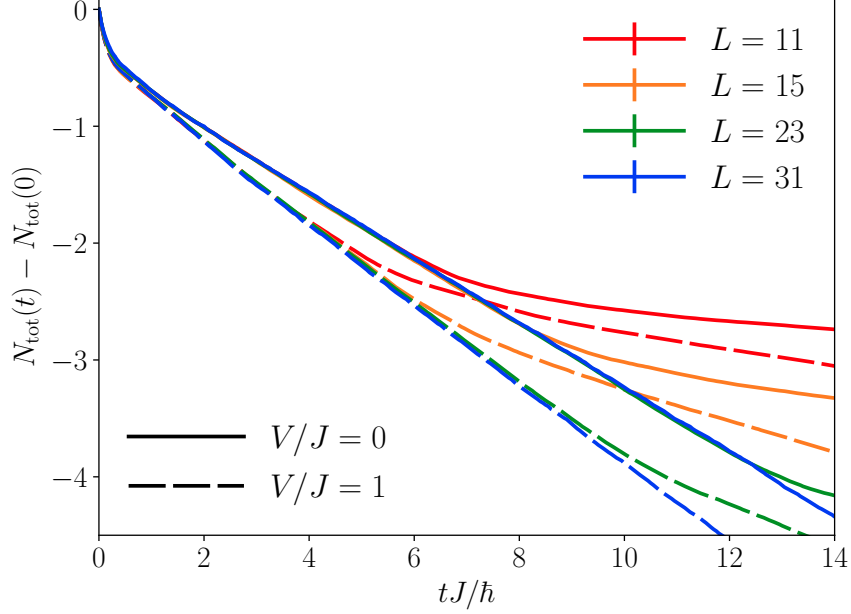
Figure 7.2.: Time-dependence of the deviation of the total particle number from the initial value for different system sizes and interaction strengths and a dissipative coupling of $\hbar\gamma/J = 6$. The data shown is an average of 10^4 MC samples and statistical errors are smaller than the line width. Suzuki-Trotter time step is $\Delta tJ/\hbar = 0.05$ and maximal bond dimension $D = 300$.

affected by the dissipator

$$\Lambda^0 = \left\{\rho^0 \big| \mathcal{D}(\rho^0) = 0\right\} = \left\{\sum_{\{n\},\{n'\}} \rho^0_{\{n\},\{n'\}} |\ldots n_{-1}, 0, n_1 \ldots\rangle\langle\ldots n'_{-1}, 0, n'_1 \ldots| \right\}. \qquad (7.4)$$

Furthermore, following the description in Sec. 3.3, the Lindbladian can be split up into two parts, yielding

$$\mathcal{L} = \mathcal{L}_0 + \mathcal{L}_\mathcal{V}$$
$$\text{with } \mathcal{L}_0 = \mathcal{D}(\cdot) - iV\left[n_{-1}n_0 + n_0n_1, \cdot\right]$$
$$\text{and } \mathcal{L}_\mathcal{V} = -iJ\sum_l \left[c_l^\dagger c_{l+1} + \text{h.c.}, \cdot\right] - iV\sum_{l\neq -1,0} \left[n_l n_{l+1}, \cdot\right]. \qquad (7.5)$$

The dissipative nature of the system enables the extraction of dynamical quantities without perturbing the system by a collapse caused during the measurement process. In the present case, the loss of particles, can be directly observed in experiments and therefore allows conclusions on the total particle number in a non-destructive manner. We present MCWF results for the time-dependence of the deviation of the total particle number $N(t)$ from its initial value in Fig.
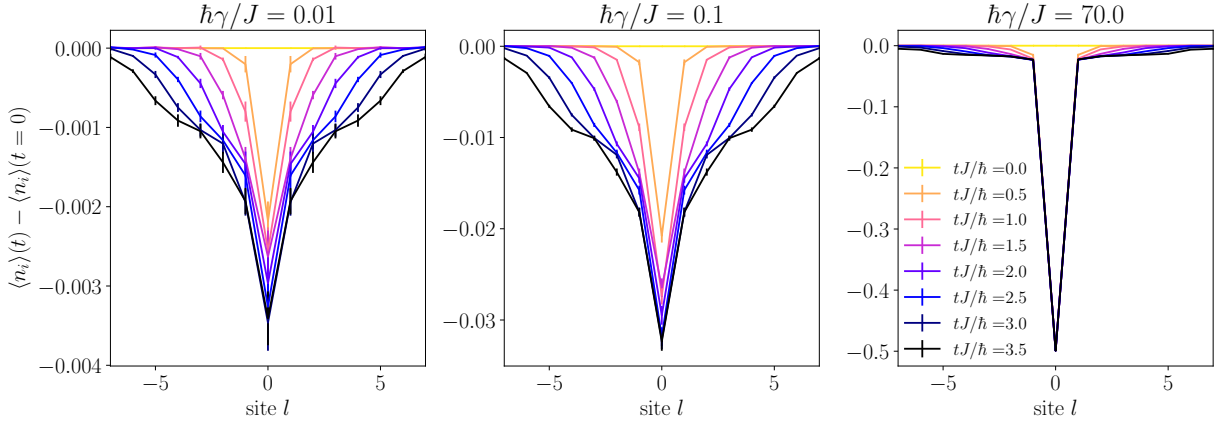
Figure 7.3.: Deviation of the density profile from the initial distribution for different dissipative coupling strengths for a free chain $V = 0$ of size $L = 15$ with 10^4 MCWF samples, an exact MPS simulation (no truncation) and a Suzuki-Trotter time step of $\Delta t J/\hbar = 0.05$. Statistical errors are marked by errorbars when larger then the line width.

7.2. The plot compares different system sizes and the different behavior of free and interacting fermions, where the initial particle number is chosen to be $N = \lfloor L/2 \rfloor$. The behavior reveals three different time regimes. After a fast early decay, an intermediate time region is reached, where the particle number depends linearly on the time. This regime eventually breaks down due to finite size effects caused by the boundary, as displayed by the different deviation points for different system sizes. The decay of the particle number is notably faster in the linear region in the presence of repulsive interactions than for free atoms. We will give a quantitative reasoning for this using adiabatic elimination later. Starting from an almost equal occupation of sites, only modulated by finite system effects, originating in the non-commensurability of particle number and system size, it is plausible, that the early loss can be mainly attributed to the emptying of the initial central site occupation. Indeed, the evolution of the density profile deviation from its initial distribution for different dissipative coupling strengths in Fig. 7.3 shows that the loss of particles at the central site is a dominant contribution at early times. Comparing different loss rates confirms a strong dependence of the corresponding time window on the dissipation. While the profile evolution for $\hbar\gamma/J = 0.01$ and $\hbar\gamma/J = 0.1$ still shows a finite particle number at the central site as a left-over from the initial state for the presented time span, the evolution for $\hbar\gamma/J = 70$, reaches the dissipation-free subspace Λ^0 in the first time step and stays in this subspace for the rest of the plotted times. Assuming a decoupling of the central site from the rest of the chain, the central occupation is expected to show an exponential decay

$$n_0(t) - n_0(0) = e^{-t/\tau_1} n_0(0), \tag{7.6}$$

with a time scale of $\tau_1 = 1/\gamma$. The dependence of this time scale τ_1 for the total number of particles N_{tot} on the dissipation strength γ is displayed in Fig. 7.4. It is extracted from exponential fits of the total particle number in the early time regime. The inverse scaling with the dissi-
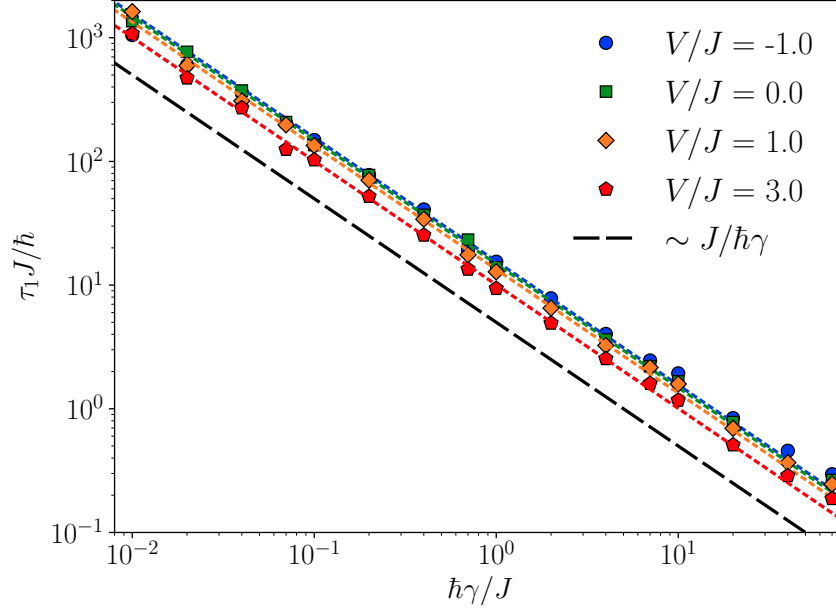
Figure 7.4.: Dissipation dependence of the time scale of the particle number in the first time regime for different interaction strengths and a system size $L = 15$, 10^4 MCWF samples, no MPS truncation and Suzuki-Trotter time step $\hbar t/J = 0.05$.
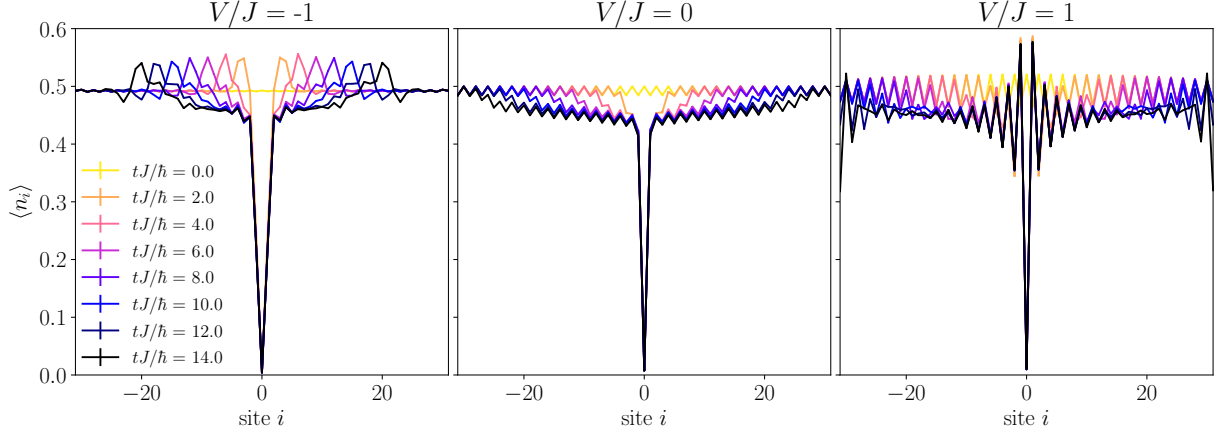

Figure 7.5.: Evolution of spatially resolved particle density for strong dissipation of $\hbar\gamma/J = 20$, chain length $L = 63$ and different interactions. We used 10^4 trajectories, $\Delta t J/\hbar = 0.05$ and no MPS truncation. Statistical errorbars are smaller than the line width.

pative coupling verifies the association of this regime with an initial emptying of the central site. The assumption that in that time interval this site can be considered as decoupled form the rest of the system is also supported by the observation, that this behavior is not influenced significantly by the presence of interactions. We now turn to the investigation of the second

regime by examining the density profile evolution presented in Fig. 7.5 for a comparably strong loss rate of $\hbar\gamma/J = 20$ for the different interactions $V/J = 0, \pm 1$. The initial state for $V/J = 0$ and $V/J = 1$ shows the local oscillations of the equilibrium ground state due to the finite size effect. Remarkably, although the overall dynamics is very different, we can detect a static behavior in all three cases, manifested by a quasi-stationary density surrounding the central site, which survives until the evolution reaches the boundary and the system starts to be emptied completely, as can be seen for $V/J = 1$. This situation can be locally viewed as the same set-up with two reservoirs connected to the ends of the chain [181], resulting in a steady particle flow towards the central site. For the free case we observe a decay of the single occupations with remanent modulation of the initial state. For repulsive interactions, the stationary regime gives rise to a density pattern that is strongly alternating in space and constant in time. The local density even surpass the initial density at some sites. This behavior is similar to Friedel oscillations, occurring in the ground state of Luttinger liquids in the presence of impurities [169]. This suggests, that the dissipative site may be conceived as a barrier, analogous to an obstacle represented by a additional potential contribution in the center. Moreover, attractive interactions result in the formation of density waves which expands towards the boundary.

As can be seen in Fig. 7.5, the expansion velocity is different for all cases. To give a quantitative statement regarding the time scales, we will continue by analyzing the properties of the time dependence and the most important contributions by employing the many-body adiabatic elimination method as derived in Sec. 3.3. Using the relation from Eq. 3.53 we consider only the first dissipative subspace corresponding to the eigenspace of $\mathcal{L}_0$ with the lowest non-vanishing real-part eigenvalue given by

$$\Lambda^1 = \left\{ |\mathcal{R}\rangle \otimes |\rho^1\rangle\langle\tilde{\rho}^1| \otimes \langle\tilde{\mathcal{R}}| \right\} \tag{7.7}$$

$$\text{where} \quad |\rho^1\rangle\langle\tilde{\rho}^1| \in \left\{ |0, 1, n_1\rangle\langle\tilde{n}_{-1}, 0, \tilde{n}_1|, \ |n_1, 1, 0\rangle\langle\tilde{n}_{-1}, 0, \tilde{n}_1|, \right.$$

$$\left. |n_{-1}, 0, n_1\rangle\langle\tilde{n}_{-1}, 1, 0|, \ |n_{-1}, 0, n_1\rangle\langle0, 1, \tilde{n}_1| \right\}$$

$$\text{and} \quad |\mathcal{R}\rangle, |\tilde{\mathcal{R}}\rangle \in \{|\{n_l\}\rangle \ : \ l \neq -1, 0, 1\} \,. \tag{7.8}$$

Note that this space is very large, as it only introduces restrictions on the central three sites, represented here by $|\tilde{\rho}^1\rangle\langle\tilde{\rho}^1|$. This gives the following effective master equation, valid for times $t \gg 1/\gamma$

$$\frac{\mathrm{d}}{\mathrm{d}t}\rho^0(t) \approx \mathcal{V}^{00}\rho^0(t) - \frac{1}{\lambda_1}\mathcal{V}^{01}\mathcal{V}^{10}\rho^0(t). \tag{7.9}$$

This equation describes the effective motion of the density matrix ρ^0 in the dissipation-free subspace. The second term in Eq. 7.9 can be expressed in terms of the application of fermionic operators on the density matrix $\rho^0(t)$ as derived in section B.1 of the appendix. The dynamics

is then described by

$$\frac{\mathrm{d}}{\mathrm{d}t}\rho^0(t) = \mathcal{V}^{00}\rho^0(t)$$

$$-J^2\left\{\left[\frac{2}{\gamma}\left(\hat{n}_{-1}+\hat{n}_1-2\hat{n}_{-1}\hat{n}_1+\hat{c}_{-1}^\dagger\hat{c}_1+\hat{c}_1^\dagger\hat{c}_{-1}\right)+2\frac{\frac{\gamma}{2}-iV}{\left(\frac{\gamma}{2}\right)^2+V^2}\hat{n}_{-1}\hat{n}_1\right]\rho^0(t)\right.$$

$$\left.+\rho^0(t)\left[\frac{2}{\gamma}\left(\hat{n}_{-1}+\hat{n}_1-2\hat{n}_{-1}\hat{n}_1+\hat{c}_{-1}^\dagger\hat{c}_1+\hat{c}_1^\dagger\hat{c}_{-1}\right)+2\frac{\frac{\gamma}{2}+iV}{\left(\frac{\gamma}{2}\right)^2+V^2}\hat{n}_{-1}\hat{n}_1\right]\right\},$$

(7.10)

with the local density operators $\hat{n}_{\pm1}$ of the sites next to the center and the creation and an-nihilation operators $\hat{c}_{\pm1}^{(\dagger)}$ on the same sites, respectively. This enables us now to compute the time-dependent change of the expectation value of the total particle number via $\frac{\mathrm{d}}{\mathrm{d}t}\langle N(t)\rangle \approx \mathrm{tr}[N\frac{\mathrm{d}}{\mathrm{d}t}\rho^0(t)]$. As the operator $\mathcal{L}_\mathcal{V}$ is particle number conserving, the first term on the right-hand side in Eq. 7.10 has no contribution to the evolution of this observable. Using the cyclic properties of the trace, we arrive at the following relation

$$\frac{\mathrm{d}}{\mathrm{d}t}\langle\hat{N}(t)\rangle = \mathrm{tr}\left(-4J^2\hat{N}\left[\frac{1}{\gamma}\left(\hat{n}_{-1}+\hat{n}_1+\hat{c}_{-1}^\dagger\hat{c}_1+\hat{c}_1^\dagger\hat{c}_{-1}-2\hat{n}_{-1}\hat{n}_1\right)\right.\right.$$

$$\left.\left.+\frac{\gamma}{2\left[\left(\frac{\gamma}{2}\right)^2+V^2\right]}\hat{n}_{-1}\hat{n}_1\right]\rho^0(t)\right).$$

(7.11)

As the density of the sites in the center is constant for the regarded time span (cf. Fig. 7.5), we decouple the expectation value of N with the local occupations and replace the latter with the constant value $n_{\pm1}$, which is equal for both sides due to the mirror symmetry of the model. We do the same for the correlator connecting the sites next to the center and represent $\langle c_{-1}^\dagger c_1\rangle$ as $C_{-1,1}$. Therefore, the density evolution is governed by

$$\frac{\mathrm{d}}{\mathrm{d}t}\langle N(t)\rangle = \left(-\frac{8J^2}{\gamma}\left[n_{\pm1}+\mathrm{Re}\left(C_{-1,1}\right)\right]+\frac{8J^2}{\gamma}n_{\pm1}^2-8J^2\frac{\gamma}{\gamma^2+(2V)^2}n_{\pm1}^2\right)\langle N(t)\rangle. \quad (7.12)$$

The differential equation is solved by an exponential ansatz, where the corresponding time scale τ_2 is given by the inverse of the prefactor of the right-hand side of Eq. 7.12. Analyzing the expression reveals, that in the limit of the adiabatic elimination approximation of strong dissipation, the relaxation time scale in the time region $t \gg 1/\gamma$ is proportional to γ, given that $\hbar\gamma/J \gg V/J$. This result is known as the Zeno effect, where here the strong particle loss plays the role of the continuous measurement process, which slows down the system dynamics.

In Fig. 7.6, we show the time scales obtained from exponential fits in the second time regime as a function of the dissipation strength. The time step needs to be adapted here to still be able to resolve dynamics on the scale of $1/\gamma$ for very strong dissipations. It can be deduced, that for low dissipation, the overall dynamics is still determined by the initial emptying of the central
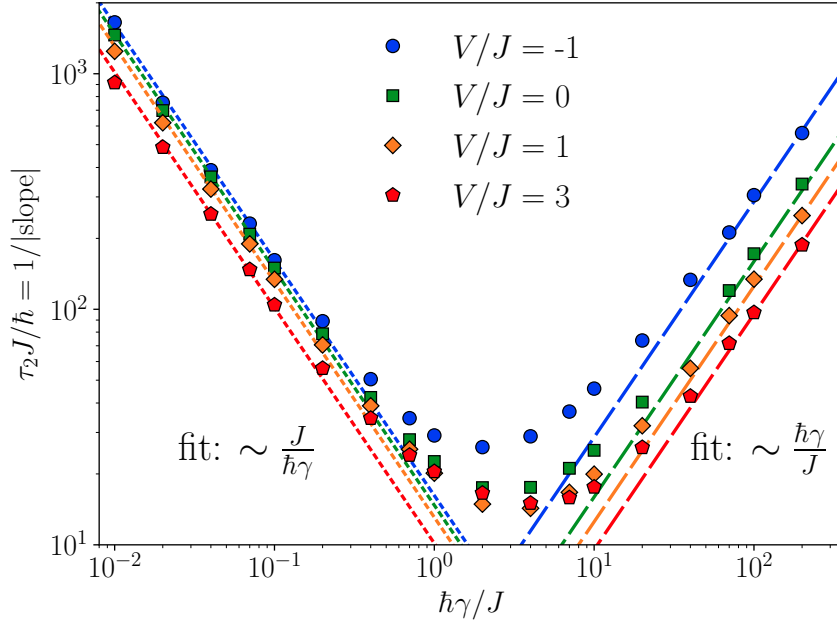
Figure 7.6.: Dissipation dependence of the time scale τ_2 of the second dynamic regime, accessed by exponential fits of the total particle number evolution. Dotted lines are fits with $1/\gamma$ and dashed lines linear fits proportional to γ. The transition to the Zeno regime is displayed for different interaction strengths. The considered size was $L = 15$, and the numerical tMPS time step is $\Delta t J/\hbar = 0.05$ for $\hbar\gamma/J \leq 10$ and $\Delta t J/\hbar = 0.01$ for $\hbar\gamma/J > 10$. The average is done over 10^4 trajectories and an exact MPS representation.

site, which results in an increasingly faster decay for larger dissipative couplings, which scales as $1/\gamma$. However, when increasing the loss rate further, a minimum is passed and the linear Zeno regime is reached, as can be seen from the good agreement with the linear fits. The starting point of the Zeno limit is influenced by the interaction. A look at Eq. 7.12 shows, that stronger interactions require higher loss rates for the time scale dependence to be dominated by the dissipation. Note that the time scales extracted from Eq. 7.12 also depend on the density next to the center, which is quite different for the different interaction scenarios presented in Fig. 7.5. The higher density caused by the oscillations for $V/J = 1$ results in a faster dynamics than in the free case, which in turn is faster than in the case of $V/J = -1$. It is important to state, that in principle both, $n_{\pm 1}$ and $C_{-1,1}$, depend on γ, whereby the dependency for the strong dissipations is found to be almost constant from the numerics, so that their influence on the time scale behavior with γ is negligible. A comparison with the extracted time scales for $\hbar\gamma/J = 20$ in Fig. 7.6 also recovers the specific behavior, regarding different expansion velocities for different interactions from Fig. 7.5.

7.3. Summary of results of Chap. 7 and outlook

In this chapter, we presented the detection of three different dynamical regimes found by numerically exact simulations for the full quantum time evolution of a dissipative chain of interacting spinless fermions. While the first regime could be assigned to the clearing of the initially finite occupation of the central site by the Markovian loss and the last regime is dominated by boundary effects, the second region is characterized by the emergence of a quasi-stationary density distribution around the center. Depending on the type of the interaction and its strength, the form of this meta stable state is quite different. Nevertheless, the evolution in this time region can be generally explained by the Zeno effect, which we could trace back to an effective motion in the dissipation-free subspace using adiabatic elimination.

As parts of this project can still be considered as work in progress, we give a short outline on future directions. While we were able to extract the overall Zeno behavior, marked by the linear relation of the time scale with the dissipation, the exact time scale values could not be recovered using the expectation values of $n_\pm$ and $C_{-1,1}$ as provided by our numerics. As we have used a mean-field decoupling of the total particle number N, it is worthwhile focusing on the affect of this decoupling in further detail. Moreover, a comparison with the results for transport properties found in Ref. [181], regarding anomalous reflection and transmission effects according to the dissipative site for momenta close to the Fermi momentum, is desirable. In order to do so, the definition of observables which are measurable with MCWF techniques and also reflect these aspects are required.

Chapter 8

Conclusion

In this thesis we have investigated the dynamics of open quantum systems in several different physical examples. The open nature of a quantum system is represented by a coupling to an external Markovian environment which establishes the notion of dissipation to the system. The main contribution of this work is twofold. First, we explore how environmental effects can be used to create interesting steady states which are approached exponentially fast in time and are stable against perturbations. This is on par with current experimental efforts that aim for the engineering of environments to enable the preparation of complex quantum states. Secondly, we analyze the properties of the dynamics before reaching the steady regime. This concerns the parameter dependence of the time scale which determines how fast a steady state is approached as well as the identification of the decisive mechanisms which govern the effective evolution.

Perhaps the most interesting settings are found in systems which combine dissipation with strongly interacting many-body systems, so that a competition among different processes arises. However, as this makes the access to the full time evolution very demanding, we explained how we transfer common efficient numeric approaches to the framework of open system and how approximations can provide analytical insights. In particular, we describe the implementation of open system adaptions of the time-dependent matrix product state algorithms with two different techniques; the Monte-Carlo wave function method and the purification method.

We demonstrate how the dissipative dynamics can be used as a stable way to prepare quantum states. A system of cold fermionic atoms confined to a ladder-shape potential created by an optical lattice has been designed such, that the phase imprint of an external pump laser acts as an artificial magnetic field for the fermions. The coupling to a cavity mode with photon losses then introduces the controlled addition of dissipation. We emphasize how it is possible to drive the system towards desired steady states by adapting the external parameters. In the presence of an induced artificial magnetic field, the steady state is a topologically non-trivial state. Thus, this system can potentially be used to switch between different topological phases. Concerning the attractor dynamics in the emergence of the steady state, we show that large dissipation strengths cause a Zeno behavior which can be perceived as a continuous measurement process that prevents the evolution of the system.

Aiming at a better understanding for the open system dynamics of interacting many-body

system, we investigated the propagation of correlations in spin-½ XXZ chains where each spin is coupled to its nearest neighbors and additionally to a Markovian environment causing dephasing. The numerically exact evaluation of two-time correlation functions enables us to distinguish three different time regimes in the evolution towards the steady state. Most notably, we detected an occurrence of aging dynamics characterized by a scaling collapse of the correlations on a slow algebraic decay. Additionally, we outline how the dissipative dynamics can be employed to extract information on the spectrum of the closed system Hamiltonian.

Finally, we discover Zeno dynamics in the evolution of interacting cold atoms in one dimension which are suddenly subjected to locally constrained particle losses. More precisely, after the initial emptying of the region the loss applies to, we observe the emergence of a quasi-stationary regime around this region which surprisingly shows a slow-down of the total particle loss when increasing the dissipative coupling.

In summary, the knowledge gained from this extensive study will potentially help in developing novel approaches to stabilize quantum states absent in equilibrium. For example, the open system preparation of a chiral state in a cavity poses a first step on the path of combining topological protection and open system control. A natural extension is to consider two-dimensional lattice geometries, such that a separation of bulk and system boundary is possible and chiral edge states can be related rigorously to the topology of the bulk. A related study for the steady state in this context is presented in Ref. [20]. Furthermore, an experimental realization requires the ability to create optical lattices for ultracold fermionic atoms in cavities as it has recently been implemented for the bosonic case [141, 182]. Moreover, it was found that the dynamics of open systems differs greatly from the equilibrium evolution. For example, we see a transition to a regime with diffusively propagating two-time correlation functions in interacting open spin-½ chains. In this context, further research is needed to achieve a more general understanding of the impact of the open nature on the evolution. Finally, the work presented here is based on the assumption of a Markovian system-environment coupling. While this is typically well-fulfilled in quantum optical applications, many examples, e.g. from the field of solid state physics, exhibit non-negligible memory effects of the environment. To cover this important situations as well, non-Markovian environments need to be taken into account. While this task has been addressed in the past [6], it adds an additional layer of complexity compared to the Lindblad dynamics and therefore leaves room for further development.

Appendix regarding Chap. 6

A.1. Auxiliary calculation for many-body adiabatic elimination

Using 3.53 while concentrating on the contributions of every single eigen vector, the time evolution reads as

$$\frac{\mathrm{d}}{\mathrm{d}t}\rho_j^\alpha(t) = \lambda_{\alpha,j}\rho_j^\alpha(t) + \sum_{k,\beta\neq\alpha} \mathcal{V}_{j,k}^{\alpha\beta}\rho_k^\beta(t) \equiv \lambda_{\alpha,j}\rho_j^\alpha(t) + b(t). \tag{A.1}$$

Solving the homogeneous part of this differential equation (i.e. $b(t) \equiv 0$) yields $\rho_j^\alpha(t) = Ce^{\lambda_{\alpha,j}t}$. Using variation of constants a solution of the inhomogeneous equation is given by $\rho_j^\alpha(t) = e^{\lambda_{\alpha,j}t}\int_0^t \mathrm{d}t' e^{-\lambda_{\alpha,j}t'}b(t')$ resulting in a general solution of Eq. A.1 as

$$\rho_j^\alpha(t) = \rho_j^\alpha(0)e^{\lambda_{\alpha,j}t} + \sum_{k,\beta\neq\alpha}\left[e^{\lambda_{\alpha,j}t}\int_0^t \mathrm{d}t' e^{-\lambda_{\alpha,j}t'}\mathcal{V}_{j,k}^{\alpha\beta}\rho_k^\beta(t')\right]. \tag{A.2}$$

As also mentioned in section 3.3, contributions from higher subspaces decay exponentially, where the non-vanishing negative real parts of the eigenvalues and therefore the time scales are proportional to γ. So the essential part of the long-time behavior for $t \gg 1/\gamma$ is dominated by the dynamics around the dissipation-free subspace. Therefore, the next step is to identify the most important contributions to $\rho_j^0(t)$ defined by Eq. A.1. First of all, the integral appearing in the last equation can be solved by integrating by parts, giving

$$\int_0^t \mathrm{d}t' e^{-\lambda_{\alpha,j}t'}\mathcal{V}_{j,k}^{\alpha\beta}\rho_k^\beta(t') = -\frac{1}{\lambda_{\alpha,j}}e^{-\lambda_{\alpha,j}t}\mathcal{V}_{j,k}^{\alpha,\beta}\rho_k^\beta(t) + \underbrace{\int_0^t \mathrm{d}t'\left[\frac{e^{-\lambda_{\alpha,j}t'}}{\lambda_{\alpha,j}}\mathcal{V}_{j,k}^{\alpha,\beta}\frac{\mathrm{d}}{\mathrm{d}t'}(\rho_k^\beta(t'))\right]}_{\mathcal{O}(1/\lambda_{\alpha,j}^2)}. \tag{A.3}$$

The expression for $\rho_j^\alpha(t)$ for $\alpha \neq 0$ is then approximately

$$\rho_j^\alpha(t) \approx \underbrace{\rho_j^\alpha(0)e^{\lambda_{\alpha,j}t}}_{\text{decays exp.}} - \frac{1}{\lambda_{\alpha,j}} \sum_{k,\beta\neq\alpha} \mathcal{V}_{j,k}^{\alpha,\beta} \rho_k^\beta(t)$$

$$\approx -\frac{1}{\lambda_{\alpha,j}} \sum_k \mathcal{V}_{j,k}^{\alpha,0} \left[\rho_k^0(t) \underbrace{e^{\lambda_{0,k}t}}_{=1} - \frac{1}{\lambda_{0,k}} \underbrace{\sum_{l,\beta\neq 0} \mathcal{V}_{j,l}^{0,\beta} \rho_l^\beta(t)}_{\mathcal{O}\left(1/\lambda_{0,k}\lambda_{\beta,l}\right)} \right]$$

$$- \frac{1}{\lambda_{\alpha,j}} \sum_{k,\beta\neq\alpha\neq 0} \mathcal{V}_{j,k}^{\alpha,\beta} \left[\rho_k^\beta(t) \underbrace{e^{\lambda_{\beta,k}t}}_{\text{decays exp.}} - \frac{1}{\lambda_{\beta,k}} \underbrace{\sum_{l,\beta'\neq\beta} \mathcal{V}_{j,l}^{\beta,\beta'} \rho_l^{\beta'}(t)}_{\mathcal{O}\left(1/\lambda_{\beta,k}\lambda_{\beta',l}\right)} \right]$$

$$\approx -\frac{1}{\lambda_{\alpha,j}} \sum_k \mathcal{V}_{j,k}^{\alpha,0} \rho_k^0(t). \tag{A.4}$$

Finally, we arrive at

$$\frac{d}{dt}\rho_j^0(t) = \lambda_{0j}\rho_j^0(t) + \sum_{k,\alpha\neq 0} \mathcal{V}_{j,k}^{0\alpha} \rho_k^\alpha(t)$$

$$\approx \lambda_{0,j}\rho_j^0(t) + \sum_{k,\alpha\neq 0} \mathcal{V}_{j,k}^{0\alpha} \left(-\frac{1}{\lambda_{\alpha,k}} \sum_l \mathcal{V}_{k,l}^{\alpha,0} \rho_l^0(t) \right) \tag{A.5}$$

for the effective dynamics in the dissipation-free subspace. In a more compact form, this can be expressed as

$$\frac{d}{dt}\rho^0(t) = \mathcal{L}_0\rho^0(t) - \sum_{\alpha\neq 0} \mathcal{V}^{0,\alpha}\mathcal{L}_0^{-1}\mathcal{V}^{\alpha,0}\rho^0(t). \tag{A.6}$$

A.2. Derivation of the classical master equation for the XXZ-chain using many-body adiabatic elimination

Here we will give a more detailed derivation of Eq. 6.8 in the main text, using the adiabatic elimination approximation from Eq. 6.7. To begin, we start with the general Lindblad equation for a general state of the dissipation-free subspace Λ^0 and apply the superoperator $\mathcal{L}$ which is

A.2 Derivation of the classical master equation for the XXZ-chain using many-body adiabatic elimination

split up in the parts $\mathcal{L}_0$ and $\mathcal{L}_\mathcal{V}$ from Eq. 6.5 and 6.6.

$$\frac{d}{dt} \sum_{\vec{\sigma}} \rho^0(\vec{\sigma}, t) = \sum_{\vec{\sigma}} \rho^0(\vec{\sigma}, t) \left(\underbrace{\mathcal{L}_0 |\vec{\sigma}\rangle\langle\vec{\sigma}|}_{=0} + \mathcal{L}_\mathcal{V} |\vec{\sigma}\rangle\langle\vec{\sigma}| \right) \tag{A.7}$$

$$= \sum_{\vec{\sigma}} \rho^0(\vec{\sigma}, t) \frac{(-iJ_x)}{2} \sum_{j=1}^{L-1} \left[S_j^+ S_{j+1}^- + S_j^- S_{j+1}^-, |\sigma_1 \ldots \sigma_L\rangle\langle\sigma_1 \ldots \sigma_L| \right] \tag{A.8}$$

$$= \sum_{\vec{\sigma}} \rho^0(\vec{\sigma}, t) \frac{(-iJ_x)}{2} \sum_{j=1}^{L-1} \delta_{\sigma_j, \bar{\sigma}_{j+1}} \left(|\sigma_1 \ldots \sigma_{j+1}\sigma_j \ldots \sigma_L\rangle\langle\sigma_1 \ldots \sigma_L| \right.$$

$$\left. - |\sigma_1 \ldots \sigma_L\rangle\langle\sigma_1 \ldots \sigma_{j+1}\sigma_j \ldots \sigma_L| \right). \tag{A.9}$$

Following Eq. 6.7, we need to calculate the eigenvalues of $\mathcal{L}_0$ of all the states from Eq. A.9. For this we compute

$$\mathcal{L}_0 |\sigma_1 \ldots \sigma_{j+1}\sigma_j \ldots \sigma_L\rangle\langle\sigma_1 \ldots \sigma_L|$$

$$= -iJ_z \left[\sum_l S_l^z S_{l+1}^z, |\sigma_1 \ldots \sigma_{j+1}\sigma_j \ldots \sigma_L\rangle\langle\sigma_1 \ldots \sigma_L| \right]$$

$$\gamma \sum_l \left(S_l^z |\sigma_1 \ldots \sigma_{j+1}\sigma_j \ldots \sigma_L\rangle\langle\sigma_1 \ldots \sigma_L| S_l^z - \frac{1}{4} |\sigma_1 \ldots \sigma_{j+1}\sigma_j \ldots \sigma_L\rangle\langle\sigma_1 \ldots \sigma_L| \right)$$

$$= \left\{ -\frac{iJ_z}{4} \left(\sigma_{j-1}\sigma_{j+1} + \sigma_j\sigma_{j+2} - \sigma_{j-1}\sigma_j - \sigma_{j+1}\sigma_{j+2} \right) + \gamma \left(\frac{1}{2}\sigma_j\sigma_{j+1} - \frac{1}{2} \right) \right\}$$

$$\times |\sigma_1 \ldots \sigma_{j+1}\sigma_j \ldots \sigma_L\rangle\langle\sigma_1 \ldots \sigma_L|. \tag{A.10}$$

This means the corresponding eigenvalues, needed for the adiabatic elimination are

$$\lambda_{j,\vec{\sigma}} = -\frac{iJ_z}{4} \underbrace{\left(\sigma_{j-1}\sigma_{j+1} + \sigma_j\sigma_{j+2} - \sigma_{j-1}\sigma_j - \sigma_{j+1}\sigma_{j+2} \right)}_{\equiv \alpha} + \gamma \left(\frac{1}{2}\sigma_j\sigma_{j+1} - \frac{1}{2} \right). \tag{A.11}$$

By mapping this back with another application of $\mathcal{L}_\mathcal{V}$, we can calculate the approximate dissipative motion, represented solely by states of the dissipation-free subspace:

$$\frac{d}{dt} \sum_{\vec{\sigma}} \rho^0(\vec{\sigma}, t) = \sum_{\vec{\sigma}} \rho^0(\vec{\sigma}, t) \left(\frac{-iJ_x}{2} \sum_j \delta_{\sigma_j, \bar{\sigma}_{j+1}} \frac{iJ_x}{2} \left(\frac{1}{\lambda_{j,\vec{\sigma}}} + \frac{1}{\lambda_{j,\vec{\sigma}}^*} \right) \right)$$

$$\left[\left(|\sigma_1 \ldots \sigma_L\rangle\langle\sigma_1 \ldots \sigma_L| - |\sigma_1 \ldots \sigma_{j+1}\sigma_j \ldots \sigma_L\rangle\langle\sigma_1 \ldots \sigma_{j+1}\sigma_j \ldots \sigma_L| \right) \right]. \tag{A.12}$$

Inserting the eigenvalues and simplifying the outcome finally leads to Eq. 6.8 for the time-dependent weights of the dissipation-free space.

A.3. Solution for the diffusive equation for the effective long-time dynamics of the XXZ-chain initially prepared in the Néel state

The following calculation is dedicated to the derivation of the solution presented in Eq. 6.14 of the diffusion equation from Eq. 6.13, i.e

$$\frac{\partial}{\partial t_1}\tilde{C}_d(t_1, t_1) = D\left(\tilde{C}_{d+1} + \tilde{C}_{d-1} - 2\tilde{C}_d\right), \qquad \text{for } d \in \left\{-\frac{L}{2}+2, \ldots, \frac{L}{2}\right\}, \qquad \text{(A.13)}$$

where $d < 0$ here corresponds to $d - 1$ in the actual lattice, as explained in the main text. We also use here periodic boundary conditions, so that $\tilde{C}_{-\frac{L}{2}+1} = \tilde{C}_{\frac{L}{2}}$ and $\tilde{C}_{-\frac{L}{2}+2} = \tilde{C}_{\frac{L}{2}+1}$. The next step is to apply a Fourier transformation to the correlation function

$$\tilde{C}_{k_m} = \sum_{d=-\frac{L}{2}+2}^{\frac{L}{2}} e^{-ik_m d}\tilde{C}_d \ , \text{ with } k_m = \frac{2\pi m}{L-1}, m \in \{0, \ldots, L-2\}$$

$$\tilde{C}_d = \frac{1}{L-1}\sum_{m=0}^{L-2} e^{ik_m d}\tilde{C}_{k_m}$$

This transforms Eq. A.13 to

$$\frac{\partial \tilde{C}_{k_m}(t_1, t_1)}{\partial t_1} = 2D(\cos(k_m) - 1)\tilde{C}_{k_m}(t_1), \qquad \text{(A.14)}$$

with the general solution

$$\tilde{C}_{k_m}(t_1) = e^{2Dt_1(\cos(k_m)-1)}\tilde{C}_{k_m}(t_1 = 0). \qquad \text{(A.15)}$$

Consequently, we also need to compute the Fourier transform of the initial condition which reads for the Néel state in terms of the defined shifted distances as

$$\tilde{C}_{k_m}(t_1 = 0) = \text{F.T.}\left[\tilde{C}_d(t_1 = 0)\right] = \text{F.T.}\left[\frac{1}{4}\left(\sum_{d'=-L/2+1}^{L/2} (-1)^{d'}(1 - 2\delta_{d'\leq 0})\delta_{d,d'}\right)\right] \qquad \text{(A.16)}$$

$$= \frac{1}{4}\sum_{d=-L/2+2}^{L/2} e^{-ik_m d}(-1)^d(1 - 2\delta_{d\leq 0}). \qquad \text{(A.17)}$$

A.4 Detailed calculation for the derivation of the dominant scaling of the two-time correlations

Inserting this back into Eq. A.15 and transforming back to real space gives the full solution

$$
\tilde{C}_d(t_1, t_1) = \frac{1}{L-1} \sum_{m=0}^{L-2} e^{ik_m d} \tilde{C}_{k_m}(t_1)
$$

$$
= \frac{1}{4} \sum_{d'=-L/2+2}^{L/2} \left[(-1)^{d'} (1 - 2\delta_{d'\leq 0}) \frac{1}{L-1} \sum_{m=0}^{L-2} e^{-ik_m(d'-d)} e^{2Dt_1(\cos(k_m)-1)} \right]. \quad \text{(A.18)}
$$

By using the continuum limit in k-space, valid for large system sizes, we can replace the momenta sums by integrals $\frac{1}{L-1} \sum_{m=0}^{L-2} \longrightarrow \frac{1}{2\pi} \int_0^{2\pi} dk$,

$$
\tilde{C}_d(t_1, t_1) = \frac{1}{4} \sum_{d'=-L/2+2}^{L/2} (-1)^{d'} (1 - 2\delta_{d'\leq 0}) e^{-2Dt_1} \int_0^{2\pi} \frac{dk}{2\pi} e^{-ik(d'-d)} e^{2Dt_1 \cos(k)}. \quad \text{(A.19)}
$$

At this point, it is now possible to use the identity for the Bessel functions of first kind mentioned in the main text, stating $I_n(z) = \int_0^{2\pi} \frac{dk}{2\pi} e^{-ikn} e^{z \cos k}$ for $n \in \mathbb{Z}$. This leads to the solution as presented in the main text

$$
\tilde{C}_d(t_1, t_1) = \frac{1}{4} e^{-2Dt_1} \sum_{d'=-L/2+2}^{L/2} \left[(-1)^{d'} (1 - 2\delta_{d'\leq 0}) I_{|d'-d|}(2Dt_1) \right]. \quad \text{(A.20)}
$$

A.4. Detailed calculation for the derivation of the dominant scaling of the two-time correlations

This part of the appendix contains side calculations related to section 6.5.3, which outlines and discusses the main steps to derive a scaling relation for the two-time correlation function $C_d(t_2, t_1) = \langle S_j^z(t_2) S_{j+d}^z(t_1) \rangle$ in the open XXZ spin chain in contact with an environment causing dephasing.

A.4.1. Intermediate representation of the two-time correlation functions

This section presents a detailed derivation of Eq.6.23 starting from the general solution of the found differential equation system from Eq. 6.22. In the following, we use the notation $\tau = t_2 - t_1$. We begin with splitting up the sum over correlation distances d' into subparts and rewrite the expression in terms of the shifted equal-time correlations $\tilde{C}_d(t_1, t_1)$ as introduced

earlier.

$$C_d(\tau, t_1) = e^{-D\tau} \left\{ \frac{1}{4} I_d(D\tau) + \sum_{d'=1}^{L/2} \tilde{C}_{d'}(t_1, t_1) I_{d'-d}(D\tau) + \sum_{d'=-\frac{L}{2}+1}^{-1} \tilde{C}_{d'+1}(t_1, t_1) I_{d'-d}(D\tau) \right.$$
$$\left. + \sum_{d'=-\frac{L}{2}+2}^{0} \tilde{C}_{d'}(t_1, t_1) I_{d'-d}(D\tau) - \sum_{d'=-\frac{L}{2}+2}^{0} \tilde{C}_{d'}(t_1, t_1) I_{d'-d}(D\tau) \right\}.$$

$$(A.21)$$

Next, we perform some rearrangements of the terms by noting that $\tilde{C}_{-d+1}(t_1, t_1)$ corresponds to $\tilde{C}_d(t_1, t_1)$.

$$C_d(\tau, t_1) = e^{-D\tau} \left\{ \frac{1}{4} I_d(D\tau) + \sum_{d'=-\frac{L}{2}+2}^{L/2} \tilde{C}_{d'}(t_1, t_1) I_{d'-d}(D\tau) \right.$$
$$\left. + \sum_{d'=-\frac{L}{2}+1}^{-1} \tilde{C}_{d'+1}(t_1, t_1) \left(I_{d'-d}(D\tau) - I_{d'+1-d}(D\tau) \right) \right\}$$
$$= e^{-D\tau} \left\{ \frac{1}{4} I_d(D\tau) + \underbrace{\sum_{d'=-\frac{L}{2}+2}^{L/2} \tilde{C}_{d'}(t_1, t_1) I_{d'-d}(D\tau)}_{\equiv T_2} \right.$$
$$\left. + \sum_{d'=1}^{L/2-1} C_{d'}(t_1, t_1) \left(I_{d'+d}(D\tau) - I_{d'+d-1}(D\tau) \right) \right\}.$$

We continue, by first considering the second term which we denote by T_2. For this, we need the solution of the shifted equal-time correlations from Eq. 6.14 which can be rewritten as

$$\tilde{C}_d(t_1, t_1) = \frac{1}{4} e^{-2Dt_1} \left(-I_d(2Dt_1) + \sum_{d'=-\frac{L}{2}+2}^{L/2} (-1)^{d'} \text{sign}(d') I_{d'-d}(2Dt_1) \right).$$

A.4 Detailed calculation for the derivation of the dominant scaling of the two-time correlations

Inserting this into the relation for T_2, we arrive at

$$
T_2 = \sum_{d'=-\frac{L}{2}+2}^{L/2} I_{d'-d}(D\tau) \frac{\mathrm{e}^{-2Dt_1}}{4} \left(-I_{d'}(2Dt_1) + \sum_{d''=-\frac{L}{2}+2}^{L/2} (-1)^{d''} \mathrm{sign}(d'') I_{d''-d'}(2Dt_1) I_{d'-d}(2D\tau) \right)
$$

$$
= \frac{\mathrm{e}^{-2Dt_1}}{4} \Bigg\{ - \underbrace{\sum_{d'=-\frac{L}{2}+2}^{L/2} I_{d'-d}(D\tau) I_{d'}(2Dt_1)}_{\equiv T_{21}}
$$

$$
+ \underbrace{\sum_{d'=-\frac{L}{2}+2}^{L/2} \sum_{d''=-\frac{L}{2}+2}^{L/2} (-1)^{d''} \mathrm{sign}(d'') I_{d''-d'}(2Dt_1) I_{d'-d}(2D\tau)}_{\equiv T_{22}} \Bigg\}
$$

Now, we will take the limit for infinitely large system sizes, employ the integral relation for the Bessel functions and the sum representation of the delta function for the two terms which we defined as T_{21} and T_{22}.

$$
T_{21} \approx - \sum_{d'=-\infty}^{\infty} I_{d'}(2Dt_1) I_{d'-d}(D\tau)
$$

$$
\approx - \sum_{d'=-\infty}^{\infty} \int_0^{2\pi} \frac{\mathrm{d}k}{2\pi} \mathrm{e}^{-id'k} \mathrm{e}^{2Dt_1 \cos k} \int_0^{2\pi} \frac{\mathrm{d}k'}{2\pi} \mathrm{e}^{-i(d-d')k'} \mathrm{e}^{D\tau \cos k'}
$$

$$
= - \int_0^{2\pi} \frac{\mathrm{d}k}{2\pi} \mathrm{e}^{-idk} \mathrm{e}^{t_1+t_2} = -I_d(D(t_1+t_2))
$$

$$
T_{22} \approx - \sum_{d''=-\frac{L}{2}+2}^{L/2} (-1)^{d''} \mathrm{sign}(d'') \sum_{d'=-\infty}^{\infty} I_{d''-d'}(2Dt_1) I_{d'-d}(D\tau)
$$

$$
\overset{\text{use } T_{21}}{=} - \sum_{d''=-\frac{L}{2}+2}^{-1} (-1)^{d''} I_{d-d''}(D(t_1+t_2)) + \sum_{d''=1}^{L/2} (-1)^{d''} I_{d-d''}(D(t_1+t_2))
$$

$$
= - \sum_{j'-d=1}^{j'-d=L/2-2} (-1)^{j'+d} I_{j'}(D(t_2+t_1)) + \sum_{j'+d=1}^{j'+d=L/2} (-1)^{j'+d} I_{j'}(D(t_2+t_1))
$$

$$
\approx - \sum_{j'=1-d}^{\infty} (-1)^{j'+d} I_{j'}(D(t_2+t_1)) + \sum_{j'=1-d}^{\infty} (-1)^{j'+d} I_{j'}(D(t_2+t_1))
$$

$$
= \begin{cases} I_d(D(t_2+t_1)) + (-1)^d \sum_{j'=1-d}^{d-1} (-1)^{j'} I_{j'}(D(t_2+t_1)) & : d > 0 \\ 0 & : d = 0 \end{cases}
$$

Collecting all terms, we arrive at Eq. 6.23 from the main text which we were to derive in this section.

A.4.2. Scaling of $G_d(t_2, t_1)$ as one part of the two-time correlation functions

This section covers a complete discussion of the scaling of $G_d(t_2, t_1)$ which itself is defined in Eq. 6.24 and is one of in total four terms characterizing the long-term behavior of the two-time correlation function $\langle S_j^z(t_2)S_{j+d}^z(t_1)\rangle$. We begin with extracting the decisive contributions of the modified Bessel functions. To do so, we employ the asymptotic expansion of the modified Bessel function, valid for large arguments $|z| \gg 1$ and integer order ν, as introduced in equation 9.7.1 of [171]

$$
\begin{aligned}
I_\nu &= \frac{e^z}{\sqrt{2\pi z}}\left(1 - \frac{4\nu^2 - 1}{8z} + \frac{(4\nu^2 - 1)(4\nu^2 - 9)}{2!(8z)^2} - \frac{(4\nu^2 - 1)(4\nu^2 - 9)(4\nu^2 - 25)}{3!(8z)^3} + \dots\right) \\
&= \frac{e^z}{\sqrt{2\pi z}}\sum_{k=0}^{\infty}\frac{(-1)^k}{k!}\frac{1}{(8z)^k}a_k(z)
\end{aligned}
$$

$$
\text{with: } a_k(z) = \begin{cases} 1 & : k = 0 \\ (4\nu^2 - 1)(4\nu^2 - 9)(4\nu^2 - 25)\dots & : \text{else} \end{cases}.
$$

From Eq. 6.14 we find that the equal-time correlations for large systems $L \gg 1$ scale as

$$
C_{d'}(t_1, t_1) \sim -\frac{1}{4}e^{-2Dt_1}I_{d'}(2Dt_1). \tag{A.22}
$$

We simplify this now by using the asymptotic series representation of $I_{d'(2Dt_1)}$ and work out the limit of vanishing lattice spacing a.

$$
\begin{aligned}
I_{d'}(2Dt_1) &\sim \frac{e^{2Dt_1}}{\sqrt{2\pi(2Dt_1)}}\sum_{k=0}^{\infty}\frac{(-1)^k}{k!}\frac{1}{(8 \cdot 2Dt_1)^k}a_k(d') \\
&\overset{d' \equiv l'/a}{\sim} \frac{e^{2Dt_1}}{\sqrt{2\pi(2Dt_1)}}\sum_{k=0}^{\infty}\frac{(-1)^k}{k!}\frac{1}{(8 \cdot 2Dt_1 a^2)^k}\left[(4l'^2 - 1)(4l'^2 - 9)\dots\right] \\
&\xrightarrow{a\to 0} \frac{e^{2Dt_1}}{\sqrt{2\pi(2Dt_1)}}\sum_{k=0}^{\infty}\frac{(-1)^k}{k!}\left(\frac{l'^2}{8 \cdot 2Dt_1 a^2}\right)^k \\
&\sim \frac{e^{2Dt_1}}{\sqrt{2\pi(2Dt_1)}}e^{-\frac{1}{2}\frac{d'^2}{2Dt_1}}.
\end{aligned}
$$

Next we insert this result into the expression for the equal-time correlation, and insert this again in the relation for $G_d(t_2, t_1)$. Approximating the appearing Bessel functions then by the

A.4 Detailed calculation for the derivation of the dominant scaling of the two-time correlations

first terms of the expansion yields the following

$$
G_d(t_2, t_1) \sim -\mathrm{e}^{-D(t_2-t_1)} \frac{1}{4\sqrt{2\pi(2Dt_1)}} \sum_{d'=1}^{\infty} \mathrm{e}^{-\frac{d'^2}{2(2Dt_1)}} \left[I_{d+d'}(D(t2_-t_1)) - I_{d+d'-1}(D(t_2-t_1))\right]
$$

$$
\sim -\mathrm{e}^{-D(t_2-t_1)} \frac{1}{4\sqrt{2\pi(2Dt_1)}} \sum_{d'=1}^{\infty} \mathrm{e}^{-\frac{d'^2}{2(2Dt_1)}} \frac{\mathrm{e}^{D(t_2-t_1)}}{\sqrt{2\pi D(t_2-t_1)}} \times
$$

$$
\times \left[1 - \frac{4(d+d')^2 - 1}{8D(t_2-t_1)} - 1\frac{4(d+d'+1)^2 - 1}{8D(t_2-t_1)}\right]
$$

$$
\sim -\frac{1}{4} \frac{1}{(2\pi(2Dt_1))^{1/2}} \frac{1}{\sqrt{2\pi}} \frac{1}{(D(t_2-t_1))^{3/2}} \sum_{d'=1}^{\infty} \mathrm{e}^{-\frac{d'^2}{2(2Dt_1)}} \left(\frac{1}{2} - d - d'\right).
$$

To continue, we perform a continuum limit in the space of lattice distances, so that we can replace the sum over all distances by known integrals.

$$
G_d(t_2, t_1) \sim -\frac{1}{4} \frac{1}{(2\pi(2Dt_1))^{1/2}} \frac{1}{\sqrt{2\pi}} \frac{1}{(D(t_2-t_1))^{3/2}} \times
$$

$$
\times \left[\left(\frac{1}{2} - d\right) \int_1^{\infty} \mathrm{d}d' \mathrm{e}^{-\frac{d'^2}{2(2Dt_1)}} - \int_1^{\infty} \mathrm{d}d' d' \mathrm{e}^{-\frac{d'^2}{2(2Dt_1)}}\right]
$$

$$
\sim -\frac{1}{4} \frac{1}{(2\pi(2Dt_1))^{1/2}} \frac{1}{\sqrt{2\pi}} \frac{1}{(D(t_2-t_1))^{3/2}} \times
$$

$$
\times \left[\left(\frac{1}{2} - d\right) \sqrt{\pi Dt_1} \mathrm{erfc}\left(\frac{1}{2\sqrt{Dt_1}}\right) - 2Dt_1 \mathrm{e}^{-\frac{1}{4Dt_1}}\right].
$$

As we work out a long time limit scaling, we can Taylor expand the erfc and the exponential function. Doing so and only keeping the largest order in t_1 finally provides a scaling formula for $G_d(t_2, t_1)$, given by

$$
G_d(t_2, t_1) \sim \left(\frac{1}{2} - d\right)\left(-\sqrt{\frac{\pi}{2}} \frac{1}{8\pi} \frac{1}{(Dt_1)^{3/2}} \left(\frac{t_1}{t_2}\right)^{3/2}\right) + \frac{1}{4\pi\sqrt{2}} \frac{1}{Dt_1} \left(\frac{t_2}{t_1}\right)^{3/2}. \tag{A.23}
$$

A.4.3. Long-time scaling of the two-time correlations

While we have found the scaling for $G_d(t_2, t_1)$ already in the previous section, we still need to consider the remaining contributions to Eq. 6.23, which we will denote by $R_d(t_2, t_1)$. As this distinguishes between on-site correlations and $|d| \geq 1$, we will treat both cases separately,

starting with the latter

$$R_d(t_2, t_1) \sim \frac{1}{4} e^{-D(t_2-t_1)} I_d(D(t_2 - t_1)) + \frac{1}{4} e^{-D(t_2+t_1)} (-1)^d \sum_{j=1-d}^{d-1} (-1)^j I_j(D(t_2 + t_1))$$

$$\sim \frac{1}{4\sqrt{2\pi D(t_2 - t_1)}} \left(1 - \frac{4d^2 - 1}{8D(t_2 - t_1)}\right)$$

$$+ \frac{1}{4\sqrt{2\pi D(t_2 + t_1)}} (-1)^d \sum_{j=1-d}^{d-1} (-1)^j \left(1 - \frac{4j^2 - 1}{8D(t_1 + t_2)}\right).$$

Using that the sum formulas $\sum_{j=1-d}^{d-1}(-1)^j = (-1)^{d+1}$ and $\sum_{j=1-d}^{d-1}(-1)^j j^2 = (-1)^{d+1}(d-1)d$ we can further simplify the terms.

$$R_d(t_2, t_1) \sim \frac{1}{4\sqrt{2\pi D(t_2 - t_1)}} \left(1 - \frac{4d^2 - 1}{8D(t_2 - t_1)}\right)$$

$$+ \frac{1}{4\sqrt{2\pi D(t_2 + t_1)}} \left(-1 - \frac{1}{8D(t_2 + t_1)} + \frac{4(d-1)d}{8D(t_2 + t_1)}\right)$$

$$\sim \frac{1}{4\sqrt{2\pi}} \left\{ \left(\frac{1}{(D(t_2 - t_1))^{1/2}} - \frac{1}{(D(t_2 + t_1))^{1/2}}\right) - \frac{d}{2} \frac{1}{(D(t_2 + t_1))^{3/2}} \right.$$

$$\left. + \left(\frac{1}{8} - \frac{d^2}{2}\right) \left(\frac{1}{(D(t_2 - t_1))^{3/2}} - \frac{1}{(D(t_2 + t_1))^{3/2}}\right) \right\}.$$

Expanding each of the three terms for small ratios t_1/t_2, we end up with a scaling formula for $|d| \geq 1$

$$R_{d\geq 1}(t_2, t_1) \sim \frac{1}{4\sqrt{2\pi}} \frac{1}{\sqrt{Dt_1}} \left(\frac{t_1}{t_2}\right)^{3/2} - \frac{d}{8\sqrt{2\pi}} \frac{1}{(Dt_2)^{3/2}}. \tag{A.24}$$

Now turning to the case of $d = 0$, the remaining parts is given by

$$R_{d=0}(t_2, t_1) \sim \frac{1}{4} e^{-D(t_2-t_1)} I_0(D(t_2 - t_1)) - \frac{1}{4} e^{-D(t_2+t_1)} I_0(D(t_2 + t_1))$$

A.4 Detailed calculation for the derivation of the dominant scaling of the two-time correlations

Applying the same scheme as for $|d| \geq 1$, i.e. expansion of the modified Bessel functions and Taylor expansion of the remaining parts leads to the scaling result.

$$
\begin{aligned}
R_{d=0} &\sim \frac{1}{4\sqrt{2\pi D(t_2 - t_1)}}\left(1 + \frac{1}{8D(t_2 - t_1)}\right) - \frac{1}{4\sqrt{2\pi D(t_2 + t_1)}}\left(1 + \frac{1}{8D(t_2 + t_1)}\right) \\
&\sim \frac{1}{4\sqrt{2\pi}}\left[\left(\frac{1}{(D(t_2 - t_1))^{1/2}} - \frac{1}{(D(t_2 + t_1))^{1/2}}\right)\right. \\
&\qquad\qquad \left. + \left(\frac{1}{(D(t_2 - t_1))^{3/2}} - \frac{1}{(D(t_2 + t_1))^{3/2}}\right)\right] \\
&\sim \frac{1}{4\sqrt{2\pi D t_1}}\left(\frac{t_1}{t_2}\right)^{3/2}
\end{aligned}
$$

Now we have all ingredients for giving the final scaling formula for the two-time correlations normalized to the equal-time correlations, which scales as

$$
C_d(t_1, t_1) \sim \begin{cases} 1/4 & : d = 0 \\ -1/\sqrt{64\pi D t_1} & : d \geq 1 \end{cases}.
$$

In summary we end up with the following scaling relation as also mentioned and discussed in the main text:

$$
\frac{C_{d>0}(t_2, t_1)}{C_{d>0}(t_1, t_1)} \sim -\sqrt{2}\left(\frac{t_2}{t_1}\right)^{-3/2}\left[1 + \frac{1}{\sqrt{\pi}}(D t_1)^{-1/2} - \frac{1}{4}(D t_1)^{-1}\right], \tag{A.25}
$$
and
$$
\frac{C_{d=0}(t_2, t_1)}{C_{d=0}(t_1, t_1)} \sim \frac{1}{\sqrt{2\pi}}(D t_1)^{-1/2}\left(\frac{t_2}{t_1}\right)^{-\frac{3}{2}}\left[1 + \frac{1}{\sqrt{\pi}}(D t_1)^{-1/2} - \frac{1}{4}(D t_1)^{-1}\right]. \tag{A.26}
$$

Appendix B

Appendix regarding Chap. 7

B.1. Derivation of the adiabatic elimination of the first dissipative subspace

Here we present a calculation of the second term of Eq. 7.9 using the definitions of $\mathcal{L}_0$ and $\mathcal{L}_\mathcal{V}$ from Eq. 7.5. Let us examine the effect of the application of $-\frac{1}{\lambda_1}\mathcal{V}^{01}\mathcal{V}^{10}$ on one basis state of the dissipation-free subspace $|\dots n_{-1}\, 0\, n_1 \dots\rangle\langle\dots n'_{-1}\, 0\, n'_1 \dots|$, where n_l, n'_l are numbers, labeling the occupation at site l and can take the values zero or one. With the definition of the projectors on the dissipative space Λ_i as $\mathcal{P}_i$, we get

$$\frac{1}{\lambda_1}\mathcal{V}^{01}\mathcal{V}^{10}|\dots n_{-1}\, 0\, n_1 \dots\rangle\langle\dots n'_{-1}\, 0\, n'_1 \dots|$$

$$= (\mathcal{P}_0\mathcal{L}_\mathcal{V}\mathcal{P}_1)\frac{-1}{\lambda_1}(\mathcal{P}_1\mathcal{L}_\mathcal{V}\mathcal{P}_0)|\dots n_{-1}\, 0\, n_1 \dots\rangle\langle\dots n'_{-1}\, 0\, n'_1 \dots|$$

$$= (\mathcal{P}_0\mathcal{L}_\mathcal{V}\mathcal{P}_1)\frac{-1}{\lambda_1}iJ\bigg(n_{-1}|\dots 0\, 1\, n_1 \dots\rangle\langle\dots n'_{-1}\, 0\, n'_1 \dots|$$

$$+ n_1|\dots n_{-1}\, 1\, 0 \dots\rangle\langle\dots n'_{-1}\, 0\, n'_1 \dots|$$

$$- n'_{-1}|\dots n_{-1}\, 0\, n_1 \dots\rangle\langle\dots 0\, 1\, n'_1 \dots|$$

$$- n'_1|\dots n_{-1}\, 0\, n_1 \dots\rangle\langle\dots n'_{-1}\, 1\, 0 \dots|\bigg) = \dots \quad \text{(B.1)}$$

Applying $\mathcal{L}_0$ to this state allows the identification of the value of λ_1 to be

$$\lambda_1 = -\frac{\gamma}{2} - iV \cdot \begin{cases} n_1 \\ n_{-1} \\ -n'_1 \\ -n'_{-1} \end{cases} \quad \Rightarrow \quad -\frac{1}{\lambda_1} = \frac{\gamma/2 - iVn_l}{\left(\frac{\gamma}{2}\right)^2 + (Vn_l)^2} \quad \text{(B.2)}$$

B.1 Derivation of the adiabatic elimination of the first dissipative subspace

We can rewrite all four variants of the last term considering the two cases for each n_l of being either zero or one, so that

$$-\frac{1}{\lambda_1} = \frac{2}{\gamma}(1 - n_l) + \frac{\gamma/2 + iV}{\left(\frac{\gamma}{2}\right)^2 + V^2}n_l. \tag{B.3}$$

Plugging this into Eq. B.1 and applying the mapping back to Λ^0 yields

$$\begin{aligned}
\ldots = -J^2 \Bigg\{ & \Bigg[\left(\frac{2}{\gamma}(1 - n_1) + \frac{\gamma/2 - iV}{\left(\frac{\gamma}{2}\right)^2 + V^2}n_1 \right) n_{-1} + \left(\frac{2}{\gamma}(1 - n_{-1}) + \frac{\gamma/2 - iV}{\left(\frac{\gamma}{2}\right)^2 + V^2}n_{-1} \right) n_1 \\
& + \left(\frac{2}{\gamma}(1 - n_1') + \frac{\gamma/2 + iV}{\left(\frac{\gamma}{2}\right)^2 + V^2}n_1 \right) n_{-1}' + \left(\frac{2}{\gamma}(1 - n_{-1}') + \frac{\gamma/2 + -iV}{\left(\frac{\gamma}{2}\right)^2 + V^2}n_{-1}' \right) n_1' \Bigg] \times \\
& \times | \ldots n_{-1}\, 0\, n_1 \ldots \rangle \langle \ldots n_{-1}'\, 0\, n_1' \ldots | \\
& + \left(\frac{2}{\gamma}(1 - n_1) + \frac{\gamma/2 - iV}{\left(\frac{\gamma}{2}\right)^2 + V^2}n_1 \right) n_{-1}(1 - n_1) | \ldots 0\, 0\, 1 \ldots \rangle \langle \ldots n_{-1}'\, 0\, n_1' \ldots | \\
& + \left(\frac{2}{\gamma}(1 - n_{-1}) + \frac{\gamma/2 - iV}{\left(\frac{\gamma}{2}\right)^2 + V^2}n_{-1} \right) n_1(1 - n_{-1}) | \ldots 1\, 0\, 0 \ldots \rangle \langle \ldots n_{-1}'\, 0\, n_1' \ldots | \\
& + \left(\frac{2}{\gamma}(1 - n_1') + \frac{\gamma/2 + iV}{\left(\frac{\gamma}{2}\right)^2 + V^2}n_1' \right) n_{-1}'(1 - n_1') | \ldots n_{-1}\, 0\, n_1 \ldots \rangle \langle \ldots 0\, 0\, 1 \ldots | \\
& + \left(\frac{2}{\gamma}(1 - n_{-1}') + \frac{\gamma/2 + iV}{\left(\frac{\gamma}{2}\right)^2 + V^2}n_{-1}' \right) n_1'(1 - n_{-1}') | \ldots n_{-1}\, 0\, n_1 \ldots \rangle \langle \ldots 1\, 0\, 0 \ldots | \Bigg\} = \ldots
\end{aligned} \tag{B.4}$$

Noting that $(1 - n_l)^2 = (1 - n_l)$ and $n_l(1 - n_l) = 0$, allows the refactoring to

$$\begin{aligned}
\ldots = -J^2 \Bigg\{ & \Bigg[\frac{2}{\gamma} \left(n_{-1} + n_1 + n_{-1}' + n_1' - 2n_{-1}n_1 - 2n_{-1}'n_1' \right) \\
& + 2\frac{\gamma/2 - iV}{\left(\frac{\gamma}{2}\right)^2 + V^2}n_{-1}n_1 + 2\frac{\gamma/2 + iV}{\left(\frac{\gamma}{2}\right)^2 + V^2}n_{-1}'n_1' \Bigg] | \ldots n_{-1}\, 0\, n_1 \ldots \rangle \langle \ldots n_{-1}'\, 0\, n_1' \ldots | \\
& + \frac{2}{\gamma}n_{-1}(1 - n_1) | \ldots 0\, 0\, 1 \ldots \rangle \langle \ldots n_{-1}'\, 0\, n_1' \ldots | + \frac{2}{\gamma}n_1(1 - n_{-1}) | \ldots 1\, 0\, 0 \ldots \rangle \langle \ldots n_{-1}'\, 0\, n_1' \ldots | \\
& + \frac{2}{\gamma}n_{-1}'(1 - n_1') | \ldots n_{-1}\, 0\, n_1 \ldots \rangle \langle \ldots 0\, 0\, 1 \ldots | + \frac{2}{\gamma}n_1'(1 - n_{-1}') | \ldots n_{-1}\, 0\, n_1 \ldots \rangle \langle \ldots 1\, 0\, 0 \ldots | \Bigg\}
\end{aligned} \tag{B.5}$$

Finally, we can use that n_l is the eigenvalue of the local density operators $\hat{n}_l$ as well as that $\hat{c}_l^\dagger \hat{c}_{l'} |\{n\}\rangle = (1 - n_l)n_{l'} |\{n\}\rangle$. Replacing the eigenvalues with operators results in the following

140

relation

$$\ldots = -J^2 \left\{ \left[\frac{2}{\gamma} \left(\hat{n}_{-1} + \hat{n}_1 - 2\hat{n}_{-1}\hat{n}_1 + \hat{c}^\dagger_{-1}\hat{c}_1 + \hat{c}^\dagger_1\hat{c}_{-1} \right) \right. \right.$$

$$\left. + 2\frac{\gamma/2 - iV}{\left(\frac{\gamma}{2}\right)^2 + V^2} \hat{n}_{-1}\hat{n}_1 \right] \lvert \ldots n_{-1}\, 0\, n_1 \ldots \rangle \langle \ldots n'_{-1}\, 0\, n'_1 \ldots \rvert$$

$$+ \lvert \ldots n_{-1}\, 0\, n_1 \ldots \rangle \langle \ldots n'_{-1}\, 0\, n'_1 \ldots \rvert \left[\frac{2}{\gamma} \left(\hat{n}_{-1} + \hat{n}_1 - 2\hat{n}_{-1}\hat{n}_1 + \hat{c}^\dagger_{-1}\hat{c}_1 + \hat{c}^\dagger_1\hat{c}_{-1} \right) \right.$$

$$\left. \left. + 2\frac{\gamma/2 - iV}{\left(\frac{\gamma}{2}\right)^2 + V^2} \hat{n}_{-1}\hat{n}_1 \right] \right\}. \tag{B.6}$$

As this is the result for an arbitrary basis state of the dissipation-free subspace, it can be applied to any linear combination ρ^0 of these basis states. Therefore, we can describe the effective dynamics in Λ^0 by Eq. 7.10.

List of Figures

142

Bibliography

[1] Yongping Wu, Hongxing Cao, and Guolin Feng. Prospective Study on Applications of Non-Equilibrium Thermodynamics to Climate Modeling. *Journal of Coastal Research*, pages 342–347, 2015.

[2] Alpha A. Lee, Dominic Vella, and John S. Wettlaufer. Fluctuation spectra and force generation in nonequilibrium systems. *Proceedings of the National Academy of Sciences*, 2017.

[3] Dirk Helbing. Traffic and related self-driven many-particle systems. *Rev. Mod. Phys.*, 73:1067–1141, Dec 2001.

[4] Herbert B Callen. *Thermodynamics and an introduction to thermostatistics; 2nd ed.* Wiley, New York, NY, 1985.

[5] C. W. Gardiner and P. Zoller. *Quantum Noise.* Springer, second edition, 2000.

[6] H. P. Breuer and F. Petruccione. *The theory of open quantum systems.* Oxford University Press, Oxford, 2002.

[7] S. Diehl, A. Micheli, A. Kantian, B. Kraus, H. P. Büchler, and P. Zoller. Quantum states and phases in driven open quantum systems with cold atoms. *Nature Physics*, 4, 09 2008.

[8] T Schulte-Herbrueggen, A Spoerl, N Khaneja, and S J Glaser. Optimal control for generating quantum gates in open dissipative systems. *Journal of Physics B: Atomic, Molecular and Optical Physics*, 44(15):154013, jul 2011.

[9] Heinz-Peter Breuer, Elsi-Mari Laine, Jyrki Piilo, and Bassano Vacchini. Colloquium: Non-Markovian dynamics in open quantum systems. *Rev. Mod. Phys.*, 88:021002, Apr 2016.

[10] Alexander Altland and Ben D. Simons. *Condensed Matter Field Theory.* Cambridge University Press, 2 edition, 2010.

[11] Immanuel Bloch, Jean Dalibard, and Sylvain Nascimbène. Quantum simulations with ultracold quantum gases. *Nature Physics*, 8:267 EP –, 04 2012.

[12] Y. S. Patil, S. Chakram, and M. Vengalattore. Measurement-Induced Localization of an Ultracold Lattice Gas. *Phys. Rev. Lett.*, 115:140402, Oct 2015.

[13] Henrik P. Lüschen, Pranjal Bordia, Sean S. Hodgman, Michael Schreiber, Saubhik Sarkar, Andrew J. Daley, Mark H. Fischer, Ehud Altman, Immanuel Bloch, and Ulrich Schneider. Signatures of Many-Body Localization in a Controlled Open Quantum System. *Phys. Rev. X*, 7:011034, Mar 2017.

[14] N. Malossi, M. M. Valado, S. Scotto, P. Huillery, P. Pillet, D. Ciampini, E. Arimondo, and O. Morsch. Full Counting Statistics and Phase Diagram of a Dissipative Rydberg Gas. *Phys. Rev. Lett.*, 113:023006, Jul 2014.

[15] F. Letscher, O. Thomas, T. Niederprüm, M. Fleischhauer, and H. Ott. Bistability Versus Metastability in Driven Dissipative Rydberg Gases. *Phys. Rev. X*, 7:021020, May 2017.

[16] Julio T. Barreiro, Markus Müller, Philipp Schindler, Daniel Nigg, Thomas Monz, Michael Chwalla, Markus Hennrich, Christian F. Roos, Peter Zoller, and Rainer Blatt. An open-system quantum simulator with trapped ions. *Nature*, 470:486 EP –, 02 2011.

[17] Markus Müller, Sebastian Diehl, Guido Pupillo, and Peter Zoller. Engineered Open Systems and Quantum Simulations with Atoms and Ions. In Paul Berman, Ennio Arimondo, and Chun Lin, editors, *Advances in Atomic, Molecular, and Optical Physics*, volume 61 of *Advances In Atomic, Molecular, and Optical Physics*, pages 1 – 80. Academic Press, 2012.

[18] Sebastian Diehl, Enrique Rico, Mikhail A. Baranov, and Peter Zoller. Topology by dissipation in atomic quantum wires. *Nature Physics*, 7:971 EP –, 10 2011.

[19] M. Aidelsburger, M. Lohse, C. Schweizer, M. Atala, J. T. Barreiro, S. Nascimbène, N. R. Cooper, I. Bloch, and N. Goldman. Measuring the Chern number of Hofstadter bands with ultracold bosonic atoms. *Nature Physics*, 11:162 EP –, 12 2014.

[20] Ameneh Sheikhan, Ferdinand Brennecke, and Corinna Kollath. Cavity-induced generation of nontrivial topological states in a two-dimensional Fermi gas. *Phys. Rev. A*, 94:061603, Dec 2016.

[21] Michael J. Larsen Michael H. Freedman, Alexei Kitaev and Zhenghan Wang. Topological quantum computation. *Bull. Amer. Math. Soc.*, 40:31–38, 2003.

[22] Michael A. Nielsen and Isaac L. Chuang. *Quantum Computation and Quantum Information: 10th Anniversary Edition.* Cambridge University Press, New York, NY, USA, 10th edition, 2011.

[23] Helmut Ritsch, Peter Domokos, Ferdinand Brennecke, and Tilman Esslinger. Cold atoms in cavity-generated dynamical optical potentials. *Rev. Mod. Phys.*, 85:553–601, Apr 2013.

[24] K. Baumann, C. Guerlin, F. Brennecke, and T. Esslinger. Dicke quantum phase transition with a superfluid gas in an optical cavity. *Nature*, 464:1301, 2010.

[25] Jens Klinder, Hans Keßler, Matthias Wolke, Ludwig Mathey, and Andreas Hemmerich. Dynamical phase transition in the open Dicke model. *Proceedings of the National Academy of Sciences*, 112(11):3290–3295, 2015.

[26] D. N. Basov, Richard D. Averitt, Dirk van der Marel, Martin Dressel, and Kristjan Haule. Electrodynamics of correlated electron materials. *Rev. Mod. Phys.*, 83:471–541, Jun 2011.

[27] Claudio Giannetti, Massimo Capone, Daniele Fausti, Michele Fabrizio, Fulvio Parmigiani, and Dragan Mihailovic. Ultrafast optical spectroscopy of strongly correlated materials and high-temperature superconductors: a non-equilibrium approach. *Advances in Physics*, 65(2):58–238, 2016.

[28] J. Zhang and R.D. Averitt. Dynamics and Control in Complex Transition Metal Oxides. *Annual Review of Materials Research*, 44(1):19–43, 2014.

[29] D. Fausti, R. I. Tobey, N. Dean, S. Kaiser, A. Dienst, M. C. Hoffmann, S. Pyon, T. Takayama, H. Takagi, and A. Cavalleri. Light-Induced Superconductivity in a Stripe-Ordered Cuprate. *Science*, 331(6014):189–191, 2011.

[30] Ulrich Schollwöck. The density-matrix renormalization group in the age of matrix product states. *Annals of Physics*, 326(1):96 – 192, 2011. January 2011 Special Issue.

[31] Ahsan Nazir. Lecture notes on open quantum systems. 2012.

[32] G. Lindblad. On the generators of quantum dynamical semigroups. *Comm. Math. Phys.*, 48(2):119–130, 1976.

Bibliography

[33] Gernot Schaller. *Open Quantum Systems Far from Equilibrium.* Springer International Publishing, 2014.

[34] Heinz-Peter Breuer, Bernd Kappler, and Francesco Petruccione. Stochastic wave-function approach to the calculation of multitime correlation functions of open quantum systems. *Phys. Rev. A*, 56:2334–2351, Sep 1997.

[35] Daniel A. Steck. *Quantum and Atom Optics, available at http://steck.us/teaching.* Open Publication License, New York, revision 0.12.5, 26 january 2019. edition, 2007.

[36] William D. Phillips. Nobel Lecture: Laser cooling and trapping of neutral atoms. *Rev. Mod. Phys.*, 70:721–741, Jul 1998.

[37] Wolfgang Ketterle and N.J. Van Druten. Evaporative Cooling of Trapped Atoms. volume 37 of *Advances In Atomic, Molecular, and Optical Physics*, pages 181 – 236. Academic Press, 1996.

[38] K. B. Davis, M. O. Mewes, M. R. Andrews, N. J. van Druten, D. S. Durfee, D. M. Kurn, and W. Ketterle. Bose-Einstein Condensation in a Gas of Sodium Atoms. *Phys. Rev. Lett.*, 75:3969–3973, Nov 1995.

[39] Michael Köhl, Henning Moritz, Thilo Stöferle, Kenneth Günter, and Tilman Esslinger. Fermionic Atoms in a Three Dimensional Optical Lattice: Observing Fermi Surfaces, Dynamics, and Interactions. *Phys. Rev. Lett.*, 94:080403, Mar 2005.

[40] Immanuel Bloch. Ultracold quantum gases in optical lattices. *Nature Physics*, 1:23 EP –, 10 2005.

[41] Neil W. Ashcroft and David N. Mermin. *Festkörperphysik.* Oldenburg-Verlag München, Wien, 2001.

[42] Ph. Courteille, R. S. Freeland, D. J. Heinzen, F. A. van Abeelen, and B. J. Verhaar. Observation of a Feshbach Resonance in Cold Atom Scattering. *Phys. Rev. Lett.*, 81:69–72, Jul 1998.

[43] S. Inouye, M. R. Andrews, J. Stenger, H. J. Miesner, D. M. Stamper-Kurn, and W. Ketterle. Observation of Feshbach resonances in a Bose–Einstein condensate. *Nature*, 392:151 EP –, 03 1998.

[44] K. M. O'Hara, S. L. Hemmer, M. E. Gehm, S. R. Granade, and J. E. Thomas. Observation of a Strongly Interacting Degenerate Fermi Gas of Atoms. *Science*, 298(5601):2179–2182, 2002.

[45] Immanuel Bloch, Jean Dalibard, and Wilhelm Zwerger. Many-body physics with ultracold gases. *Rev. Mod. Phys.*, 80:885–964, Jul 2008.

[46] Markus Greiner, Olaf Mandel, Tilman Esslinger, Theodor W. Hänsch, and Immanuel Bloch. Quantum phase transition from a superfluid to a Mott insulator in a gas of ultracold atoms. *Nature*, 415:39 EP –, 01 2002.

[47] C. A. Regal, M. Greiner, and D. S. Jin. Observation of Resonance Condensation of Fermionic Atom Pairs. *Phys. Rev. Lett.*, 92:040403, Jan 2004.

[48] C. Chin, M. Bartenstein, A. Altmeyer, S. Riedl, S. Jochim, J. Hecker Denschlag, and

R. Grimm. Observation of the Pairing Gap in a Strongly Interacting Fermi Gas. *Science*, 305(5687):1128–1130, 2004.

[49] M. Aidelsburger, M. Atala, M. Lohse, J. T. Barreiro, B. Paredes, and I. Bloch. Realization of the Hofstadter Hamiltonian with Ultracold Atoms in Optical Lattices. *Phys. Rev. Lett.*, 111:185301, Oct 2013.

[50] S. Diehl, A. Micheli, A. Kantian, B. Kraus, H. P. Büchler, and P. Zoller. Quantum states and phases in driven open quantum systems with cold atoms. *Nature Physics*, 4:878 EP –, 09 2008.

[51] J. Eisert, M. Cramer, and M. B. Plenio. Colloquium: Area laws for the entanglement entropy. *Rev. Mod. Phys.*, 82:277–306, Feb 2010.

[52] F. Verstraete and J. I. Cirac. Matrix product states represent ground states faithfully. *Phys. Rev. B*, 73:094423, Mar 2006.

[53] Till D. Kühner, Steven R. White, and H. Monien. One-dimensional Bose-Hubbard model with nearest-neighbor interaction. *Phys. Rev. B*, 61:12474–12489, May 2000.

[54] Ryotaro Arita, Kazuhiko Kuroki, Hideo Aoki, and Michele Fabrizio. Density-matrix renormalization-group study of the spin gap in a one-dimensional Hubbard model: Effect of the distant transfer and exchange coupling. *Phys. Rev. B*, 57:10324–10327, May 1998.

[55] G. Vidal. Entanglement Renormalization. *Phys. Rev. Lett.*, 99:220405, Nov 2007.

[56] F. Verstraete, D. Porras, and J. I. Cirac. Density Matrix Renormalization Group and Periodic Boundary Conditions: A Quantum Information Perspective. *Phys. Rev. Lett.*, 93:227205, Nov 2004.

[57] Tomotoshi Nishino, Yasuhiro Hieida, Kouichi Okunishi, Nobuya Maeshima, Yasuhiro Akutsu, and Andrej Gendiar. Two-Dimensional Tensor Product Variational Formulation. *Progress of Theoretical Physics*, 105(3):409–417, 2001.

[58] A J Daley, C Kollath, U Schollwöck, and G Vidal. Time-dependent density-matrix renormalization-group using adaptive effective Hilbert spaces. *Journal of Statistical Mechanics: Theory and Experiment*, 2004(04):P04005, 2004.

[59] Elliott H. Lieb and Derek W. Robinson. The finite group velocity of quantum spin systems. *Communications in Mathematical Physics*, 28(3):251–257, Sep 1972.

[60] Michele Dolfi, Bela Bauer, Sebastian Keller, Alexandr Kosenkov, Timothée Ewart, Adrian Kantian, Thierry Giamarchi, and Matthias Troyer. Matrix product state applications for the ALPS project. *Computer Physics Communications*, 185(12):3430 – 3440, 2014.

[61] Daniel Jaschke, Michael L. Wall, and Lincoln D. Carr. Open source Matrix Product States: Opening ways to simulate entangled many-body quantum systems in one dimension. *Computer Physics Communications*, 225:59 – 91, 2018.

[62] M. et. al. Stoudenmire. ITensor C++ library, available at `http://itensor.org`. Release 2.1, 2018.

[63] Osslan Vergara, Raul Pinto Elias, and Vianey Sanchez. Singular value decomposition image compression system for automatic object recognition. pages 95–100, 01 2006.

Bibliography

[64] I. T. Jolliffe. *Principal Component Analysis, Second Edition.* Springer New York, second edition edition, 2002.

[65] Roman Orus. A practical introduction to tensor networks: Matrix product states and projected entangled pair states. *Annals of Physics*, 349:117 − 158, 2014.

[66] Andreas Weichselbaum. Non-abelian symmetries in tensor networks: A quantum symmetry space approach. *Annals of Physics*, 327(12):2972 − 3047, 2012.

[67] M. et. al. Stoudenmire. ITensor C++ library documentation on IQTensors, available at `http://itensor.org`. Release 2.1, 2018.

[68] Steven R. White. Density matrix formulation for quantum renormalization groups. *Phys. Rev. Lett.*, 69:2863–2866, Nov 1992.

[69] F. Verstraete, V. Murg, and J.I. Cirac. Matrix product states, projected entangled pair states, and variational renormalization group methods for quantum spin systems. *Advances in Physics*, 57(2):143–224, 2008.

[70] Michael P. Zaletel, Roger S. K. Mong, Christoph Karrasch, Joel E. Moore, and Frank Pollmann. Time-evolving a matrix product state with long-ranged interactions. *Phys. Rev. B*, 91:165112, Apr 2015.

[71] Jutho Haegeman, J. Ignacio Cirac, Tobias J. Osborne, Iztok Piorn, Henri Verschelde, and Frank Verstraete. Time-Dependent Variational Principle for Quantum Lattices. *Phys. Rev. Lett.*, 107:070601, Aug 2011.

[72] Jutho Haegeman, Christian Lubich, Ivan Oseledets, Bart Vandereycken, and Frank Verstraete. Unifying time evolution and optimization with matrix product states. *Phys. Rev. B*, 94:165116, Oct 2016.

[73] Masuo Suzuki. Generalized Trotter's formula and systematic approximants of exponential operators and inner derivations with applications to many-body problems. *Communications in Mathematical Physics*, 51(2):183–190, Jun 1976.

[74] Naomichi Hatano and Masuo Suzuki. *Finding Exponential Product Formulas of Higher Orders.* Springer Berlin Heidelberg, Berlin, Heidelberg, 2005.

[75] Pasquale Calabrese and John Cardy. Entanglement entropy and quantum field theory. *Journal of Statistical Mechanics: Theory and Experiment*, 2004(06):P06002, 2004.

[76] Tobias J. Osborne. Efficient Approximation of the Dynamics of One-Dimensional Quantum Spin Systems. *Phys. Rev. Lett.*, 97:157202, Oct 2006.

[77] T. Antal, Z. Rácz, A. Rákos, and G. M. Schütz. Transport in the XX chain at zero temperature: Emergence of flat magnetization profiles. *Phys. Rev. E*, 59:4912–4918, May 1999.

[78] Dominique Gobert, Corinna Kollath, Ulrich Schollwöck, and Gunter Schütz. Real-time dynamics in spin-$\frac{1}{2}$ chains with adaptive time-dependent density matrix renormalization group. *Phys. Rev. E*, 71:036102, Mar 2005.

[79] Alexander Weisse and Holger Fehske. *Exact Diagonalization Techniques.* Springer Berlin Heidelberg, Berlin, Heidelberg, 2008.

[80] Reinhard M. Noack and Salvatore R. Manmana. Diagonalization and Numerical Renormalization Group Based Methods for Interacting Quantum Systems. *AIP Conference Pro-*

ceedings, 789(1):93–163, 2005.

[81] H. Q. Lin. Exact diagonalization of quantum-spin models. *Phys. Rev. B*, 42:6561–6567, Oct 1990.

[82] F. Heidrich-Meisner, A. Honecker, and T. Vekua. Frustrated ferromagnetic spin-$\frac{1}{2}$ chain in a magnetic field: The phase diagram and thermodynamic properties. *Phys. Rev. B*, 74:020403, Jul 2006.

[83] Andreas M. Läuchli, Julien Sudan, and Erik S. Sørensen. Ground-state energy and spin gap of spin-$\frac{1}{2}$ Kagomé-Heisenberg antiferromagnetic clusters: Large-scale exact diagonalization results. *Phys. Rev. B*, 83:212401, Jun 2011.

[84] Masao Ogata, M. U. Luchini, S. Sorella, and F. F. Assaad. Phase diagram of the one-dimensional t-J model. *Phys. Rev. Lett.*, 66:2388–2391, May 1991.

[85] Gerardo Martinez and Peter Horsch. Spin polarons in the t-J model. *Phys. Rev. B*, 44:317–331, Jul 1991.

[86] Michel Caffarel and Werner Krauth. Exact diagonalization approach to correlated fermions in infinite dimensions: Mott transition and superconductivity. *Phys. Rev. Lett.*, 72:1545–1548, Mar 1994.

[87] Shi-Jian Gu, Shu-Sa Deng, You-Quan Li, and Hai-Qing Lin. Entanglement and Quantum Phase Transition in the Extended Hubbard Model. *Phys. Rev. Lett.*, 93:086402, Aug 2004.

[88] William H. Press, Saul A. Teukolsky, William T. Vetterling, and Brian P. Flannery. *Numerical Recipes 3rd Edition: The Art of Scientific Computing*. Cambridge University Press, New York, NY, USA, 3 edition, 2007.

[89] Z. Bai, J. Demmel, J. Dongarra, A. Ruhe, and H. van der Vorst. Templates for the Solution of Algebraic Eigenvalue Problems: A Practical Guide. *SIAM*, 2000.

[90] C. Kollath, A.M. Läuchli, and E. Altman. Quench dynamics and non-equilibrium phase diagram of the Bose-Hubbard model. *Phys. Rev. Lett.*, 98:180601, 2007.

[91] Alexander Wietek and Andreas M. Läuchli. Sublattice coding algorithm and distributed memory parallelization for large-scale exact diagonalizations of quantum many-body systems. *Phys. Rev. E*, 98:033309, Sep 2018.

[92] Berislav Buča and Tomaž Prosen. Strongly correlated non-equilibrium steady states with currents – quantum and classical picture. *The European Physical Journal Special Topics*, 227(3):421–444, Sep 2018.

[93] F. Gantmacher. *The Theory of Matrices, Volume 2*. Chelsea Publishing, reprinted by American Mathematical Society, volume 2 edition, 2000.

[94] Berislav Buča and Tomaž Prosen. A note on symmetry reductions of the Lindblad equation: transport in constrained open spin chains. *New Journal of Physics*, 14(7):073007, jul 2012.

[95] Victor V. Albert and Liang Jiang. Symmetries and conserved quantities in Lindblad master equations. *Phys. Rev. A*, 89:022118, Feb 2014.

[96] Bruno Sciolla, Dario Poletti, and Corinna Kollath. Two-Time Correlations Probing the Dynamics of Dissipative Many-Body Quantum Systems: Aging and Fast Relaxation. *Phys.*

Rev. Lett., 114:170401, Apr 2015.

[97] David P Landau and Kurt Binder. *A guide to Monte Carlo simulations in statistical physics*. Cambridge university press, 2014.

[98] B. Meng and W. H. Weinberg. Monte Carlo simulations of temperature programmed desorption spectra. *The Journal of Chemical Physics*, 100(7):5280–5289, 1994.

[99] Dario Poletti, Jean-Sébastien Bernier, Antoine Georges, and Corinna Kollath. Interaction-Induced Impeding of Decoherence and Anomalous Diffusion. *Phys. Rev. Lett.*, 109:045302, Jul 2012.

[100] Benjamin Everest, Igor Lesanovsky, Juan P. Garrahan, and Emanuele Levi. Role of interactions in a dissipative many-body localized system. *Phys. Rev. B*, 95:024310, Jan 2017.

[101] Daniel Jaschke, Simone Montangero, and Lincoln D Carr. One-dimensional many-body entangled open quantum systems with tensor network methods. *Quantum Science and Technology*, 4(1):013001, 2018.

[102] F. Verstraete, J. J. Garcia-Ripoll, and J. I. Cirac. Matrix Product Density Operators: Simulation of Finite-Temperature and Dissipative Systems. *Phys. Rev. Lett.*, 93:207204, Nov 2004.

[103] Michael Zwolak and Guifre Vidal. Mixed-State Dynamics in One-Dimensional Quantum Lattice Systems: A Time-Dependent Superoperator Renormalization Algorithm. *Phys. Rev. Lett.*, 93:207205, Nov 2004.

[104] Jean Dalibard, Yvan Castin, and Klaus Molmer. Wave-function approach to dissipative processes in quantum optics. *Phys. Rev. Lett.*, 68:580–583, Feb 1992.

[105] C. W. Gardiner, A. S. Parkins, and P. Zoller. Wave-function quantum stochastic differential equations and quantum-jump simulation methods. *Phys. Rev. A*, 46:4363–4381, Oct 1992.

[106] Andrew J. Daley. Quantum trajectories and open many-body quantum systems. *Advances in Physics*, 63(2):77–149, 2014.

[107] A. J. Daley, J. M. Taylor, S. Diehl, M. Baranov, and P. Zoller. Atomic Three-Body Loss as a Dynamical Three-Body Interaction. *Phys. Rev. Lett.*, 102:040402, Jan 2009.

[108] A. Kantian, M. Dalmonte, S. Diehl, W. Hofstetter, P. Zoller, and A. J. Daley. Atomic Color Superfluid via Three-Body Loss. *Phys. Rev. Lett.*, 103:240401, Dec 2009.

[109] Peter Barmettler and Corinna Kollath. Controllable manipulation and detection of local densities and bipartite entanglement in a quantum gas by a dissipative defect. *Phys. Rev. A*, 84:041606, Oct 2011.

[110] Klaus Mølmer, Yvan Castin, and Jean Dalibard. Monte Carlo wave-function method in quantum optics. *J. Opt. Soc. Am. B*, 10(3):524–538, Mar 1993.

[111] Man-Duen Choi. Completely positive linear maps on complex matrices. *Linear Algebra and its Applications*, 10(3):285 – 290, 1975.

[112] E M Stoudenmire and Steven R White. Minimally entangled typical thermal state algorithms. *New Journal of Physics*, 12(5):055026, 2010.

[113] Jian Cui, J. Ignacio Cirac, and Mari Carmen Bañuls. Variational Matrix Product Operators

for the Steady State of Dissipative Quantum Systems. *Phys. Rev. Lett.*, 114:220601, Jun 2015.

[114] B. M. Garraway and P. L. Knight. Evolution of quantum superpositions in open environments: Quantum trajectories, jumps, and localization in phase space. *Phys. Rev. A*, 50:2548–2563, Sep 1994.

[115] Peter Goetsch and Robert Graham. Linear stochastic wave equations for continuously measured quantum systems. *Phys. Rev. A*, 50:5242–5255, Dec 1994.

[116] David Landau and Kurt Binder. *A Guide to Monte Carlo Simulations in Statistical Physics.* Cambridge University Press, New York, NY, USA, 2005.

[117] SPI Inc. OpenMPI High Performance Message Passing Library, availiable at `https://www.open-mpi.org`. Release 1.6.5, 2013.

[118] Lars Bonnes and Andreas M. Läuchli. Superoperators vs. Trajectories for Matrix Product State Simulations of Open Quantum System: A Case Study. *arXiv:1411.4831*, 2014.

[119] Masami Yasuda and Fujio Shimizu. Observation of Two-Atom Correlation of an Ultracold Neon Atomic Beam. *Phys. Rev. Lett.*, 77:3090–3093, Oct 1996.

[120] L. Feligioni, O. Panella, Y. N. Srivastava, and A. Widom. Two-time correlation functions: stochastic and conventional quantum mechanics. *The European Physical Journal B - Condensed Matter and Complex Systems*, 48(2):233–242, Nov 2005.

[121] H.P. Breuer, B. Kappler, and F. Petruccione. Heisenberg picture operators in the stochastic wave function approach to open quantum systems. *The European Physical Journal D - Atomic, Molecular, Optical and Plasma Physics*, 1(1):9–13, Jan 1998.

[122] K. v. Klitzing, G. Dorda, and M. Pepper. New Method for High-Accuracy Determination of the Fine-Structure Constant Based on Quantized Hall Resistance. *Phys. Rev. Lett.*, 45:494–497, Aug 1980.

[123] D. J. Thouless, M. Kohmoto, M. P. Nightingale, and M. den Nijs. Quantized Hall Conductance in a Two-Dimensional Periodic Potential. *Phys. Rev. Lett.*, 49:405–408, Aug 1982.

[124] Di Xiao, Ming-Che Chang, and Qian Niu. Berry phase effects on electronic properties. *Rev. Mod. Phys.*, 82:1959–2007, Jul 2010.

[125] Xiao-Liang Qi and Shou-Cheng Zhang. Topological insulators and superconductors. *Rev. Mod. Phys.*, 83:1057–1110, Oct 2011.

[126] M. Z. Hasan and C. L. Kane. Colloquium: Topological insulators. *Rev. Mod. Phys.*, 82:3045–3067, Nov 2010.

[127] N. Goldman, J. C. Budich, and P. Zoller. Topological quantum matter with ultracold gases in optical lattices. *Nature Physics*, 12:639 EP –, 06 2016.

[128] Jean Dalibard, Fabrice Gerbier, Gediminas Juzeliunas, and Patrik Öhberg. Colloquium: Artificial gauge potentials for neutral atoms. *Rev. Mod. Phys.*, 83:1523–1543, Nov 2011.

[129] Hirokazu Miyake, Georgios A. Siviloglou, Colin J. Kennedy, William Cody Burton, and Wolfgang Ketterle. Realizing the Harper Hamiltonian with Laser-Assisted Tunneling in Optical Lattices. *Phys. Rev. Lett.*, 111:185302, Oct 2013.

[130] Marcos Atala, Monika Aidelsburger, Michael Lohse, Julio T. Barreiro, Belén Paredes, and

Immanuel Bloch. Observation of chiral currents with ultracold atoms in bosonic ladders. *Nature Physics*, 10:588 EP –, 07 2014.

[131] A. Celi, P. Massignan, J. Ruseckas, N. Goldman, I. B. Spielman, G. Juzeliūnas, and M. Lewenstein. Synthetic Gauge Fields in Synthetic Dimensions. *Phys. Rev. Lett.*, 112:043001, Jan 2014.

[132] Eyal Cornfeld and Eran Sela. Chiral currents in one-dimensional fractional quantum Hall states. *Phys. Rev. B*, 92:115446, Sep 2015.

[133] Marcello Calvanese Strinati, Eyal Cornfeld, Davide Rossini, Simone Barbarino, Marcello Dalmonte, Rosario Fazio, Eran Sela, and Leonardo Mazza. Laughlin-like States in Bosonic and Fermionic Atomic Synthetic Ladders. *Phys. Rev. X*, 7:021033, Jun 2017.

[134] Sebastian Greschner, Michele Filippone, and Thierry Giamarchi. Universal Hall Response in Synthetic Dimensions. 2018.

[135] Markus Müller, Sebastian Diehl, Guido Pupillo, and Peter Zoller. Engineered Open Systems and Quantum Simulations with Atoms and Ions. In Paul Berman, Ennio Arimondo, and Chun Lin, editors, *Advances in Atomic, Molecular, and Optical Physics*, volume 61 of *Advances In Atomic, Molecular, and Optical Physics*, pages 1 – 80. Academic Press, 2012.

[136] Peter Domokos and Helmut Ritsch. Collective Cooling and Self-Organization of Atoms in a Cavity. *Phys. Rev. Lett.*, 89:253003, Dec 2002.

[137] F. Dimer, B. Estienne, A. S. Parkins, and H. J. Carmichael. Proposed realization of the Dicke-model quantum phase transition in an optical cavity QED system. *Phys. Rev. A*, 75:013804, Jan 2007.

[138] Nagy, D., Szirmai, G., and Domokos, P. Self-organization of a Bose-Einstein condensate in an optical cavity. *Eur. Phys. J. D*, 48(1):127–137, 2008.

[139] Francesco Piazza, Philipp Strack, and Wilhelm Zwerger. Bose-Einstein condensation versus Dicke-Hepp-Lieb transition in an optical cavity. *Annals of Physics*, 339:135 – 159, 2013.

[140] M. Reza Bakhtiari, A. Hemmerich, H. Ritsch, and M. Thorwart. Nonequilibrium Phase Transition of Interacting Bosons in an Intra-Cavity Optical Lattice. *Phys. Rev. Lett.*, 114:123601, Mar 2015.

[141] Renate Landig, Lorenz Hruby, Nishant Dogra, Manuele Landini, Rafael Mottl, Tobias Donner, and Tilman Esslinger. Quantum phases from competing short- and long-range interactions in an optical lattice. *Nature*, 532:476 EP –, 04 2016.

[142] Corinna Kollath, Ameneh Sheikhan, Stefan Wolff, and Ferdinand Brennecke. Ultracold Fermions in a Cavity-Induced Artificial Magnetic Field. *Phys. Rev. Lett.*, 116:060401, Feb 2016.

[143] Ameneh Sheikhan, Ferdinand Brennecke, and Corinna Kollath. Cavity-induced chiral states of fermionic quantum gases. *Phys. Rev. A*, 93:043609, Apr 2016.

[144] Stefan Wolff, Ameneh Sheikhan, and Corinna Kollath. Dissipative time evolution of a chiral state after a quantum quench. *Phys. Rev. A*, 94:043609, Oct 2016.

[145] Y. J. Lin, R. L. Compton, K. Jiménez-García, J. V. Porto, and I. B. Spielman. Synthetic

magnetic fields for ultracold neutral atoms. *Nature*, 462:628 EP –, 12 2009.

[146] Y.-J. Lin, R. L. Compton, A. R. Perry, W. D. Phillips, J. V. Porto, and I. B. Spielman. Bose-Einstein Condensate in a Uniform Light-Induced Vector Potential. *Phys. Rev. Lett.*, 102:130401, Mar 2009.

[147] Jean Dalibard, Fabrice Gerbier, Gediminas Juzeliunas, and Patrik Öhberg. Colloquium: Artificial gauge potentials for neutral atoms. *Rev. Mod. Phys.*, 83:1523–1543, Nov 2011.

[148] D Jaksch and P Zoller. Creation of effective magnetic fields in optical lattices: the Hofstadter butterfly for cold neutral atoms. *New Journal of Physics*, 5(1):56, 2003.

[149] Hirokazu Miyake, Georgios A. Siviloglou, Colin J. Kennedy, William Cody Burton, and Wolfgang Ketterle. Realizing the Harper Hamiltonian with Laser-Assisted Tunneling in Optical Lattices. *Phys. Rev. Lett.*, 111:185302, Oct 2013.

[150] C. Maschler, I. B. Mekhov, and H. Ritsch. Ultracold atoms in optical lattices generated by quantized light fields. *The European Physical Journal D*, 46(3):545–560, 2008.

[151] Eric Jones, Travis Oliphant, Pearu Peterson, et al. scipy.stats.kstestSciPy: Open source scientific tools for Python, 2001–. [Online; accessed 19.12.2018].

[152] B. Misra and E. C. G. Sudarshan. The Zeno's paradox in quantum theory. *Journal of Mathematical Physics*, 18(4):756–763, 1977.

[153] Stefan Wolff, Jean-Sebastien Bernier, Dario Poletti, Ameneh Sheikhan, and Corinna Kollath. Evolution of two-time correlations in dissipative quantum spin systems: aging and hierarchical dynamics. 2018.

[154] Donghui Lu, Inna M. Vishik, Ming Yi, Yulin Chen, Rob G. Moore, and Zhi-Xun Shen. Angle-Resolved Photoemission Studies of Quantum Materials. *Annual Review of Condensed Matter Physics*, 3(1):129–167, 2012.

[155] Steven T. Bramwell and Bernhard Keimer. Neutron scattering from quantum condensed matter. *Nature Materials*, 13:763–767, 2014.

[156] Tilman Esslinger. Fermi-Hubbard Physics with Atoms in an Optical Lattice. *Annual Review of Condensed Matter Physics*, 1(1):129–152, 2010.

[157] Jean-Sébastien Bernier, Ryan Tan, Lars Bonnes, Chu Guo, Dario Poletti, and Corinna Kollath. Light-Cone and Diffusive Propagation of Correlations in a Many-Body Dissipative System. *Phys. Rev. Lett.*, 120:020401, Jan 2018.

[158] Jamir Marino and Alessandro Silva. Relaxation, prethermalization, and diffusion in a noisy quantum Ising chain. *Phys. Rev. B*, 86:060408, Aug 2012.

[159] Michael Buchhold and Sebastian Diehl. Nonequilibrium universality in the heating dynamics of interacting Luttinger liquids. *Phys. Rev. A*, 92:013603, Jul 2015.

[160] L. Berthier and G. Biroli. Theoretical perspective on the glass transition and amorphous materials. *Review of Modern Physics*, 83:587, 2011.

[161] F. Yoshihara, K. Harrabi, A. O. Niskanen, Y. Nakamura, and J. S. Tsai. Decoherence of Flux Qubits due to $1/f$ Flux Noise. *Phys. Rev. Lett.*, 97:167001, Oct 2006.

[162] H. Pichler, A. J. Daley, and P. Zoller. Nonequilibrium dynamics of bosonic atoms in optical lattices: Decoherence of many-body states due to spontaneous emission. *Phys. Rev. A*,

Bibliography

82:063605, Dec 2010.

[163] Heike Schwager, J. Ignacio Cirac, and Géza Giedke. Dissipative spin chains: Implementation with cold atoms and steady-state properties. *Phys. Rev. A*, 87:022110, Feb 2013.

[164] J. J. Mendoza-Arenas, T. Grujic, D. Jaksch, and S. R. Clark. Dephasing enhanced transport in nonequilibrium strongly correlated quantum systems. *Phys. Rev. B*, 87:235130, Jun 2013.

[165] Zi Cai and Thomas Barthel. Algebraic versus Exponential Decoherence in Dissipative Many-Particle Systems. *Phys. Rev. Lett.*, 111:150403, Oct 2013.

[166] H. J. Mikeska and A. Kolezhuk. One-dimensional magnetism. In U. Schollwöck, J. Richter, D. Farnell, and R. Bishop, editors, *Quantum magnetism*, volume 645, page 1. Springer, Lecture notes in Physics, 2004.

[167] Jeffrey Goldstone, Abdus Salam, and Steven Weinberg. Broken Symmetries. *Phys. Rev.*, 127:965–970, Aug 1962.

[168] T Koma and B Nachtergaele. The Spectral Gap of the Ferromagnetic XXZ-Chain. *Letters in Mathematical Physics*, 40(1):1–16, Apr 1997.

[169] T. Giamarchi. *Quantum Physics in One Dimension.* Oxford University Press, Oxford, 2004.

[170] Henkel Malte, Pleimling Michel, and Sanctuary Roland. *Ageing and the Glass Transition.* Springer, ninth dover printing, tenth gpo printing edition, 2007.

[171] Milton Abramowitz and Irene A. Stegun. *Handbook of Mathematical Functions with Formulas, Graphs, and Mathematical Tables.* Dover, New York, ninth dover printing, tenth gpo printing edition, 1964.

[172] M. C. Fischer, B. Gutiérrez-Medina, and M. G. Raizen. Observation of the Quantum Zeno and Anti-Zeno Effects in an Unstable System. *Phys. Rev. Lett.*, 87:040402, Jul 2001.

[173] N. Syassen, D. M. Bauer, M. Lettner, T. Volz, D. Dietze, J. J. García-Ripoll, J. I. Cirac, G. Rempe, and S. Dürr. Strong Dissipation Inhibits Losses and Induces Correlations in Cold Molecular Gases. *Science*, 320(5881):1329–1331, 2008.

[174] G. Barontini, R. Labouvie, F. Stubenrauch, A. Vogler, V. Guarrera, and H. Ott. Controlling the Dynamics of an Open Many-Body Quantum System with Localized Dissipation. *Phys. Rev. Lett.*, 110:035302, Jan 2013.

[175] Waseem S. Bakr, Jonathon I. Gillen, Amy Peng, Simon Fölling, and Markus Greiner. A quantum gas microscope for detecting single atoms in a Hubbard-regime optical lattice. *Nature*, 462:74 EP –, 11 2009.

[176] Jacob F. Sherson, Christof Weitenberg, Manuel Endres, Marc Cheneau, Immanuel Bloch, and Stefan Kuhr. Single-atom-resolved fluorescence imaging of an atomic Mott insulator. *Nature*, 467:68 EP –, 08 2010.

[177] Samuel Häusler, Shuta Nakajima, Martin Lebrat, Dominik Husmann, Sebastian Krinner, Tilman Esslinger, and Jean-Philippe Brantut. Scanning Gate Microscope for Cold Atomic Gases. *Phys. Rev. Lett.*, 119:030403, Jul 2017.

[178] V. S. Shchesnovich and D. S. Mogilevtsev. Three-site Bose-Hubbard model subject to atom losses: Boson-pair dissipation channel and failure of the mean-field approach. *Phys. Rev. A*, 82:043621, Oct 2010.

[179] Belén Paredes, Artur Widera, Valentin Murg, Olaf Mandel, Simon Fölling, Ignacio Cirac, Gora V. Shlyapnikov, Theodor W. Hänsch, and Immanuel Bloch. Tonks–Girardeau gas of ultracold atoms in an optical lattice. *Nature*, 429:277 EP –, 05 2004.

[180] Toshiya Kinoshita, Trevor Wenger, and David S. Weiss. Observation of a One-Dimensional Tonks-Girardeau Gas. *Science*, 305(5687):1125–1128, 2004.

[181] Heinrich Frö ml, Alessio Chiocchetta, Corinna Kollath, and Sebastian Diehl. Fluctuation-induced quantum Zeno effect. 2018.

[182] T. Kock, M. Ölschläger, A. Ewerbeck, W.-M. Huang, L. Mathey, and A. Hemmerich. Observing Chiral Superfluid Order by Matter-Wave Interference. *Phys. Rev. Lett.*, 114:115301, Mar 2015.

[183] Heinz-Peter Breuer. Foundations and measures of quantum non-Markovianity. *Journal of Physics B: Atomic, Molecular and Optical Physics*, 45(15):154001, jul 2012.

[184] Xiansong Xu, Juzar Thingna, Chu Guo, and Dario Poletti. Many-body open quantum systems beyond Lindblad master equations. *Phys. Rev. A*, 99:012106, Jan 2019.

[185] M. T. Hutchings, G. Shirane, R. J. Birgeneau, and S. L. Holt. Spin Dynamics in the One-Dimensional Antiferromagnet $(CD_3)_4$ $NMnCl_3$. *Phys. Rev. B*, 5:1999–2014, Mar 1972.

[186] Fabrice Gerbier and Yvan Castin. Heating rates for an atom in a far-detuned optical lattice. *Phys. Rev. A*, 82:013615, Jul 2010.

[187] Abraham Berman and Robert Plemmons. *Plemmons, R.J.: Nonnegative Matrices in the Mathematical Sciences. SIAM, Philadelphia, PA*. 01 1994.

[188] Jill C. Bonner and Michael E. Fisher. Linear Magnetic Chains with Anisotropic Coupling. *Phys. Rev.*, 135:A640–A658, Aug 1964.

[189] I Affleck, D Gepner, H J Schulz, and T Ziman. Critical behaviour of spin-s Heisenberg antiferromagnetic chains: analytic and numerical results. *Journal of Physics A: Mathematical and General*, 23(20):4725, 1990.

[190] Anders W. Sandvik. Computational Studies of Quantum Spin Systems. *AIP Conference Proceedings*, 1297(1):135–338, 2010.

[191] Elbio Dagotto and T. M. Rice. Surprises on the Way from One- to Two-Dimensional Quantum Magnets: The Ladder Materials. *Science*, 271(5249):618–623, 1996.

[192] H. Bethe. Zur Theorie der Metalle. *Zeitschrift für Physik*, 71(3):205–226, Mar 1931.

[193] M. Reza Bakhtiari, A. Hemmerich, H. Ritsch, and M. Thorwart. Nonequilibrium Phase Transition of Interacting Bosons in an Intra-Cavity Optical Lattice. *Phys. Rev. Lett.*, 114:123601, Mar 2015.

[194] J. Eisert, M. Friesdorf, and C. Gogolin. Quantum many-body systems out of equilibrium. *Nature Physics*, 11:124 EP –, 02 2015.

[195] Tim Langen, Remi Geiger, and Jörg Schmiedmayer. Ultracold Atoms Out of Equilibrium. *Annual Review of Condensed Matter Physics*, 6(1):201–217, 2015.

[196] David R. Dion and Joseph O. Hirschfelder. *Time-Dependent Perturbation of a Two-State Quantum System by a Sinusoidal Field*, pages 265–350. John Wiley and Sons, Ltd, 2007.

[197] Aditi Mitra. Quantum Quench Dynamics. *Annual Review of Condensed Matter Physics*,

9(1):245–259, 2018.

[198] André Eckardt. Colloquium: Atomic quantum gases in periodically driven optical lattices. *Rev. Mod. Phys.*, 89:011004, Mar 2017.

[199] Wolfgang Domcke, Peter Hänggi, and David Tannor. Dynamics of Driven Quantum Systems. *Chemical Physics*, 217(2):117, 1997.

[200] Gianluca Stefanucci and Robert van Leeuwen. *Nonequilibrium Many-Body Theory of Quantum Systems: A Modern Introduction.* Cambridge University Press, Cambridge, 2013.

[201] D. N. Basov, R. D. Averitt, and D. Hsieh. Towards properties on demand in quantum materials. *Nature Materials*, 16:1077 EP –, 10 2017.

[202] D. N. Basov, R. D. Averitt, and D. Hsieh. Towards properties on demand in quantum materials. *Nature Materials*, 16:1077 EP –, 10 2017.

[203] Nicolas Gisin, Grégoire Ribordy, Wolfgang Tittel, and Hugo Zbinden. Quantum cryptography. *Rev. Mod. Phys.*, 74:145–195, Mar 2002.

[204] Dik Bouwmeester, Jian-Wei Pan, Klaus Mattle, Manfred Eibl, Harald Weinfurter, and Anton Zeilinger. Experimental quantum teleportation. *Nature*, 390:575 EP –, 12 1997.